Title
Quantum sensing at high pressures using nitrogen-vacancy centers in diamond

Author
Hsieh, Satcher

Publication Date
2022

Peer reviewed|Thesis/dissertation

Quantum sensing at high pressures using nitrogen-vacancy centers in diamond

by

Satcher Hsieh

A dissertation submitted in partial satisfaction of the

requirements for the degree of

Doctor of Philosophy

in

Physics

in the

Graduate Division

of the

University of California, Berkeley

Committee in charge:

Professor Norman Yao, Chair
Professor Raymond Jeanloz
Professor Joel Moore

Spring 2022

Quantum sensing at high pressures using nitrogen-vacancy centers in diamond

Abstract

Quantum sensing at high pressures using nitrogen-vacancy centers in diamond

by

Satcher Hsieh

Doctor of Philosophy in Physics

University of California, Berkeley

Professor Norman Yao, Chair

Pressure alters all properties of matter. The development of the diamond anvil cell enables the exploration of high pressure phenomena in tabletop experiments. This thesis introduces an optical sensing platform based on nitrogen-vacancy color centers embedded into the culet (tip) of a diamond anvil. The micron-scale spatial resolution and high sensitivity of this platform to stress, magnetic and electric fields opens the door to a hitherto unexplored range of experiments. We demonstrate the versatility of this platform through several applications. In the context of stress, we demonstrate imaging of all normal and shear components of the stress tensor, which enables us to probe the accumulation and dissipation of shear stresses of chrysotile serpentine ($Mg_3(Si_2O_5)(OH)_4$) undergoing brittle failure. In the context of magnetism, we demonstrate imaging of vector magnetic fields under gigapascal pressure, enabling measurement of the $\alpha \rightarrow \epsilon$ transition in elemental iron as well as the complex pressure-temperature phase diagram of elemental gadolinium. We further extend these magnetic imaging capabilities to probe the pressure-induced demagnetization of $4C$ monoclinic pyrrhotite (Fe_7S_8), an iron sulfide mineral found in the Earth's crust as well as in Martian and chondritic meteorites. In the context of electric fields, we show that a spectral feature commonly observed in NV centers originates from the local charge environment of the diamond lattice, and we utilize this understanding to image individual electronic charges with nanometer precision. We extend this understanding to the NV center orbital excited state, whose strong coupling to electric fields enables a protocol that enhances measurement sensitivity by several orders of magnitude. Finally, motivated by the sensitivity of NV centers to electric noise, we theoretically consider polarization fluctuations from polar and dielectric materials and show that this electric noise encodes valuable information about dielectric properties over a range of frequencies and length scales.

To my parents

Contents

List of Figures

List of Tables

Acknowledgments

I would first like to acknowledge my advisor, Prof. Norm Yao. Norm taught me to approach science the way a great artist approaches art: requiring constant practice and refinement, ignoring all the noise in pursuit of the truth, and much better when performed with friends than alone. Norm always encouraged me to pursue the most interesting science and knew how to provide challenges that were always one step beyond what I thought I was capable of doing. I am honored to have have been in the first cohort of the Yao lab and I could not have imagined a more fun and rewarding PhD experience under his mentorship.

I wish to thank the other members of my committee, Profs. Joel Moore and Raymond Jeanloz. I am indebted to Joel for his always-insightful theoretical assistance, as well as for introducing me to many helpful connections through his research center. Raymond acted as my *de facto* co-advisor throughout my PhD, always making time for discussions about science whenever I wasn't sure where to take our experiment next. I learned a great deal from his seemingly limitless expertise of high pressure science, and his deep technical intuition played a key role in a series of experimental advances that enabled the work in Chapters 2 and 3.

It has been an incredible opportunity to watch the Yao group blossom from a ragtag quartet of troublemakers to a tight-knit community of (troublemaking) scientists, each with completely different backgrounds and skill sets. The presence of this community facilitated a very unique PhD experience for me, with the opportunity to interface with experts in condensed matter theory, laser optics, high pressure science, and geophysics. Beyond scientific pursuits, it was sharing the innumerable meals, hikes, concerts, journal clubs, bubble teas, coffees, conferences, beam times, kombuchas, escape rooms, and group retreats with this team that made my graduate years some of my most memorable. I want to acknowledge in particular Thomas Mittiga and Chong Zu, who were with me at the inception of the experimental effort and set the tone for the warm and world-class enterprise that is the Yao lab of today. I am grateful for many fond memories working together on experiments with Weijie Wu, Tom Smart, Emily Davis, Prabudhya Bhattacharyya, Yuanqi Lyu, Jon Kruppe, Tim Höhn, Jordan Hines, Yonna Kim, Nicholas Rui, and Benjamin Lloyd. From the theory side, I was very fortunate to be able to walk by the theorist offices and have many insightful (usually impromptu) discussions with Bryce Kobrin, Francisco Machado, Rahul Sahay, Max Block, Soonwon Choi, and Shubhayu Chatterjee, all of whom somehow found time to think about experiments when they weren't busy advancing the state of condensed matter theory. I'm also grateful for many enlightening conversations with theorists Kamphol Akkaravarawong, Jack Kemp, Tommy Schuster, Bingtian Ye, Greg Kahanamoku-Meyer, and Chris Olund.

Prior to graduate school, I had many fantastic mentors. In high school, I was fortunate to take my first physics classes with Tyler Berzina, whose daily cat stories and love of "cornservation" laws showed me the beauty and joy that comes from learning science. During my undergraduate years at Washington University in St. Louis, I was extremely fortunate to have worked with Prof. Kater Murch. Kater's enthusiasm for science and hands-on advising shaped my formative years as a scientist and ultimately inspired me to go to graduate school. I am thankful for the many cheerful memories brainstorming, playing music, tasting

homemade wine, eating traditional Persian and Chinese foods, and doing experiments with him and his team, including Dian Tan, Mahdi Naghiloo, Neda Forouzani, Chris Munley, and Arian Jadbabaie. I'd also like to extend my gratitude to my mentors in the electrical engineering department at WashU, Profs. Ed Richter and Bob Morley, who always managed to make time to troubleshoot problems with me and taught me never to fear stupid questions.

My first semester of graduate school was under the guidance of Prof. Dan Stamper-Kurn. He and his group welcomed me into the Berkeley AMO community and would go on to help me countless times during my PhD, including sharing their lab space with us while we awaited room renovations. In particular, I'd like to acknowledge Emma Deist, Justin Gerber, Fang Fang, and Zephy Leung.

In the early days of the Yao lab, we visited Misha Lukin and his group at Harvard. There, they welcomed us as though we were part of their group and shared their expertise in color center experiments. In particular, I want to thank Joonhee Choi, Georg Kucsko, Igor Lovchinsky, Kristiaan De Greve, Elana Urbach, Harry Zhou, and Birgit Hausmann, whose experimental help benefited us immensely and set the standard for my subsequent interactions with the diamond community at conferences and beyond.

I am grateful for many wonderful collaborations both in and outside of Berkeley. I thank Prof. Dima Budker and Andrey Jarmola for their boundless generosity, providing us with lab space and valuable equipment in the early days as well as on-demand expertise just down the hallway from our labs. Their commitment to consistently excellent experiments strongly influenced the trajectory of the works presented in Chapter 5 and the first half of Chapter 6. A chance encounter with Prof. Nick Swanson-Hysell in the hallways of the Earth science building led to a very fun and interesting collaboration, which is the subject of Chapter 4; I thank him for welcoming me to his group meetings and encouraging me to present our results at the AGU Meeting. Nick also introduced me to Prof. Roger Fu and Mike Volk at Harvard, with whom I have had the pleasure of collaborating and learning about rock physics; I am humbled to have played a small role helping them advance the high pressure technology described in this thesis to enable exciting new discoveries in rock and mineral magnetism. I am grateful to Prof. Valery Levitas at Iowa State, who taught me how to think deeply about high pressure science. I thank Prof. Danna Freedman and Alison Altman, previously at Northwestern and now at MIT, for demonstrating unrelenting tenacity and optimism in our ongoing exploratory collaboration. Thanks to Biplab Bhawal, Jürgen Dienstmaier, and the rest of the team at attocube for their world-class service and tact despite my often frantic SOS emails—the detailed technical instructions in Jürgen's emails could have provided enough content for its own thesis!

I'm also indebted to the many staff members in the physics department that made my research possible. This includes Donna Sakima, Anne Takizawa, Joelle Miles, Anthony Vitan, Carlos Bustamante, Beth McCleary, Stephen Pride Raffel, and Ying Zhang. I also want to acknowledge the machinists of the Physics and Chemistry Machine Shops, who are true wizards of their craft and who exhibited incredible patience with my often contradictory requests and drawings. This includes Warner Carlisle, Tommy Gutierrez, Abel Gonzalez, Gordon Long, and Doug Scudder. I particularly want to thank Jesse Lopez and Joseph Kant,

who trained me in the student shop and somehow always found a way to fix machining issues that I thought were hopeless.

Near the end of my PhD as I decided to pivot my career towards sustainable foods, I participated in a rotation project with the Alternative Meats Lab at Berkeley. I am deeply indebted to director Ricardo San Martin and his team, including Erin Rieckmann and Catalina Villouta, for welcoming me into their group and their infinite patience as I learned the ropes in a chemistry lab. I also want to thank my officemate Tanya Svitova from Prof. Clayton Radke's group, with whom I shared many fond memories (and clementines), and Kora Rade Kukic from the Louis Dreyfus Company for devising and advising the rotation project.

Outside of the lab, my time in graduate school was made considerably more memorable by my involvement in the UC Jazz Ensembles as well as the Nu Jazz Collective. I was extremely fortunate to have performed alongside several outstanding student musicians and received mentorship from some of the finest jazz musicians in the Bay Area. I particularly want to acknowledge Ted Moore, director of the UC Jazz program, for his constant support and encouragement during my six years in the program, and Dann Zinn, whose coaching and private lessons accelerated my playing considerably. I also wish to acknowledge Myra Melford, whose expert mentorship taught me to think creatively and greatly expanded the realm of possibilities in my musical language.

I gratefully acknowledge my parents, Hudson and Jean-Shou, for their boundless love. From buying my first microscope and helping me build Gundam model kits to their unwavering support throughout my many years of education, I thank them for always encouraging me to tinker and explore. Thanks to my sister, Shauyene, brother-in-law, Dave, and nephew, Callan, for their love and encouragement. I also want to thank my *a-kong* and *a-ma*, Yuin-Chi Hsu and Ai Lein Wang Hsu, for their support; I am honored to continue the family lineage of physicists.

Finally, I want to thank my best friend and life partner, Sarah Plovnick, whose unconditional love propelled me through all the highs and lows of graduate school. None of the works in this thesis would have been possible without her support.

Citations to Previously Published Work

Parts of Chapter 1 and all of Chapter 2 has been published as

> S. Hsieh*, P. Bhattacharyya*, C. Zu*, T. Mittiga, T. J. Smart, F. Machado, B. Kobrin, T. O. Höhn, N. Z. Rui, M. Kamrani, S. Chatterjee, S. Choi, M. Zaletel, V. V. Struzhkin, J. E. Moore, V. I. Levitas, R. Jeanloz, N. Y. Yao. Imaging stress and magnetism at high pressures using a nanoscale quantum sensor. *Science* **366**, 1349 (2019).

Chapter 3 is in preparation for publication as

> S. Hsieh, M. W. R. Volk, B. Kobrin, R. R. Fu, N. Y. Yao, N. Swanson-Hysell. Pressure-induced magnetic transition in a single micrometer-scale grain of pyrrhotite (in preparation, 2022).

Chapter 4 is in preparation for publication as

> T. Smart, J. Parker, P. Bhattacharyya, S. Hsieh, B. Kobrin, Y.Lyu, S. Glaser, N. Yao, R. Jeanloz. Nano-Seismic Shear Sources and Imaging of Shear Stresses from Serpentine at Lower Mantle Pressures (in preparation, 2022).

Chapter 5 has been published as

> T. Mittiga*, S. Hsieh*, C. Zu*, B. Kobrin, F. Machado, P. Bhattacharyya, N. Z. Rui, A. Jarmola, S. Choi, D. Budker, N. Y. Yao. Imaging the local charge environment of nitrogen-vacancy centers in diamond. *Phys. Rev. Lett.* **121**, 246402 (2018).

Chapter 6 combines work published in the following two papers:

> M. Block*, B. Kobrin*, A. Jarmola*, S. Hsieh, C. Zu, N. L. Figueroa, V. M. Acosta, J. Minguzzi, J. R. Maze, D. Budker, N. Y. Yao. Optically enhanced electric field sensing using nitrogen-vacancy ensembles. *Phys. Rev. Applied* **16**, 024024 (2021).

> R. Sahay, S. Hsieh, E. Parsonnet, L. W. Martin, R. Ramesh, N. Y. Yao, S. Chatterjee. Noise Electrometry of Polar and Dielectric Materials. arXiv:2111.09315 [cond-mat.mtrl-sci] (2021).

Chapter 1

Introduction

> Those who have the highest-resolution tools in science can ask the most important questions, and those that have such tools first can answer the important questions first. Instrumentation gives one the competitive edge and underlies almost everything that goes on in science.
>
> *Mark Wrighton, 2000 Ullyot Public Affairs Lecture*

Pressure, as a thermodynamic variable, unlocks an extraordinary range of tunability for the physical and chemical properties of matter. The effect of pressure on water is an illustrative example: in daily life, we commonly experience water in one of three phases, yet in combination with temperature, water under pressure exhibits more than thirty distinct phases [217].

The diamond anvil cell (DAC) is the preëminent apparatus for achieving static high pressures. By compressing a sample between two opposing diamond anvils, pressures greater than 100 GPa are routinely generated. Just in the last few decades, high pressure experiments using DACs have identified a room-temperature superconductor, quantum criticality in an elemental metal, and the synthesis of metallic hydrogen [303, 162, 80].

This thesis introduces a novel quantum sensor embedded within the tip of a diamond anvil whose high sensitivity and micron-scale spatial resolution enables a range of experiments that are difficult or impossible with conventional high pressure techniques. In this Chapter, we introduce this sensor, the so-called nitrogen-vacancy (NV) center in diamond, and its coupling to stress, magnetic, and electric fields which enables its use as a sensor. We further introduce the DAC and a survey of its associated sensing technologies, focusing on two classes of sensors: those used to quantify the stress environment in the sample chamber and those used to measure magnetism of samples under pressure.

In Chapter 2, we demonstrate the operation of our sensing platform at high pressure. We propose and utilize a protocol to measure the complete stress tensor and use this to constrain finite element simulations of the complete stress tensor distribution within the diamond anvil. Furthermore, we demonstrate magnetic imaging and use this to measure

the pressure-induced $\alpha \rightarrow \epsilon$ transition in elemental iron as well as the pressure-temperature phase diagram of gadolinium. Finally, we introduce a magnetic noise spectroscopy modality which offers a complementary perspective to d.c. magnetometry.

In Chapter 3, we apply our sensing platform to the domain of geoscience. Specifically, we consider the amorphization of chrysotile serpentine, which has implications for the mechanisms underpinning deep-focus earthquakes. We use a truncated stress sensing protocol to image the shear stresses within the sample chamber and show that they are consistently reduced following an amorphization event.

Along the same geoscientific vein, Chapter 4 applies our magnetic imaging technique to the study of pyrrhotite, an iron sulfide mineral whose strong magnetic remanence likely contributes significantly to Martian crustal magnetization. We report the demagnetization of a single micron-scale grain of pyrrhotite under pressure and show that its remanence completely revives upon decompression, which has implications on the viability of pyrrhotite-bearing meteorites to carry remanence.

An exhaustive understanding of our sensor is critical to the sensing of external signals. To this end, in Chapter 5, we step away from external stimuli and turn inward to the diamond host itself. Specifically, we consider a spectral feature in the NV center magnetic resonance response that is generically found in diamond samples prepared with high defect densities. We demonstrate that the feature originates from the local charge environment surrounding the NV centers, and we use this understanding to demonstrate imaging of individual electronic charges with nanometer precision.

In Chapter 6, we utilize the understanding of the electric field sensitivity developed in Chapter 5 along two fronts. Firstly, we extend the effect of the local charge environment to the NV orbital excited state. Besides leading to fundamental insights (including an estimate of the excited state electric field susceptibility), these considerations lead us to propose an electrometry protocol that is two orders of magnitude more sensitive than existing state-of-the-art defect sensing methods. Secondly, we propose the use of the NV center's T_1 lifetime as a probe of electric noise. We contextualize this protocol by theoretically considering the electric field noise emanating from polarization fluctuations of polar and dielectric materials and show how this enables access to frequencies and length scales that are challenging to probe through other means.

1.1 The nitrogen-vacancy center in diamond

A vast body of work introduces the level structure and photophysics of the NV center in great detail. The curious reader is encouraged to consult any of the following excellent references [224, 62, 267]. In this Chapter, I will briefly review this work with an emphasis on quantum sensing applications at high pressure.

The NV center is an atomic defect in diamond in which two adjacent carbon atoms are replaced by a nitrogen atom and a lattice vacancy. Its discrete energy levels are situated within the 5.5 eV band gap of diamond (Figure 1.1). The defect is commonly found in either

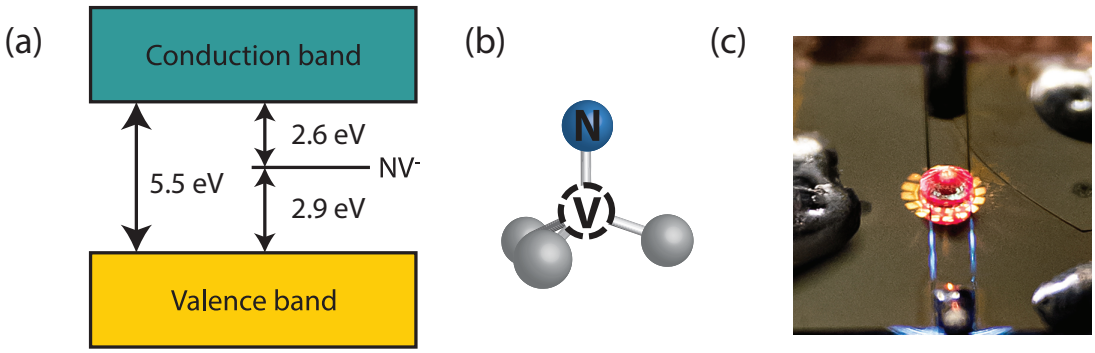

Figure 1.1: (a) Band structure of diamond and location of NV^- levels. (b) Schematic depiction of an NV center. Gray circles represent carbon atoms; blue circles represent substitutional nitrogen atoms; dashed circles represent vacant lattice sites. (c) Photograph of a diamond prepared with a high density of NV centers, which leads to strong red fluorescence. Photo credit: Noah Berger

neutral (NV^0) or negatively (NV^-) charged states, with a positive charge state accessible via electrical gating [264, 85]. NV^0 exhibits a spin-$\frac{1}{2}$ electronic ground state, while NV^- exhibits a spin-1 ground state of technological interest due to its ability to be optically polarized even at room temperature. For the remainder of this thesis, we will refer to NV^- as the NV center.

1.1.1 NV level structure

The four dangling bonds around the NV center (denoted σ_1, σ_2, and σ_3 for the carbon bonds and σ_N for the nitrogen bond) can be used to represent the single electron orbitals that comprise the defect level structure. To determine the appropriate basis and ordering of these states, one should consider the defect symmetry: the NV center belongs to the C_{3v} (sometimes notated 3m) point group which is characterized by the following symmetries:

- Identity
- Threefold rotational symmetry about the high symmetry axis
- Threefold vertical reflection symmetry

Using group theory, we can project the four orbitals onto each irreducible representation of the C_{3v} point group, resulting in an appropriate single electron orbital basis. Then, to determine the ordering of these states, one can consider the Coulomb attraction between the electron and nuclei, which mixes these states to yield the final basis:

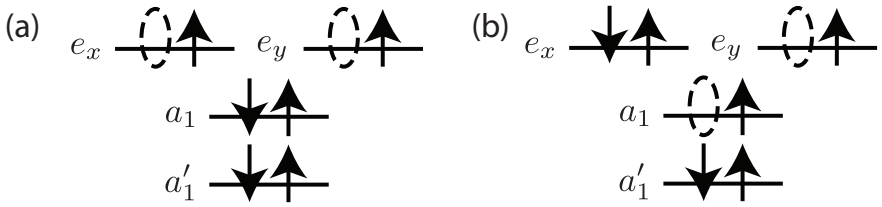

Figure 1.2: NV center single electron orbitals after being filled with six electrons. Dashed ellipses represent holes. (a) In the ground state, the holes occupy the $e_{x,y}$ orbitals. (b) In the first excited state, one of the two holes is promoted to the a_1 orbital.

$$a_1 = \alpha\sigma_N + \frac{\beta}{\sqrt{3}}(\sigma_1 + \sigma_2 + \sigma_3) \tag{1.1}$$

$$a_1' = \beta\sigma_N + \frac{\alpha}{\sqrt{3}}(\sigma_1 + \sigma_2 + \sigma_3) \tag{1.2}$$

$$e_x = \frac{1}{\sqrt{6}}(2\sigma_1 - \sigma_2 - \sigma_3) \tag{1.3}$$

$$e_y = \frac{1}{\sqrt{2}}(\sigma_2 - \sigma_3) \tag{1.4}$$

The predicted ordering of states is shown in Figure 1.2, which is corroborated by *ab initio* calculations [125, 116, 224]. We can now fill these orbitals with electrons. Six electrons contribute to the level structure of the NV center: one from each of the three carbon atoms, two from the nitrogen atom (which acts as an n-type dopant), and one from an electron donor in the environment. Filling these states with electrons in accordance with Hund's rules, we find that the ground state can be represented by four electrons in the fully symmetric states and two electrons in the $e_{x,y}$ orbitals. Alternatively, we can consider the more convenient hole representation, wherein we need only consider the ground state as two holes in the $e_{x,y}$ orbitals. In this representation, the first excited state is given as a hole promoted from $e_{x,y}$ to a_1.

Finally, we note that the total wavefunction of the electronic system should be antisymmetric. The large energy scale associated with Coulomb repulsion, compared to the spin-spin interaction, should be minimized in the ground state; therefore, the ground state is a spin triplet (orbital singlet) consisting of two unpaired holes, resulting in an effective spin $S = 1$. The resulting energy level structure is shown in Figure 1.3. The ground state $^3A_2$ exhibits a room temperature zero-field splitting $D_{\mathrm{gs}} = 2.87\,\mathrm{GHz}$ between $|m_{\mathrm{s}} = 0\rangle$ and $|m_{\mathrm{s}} = \pm 1\rangle$ sublevels. $^3A_2$ is separated by 637 nm from the spin triplet excited state, ^3E. The spin singlet states can be accessed through an intersystem crossing (ISC) that plays an important role in state preparation and readout, as will be discussed next.

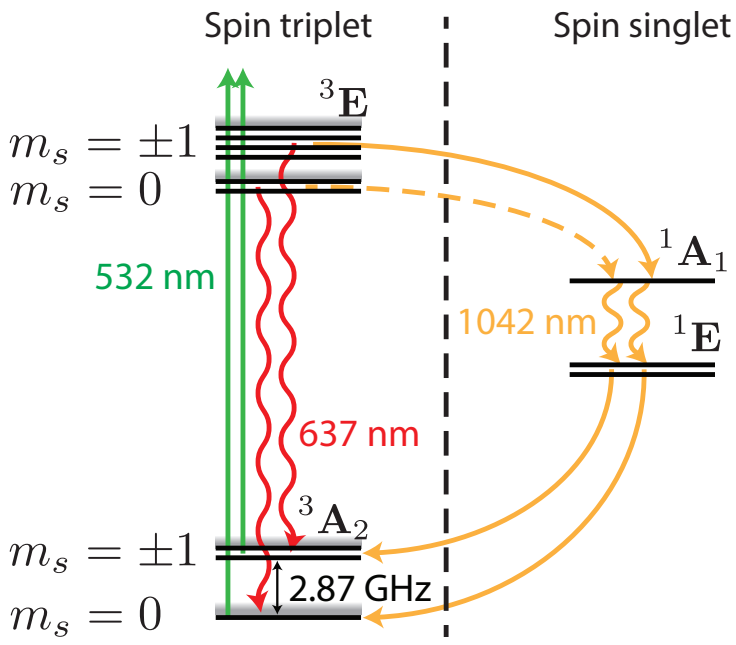

Figure 1.3: NV center level diagram.

1.1.2 Optical state preparation and readout

Under illumination of a green laser (e.g. at wavelength 532 nm), the NV center exhibits fluorescence with a zero-phonon line at 637 nm and a broad phonon sideband between approximately 637-800 nm. During this process, electrons in the $^3A_2$ state are excited to ^3E and mostly return to $^3A_2$ in a spin-conserving cycle (red wavy arrows, Figure 1.3). However, a fraction of these excitations undergoes an ISC to the singlet states which is crucially spin-non-conserving; in particular, the ISC preferentially favors transitions from the $|m_s = \pm 1\rangle$ sublevels yet returns to the triplet state with roughly equal probability of decay to $|m_s = 0\rangle$ and $|m_s = \pm 1\rangle$ (yellow arrows). The steady-state population under green illumination is subsequently polarized to $|m_s = 0\rangle$ with ~80-90% efficiency at room temperature [275]. This mechanism of state preparation enables coherent manipulation of the spin state using microwave driving fields.

The ISC also plays a crucial role in state readout: the singlet decay channel is slow compared to the ^3E lifetime (~ 200 ns versus ~ 10 ns) and nonradiative, so the fluorescence intensity is reduced when undergoing the ISC. Because the ISC preferentially favors the $|m_s = \pm 1\rangle$ states, this implies that the fluorescence intensity can be used to read out the spin state.

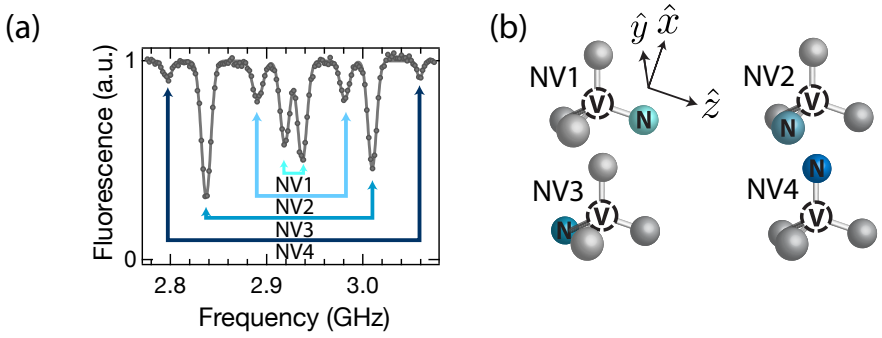

Figure 1.4: (a) Example of ODMR spectroscopy. (b) Four orientations of NV centers each exhibit two resonances to the spectrum, leading to eight resonances in total.

1.1.3 Optically detected magnetic resonance

In most of the experiments described in this thesis, the NV centers are probed using optically detected magnetic resonance (ODMR). In this modality, the laser and microwave fields are continuously active throughout the measurement while the microwave frequency is swept.[1] When the microwave frequency is off-resonant from any NV spin transitions, the microwaves have no effect and the laser serves to initialize the spin state into $|m_s = 0\rangle$. Conversely, when the microwave frequency comes close to resonance with an NV spin transition, some of the population is driven into the $|m_s = \pm 1\rangle$ states and the fluorescence intensity is subsequently decreased (Figure 1.4).

The presence of external signals affects the energy levels of the NV, and, in general, lifts the degeneracy of the $|m_s = \pm 1\rangle$ states. Using ODMR to characterize the change in the energy levels, one can directly measure such external signals. More specifically, combining the information from the four possible crystallographic orientation of the NV centers enables the reconstruction of a signal's vector (e.g. magnetic field) or tensorial (e.g. stress) information.

1.1.4 Spin coupling to magnetism and stress

Here, we focus on the sensing of stress and magnetic fields, wherein the NV is governed by the Hamiltonian [29, 326], $H = H_0 + H_B + H_S$, with

$$H_0 = D_{gs} S_z^2 \tag{1.5}$$

$$H_B = \gamma_B \vec{B} \cdot \vec{S} \tag{1.6}$$

$$H_S = \Pi_z S_z^2 + \Pi_x (S_y^2 - S_x^2) + \Pi_y (S_x S_y + S_y S_x) \tag{1.7}$$

[1] This procedure describes the continuous-wave modality of ODMR. A pulsed variation also can be performed which can be advantageous to reduce the duty cycle of the microwave/laser fields e.g. when heating is a concern, or to avoid spectral power broadening [93].

where

$$\Pi_z = \alpha_1 (\sigma_{xx} + \sigma_{yy}) + \beta_1 \sigma_{zz} \tag{1.8}$$
$$\Pi_x = \alpha_2 (\sigma_{yy} - \sigma_{xx}) + \beta_2 (2\sigma_{xz}) \tag{1.9}$$
$$\Pi_y = \alpha_2 (2\sigma_{xy}) + \beta_2 (2\sigma_{yz}) \tag{1.10}$$

Equation 1.5 is known as the zero-field splitting with $D_{\text{gs}} = 2.87\,\text{GHz}$ at ambient pressure and temperature. Equation 1.6 is known as the Zeeman splitting, where $\gamma_{\text{B}} \approx 2.8$ MHz/G is the gyromagnetic ratio and B is a magnetic field. Equation 1.7 captures the NV's response to the local diamond stress tensor, $\overleftrightarrow{\sigma}$.[2] $\hat{z}$ is the NV orientation axis, $\hat{x}$ is defined such that the xz-plane contains one of the carbon-vacancy bonds, and $\{\alpha_{1,2}, \beta_{1,2}\}$ are the stress susceptibility coefficients given by [29, 148][3]

$$\{\alpha_1, \beta_1, \alpha_2, \beta_2\} = \{8.6(2), -2.5(4), -1.95(9), -4.50(8)\}\ \text{MHz/GPa}. \tag{1.11}$$

In order to develop intuition for the NV coupling to stress, one can consider classifying stress perturbations as either conserving or breaking the C_{3v} defect symmetry. From this perspective, Π_z compiles all stresses that conserve the C_{3v} symmetry, so application of this term leads to a *shift* of the energy spectrum with no breaking of degeneracies. Conversely, $\Pi_{x,y}$ compiles all stresses that break this symmetry, leading to a *splitting* of the degeneracy between the states $|m_s = \pm 1\rangle$. In particular, this symmetry-breaking stress leads to the new eigenstates

$$|+\rangle = \frac{1}{\sqrt{2}} \left(|m_s = +1\rangle - e^{-i\phi_E} |m_s = -1\rangle \right) \tag{1.12}$$
$$|-\rangle = \frac{1}{\sqrt{2}} \left(e^{i\phi_E} |m_s = +1\rangle + |m_s = -1\rangle \right) \tag{1.13}$$

with $\phi_E \equiv \arctan(\Pi_y / \Pi_x)$ and energy splitting $2\Pi_\perp \equiv 2\sqrt{\Pi_x^2 + \Pi_y^2}$.

From this we see that ODMR spectroscopy measures the coupling coefficients Π_z and $\Pi_\perp$ for each NV center.[4] In general, the ODMR spectra exhibit eight resonances arising from the four possible crystallographic orientations of the NV (Fig. 1.4). By extracting the energy shifting and splitting of the spin sublevels for each NV orientation group, one obtains an overconstrained set of equations enabling the reconstruction of either the (six component) local stress tensor or the (three component) vector magnetic field.

[2] In addition to the terms listed here, stress-induced coupling to the anticommutator terms $\{S_x, S_z\}$ and $\{S_y, S_z\}$ also exists, but its effect is energetically suppressed by the zero-field splitting.

[3] We note that these coefficients were determined by reinterpreting data from Ref. [29] after considering the effect of local charge perturbations on their measurements. This analysis is reproduced in Chapter 2.

[4] Here, we consider only the effect of Eq. 1.7 in the absence of magnetic fields. The case of simultaneous stress and magnetic perturbations is considered in Chapter 2.

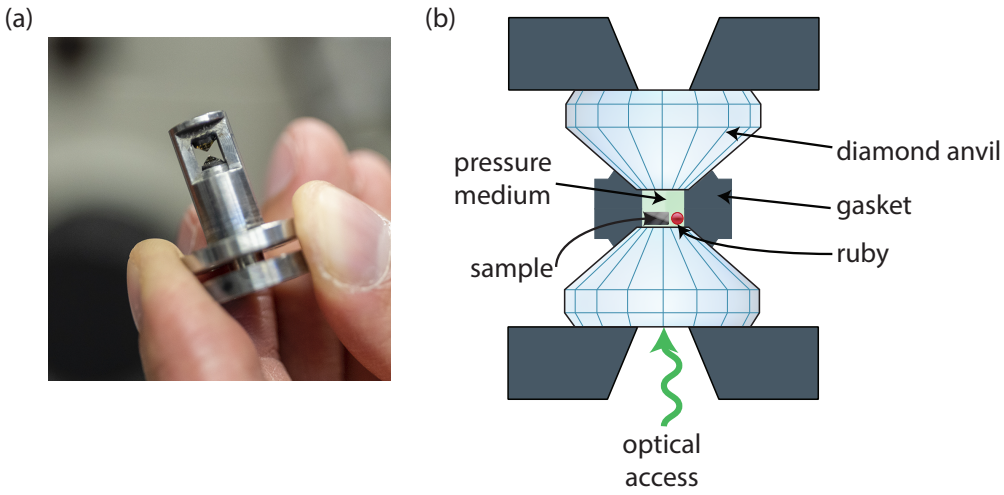

Figure 1.5: (a) Photograph of a miniature diamond anvil cell containing two opposing diamond anvils. Photo credit: Marilyn Sargent, Berkeley Lab. (b) Schematic depiction of a fully loaded diamond anvil cell.

1.1.5 Comparison between stress and electric field coupling

The NV center couples to electric fields with the same form as to stress (Equation 1.7):

$$H_E = d_{\parallel} E_z S_z^2 + d_{\perp}(E_x(S_y^2 - S_x^2) + E_y(S_x S_y + S_y S_x)), \tag{1.14}$$

where $\{d_{\parallel}, d_{\perp}\} = \{0.35, 17\}$ Hz cm/V are the electric field susceptibilities [254]. Despite the similarities in the form of coupling to stress and electric fields, we note that the stress susceptibilities share similar magnitudes, while the electric field susceptibilities differ from each other by a factor of 50. We present a microscopic theory to explain this anisotropy in Chapter 6.

1.2 Diamond anvil cell

The diamond anvil cell (DAC) is the leading high pressure apparatus for achieving static pressures in the 100 GPa range (Figure 1.5). In the DAC, the sample of interest is compressed between two opposing diamond anvils whose tips have been polished flat (the so-called culet). The sample chamber is defined by a gasket typically comprised of a metallic foil with a hole drilled through its center. The sample chamber can be filled with a pressure-transmitting medium such as a liquid or a gas in order to provide a hydrostatic pressure environment.

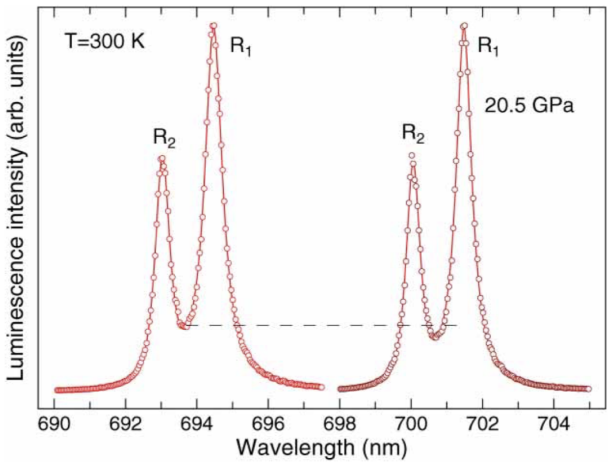

Figure 1.6: Example ruby R-line spectrum at $P = 0\,\text{GPa}$ (left) and $20.5\,\text{GPa}$ (right). Adapted from [312].

1.3 Stress determination measurements

1.3.1 Ruby fluorescence

The optical properties of ruby (chromium-doped Al_2O_3) have been intensively studied since the 1950s due to its use in the first solid-state laser [211] and the development of ligand field theory [209]. Upon green illumination, two zero-phonon transitions known as R1 and R2 are observed at room temperature at 694.25 and 692.86 nm, respectively (Figure 1.6) [312]. The shift of these transitions under pressure has been meticulously characterized over several decades varying pressure-transmitting media and primary pressure scales (see e.g. [296]). In a typical ruby fluorescence measurement, ruby powder with grain size $\sim$1 µm or individual microspheres of size 5-100 µm are placed into the DAC sample chamber and excited by a focused green laser. The resulting fluorescence is coupled to a spectrometer.

Ruby fluorescence is the method of choice for pressure determination below $\sim$100 GPa; above this, the optical absorption bands are significantly blueshifted and fluorescence becomes inefficient.

1.3.2 Diamond anvil Raman

Diamond exhibits a first-order Raman signal at $1333\,\text{cm}^{-1}$ at ambient pressure and temperature, and this signal shifts under stress. In their seminal paper from 1985, Hanfland and Syassen proposed to utilize the Raman signal from the diamond culet to determine the pressure within the DAC sample chamber [140]. This method has the unique benefit of requiring no additional *in situ* instrumentation; a typical measurement setup involves just a green excitation laser focused into the diamond anvil with the reflected Raman signal coupled to a

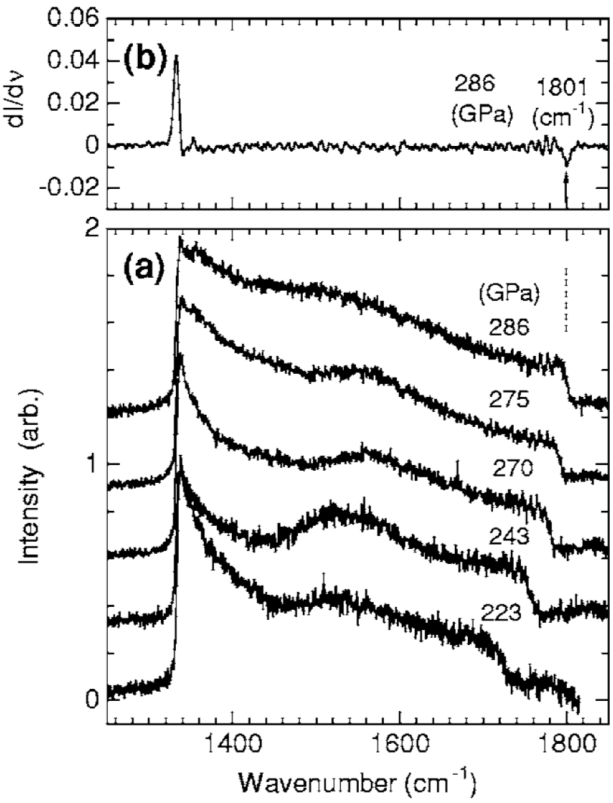

Figure 1.7: (a) Example Raman spectra from a stressed diamond culet at various pressures. The high frequency edge, defined by a dip in the differential signal as in (b), is used for pressure determination. Adapted from [10].

spectrometer. Spatial resolution can be further improved by using a long working distance objective lens and operating in a confocal geometry. Use of this scale has been calibrated as high as 410 GPa and is the method of choice for the determination of megabar pressures [11].

Despite its widespread use, different groups have reported differing calibration scales, calling into question the degree of accuracy of this method. In practice, two challenges may limit its accuracy. Firstly, this method interrogates a spatial volume which is dependent on the optics geometry. Due to the high refractive index of diamond, even a tightly focused laser will be stretched along the propagation direction to $\sim$10 µm, which implies that the measurement will integrate over a significant stress gradient. This can be mitigated by measuring the high frequency edge, as determined by a peak in the first derivative (Figure 1.7), but a dependence on the laser depth of focus remains. Secondly, as will be discussed in more detail in Chapter 2, the culet experiences a stress tensor dominated by the terms σ_{RR}, $\sigma_{\Theta\Theta}$, and σ_{ZZ}, where $\hat{Z}$ is defined along the culet normal direction. Crucially, the relative

magnitudes of these stress contributions depend on the culet diameter as well as the gasket geometry and material. Thus, for a given pressure in the sample chamber, the stress on the culet will be dependent on the DAC geometry.

1.3.3 Comparison to NV-based stress sensing

While accurate determination of the hydrostatic pressure on a sample is important, it is far from a complete characterization of the stress environment. Indeed, the distribution and magnitude of deviatoric (that is, non-hydrostatic) stresses are known to play a key role in the dynamics of high pressure phenomena [199]. To this end, the NV center is the only high pressure stress platform that can reconstruct all six unique components of the stress tensor. The ability to map the stress tensor across the culet surface provides strong constraints on the stress state of the entire the pressure cell; in Chapter 2 we show how the experimentally determined stress along the culet severely constrains the tensorial stress state throughout the diamond anvil in finite element simulations, and additional measurements to characterize the loading geometry may enable us to infer the stress state on the sample itself.

An additional benefit of NV-based stress sensing is its imaging capability. Unlike ruby photoluminescence and Raman measurements, fluorescence from ODMR measurements performed on NV centers can be straightforwardly coupled to a camera with micron-scale spatial resolution and without rastering the laser position. The spatial distribution of stresses encodes information about the propagation of structural defects in materials (e.g. during pressure-driven phase transitions) as well as the hydrostaticity of pressure-transmitting media.

Use of NV sensing also comes with its own technical challenges, among them the delivery of microwave frequency electromagnetic fields. In the experiments described in this thesis, microwave delivery is performed with a 4 µm-thick platinum foil compressed between the gasket and diamond anvil pavilion facets; anecdotally, this configuration remains stable up to at least 50 GPa but worsens in transmission efficiency at higher pressures, leading to reduced ODMR contrast and thus worsened sensitivity. Future experiments using a combination of insulating gaskets and improved waveguide circuit designs may alleviate these technical challenges.

Besides microwave delivery considerations, complete characterization of the stress tensor at the culet requires the application of precisely aligned magnetic fields (see Chapter 2 for more details). In special cases, application of an arbitrarily oriented field may be sufficient to recover a subset of stress tensor components (see Chapters 3 and 4 for examples). A summary of the comparison between the stress sensing modalities outlined in this section is shown in Table 1.1.

Sensor	Advantages	Disadvantages
Ruby fluorescence	• Extremely well-calibrated	• Limited signal beyond 100 GPa • No tensorial resolution • Imaging is not straightforward
Diamond culet Raman	• Operable in the megabar regime • Requires no additional sensors	• Calibration is sensitive to diamond anvil, gasket, and optics configuration • No tensorial resolution (only pressure) • Imaging requires rastering
NV centers	• Full stress tensor can be measured • Imaging is straightforward	• Requires delivery of microwave fields (and in some cases, precisely aligned magnetic fields) • Upper pressure limit is unclear

Table 1.1: Summary of advantages and disadvantages of various stress sensors.

1.4 High pressure magnetic measurements

1.4.1 Induction coil/SQUID magnetometers

Induction coil-based magnetometers operate based on Faraday's law of induction, where the output voltage from a loop of wire is proportional to the negative time derivative of the magnetic flux through the loop. A similar relation is found for superconducting quantum interference device (SQUID) magnetometers, where the output voltage is proportional to the magnetic flux signal itself [74]. A typical high pressure induction measurement may consist of an induction loop with a loop diameter around 2-10 mm surrounding the diamond anvils or the entire DAC; an excitation coil placed near the sample can be driven to perform ac susceptibility measurements [321], or the DAC itself can be vibrated with the vibration frequency coupled to a lock-in amplifier [154]. Induction coil-based magnetometers have been used up to 230 GPa to measure a superconducting transition in elemental sulfur [321]. A notable DAC design placed in the bore of a Quantum Designs MPMS (diameter 8.8 mm) was recently used to measure the superconducting transition of superconducting hydrides [238].

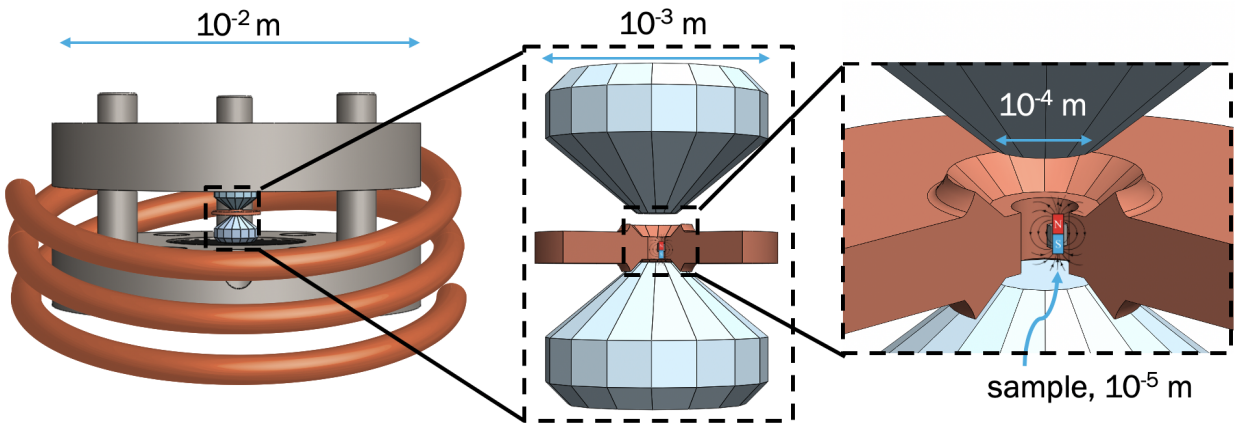

Figure 1.8: Schematic representation of an induction coil used for magnetometry.

1.4.2 Comparison to NV-based magnetometry

A case for using NV centers as magnetometers, as opposed to conventional induction coils, becomes clear if one considers the DAC geometry. A schematic of a typical DAC implementation used in our laboratory is depicted in Figure 1.8. The entire DAC assembly is a few centimeters in diameter, whereas the sample of interest is typically tens of microns in diameter. High pressure induction coils are commonly prepared *ex situ* such that the coil picks up magnetic flux from both the sample as well as the DAC itself. This implies that the expected signal-to-noise will be proportional to the volume ratio of the sample to the DAC, i.e. $(\frac{10\,\mu m}{1\,cm})^3 \sim 10^{-9}$. Thus, in practice, the minimum detectable signal using high pressure magnetometers is typically limited by the challenge of performing background subtraction of the undesired DAC magnetization. This challenge is further exacerbated at pressures above 50 GPa, where it is necessary to reduce the diameter of the diamond anvil culets such that the sample dimensions are further reduced. This typically limits induction coil-based magnetometers to magnetic sources larger than $10^{-10}\,Am^2$.

In comparison, the NV centers utilized in our sensing platform are prepared within 0.5 µm from the diamond anvil culet. Even accounting for the standoff distance between the sample and the culet, this implies that the sensor can be straightforwardly prepared within a few microns of the sample of interest such that the magnetization of the DAC assembly is not a concern. This improves our detection limits significantly; we routinely resolve sources below $10^{-12}\,Am^2$, and our magnetic sensitivity ($\sim 10\,\mu T \cdot \mu m/\sqrt{Hz}$) is consistent with previously reported values that are able to resolve sources down to $10^{-16}\,Am^2$ at ambient pressure [123].[5] Nevertheless, the use of NV magnetometry also comes with its own unique technical

[5]We note that these two modes of magnetometry measure distinct phenomena: in induction coil magnetometry, the measured magnetic flux is related to the total sample magnetization, whereas NV magnetometry measures micron-scale stray magnetic fields from the sample. Crucially, the stray field encodes information about both the total sample magnetization as well as the spatial distribution of magnetic carriers in the

challenges; specifically, concerns with delivery of microwave fields as discussed in Section 1.3.3 also apply in this sensing modality.

1.5 A history of this experiment

In the last section of this Chapter, I hope to contextualize the decisions that motivated some of the experiments in which I participated during my PhD. In academic research, I find that this context can often be insightful yet is rarely recorded or only passed on through word-of-mouth. I hope this will prove helpful for future members of the Yao group and high pressure scientists at large.

1.5.1 Early days

I joined the Yao lab in spring of 2016. Together with graduate student Thomas Mittiga, we started the experimental effort with just an empty optical table and a shared lab space graciously provided by Professor Dan Stamper-Kurn. These early days were frenzied and electric, assembling our scanning confocal microscope system while purchasing five-figure orders in the daytime and long planning and troubleshooting meetings late into the evenings. We were fortunate to have on-demand help from Chong Zu, who advised us remotely while finishing his PhD at Tsinghua University in Beijing.

After several failed attempts to identify fluorescence from single defect centers, in March 2016, we paid a visit to Misha Lukin's labs at Harvard, where graduate students Joonhee Choi, Georg Kucsko, Igor Lovchinsky, and Elana Urbach, as well as postdoc Kristiaan De Greve, patiently walked us through every aspect of their experimental apparatus in excruciating detail and showed us their fabrication procedures in the clean room. Birgit Hausmann, a recently graduated PhD student in Professor Marko Lončar's group and the so-called "Queen of Diamond," graciously wrote up an inventory of all the supplies we needed for diamond fabrication and connected us to her contacts at major diamond manufacturers in the world. Upon our return to Berkeley, which closely coincided with Chong's official arrival as our first experimental postdoc, we finally began to see single defect fluorescence and start taking measurements. Our first project was a collaboration with Professor Feng Wang to interface shallow implanted NV centers with two-dimensional transition metal dichalcogenides, which we dubbed RT1.

1.5.2 The birth of RT2

In May 2016, we met Professor Raymond Jeanloz in the Department of Earth and Planetary Sciences, as well as his graduate student, Thomas Smart. This began our foray into our next experiment, RT2, exploring defect centers at high pressure, on which I became the lead student. It was quickly apparent that the geometry of the diamond anvil, with a typical

sample [115].

thickness of 2 mm, significantly hampered the efficiency of fluorescence collection. We explored several avenues to get around this problem, including diamond samples prepared with very high defect concentrations, as well as micro/nanodiamonds to insert within the sample chamber. A curious finding was that for all samples containing high defect concentrations at zero magnetic field, we consistently saw a two-resonance spectrum that could not be fit to two lorentzian or gaussian distributions. This had been reported in NV center literature in the past but was always attributed to lattice strain. This explanation was not satisfactory for our recently-joined theory graduate student, Bryce Kobrin, who insisted that every conceivable strain distribution would only lead to pure broadening of the spectrum, not two resonances.

A breakthrough came in June 2017 on our way home from the DAMOP conference in Sacramento, California. Bryce had driven his minivan to the conference and offered a ride back to Berkeley for anyone who wished to join. In addition to myself, he picked up Pauli Kehayias, a postdoc in Ron Walsworth's lab, and Soonwon Choi, a graduate student in Misha Lukin's lab. As inevitably happens in any group of physicists trapped in an enclosed space, the conversation quickly shifted to physics, and Bryce, Pauli, and Soonwon spent the next two hours debating every conceivable microscopic origin of this spectral feature. By the time we arrived in Berkeley, only one possibility had not been universally eliminated by all participants: the spectrum must emerge from electric fields from local charges. The experimentalists, together with Bryce and another recent graduate student, Francisco Machado, as well as remote discussions with Soonwon, developed a microscopic model to quantify this picture and found excellent agreement with our compilation of zero-field spectra over a wide range of sample parameters. This conclusion led to our first paper, published in Physical Review Letters.

1.5.3 A race to high pressure

In July 2018, we remotely attended a talk by Professor Jean-François Roch from the École Normale Supérieure Paris-Saclay, where he showed beautiful preliminary results of a high pressure phase transition measured by *in situ* NV center magnetometry, which at the time we had considered to be a long-term goal with dubious likelihood of success in our RT2 experiment. This ignited something of a four-alarm-fire in our group as we quickly pivoted from a largely exploratory phase of the high pressure experiment to a demonstrative phase. It was all hands on deck for five months as we prepared every novel demonstration we could imagine: By developing an algorithm employing carefully controlled vector magnetic fields, I measured all eight resonances of the NV spectra at high pressure to determine the resulting stress tensor, while also measuring a new data point for the $\alpha \rightarrow \epsilon$ transition in elemental iron every day; Thomas led a herculean effort to clean up and fit the spectra of the iron data at every pressure point (approximately 3×10^5 resonances in total), which required significant human input due to saturation effects from the very magnetized iron pellet; Chong and Thomas devised a Peltier cooling system to cool and measure the noise spectrum of elemental gadolinium; graduate students Pra Bhattacharyya and Tim Höhn traded 12-hour shifts to

measure the $P-T$ phase diagram of elemental gadolinium within our new cryostat; Bryce adapted the stress susceptibilities reported in literature to our data and analyzed our spectral images to determine the complete six-component stress tensor; Francisco analyzed the iron and gadolinium data, including an impressive effort to salvage a crucial iron data point that I had botched during an overnight measurement; undergraduate student Nicholas Rui performed an extensive literature search on existing high pressure magnetometry methods and designed approximately 20 iterations of a summarizing subfigure, each one more excellent than the last; Professor Mike Zaletel and his postdoc, Shubhayu Chatterjee, proposed a noise spectroscopy protocol to supplement our results on gadolinium and wrote a theoretical justification for our unintuitive experimental findings that could have stood alone as its own manuscript; our collaborators, Professor Valery Levitas and his graduate student, Mehdi Kamrani, iterated over hundreds of finite element simulations to reproduce the stress tensor maps. We submitted our manuscript simultaneously with Professor Jean-François Roch's group and another group led by Professor Sen Yang at the Chinese University of Hong Kong on Christmas of 2018, and legend has it that a collective sigh was heard reverberating the halls of the third floor of Old LeConte Hall.

I concede that I have made many omissions in this retelling—notable omissions include impressive efforts by graduate students Tim Höhn, Jordan Hines, and Yuanqi Lyu to measure a zoo of ferroelectrics, magnetic materials, and superconductors, as well as undertakings by many star undergraduate students to explore new defects under pressure—but for the sake of brevity, I will leave this story for future theses.

Chapter 2

High Pressure Sensing Using Nitrogen-Vacancy Centers in Diamond

2.1 Introduction

In the previous Chapter, we outlined the motivation and the physics that underpins the use of the NV center as a sensor of mechanical stress and magnetic fields. In this Chapter, we experimentally realize and demonstrate this platform by embedding NV centers into the culet (tip) of a diamond anvil. We demonstrate the utility of this sensing platform through a series of proof-of-concept experiments up to pressures $\sim$48 GPa and for temperatures ranging from 25-340 K. In the context of stress, we develop a protocol to reconstruct all six unique components of the stress tensor at the culet surface, which both constrains the stress tensor in the entire diamond anvil in finite element simulations and offers a unique sensing modality for characterizing the strength and effective viscosity of solids and fluids under pressure. In the context of magnetic fields, we demonstrate vector magnetic field imaging with dipole precision $\lesssim 10^{-11}$ emu,[1] enabling us to measure the pressure-driven $\alpha \leftrightarrow \epsilon$ phase transition in iron as well as the complex pressure-temperature phase diagram of gadolinium. In addition to DC vector magnetometry, we highlight a complementary NV-sensing modality using T_1 *noise* spectroscopy; crucially, this demonstrates our ability to characterize phase transitions even in the absence of *static* magnetic signatures.

A tremendous amount of recent attention has focused on the development of hybrid quantum sensing devices, in which sensors are directly integrated into existing toolsets ranging from biological imaging to materials spectroscopy [191, 212, 50, 91]. Here, we instrument diamond anvil cells with a layer of nitrogen-vacancy (NV) centers directly at the culet, enabling the pursuit of two complementary objectives in high pressure science: first, to understand the strength and failure of materials under pressure (e.g. the brittle-ductile transition) and

[1] 1 emu = 10^{-3} A·m^2.

second, to discover and characterize new phases of matter (e.g. high temperature superconductors) [344, 146, 120, 94, 304]. Achieving these goals hinges upon the sensitive *in situ* imaging of signals within the high pressure chamber. In the former case, measuring the *local* stress environment permits the direct observation of inhomogeneities in plastic flow and the formation of line defects. In the latter case, the ability to spatially resolve field distributions can provide a direct image of complex order parameters and textured phenomena such as magnetic domains. Unfortunately, the enormous stress gradients generated near the sample limit the utility of most conventional tabletop spectroscopy techniques; as a result, one is often restricted to measuring bulk properties averaged over the entire DAC geometry.

2.2 Methods

Our approach to these challenges is to utilize an ensemble of NV centers ($\sim$1 ppm density) implanted $\sim$50 nm from the surface of the diamond anvil culet (Fig. 2.1, (a) and (b)). Each NV center represents an atomic-scale defect (i.e. a substitutional nitrogen impurity adjacent to a vacancy) inside the diamond lattice and exhibits an $S = 1$ electronic spin ground state [85]. In the absence of external fields, the $|m_s = \pm 1\rangle$ spin sublevels are degenerate and separated by $D_{gs} = (2\pi) \times 2.87$ GHz from the $|m_s = 0\rangle$ state. Crucially, both the nature and energy of these spin states are sensitive to local changes in stress, temperature, magnetic and electric fields (Fig. 2.1(c)) [5, 226, 88, 256, 83, 29, 308]. These spin states can be optically initialized and read out, as well as coherently manipulated via microwave fields. Their energy levels can be probed by performing optically detected magnetic resonance (ODMR) spectroscopy where one measures a change in the NV's fluorescence intensity when an applied microwave field is on resonance between two NV spin sublevels (Fig. 1.4(a)), thus enabling sensing of a variety of external signals over a wide range of environmental conditions [191, 53, 241].

Here, we focus on the sensing of stress and magnetic fields, wherein the NV is governed by the Hamiltonian [29, 326], $H = H_0 + H_B + H_S$, with $H_0 = D_{gs} S_z^2$ (zero-field splitting), $H_B = \gamma_B \vec{B} \cdot \vec{S}$ (Zeeman splitting), and $H_S = [\alpha_1(\sigma_{xx} + \sigma_{yy}) + \beta_1 \sigma_{zz}] S_z^2 + [\alpha_2(\sigma_{yy} - \sigma_{xx}) + \beta_2(2\sigma_{xz})] (S_y^2 - S_x^2) + [\alpha_2(2\sigma_{xy}) + \beta_2(2\sigma_{yz})] (S_x S_y + S_y S_x)$ capturing the NV's response to the local diamond stress tensor, $\overleftrightarrow{\sigma}$ (Fig. 2.1(c)). Note that in the above, $\gamma_B \approx (2\pi) \times 2.8$ MHz/G is the gyromagnetic ratio, $\{\alpha_{1,2}, \beta_{1,2}\}$ are the stress susceptibility coefficients [83, 29, 308], $\hat{z}$ is the NV orientation axis, and $\hat{x}$ is defined such that the xz-plane contains one of the carbon-vacancy bonds (Fig. 1.4(b)). In general, the resulting ODMR spectra exhibit eight resonances arising from the four possible crystallographic orientations of the NV (Fig. 1.4(a)). By extracting the energy shifting and splitting of the spin sublevels for each NV orientation group, one obtains an overconstrained set of equations enabling the reconstruction of either the (six component) local stress tensor or the (three component) vector magnetic field.

In our experiments, we utilize a miniature DAC (Fig. 2.1, (a) and (b)) consisting of two opposing anvils compressing either a beryllium copper or rhenium gasket [311]. The sample chamber defined by the gasket and diamond-anvil culets is filled with a pressure-

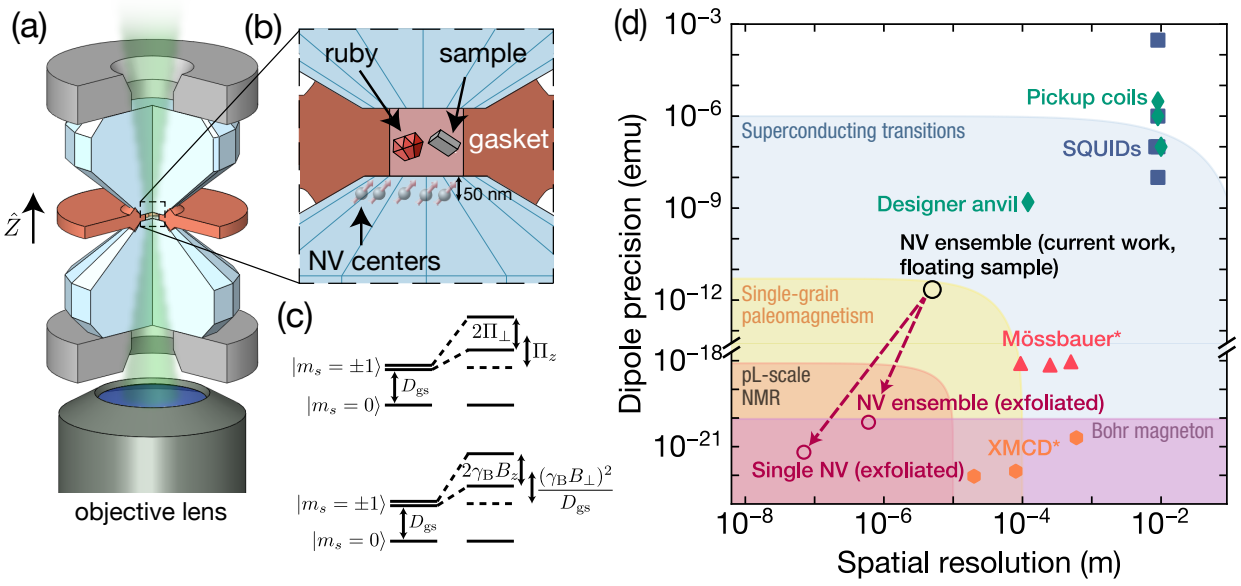

Figure 2.1: NV centers integrated into a diamond anvil cell. (a) Schematic of the DAC geometry. Two opposing anvils are compressed by a nonmagnetic steel cell and cubic boron nitride backing plates (gray). NV centers are initialized and read out using a 532 nm laser focused to a diffraction-limited spot (∼600 nm) which is scanned across the culet surface. (b) The DAC sample chamber is defined by the gasket-anvil assembly (diagram not to scale); it is loaded with the sample of interest, a pressure-transmitting medium, and a single ruby microsphere (pressure calibration). A ∼50 nm layer of NV centers is embedded into the diamond anvil directly below the sample chamber. (c) Stress (top) both shifts and splits the $|m_s = \pm1\rangle$ sublevels at first order; in particular, the shifting is characterized by $\Pi_z = \alpha_1(\sigma_{xx} + \sigma_{yy}) + \beta_1\sigma_{zz}$, and the splitting is characterized by $\Pi_\perp^2 = [\alpha_2(\sigma_{yy} - \sigma_{xx}) + \beta_2(2\sigma_{xz})]^2 + [\alpha_2(2\sigma_{xy}) + \beta_2(2\sigma_{yz})]^2$. An axial magnetic field (bottom) splits the $|m_s = \pm1\rangle$ sublevels at first order, but a transverse magnetic field leads to shifts only at second order. (d) Comparison of high pressure magnetometry techniques. We define the spatial resolution as a characteristic sensor length scale over which the sample magnetism is *integrated*. Estimates for our current work are shown assuming a sample suspended in a pressure medium 5 μm away from the culet (black open circle). We project that by exfoliating a sample directly onto the culet surface and using 5 nm implanted NV centers, the distance from the sample can be significantly reduced, thus improving both dipole precision and spatial resolution (open red circles). Inductive methods (pickup coils [green diamonds] and SQUIDs [blue squares]) integrate the magnetization of a sample over the coil's area; to this end, the diameter associated with the coil is taken as the "spatial resolution" although in principle, the sample inside the chamber can be significantly smaller. In contrast, high energy photon scattering techniques (x-ray magnetic circular dichroism [orange hexagons], and Mössbauer spectroscopy [pink triangles]) probe atomic scale magnetism; the length scale for these methods is shown here as the spot size of the excitation beam.

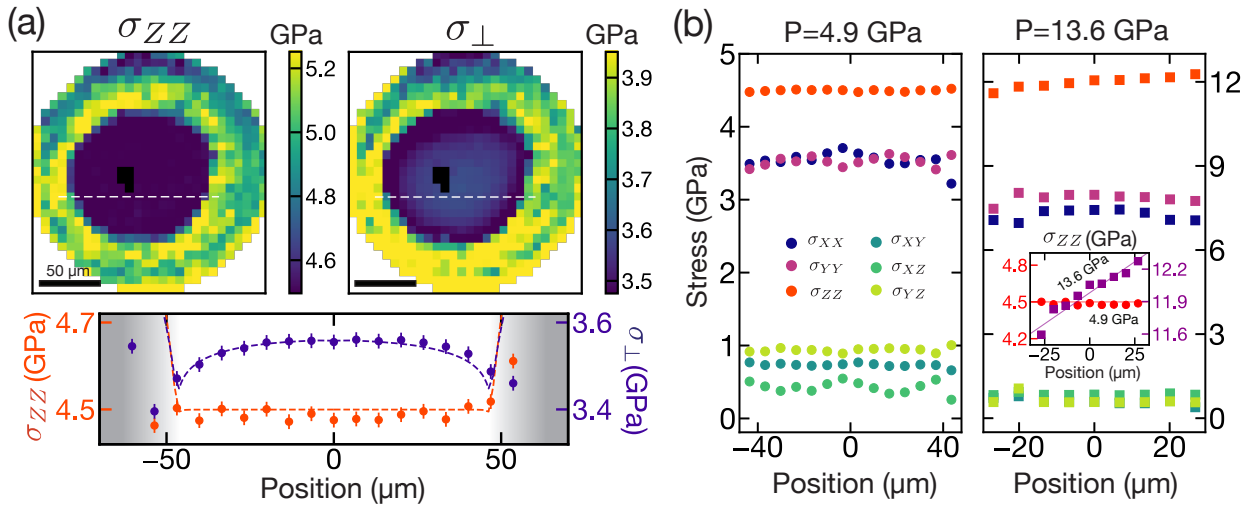

Figure 2.2: Full tensorial reconstruction of the stresses in a (111)-cut diamond anvil. (a) Spatially resolved maps of the loading stress (left) and mean lateral stress (right), $\sigma_\perp = \frac{1}{2}(\sigma_{XX} + \sigma_{YY})$, across the culet surface. In the inner region, where the culet surface contacts the pressure-transmitting medium (16:3:1 methanol/ethanol/water), the loading stress is spatially uniform, while the lateral stress is concentrated towards the center; this qualitative difference is highlighted by a linecut of the two stresses (below), and reconstructed by finite element analysis (orange and purple dashed lines). The black pixels indicate where the NV spectrum was obfuscated by the ruby microsphere. (b) Comparison of all stress tensor components in the fluid-contact region at $P = 4.9$ GPa and $P = 13.6$ GPa. At $P = 13.6$ GPa, the pressure-transmitting medium has entered its glassy phase and we observe a spatial gradient in the loading stress σ_{ZZ} (inset).

transmitting medium (either a 16:3:1 methanol/ethanol/water solution or cesium iodide) to provide a quasi-hydrostatic environment. Microwave excitation is applied via a 4 μm thick platinum foil compressed between the gasket and anvil pavilion facets, while scanning confocal microscopy (with a transverse diffraction-limited spot size ~600 nm, containing ~10^3 NVs) allows us to obtain two-dimensional ODMR maps across the culet.

2.3 Stress sensing

We begin by probing the stress tensor across the culet surface using two different cuts of diamond (i.e. (111)-cut and (110)-cut culet). For a generic stress environment, the intrinsic degeneracy associated with the four NV orientations is not sufficiently lifted, implying that individual resonances cannot be resolved. In order to resolve these resonances while preserving the stress contribution, we sequentially tune a well-controlled external magnetic field to be perpendicular to each of the different NV orientations . For each perpendicular

field choice, three of the four NV orientations exhibit a strong Zeeman splitting proportional to the projection of the external magnetic field along their symmetry axes. Crucially, this enables one to resolve the stress information encoded in the remaining NV orientation, while the other three groups of NVs are spectroscopically split away. Using this method, we obtain sufficient information to extract the full stress tensor, as depicted in Fig. 2.2. A number of intriguing features are observed at the interface between the culet and the sample chamber, which provide insight into both elastic (reversible) and plastic (irreversible) deformations.

At low pressures ($P = 4.9$ GPa), the normal stress along the loading axis, σ_{ZZ}, is spatially uniform (Fig. 2.2(a)), while all shear stresses, $\{\sigma_{XY}, \sigma_{XZ}, \sigma_{YZ}\}$, are minimal (Fig. 2.2(b)).[2] These observations are in agreement with conventional stress continuity predictions for the interface between a solid and an ideal fluid [104]. Moreover, σ_{ZZ} is consistent with the independently measured pressure inside the sample chamber (via ruby fluorescence), demonstrating the NV's potential as a built-in pressure scale [77]. In contrast to the uniformity of σ_{ZZ}, the field profile for the mean lateral stress, $\sigma_\perp \equiv \frac{1}{2}(\sigma_{XX}+\sigma_{YY})$, exhibits a concentration of forces toward the center of the culet (Fig. 2.2(a)). Using the measured σ_{ZZ} as a boundary condition, we perform finite element simulations to reproduce this spatial pattern.

Upon increasing pressure ($P = 13.6$ GPa), a pronounced spatial gradient in σ_{ZZ} emerges (Fig. 2.2(b), inset). This qualitatively distinct feature is consistent with the solidification of the pressure-transmitting medium into its glassy phase above $P_g \approx 10.5$ GPa [181]. Crucially, this demonstrates our ability to characterize the effective viscosity of solids and liquids under pressure. To characterize the sensitivity of our system, we perform ODMR spectroscopy with a static applied magnetic field and pressure under varying integration times and extract the frequency uncertainty from a Gaussian fit. We observe a stress sensitivity of $\{0.023, 0.030, 0.027\}$ GPa$/\sqrt{\text{Hz}}$ for hydrostatic, average normal, and average shear stresses, respectively. This is consistent with the theoretically derived stress sensitivity, $\eta_S \sim \frac{\Delta\nu}{\xi C\sqrt{Nt}} = \{0.017, 0.022, 0.020\}$ GPa$/\sqrt{\text{Hz}}$, respectively, where N is the number of NV centers, $\Delta\nu$ is the linewidth, ξ is the relevant stress susceptibility, t is the integration time, and C is an overall factor accounting for measurement infidelity. In combination with diffraction-limited imaging resolution, this sensitivity opens the door to measuring and ultimately controlling the full stress tensor distribution across a sample.

2.4 High pressure magnetometry

Having characterized the stress environment, we now utilize the NV centers as an *in situ* magnetometer to detect phase transitions inside the high-pressure chamber. Analogous to the case of stress, we observe a magnetic sensitivity of 12 μT$/\sqrt{\text{Hz}}$, in agreement with the theoretically estimated value, $\eta_B \sim \frac{\delta\nu}{C\gamma_B\sqrt{Nt}} = 8.8\ \mu$T$/\sqrt{\text{Hz}}$. Assuming a point dipole located

[2] We note that $\{\hat{X}, \hat{Y}, \hat{Z}\}$ corresponds to the lab frame while $\{\hat{x}, \hat{y}, \hat{z}\}$ corresponds to the NV frame (Fig. 1.4(b)).

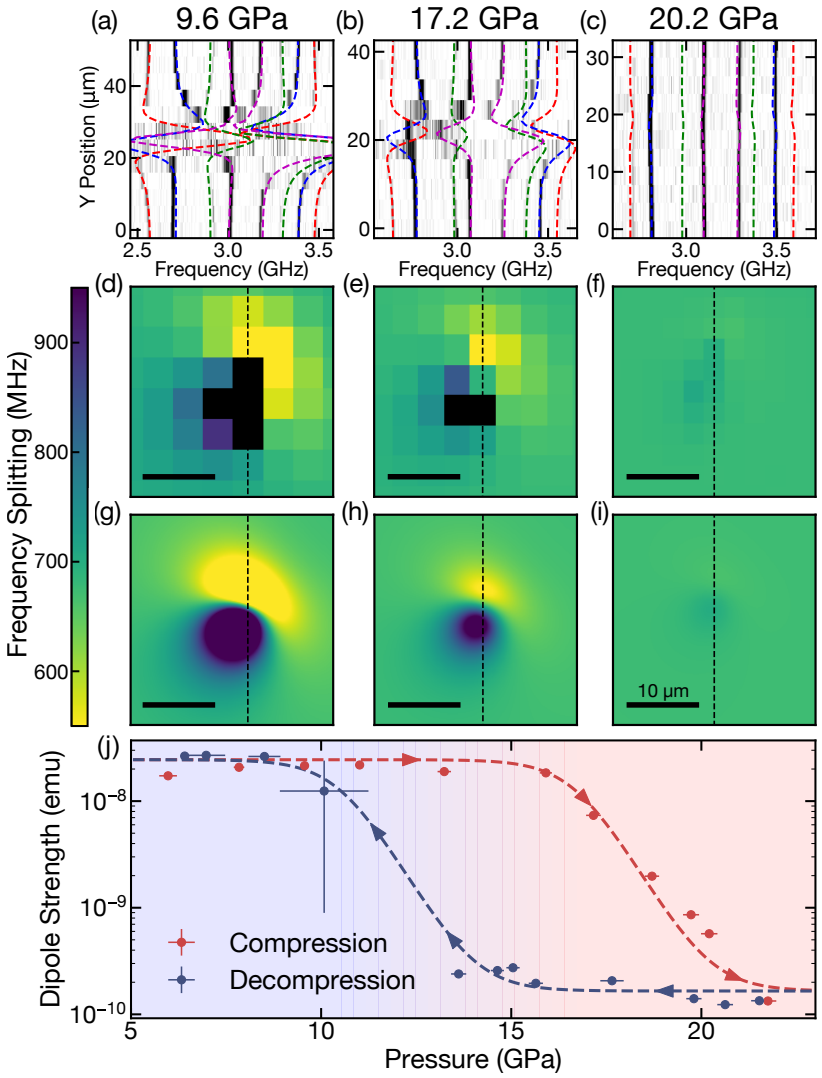

Figure 2.3: Imaging iron's $\alpha \leftrightarrow \epsilon$ phase transition. Applying an external magnetic field ($\mathbf{B}_{\text{ext}}$~180 G) induces a dipole moment in the polycrystalline iron pellet which generates a spatially varying magnetic field across the culet of the diamond anvil. By mapping the ODMR spectra across the culet surface, we reconstruct the local magnetic field which characterizes the iron pellet's magnetization. (a-c) Comparison between the measured ODMR spectra (dark regions correspond to resonances) and the theoretical resonance positions (different colors correspond to different NV crystallographic orientations) across vertical spatial cuts at pressures 9.6 GPa, 17.2 GPa and 20.2 GPa, respectively (16:3:1 methanol/ethanol/water solution). (d-f) Map of the measured energy difference of a particular NV crystallographic orientation (blue lines in (a-c)). Black pixels correspond to ODMR spectra where the splitting could not be accurately extracted owing to large magnetic field gradients. (g-i) Theoretical reconstruction of the energy differences shown in (d-f). Data depicted in (a-c) are taken along the thin black dashed lines. (j) Measured dipole moment of the iron pellet as a function of applied pressure at room temperature, for both compression (red) and decompression (blue). Based on the hysteresis observed (~6 GPa), we find the critical pressure $P_c = 13.6 \pm 3.6$ GPa, in excellent agreement with previous studies [318].

a distance $d \sim 5$ μm from the NV layer, this corresponds to an experimentally measured magnetic moment sensitivity: 7.5×10^{-12} emu/$\sqrt{\text{Hz}}$ (Fig. 2.1(d)).

2.4.1 Pressure-induced magnetic transition in elemental iron

Sensitivity in hand, we begin by directly measuring the magnetization of iron as it undergoes the pressure-driven $\alpha \leftrightarrow \epsilon$ phase transition from body-centered cubic (bcc) to hexagonal close-packed (hcp) crystal structures [318]; crucially, this structural phase transition is accompanied by the depletion of the magnetic moment, and it is this change in the iron's magnetic behavior that we image. Our sample chamber is loaded with a $\sim$10 μm polycrystalline iron pellet as well as a ruby microsphere (pressure scale), and we apply an external magnetic field $\mathbf{B}_{\text{ext}}\sim$180 G. As before, by performing a confocal scan across the culet, we acquire a two-dimensional magnetic resonance map (Fig. 2.3). At low pressures (Fig. 2.3(a)), near the iron pellet, we observe significant shifts in the eight NV resonances, owing to the presence of a ferromagnetic field from the iron pellet. As one increases pressure (Fig. 2.3(b)), these shifts begin to diminish, signaling a reduction in the magnetic susceptibility. Finally, at the highest pressures ($P \sim 22$ GPa, Fig. 2.3(c)), the magnetic field from the pellet has reduced by over two orders of magnitude.

To quantify this phase transition, we reconstruct the full vector magnetic field produced by the iron sample from the aforementioned two-dimensional NV magnetic resonance maps (Fig. 2.3, (d)-(f)). We then compare this information with the expected field distribution at the NV layer inside the culet, assuming the iron pellet generates a dipole field. This enables us to extract an effective dipole moment as a function of applied pressure (Fig. 2.3(g)). In order to identify the critical pressure, we fit the transition using a logistic function. This procedure yields the transition at $P = 16.7 \pm 0.7$ GPa (Fig. 2.3(j)).

In addition to changes in the magnetic behavior, another key signature of this first order transition is the presence of hysteresis. We investigate this by slowly decompressing the diamond anvil cell and monitoring the dipole moment; the decompression transition occurs at $P = 10.5 \pm 0.7$ GPa (Fig. 2.3(j)), suggesting a hysteresis width of approximately $\sim$6 GPa, consistent with a combination of intrinsic hysteresis and finite shear stresses in the methanol/ethanol/water pressure-transmitting medium [318]. Taking the average of the forward and backward hysteresis pressures, we find a critical pressure of $P_{\text{c}} = 13.6 \pm 3.6$ GPa, in excellent agreement with independent measurements by Mössbauer spectroscopy, where $P_{\text{c}} \approx 12$ GPa (Fig. 2.3(j)) [318].

2.4.2 Mapping the $P - T$ phase diagram of gadolinium

Next, we demonstrate the integration of our platform into a cryogenic system, enabling us to make spatially resolved *in situ* measurements across the pressure-temperature (P-T) phase diagram of materials. Specifically, we investigate the magnetic P-T phase diagram of the rare-earth element gadolinium (Gd) up to pressures $P \approx 8$ GPa and between temperatures $T = 25 - 340$ K. Owing to an interplay between localized 4f electrons and mobile conduction

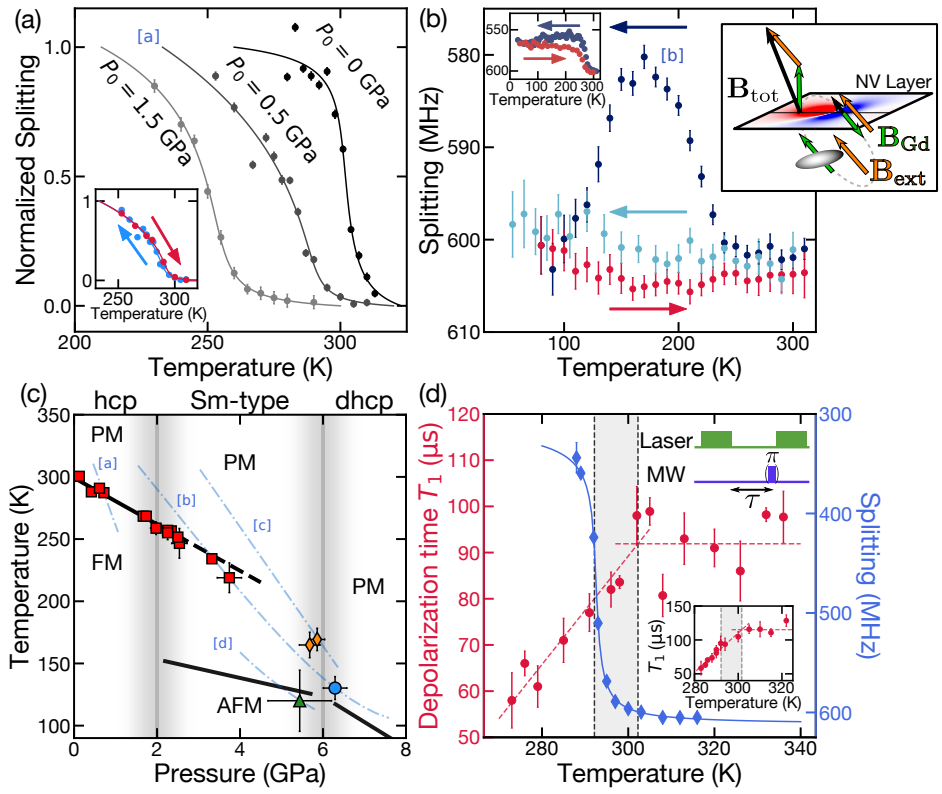

Figure 2.4: Magnetic P-T phase diagram of gadolinium. A $\sim 30\,\mu m \times 30\,\mu m \times 25\,\mu m$ polycrystalline Gd foil is loaded into a beryllium copper gasket with a cesium iodide pressure medium. An external magnetic field, $\mathbf{B}_{ext}$~120 G, induces a dipole field, $\mathbf{B}_{Gd}$, detected by the splitting of the NVs (right inset, (B)). (a) The FM Curie temperature T_C decreases with increasing pressure up to ~ 4 GPa. NV splittings for three P-T paths, labeled by their initial pressure P_0, are shown. The P-T path for run [a] ($P_0 = 0.5$ GPa) is shown in (c). The cool-down (blue) and heat-up (red) of a single P-T cycle shows negligible hysteresis (inset). (b) If a P-T path starting in hcp is taken into the dhcp phase (at pressures $\gtrsim 6$ GPa) [165], the FM signal is lost and not reversible, as shown in (c) (path [b]). Upon cool-down (dark blue), we observe the aforementioned Curie transition, followed by the loss of FM signal at 6.3 GPa, 130 K. But upon heat-up (red) and second cool-down (light blue), the FM signal is not recovered. When the pressure does not go beyond ~ 6 GPa, the FM signal is recoverable (left inset). (c) Magnetic P-T phase diagram of Gd. At low pressures, we observe the linear decrease of T_C (black line) with slope -18.7 ± 0.2 K/GPa, in agreement with previous measurements [165]. This linear regime extends into the Sm-type phase (black dashed line) due to the slow dynamics of the hcp $\rightarrow$ Sm-type transition [165]. When starting in the Sm-type phase, we no longer observe a FM signal, but rather a small change in the magnetic field at either the transition from Sm-type to dhcp (orange diamonds) or from PM to AFM (green triangle), depending on the P-T path. The bottom two phase boundaries (black lines) are taken from Ref. [287]. (d) At ambient pressure, we observe a Curie temperature, $T_C = 292.2 \pm 0.1$ K, via DC magnetometry (blue data). Using nanodiamonds drop-cast onto a Gd foil (and no applied external magnetic field), we find that the depolarization time (T_1) of the NVs is qualitatively different in the two phases (red data). T_1 is measured using the pulse sequence shown in the top right inset. The T_1 measurement on another nanodiamond exhibits nearly identical behavior (bottom inset).

electrons, Gd represents an interesting playground for studying metallic magnetism; in particular, the itinerant electrons mediate RKKY-type interactions between the local moments, which in turn induce spin-polarization of the itinerant electrons [255]. Moreover, much like its other rare-earth cousins, Gd exhibits a series of pressure-driven structural phase transitions from hexagonal close-packed (hcp) to samarium-type (Sm-type) to double hexagonal close-packed (dhcp) (Fig. 2.4)[165]. The interplay between these different structural phases, various types of magnetic ordering and metastable transition dynamics leads to a complex magnetic P-T phase diagram that remains the object of study to this day [165, 287, 255].

In analogy to our measurements of iron, we monitor the magnetic ordering of a Gd flake via the NV's ODMR spectra at two different locations inside the culet: close to and far away from the sample (the latter to be used as a control). Due to thermal contraction of the DAC (which induces a change in pressure), each experimental run traces a distinct non-isobaric path through the P-T phase diagram (Fig. 2.4(c), blue curves). In addition to these DC magnetometry measurements, we also operate the NV sensors in a complementary mode, i.e. as a noise spectrometer.

We begin by characterizing Gd's well-known ferromagnetic Curie transition at ambient pressure, which induces a sharp jump in the splitting of the NV resonances at $T_{\mathrm{C}} = 292.2 \pm 0.1$ K (Fig. 2.4(d)). As depicted in Fig. 2.4(a), upon increasing pressure, this transition shifts to lower temperatures, and consonant with its second order nature [142], we observe no hysteresis; this motivates us to fit the data and extract T_{C} by solving a regularized Landau free-energy equation. Combining all of the low pressure data (Fig. 2.4(c), red squares), we find a linear decrease in the Curie temperature at a rate: $dT_{\mathrm{C}}/dP = -18.7 \pm 0.2$ K/GPa, consistent with prior studies via both DC conductivity and AC-magnetic susceptibility [165]. Surprisingly, this linear decrease extends well into the Sm-type phase. Upon increasing pressure above ~ 6 GPa (path [b] in Fig. 2.4(c)), we observe the loss of ferromagnetic (FM) signal (Fig. 2.4(b)), indicating a first order structural transition into the paramagnetic (PM) dhcp phase [165]. In stark contrast to the previous Curie transition, there is no revival of a ferromagnetic signal even after heating up ($\sim$315 K) and significantly reducing the pressure (< 0.1 GPa).

A few remarks are in order. The linear decrease of T_{C} well beyond the $\sim$2 GPa structural transition between hcp and Sm-type is consistent with the "sluggish" equilibration between these two phases at low temperatures [165]. The metastable dynamics of this transition are strongly pressure and temperature dependent, suggesting that different starting points (in the P-T phase diagram) can exhibit dramatically different behaviors [165]. To highlight this, we probe two *different* transitions out of the paramagnetic Sm-type phase by tailoring specific paths in the P-T phase diagram. By taking a shallow path in P-T space, we observe a small change in the local magnetic field across the *structural* transition into the PM dhcp phase at $\sim$6 GPa (Fig. 2.4(c), path [c], orange diamonds). By taking a steeper path in P-T space, one can also investigate the *magnetic* transition into the antiferromagnetic (AFM) Sm-type phase at $\sim$150 K (Fig. 2.4(c), path [d], green triangle). In general, these two transitions are extremely challenging to probe via DC magnetometry since their signals arise only from small differences in the susceptibilities between the various phases.

To this end, we demonstrate a complementary NV sensing modality based upon noise spectroscopy, which can probe phase transitions even in the absence of a direct magnetic signal [59]. Specifically, returning to Gd's ferromagnetic Curie transition, we monitor the NV's depolarization time, T_1, as one crosses the phase transition (Fig. 2.4(d)). Normally, the NV's T_1 time is limited by spin-phonon interactions and *increases* dramatically as one decreases temperature. Here, we observe a strikingly disparate behavior. In particular, using nanodiamonds drop-cast on a Gd foil at ambient pressure, we find that the NV T_1 is nearly temperature independent in the paramagnetic phase, before exhibiting a kink and subsequent *decrease* as one enters the ferromagnetic phase (Fig. 2.4(d)). We note two intriguing observations: first, one possible microscopic explanation for this behavior is that T_1 is dominated by Johnson-Nyquist noise from the thermal fluctuations of charge carriers inside Gd [185].[3] Gapless critical spin fluctuations or magnons in the ordered phase, while expected, are less likely to cause this signal. Second, we observe that the Curie temperature, as identified via T_1-noise spectroscopy, is $\sim$10 K higher than that observed via DC magnetometry (Fig. 2.4(d)). Similar behavior has previously been reported for the surface of Gd [255, 316], suggesting that our noise spectroscopy could be more sensitive to surface physics.

2.5 Experimental details

2.5.1 Diamond anvil cell and sample preparation

All diamond anvils used in this work are synthetic type-Ib ([N] $\lesssim$ 200 ppm) single crystal diamonds cut into a 16-sided standard design with dimensions 0.2 mm diameter culet, 2.75 mm diameter girdle, and 2 mm height (Almax-easyLab and Syntek Co., Ltd.). For stress measurement, both anvils with (111)-cut-culet and (110)-cut-culet are used, while for magentic measurement on iron and gadolinium, (110)-cut-culet anvil is used. We perform $^{12}C^{+}$ ion implantation (CuttingEdge Ions, 30 keV energy, 5×10^{12} cm^{-2}) to generate a $\sim$50 nm layer of vacancies near the culet surface. After implantation, the diamonds are annealed in vacuum ($< 10^{-6}$ Torr) using a home-built furnace with the following recipe: 12 hours ramp to 400°C, dwell for 8 hours, 12 hours ramp to 800°C, dwell for 8 hours, 12 hours ramp to 1200°C, dwell for 2 hours. During annealing, the vacancies become mobile, and probabilistically form NV centers with intrinsic nitrogen defects. After annealing, the NV concentration is estimated to be around 1 ppm as measured by flourescence intensity. The NV centers are photostable after many iterations of compression and decompression up to 27 GPa, with spin-echo coherence time $T_2 \approx 1\ \mu s$, mainly limited by nitrogen spin bath.

The miniature diamond anvil cell body is made of nonmagnetic Vascomax with cubic boron nitride backing plates (Technodiamant). Nonmagnetic gaskets (rhenium or beryllium copper) and pressure media (cesium iodide, methanol/ethanol/water) are used for all experiments.

[3] As opposed to isolated NV samples, where T_1 is limited by spin-phonon interactions.

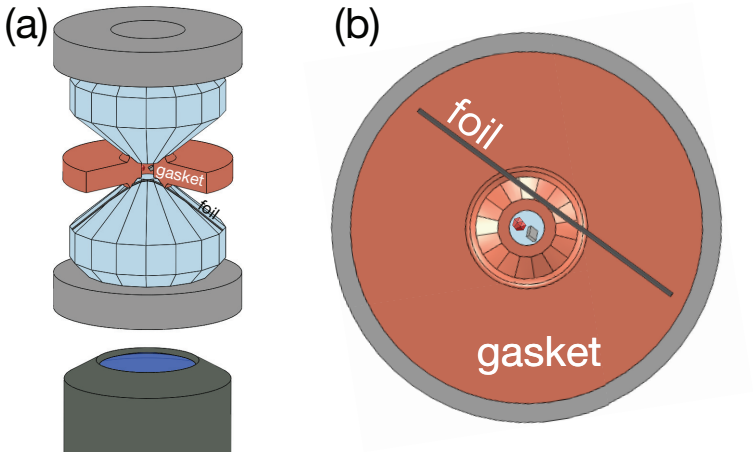

Figure 2.5: (a) Schematic of the setup explicitly depicting the platinum foil used for microwave excitation. The gasket has been cross sectioned for visual clarity. (b) Schematic from the perspective of the objective lens. The anvil has been omitted for visual clarity. Diagrams are not to scale.

2.5.2 Experimental setup

We address NV ensembles integrated inside the DAC using a home-built confocal microscope. A 100 mW 532 nm diode-pumped solid-state laser (Coherent Compass), controlled by an acousto-optic modulator (AOM, Gooch & Housego AOMO 3110-120) in a double-pass configuration, is used for both NV spin initialization and detection. The laser beam is focused through the light port of the DAC to the NV layer using a long working distance objective lens (Mitutoyo 378-804-3, NA 0.42, for stress and iron measurements; Olympus LCPLFLN-LCD 20X, NA 0.45, for gadolinium measurement in cryogenic environment), with a diffraction-limit spot size $\approx$ 600 nm. The NV fluorescence is collected using the same objective lens, spectrally separated from the laser using a dichroic mirror, further filtered using a 633 nm long-pass filter, and then detected by a fiber coupled single photon counting module (SPCM, Excelitas SPCM-AQRH-64FC). A data aquisition card (National Instruments USB-6343) is used for fluorescence counting and subsequent data processing. The lateral scanning of the laser beam is performed using a two-dimensional galvanometer (Thorlabs GVS212), while the vertical focal spot position is controlled by a piezo-driven positioner (Edmund Optics at room temperture; attocube at cryogenic temperature). For gadolinium measurements, we put the DAC into a closed-cycle cryostat (attocube attoDRY 800) for temperature control from $35 - 320$ K. The AOM and the SPCM are gated by a programmable multi-channel pulse generator (SpinCore PulseBlasterESR-PRO 500) with 2 ns temporal resolution.

A microwave source (Stanford Research Systems SG384) in combination with a 16W amplifier (Mini-Circuits ZHL-16W-43+) serves to generate signals for NV spin state manipulation. The microwave field is delivered to DAC through a 4 μm thick platinum foil

compressed between the gasket and anvil pavilion facets (Fig. 2.5), followed by a 40 dB attenuator and a 50 Ω termination.

2.6 Sensitivity and accuracy

2.6.1 Theoretical sensitivity

The magnetic field sensitivity for continuous-wave ODMR [93] is given by:

$$\eta_{\mathrm{B}} = \mathcal{P}_G \frac{1}{\gamma_{\mathrm{B}}} \frac{\Delta\nu}{\mathcal{C}\sqrt{\mathcal{R}}}, \tag{2.1}$$

where γ_{B} is the gyromagnetic ratio, $\mathcal{P}_G \approx 0.7$ is a unitless numerical factor for a Gaussian lineshape, $\Delta\nu = 10$ MHz is the resonance linewidth, $\mathcal{C} \approx 1.8\%$ is the resonance contrast, and $\mathcal{R} \approx 2.5 \times 10^6$ s^{-1} is the photon collection rate. One can relate this to magnetic moment sensitivity by assuming that the field is generated by a point dipole located a distance d from the NV center (pointing along the NV axis). Then the dipole moment sensitivity is given by

$$\eta_{\mathrm{m}} = \mathcal{P}_G \frac{1}{\gamma_{\mathrm{B}}} \frac{\Delta\nu}{\mathcal{C}\sqrt{\mathcal{R}}} \frac{2\pi d^3}{\mu_0}, \tag{2.2}$$

where μ_0 is the vacuum permeability.

Analogous to Eq. 2.1, the stress sensitivity for continuous-wave ODMR is given by

$$\eta_{\mathrm{S}} = \mathcal{P}_G \frac{1}{\xi} \frac{\Delta\nu}{\mathcal{C}\sqrt{\mathcal{R}}}, \tag{2.3}$$

where ξ is the susceptibility for the relevant stress quantity. More specifically, ξ is a tensor defined by:

$$\xi_{\alpha\beta} = \left| \frac{\delta f_\alpha}{\delta \sigma_\beta} \right|_{\sigma^{(0)}} \tag{2.4}$$

where f_α, $\alpha \in [1, 8]$ are the resonance frequences associated with the 4 NV crytallographic orientations; $\sigma^{(0)}$ is an initial stress state; and $\delta\sigma_\beta$ is a small perturbation to a given stress component, e.g. $\beta \in \{XX, YY, ZZ, XY, XZ, YZ\}$. For optimal sensitivity, we consider perturbations about an unstressed state (i.e. $\sigma^{(0)} = \mathbf{0}$) [4]. The resulting susceptibilities for stress components in a (111)-cut diamond frame[5] are

[4] Equivalently, one can begin from any hydrostatic stress, i.e. $\sigma^{(0)} \sim \mathbf{I}$. Non-hydrostatic stress, however, will generally reduce the stress susceptibilities, as will the presence of electric or magnetic fields.

[5] The Z axis is normal to the diamond surface, and the XZ plane contains two of the NV axes (the vertical axis and one of the three non-vertical axes).

$$\xi_{\alpha\beta} = (2\pi)\times \begin{bmatrix} 10.5 & 10.5 & 2.5 & 3.9 & 9.0 & 9.0 \\ 6.6 & 6.6 & 2.5 & 3.9 & 9.0 & 9.0 \\ 1.3 & 10.5 & 11.9 & 9.8 & 12.7 & 0.7 \\ 3.9 & 6.6 & 2.8 & 9.8 & 1.2 & 0.7 \\ 10.8 & 6.1 & 11.9 & 13.5 & 0.5 & 11.1 \\ 1.4 & 3.7 & 2.8 & 3.6 & 6.4 & 1.0 \\ 10.8 & 6.1 & 11.9 & 3.6 & 0.5 & 1.0 \\ 1.4 & 3.7 & 2.8 & 13.5 & 6.4 & 11.1 \end{bmatrix} \text{[MHz/GPa]}.$$

In Table 2.1, we compute the sensitivity using the maximum susceptibility for each stress component:

$$\xi_\beta^{(max)} = \max_\alpha \xi_{\alpha\beta} \tag{2.5}$$

2.6.2 Experimental sensitivity and accuracy

In order to characterize the sensitivity of our system, we perform ODMR spectroscopy on a single resonance. We fit a Gaussian lineshape to this resonance and observe the fitting error on the center frequency as a function of the total integration time, T (Fig. 2.6). In particular, we fit the time scaling behavior of the fitting error to $AT^{-1/2}$, where A, divided by the susceptibility of interest, characterizes the experimental sensitivity for a given signal. For $T \gtrsim 100$ s, the experimental accuracy saturates due to systematic noise, which we define here as the "systematic accuracy" for each type of signal.

For scalar signals (e.g. axial magnetic fields, temperature, etc.), the accuracy is directly proportional to the minimum fitting error. For stress components, however, determining the accuracy is more complicated as the relation between resonance frequencies and the full stress tensor is a multi-dimensional, nonlinear function (Section 2.7.1). To this end, we quantify the accuracy of each stress component using a Monte Carlo procedure. We begin with an unstressed state, which corresponds to the initial set of frequencies $f_\alpha^{(0)} = D_{\text{gs}}$. We then apply noise to each of the freqencies based on the minimum fitting error determined above—i.e. $f_\alpha^{(0)} + \delta f_\alpha$, where δf_α are sampled from a Gaussian distribution with a width of the fitting error—and calculate the corresponding stress tensor using a least-squared fit (Sec. 2.7.1). Repeating this procedure over many noise realizations, we compute the standard deviation of each stress component. The results of this procedure are shown in Table 2.1.

2.6.3 Comparison to other magnetometry techniques

In this section, we discuss the comparison of magnetometry techniques presented in Fig. 2.1(d) of the main text. For each sensor, the corresponding dipole accuracy (as defined in Section 2.6.2) is plotted against its relevant "spatial resolution," roughly defined as the length scale within which one can localize the source of a magnetic signal. In the following discussion, we specify the length scale plotted for each method in Fig. 2.1(d). We consider two broad categories of high pressure magnetometers.

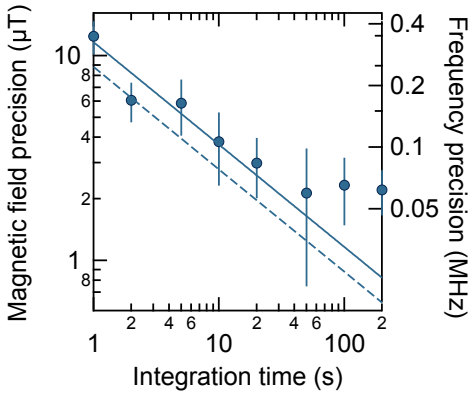

Figure 2.6: Scaling of magnetic field precision as a function of total integration time on a single resonance. Right axis corresponds to standard deviation of center frequency fitting. Solid line corresponds to a fit to $AT^{-1/2}$ where A is the sensitivity reported in Section 2.4 and T is the total integration time. Dashed line corresponds to the scaling predicted by Eq. 2.1. The experimental accuracy saturates for $T \gtrsim 100$ s due to systematic noise.

The first category encompasses inductive methods such as pickup coils [107, 239, 158] and superconducting quantum interference devices (SQUIDs) [15, 240, 122, 313, 218][6]. Magnetic dipole measurement accuracies are readily reported in various studies employing inductive methods. We estimate the relevant length scale of each implementation as the pickup coil or sample bore diameter.

The second class of magnetometers comprises high energy methods including Mössbauer spectroscopy [260, 261, 173] and x-ray magnetic circular dichroism (XMCD) [222, 152, 339, 61], which probe atomic scale magnetic environments. For the Mössbauer studies considered in our analysis, we calculate magnetic dipole moment accuracies by converting B-field uncertainties into magnetic moments, assuming a distance to the dipole on order of the lattice spacing of the sample. We assess the length scale as either the size of the absorbing sample or the length scale associated with the sample chamber/culet area. For XMCD studies, we accept the moment accuracies reported in the text. Length scales are reported as the square root of the spot size area. Notably, we emphasize that both methods provide information about atomic scale dipole moments rather than a sample-integrated magnetic moment; these methods are thus not directly comparable to inductive methods.

We compare these methods alongside the NV center, whose accuracy is defined in Section 2.6.2 and shown in Table 2.1. For the current work, we estimate a length scale ~ 5 μm, corresponding to the approximate distance between a sample (suspended in a pressure-transmitting medium) and the anvil culet. By exfoliating a sample onto the diamond surface,

[6]Under the category of inductive methods, we also include the "designer anvil" which embeds a pickup coil directly into the diamond anvil.

Signal (unit)	Theo Sensitivity (unit/$\sqrt{\text{Hz}}$)	Exp Sensitivity (unit/$\sqrt{\text{Hz}}$)	Accuracy (unit)
Hydrostatic stress (GPa)	0.017	0.023	0.0012
Average normal stress (GPa)	0.022	0.03	0.0032
Average shear stress (GPa)	0.020	0.027	0.0031
Magnetic field (μT)	8.8	12	2.2
Magnetic dipole (emu), floating sample ($d = 5$ μm)	5.5×10^{-12}	7.5×10^{-12}	1.4×10^{-12}
Magnetic dipole (emu), exfoliated sample ($d = 5$ nm)$^{(*)}$	1.7×10^{-20}	2.3×10^{-20}	4.3×10^{-21}
Magnetic dipole (emu), exfoliated sample, single NV ($d = 5$ nm)$^{(\dagger)}$	1.6×10^{-21}	2.2×10^{-21}	4.0×10^{-22}
Electric field (kV/cm), single NV$^{(\dagger)}$	1.8	2.5	0.45
Temperature (K), single NV$^{(\dagger)}$	0.4	0.55	0.10

Table 2.1: NV sensitivity and accuracy for various signals. Sensitivity is calculated using Eqs. 2.2-2.3. We also report the typical fitting error of the center frequency. Gray rows correspond to projected sensitivity given an exfoliated sample atop $^{(*)}$ an ensemble of 5 nm depth NV centers or $^{(\dagger)}$ a single 5 nm depth NV center with $\Delta\nu = 1$ MHz, $\mathcal{C} = 0.1, \mathcal{R} = 10^4$ s^{-1}. Magnetic dipoles are reported in units of emu, where 1 emu $= 10^{-3}$ A$\cdot$m^2.

the diffraction-limit ~ 600 nm bounds the transverse imaging resolution for ensemble NV centers; this limit can be further improved for single NV centers via super-resolution techniques [274].

2.7 Stress tensor

2.7.1 Overview

In this section, we describe our procedure for reconstructing the full stress tensor using NV spectroscopy. This technique relies on the fact that the four NV crystallographic orientations experience different projections of the stress tensor within their local reference frames. In particular, the full Hamiltonian describing the stress interaction is given by:

$$H_{\text{S}} = \sum_i \Pi_{z,i} S_{z,i}^2 + \Pi_{x,i} \left(S_{y,i}^2 - S_{x,i}^2 \right) + \Pi_{y,i} \left(S_{x,i} S_{y,i} + S_{y,i} S_{x,i} \right) \tag{2.6}$$

where

$$\Pi_{z,i} = \alpha_1 \left(\sigma_{xx}^{(i)} + \sigma_{yy}^{(i)}\right) + \beta_1 \sigma_{zz}^{(i)} \tag{2.7}$$

$$\Pi_{x,i} = \alpha_2 \left(\sigma_{yy}^{(i)} - \sigma_{xx}^{(i)}\right) + \beta_2 \left(2\sigma_{xz}^{(i)}\right) \tag{2.8}$$

$$\Pi_{y,i} = \alpha_2 \left(2\sigma_{xy}^{(i)}\right) + \beta_2 \left(2\sigma_{yz}^{(i)}\right) \tag{2.9}$$

$\sigma^{(i)}$ is the stress tensor in the local frame of each of NV orientations labeled by $\{i = 1, 2, 3, 4\}$, and $\{\alpha_{1,2}, \beta_{1,2}\}$ are stress susceptibility parameters (Section 2.7.3.3). Diagonalizing this Hamiltonian, one finds that the energy levels of each NV orientation exhibit two distinct effects: the $|m_s = \pm 1\rangle$ states are *shifted* in energy by $\Pi_{z,i}$ and *split* by $2\Pi_{\perp,i} = 2\sqrt{\Pi_{x,i}^2 + \Pi_{y,i}^2}$. Thus, the Hamiltonian can be thought of as a function that maps the stress tensor in the lab frame to eight observables: $H_{\mathrm{S}}(\sigma^{(\mathrm{lab})}) = \{\Pi_{z,1}, \Pi_{\perp,1}, \Pi_{z,2}, \Pi_{\perp,2}, ...\}$. Obtaining these observables through spectroscopy, one can numerically invert this function and solve for all six components of the corresponding stress tensor.

In practice, resolving the resonances of the four NV orientation groups is not straightforward because the ensemble spectra can exhibit near degeneracies. When performing ensemble NV magnetometry, a common approach is to spectroscopically separate the resonances using an external bias magnetic field. However, unlike magnetic contributions to the Hamiltonian, stress that couples via $\Pi_\perp$ is suppressed by an axial magnetic field. Therefore, a generic magnetic field provides only stress information via the shifting parameters, $\Pi_{z,i}$, which is insufficient for reconstructing the full tensor.

To address this issue, we demonstrate a novel technique that consists of applying a well-controlled external magnetic field perpendicular to each of the NV orientations. This technique leverages the symmetry of the NV center, which suppresses its sensitivity to transverse magnetic fields. In particular, for each perpendicular field choice, three of the four NV orientations exhibit a strong Zeeman splitting proportional to the projection of the external magnetic field along their symmetry axes, while the fourth (perpendicular) orientation is essentially unperturbed [7]. This enables one to resolve $\Pi_{z,i}$ for all four orientations and $\Pi_{\perp,i}$ for the orientation that is perpendicular to the field. Repeating this procedure for each NV orientation, one can obtain the remaining splitting parameters and thus reconstruct the full stress tensor.

In the following sections, we provide additional details regarding our experimental procedure and analysis. In Section 2.7.2, we describe how to use the four NV orientations to calibrate three-dimensional magnetic coils and to determine the crystal frame relative to the lab frame. In Section 2.7.3, we discuss our fitting procedure, the role of the NV's local charge environment, and the origin of the stress susceptibility parameters. In Section 2.7.4, we present the results of our stress reconstruction procedure for both (111)- and (110)-cut diamond. In Section 2.7.5, we compare our experimental results to finite element simulations.

[7] A transverse magnetic field leads to shifting and splitting at second order in field strength. We account for the former through a correction described in Section 2.7.3, while the latter effect is small enough to be neglected. More specifically, the effective splitting caused by magnetic fields is $(\gamma_{\mathrm{B}} B_\perp)^2 / D_{gs} \approx 5 - 10$ MHz, which is smaller than the typical splitting observed at zero field.

2.7.2 External field details

2.7.2.1 Electromagnet calibration procedure

To apply carefully aligned magnetic fields, we utilize a set of three electromagnets that are approximately spatially orthogonal with one another and can be controlled independently via the application of current. Each coil is placed >10 cm away from the sample to reduce the magnetic gradient across the $(200\ \mu\text{m})^2$ culet area.[8]

To calibrate the magnetic field at the location of the sample, we assume that the field produced by each coil is linearly porportional to the applied current, I. Our goal is then to find the set of coefficients, a_{mn} such that

$$B_m = \sum_m a_{mn} I_n, \tag{2.10}$$

where $B_m = \{B_{\mathcal{X}}, B_{\mathcal{Y}}, B_{\mathcal{Z}}\}$ is the magnetic field in the crystal frame and $n = \{1, 2, 3\}$ indexes the three electromagnets. We note that this construction does not require the electromagnets to be spatially orthogonal.

To determine the nine coefficients, we apply arbitrary currents and measure the Zeeman splitting of the four NV orientations via ODMR spectroscopy. Notably, this requires the ability to accurately assign each pair of resonances to their NV crystallographic orientation. We achieve this by considering the amplitudes of the four pairs of resonances, which are proportional to the relative angles between the polarization of the excitation laser and the four crystallagraphic orientations. In particular, the $|m_s = 0\rangle \leftrightarrow |m_s = \pm 1\rangle$ transition is driven by the perpendicular component of the laser field polarization with respect to the NV's symmetry axis. Therefore, tuning the laser polarization allows us to assign each pair of resonances to a particular NV orientation.

In order to minimize the number of fitting variables, we choose magnetic fields whose projection along each NV orientation is sufficient to suppress their transverse stress-induced energy splitting, i.e. $\gamma_{\text{B}} B \gg \Pi_{\perp}$. As a result, the spectrum measured at each magnetic field is determined by (a) the stress-induced shift $\Pi_{z,i}$ for each NV orientation, which is constant for all applied fields, and (b) the applied vector magnetic field $\{B_{\mathcal{X}}, B_{\mathcal{Y}}, B_{\mathcal{Z}}\}$. Sequentially applying different currents to the electromagnet coils and determining the subsequent vector magnetic field at the sample three times, we obtain sufficient information to determine the matrix a_{mn} as well as the shift Π_z for all NV orientations. We find that the calibration technique is precise to within 2%.

2.7.2.2 Calibration of crystal and laboratory frames

To determine the orientation of the crystal frame (i.e. the [100] diamond axis) with respect to the lab frame, we apply an arbitrary magnetic field and measure its angle (a) in the lab frame via a handheld magnetometer, and (b) in the crystal frame via the Zeeman splittings

[8] We note that the pressure cell, pressure medium and gasket are nonmagnetic.

(see 2.7.2). Together with the known diamond cut, this provides a system of equations for the rotation matrix, R_c, that relates the lab frame and the crystal frame:

$$R_{\mathrm{c}}\hat{B}^{(\mathrm{lab})} = \hat{B}^{(\mathrm{crystal})}\,, \quad R_{\mathrm{c}}\hat{Z} = \hat{e}^{(\mathrm{crystal})} \tag{2.11}$$

where $\hat{Z} = (0,0,1)^\top$ is the longitudinal axis in the lab frame, and $\hat{e}^{(\mathrm{crystal})}$ is the unit vector perpendicular to the diamond cut surface in crystal frame, e.g. $\hat{e}^{(\mathrm{crystal})} \propto (1,1,1)^\top$ for the (111)-cut diamond. We solve for R_c by numerically minimizing the least-squared residue of these two equations.

However, we note that the magnetic field determined by the Zeeman splittings contains an overall sign ambiguity. To account for this, we numerically solve Eq. (2.11) using both signs for $\hat{B}^{(\mathrm{crystal})}$ and select the solution for R_{c} with the smaller residue. Based on this residue, we estimate that our calibration is precise to within a few degrees.

2.7.3 Analysis

2.7.3.1 Extracting splitting and shifting information

Having developed a technique to spectrally resolve the resonances, we fit the resulting spectra to four pairs of Lorentzian lineshapes. Each pair of Lorentzians is defined by a center frequency, a splitting, and a common amplitude and width. To sweep across the two-dimensional layer of implanted NV centers, we sequentially fit the spectrum at each point by seeding with the best-fit parameters of nearby points. We ensure the accuracy of the fits by inspecting the frequencies of each resonance across linecuts of the 2D data (Fig. 2.7(b)).

Converting the fitted energies to shifting ($\Pi_{z,i}$) and splitting parameters ($\Pi_{\perp,i}$) requires us to take into account two additional effects. First, in the case of the shifting parameter, we subtract off the second-order shifting induced by transverse magnetic fields. In particular, the effective shifting is given by $\Pi_{z,\mathrm{B}} \approx (\gamma_{\mathrm{B}} B_\perp)^2 / D_{\mathrm{gs}}$, which, under our experimental conditions, corresponds to $\Pi_{z,\mathrm{B}} \approx 5 - 10$ MHz. To characterize this shift, one can measure each of the NV orientations with a magnetic field aligned parallel to its principal axis, such that the transverse magnetic shift vanishes. In practice, we obtain the zero-field shifting for each of the NV orientations without the need for additional measurements, as part of our electromagnet calibration scheme (Section 2.7.2). We perform this calibration at a single point in the two-dimensional map and use this point to characterize and subtract off the magnetic-induced shift in subsequent measurements with arbitrary applied field. Second, in the case of the splitting parameter, we correct for an effect arising from the NV's charge environment. We discuss this effect in the following section. The final results for the shifting ($\Pi_{z,i}$) and splitting ($\Pi_{\perp,i}$) parameters for the (111)-cut diamond at 4.9 GPa are shown in Fig. 2.7(c).

2.7.3.2 Effect of local charge environment

It is routinely observed that ensemble spectra of high-density samples (i.e. Type 1b) exhibit a large ($5 - 10$ MHz) splitting even under ambient conditions. While commonly attributed

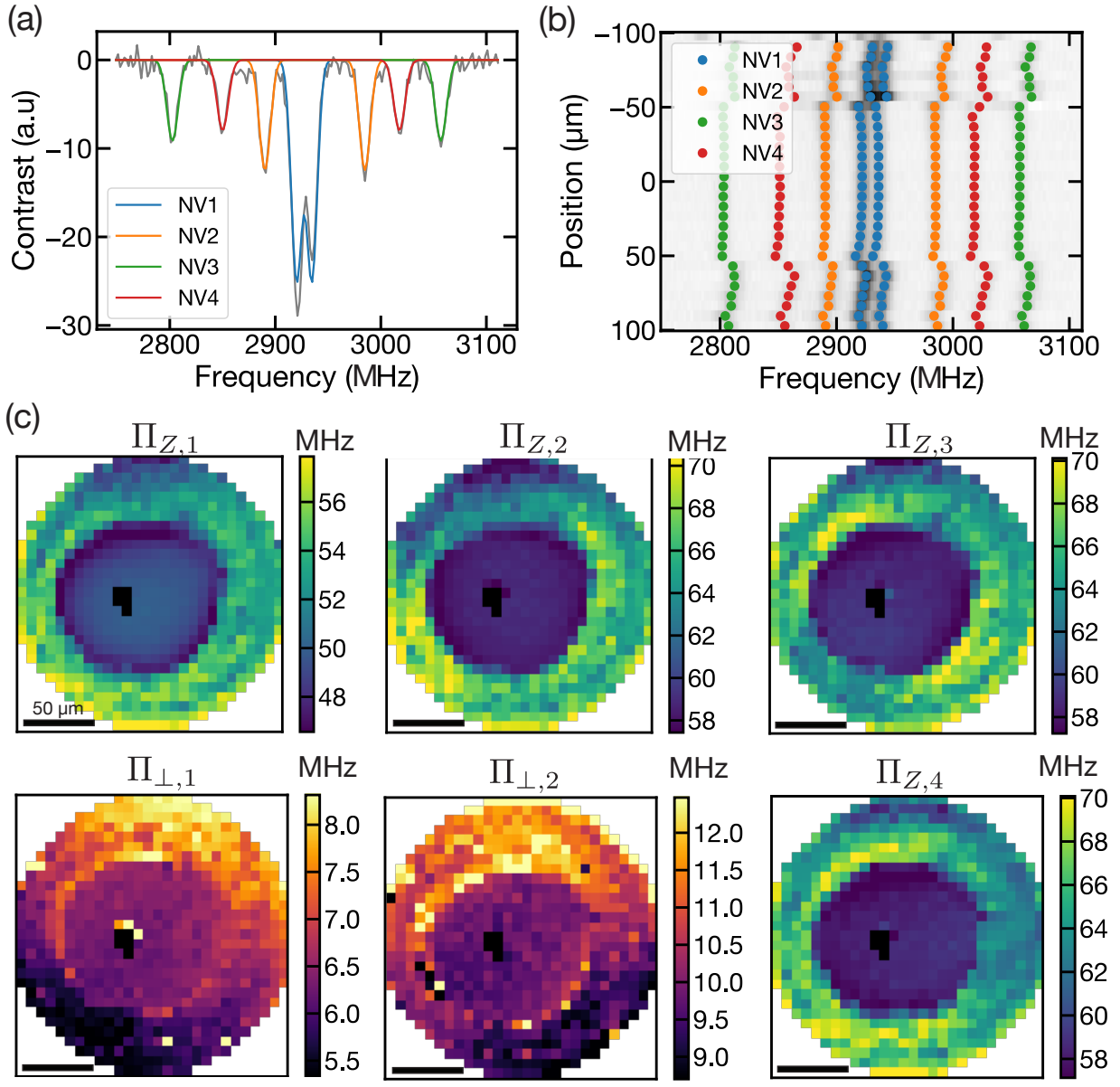

Figure 2.7: Stress reconstruction procedure applied to the (111)-cut diamond at 4.9 GPa. (a) A typical ODMR spectrum with the resonances corresponding to each NV orientation fit a pair of Lorentzian lineshapes. (b) A linecut indicating the fitted resonance energies (colored points) superimposed on the measured spectra (grey colormap). (c) 2D maps of the shifting ($\Pi_{z,i}$) and splitting parameters ($\Pi_{\perp,i}$) for each NV orientation across the entire culet.

to instrinsic stresses in the diamond, it has since been suggested that the splitting is, in fact, due to electric fields originating from nearby charges [241]. This effect should be subtracted from the total splitting to determine the stress-induced splitting.

To this end, let us first recall the NV interaction with transverse electric fields:

$$H_E = d_\perp \left[\mathcal{E}_x(S_y^2 - S_x^2) + \mathcal{E}_x(S_x S_y + S_y S_x)\right] \tag{2.12}$$

where $d_\perp = 17$ Hz cm/V. Observing the similarity with Eq. (2.6), we can define

$$\tilde{\Pi}_x = \Pi_{\mathrm{s},x} + \Pi_{\mathrm{E},x} \tag{2.13}$$

$$\tilde{\Pi}_y = \Pi_{\mathrm{s},y} + \Pi_{\mathrm{E},y} \tag{2.14}$$

where $\Pi_{\mathrm{S},\{x,y\}}$ are defined in Eq. (2.7) and $\Pi_{\mathrm{E},\{x,y\}} = d_\perp \mathrm{E}_{\{x,y\}}$. The combined splitting for electric fields and stress is then given by

$$2\tilde{\Pi}_\perp = 2\left((\Pi_{\mathrm{s},x} + \Pi_{\mathrm{E},x})^2 + (\Pi_{\mathrm{s},y} + \Pi_{\mathrm{E},y})^2\right)^{1/2} . \tag{2.15}$$

We note that the NV center also couples to longitudinal fields, but its susceptibility is ~ 50 times weaker and is thus negligible in the present context.

To model the charge environment, we consider a distribution of transverse electric fields. For simplicity, we assume that the electric field strength is given by a single value $\mathcal{E}_0$, and its angle is randomly sampled in the perpendicular plane. Adding the contributions from stress and electric fields and averaging over angles, the total splitting becomes

$$\begin{aligned}\tilde{\Pi}_{\perp,\mathrm{avg}} &= \int d\theta (\Pi_{\mathrm{S},\perp}^2 + \Pi_{\mathrm{E},\perp}^2 + 2\Pi_{\mathrm{S},\perp}\Pi_{\mathrm{E},\perp}\cos\theta)^{1/2} \\ &= \frac{1}{\pi}\left[\sqrt{\Pi_{\mathrm{s},\perp}^2 - \Pi_{\mathrm{E},\perp}^2}\,\mathrm{EllipticE}\left(-\frac{4\Pi_{\mathrm{S},\perp}\Pi_{\mathrm{E},\perp}}{\sqrt{\Pi_{\mathrm{S},\perp}^2 - \Pi_{\mathrm{E},\perp}^2}}\right)\right. \\ &\qquad \left. + \sqrt{\Pi_{\mathrm{S},\perp}^2 + \Pi_{\mathrm{E},\perp}^2}\,\mathrm{EllipticE}\left(-\frac{4\Pi_{\mathrm{s},\perp}\Pi_{\mathrm{E},\perp}}{\sqrt{\Pi_{\mathrm{S},\perp}^2 + \Pi_{\mathrm{E},\perp}^2}}\right)\right]\end{aligned} \tag{2.16}$$

where $\mathrm{EllipticE}(z)$ is the elliptic integral of the second kind. This function is plotted in Fig. 2.8(a), and we note its qualitative similarity to a quadrature sum.

To characterize the intrinsic charge splitting ($\Pi_{\mathrm{E},\perp}$), we first aquire an ODMR spectrum for each diamond sample under ambient conditions. For example, for the (111)-cut diamond, we measured $\Pi_{\mathrm{E},\perp} \approx 4.5$ MHz. For subsequent measures under pressure, we then subtract off the charge contribution from the observed splitting by numerically from inverting Eq. (2.16) and solving for $\Pi_{\mathrm{s},\perp}$.

2.7.3.3 Susceptibility parameters

A recent calibration experiment established the four stress susceptibilities relevant to this work [29]. In this section, we discuss the conversion of their susceptibilities to our choice of basis (the local NV frame), and we reinterpret their results for the splitting parameters taking into account the effect of charge.

In their paper, Barson et. al. define the stress susceptilities with respect diamond crystal frame:

$$\Pi_z = a_1(\sigma_{\mathcal{X}\mathcal{X}} + \sigma_{\mathcal{Y}\mathcal{Y}} + \sigma_{\mathcal{Z}\mathcal{Z}}) + 2a_2(\sigma_{\mathcal{Y}\mathcal{Z}} + \sigma_{\mathcal{Z}\mathcal{X}} + \sigma_{\mathcal{X}\mathcal{Y}}) \tag{2.17}$$

$$\Pi_x = b(2\sigma_{\mathcal{Z}\mathcal{Z}} - \sigma_{\mathcal{X}\mathcal{X}} - \sigma_{\mathcal{Y}\mathcal{Y}}) + c(2\sigma_{\mathcal{X}\mathcal{Y}} - \sigma_{\mathcal{Y}\mathcal{Z}} - \sigma_{\mathcal{Z}\mathcal{X}}) \tag{2.18}$$

$$\Pi_y = \sqrt{3}\left[b(\sigma_{\mathcal{X}\mathcal{X}} - \sigma_{\mathcal{Y}\mathcal{Y}}) + c(\sigma_{\mathcal{Y}\mathcal{Z}} - \sigma_{\mathcal{Z}\mathcal{X}})\right] \tag{2.19}$$

where $\mathcal{X}\mathcal{Y}\mathcal{Z}$ are the principal axes of the crystal frame. Their reported results are $\{a_1, a_2, b, c\} = (2\pi) \times \{4.86(2), -3.7(2), -2.3(3), 3.5(3)\}$ MHz/GPa.

To convert these susceptibilities to our notation (Eq. 2.6), one must rotate the stress tensor from the crystal frame to the NV frame, i.e. $\sigma_{xyz} = R\sigma_{\mathcal{X}\mathcal{Y}\mathcal{Z}}R^\top$. The rotation matrix that accomplishes this is:

$$R = \begin{pmatrix} -\frac{1}{\sqrt{6}} & -\frac{1}{\sqrt{6}} & \sqrt{\frac{2}{3}} \\ \frac{1}{\sqrt{2}} & -\frac{1}{\sqrt{2}} & 0 \\ \frac{1}{\sqrt{3}} & \frac{1}{\sqrt{3}} & \frac{1}{\sqrt{3}} \end{pmatrix}. \tag{2.20}$$

Applying this rotation, one finds that the above equations become (in the NV frame)

$$\Pi_z = (a_1 - a_2)(\sigma_{xx} + \sigma_{yy}) + (a_1 + 2a_2)\sigma_{zz} \tag{2.21}$$

$$\Pi_x = (-b - c)(\sigma_{yy} - \sigma_{xx}) + (\sqrt{2}b - \frac{\sqrt{2}}{2}c)(2\sigma_{xz}) \tag{2.22}$$

$$\Pi_x = (-b - c)(2\sigma_{xy}) + (\sqrt{2}b - \frac{\sqrt{2}}{2}c)(2\sigma_{yz}) \tag{2.23}$$

Thus, the conversion between the two notations is

$$\begin{aligned} \begin{pmatrix} \alpha_1 \\ \beta_1 \end{pmatrix} &= \begin{pmatrix} 1 & -1 \\ 1 & 2 \end{pmatrix} \begin{pmatrix} a_1 \\ a_2 \end{pmatrix} \\ \begin{pmatrix} \alpha_2 \\ \beta_2 \end{pmatrix} &= \begin{pmatrix} -1 & -1 \\ \sqrt{2} & -\frac{\sqrt{2}}{2} \end{pmatrix} \begin{pmatrix} b \\ c \end{pmatrix} \end{aligned} \tag{2.24}$$

In characterizing the splitting parameters (b and c), Barson et. al. assumed a linear dependence between the observed splitting and $\Pi_{\mathrm{S},\perp}$. However, our charge model suggests that for $\Pi_{\mathrm{S},\perp} \lesssim \Pi_{\mathrm{E},\perp}$ the dependence should be nonlinear. To account for this, we re-analyze their data using Eq. 2.16 as our fitting form, rather than a linear function as in the original work. The results are shown in Fig. 2.8 for two NV orientation groups measured in the

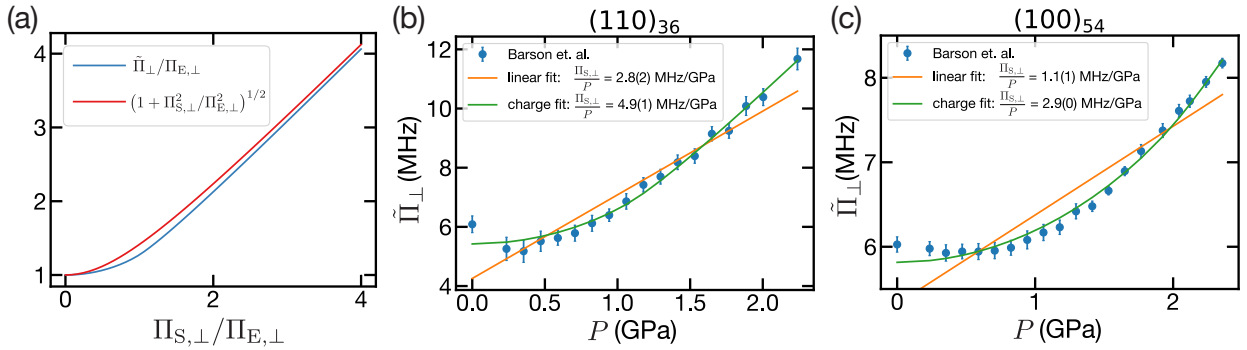

Figure 2.8: Interplay between stress and random electric fields. (a) Theoretical curve (blue) for the total splitting in the presence of stress and electric fields, Eq. (2.16). We compare this to a quadratic sum (red). (b-c) Measured splitting parameter (blue) for uniaxial pressure applied to a (110)-cut and (100)-cut diamond, reprinted with permission from [29]. We fit the data using (i) a linear function (orange), $\tilde{\Pi}_\perp = \Pi_{E,\perp} + \Pi_{S,\perp}$, and (ii) the aforementioned theoretical curve, Eq. (2.16) (green). Both fits include two free parameters: $\Pi_{E,\perp}$ and $a = \Pi_{S,\perp}/P$. We report the best-fit value for the latter parameter in the inset.

experiment: $(110)_{36}$ and $(100)_{54}$, where $(\cdots)$ denotes the crystal cut and the subscript is the angle of the NV group with respect to the crystal surface. From the fits, we extract the linear response, $\Pi_{s,\perp}/P$, for the two groups. These are related to the stress parameters by $b - c$ and $2b$, respectively. Using these relations and the results of the fits, one finds $\{b, c\} = (2\pi) \times \{-1.47(2), 3.42(7)\}$ MHz/GPa.[9] Finally, we convert these and the original reported for $\{a_1, a_2\}$ to the NV frame using Eq. 2.24. This leads to the susceptibilites that we use for our analysis:

$$\{\alpha_1, \beta_1, \alpha_2, \beta_2\} = (2\pi) \times \{8.6(2), -2.5(4), -1.95(9), -4.50(8)\} \text{ MHz/GPa}. \tag{2.25}$$

2.7.4 Results

In this section, we discuss our stress reconstruction results for (i) the (111)-cut diamond at 4.9 GPa and 13.6 GPa (Fig. 2.9), and (ii) the (110)-cut diamond at 4.8 GPa (Fig. 2.10). The stress tensors were obtained by numerically minimizing the least-squared residue with respect to the measured shifting and splitting parameters (i.e. $\Pi_{z,i}, \Pi_{\perp,i}$). While ideally we would measure all eight observables, in this experiment we measured only six: all four shifting parameters and two splitting parameters. We find that this information allows for the robust

[9]Note that the overall sign of these parameters cannot be determined through these methods, as the energy splitting is related to the quadrature sum of Π_x and Π_y. To determine the sign, one would need to measure the phase of the perturbed states [241].

characterization of σ_{ZZ} and $\sigma_\perp = \frac{1}{2}(\sigma_{XX} + \sigma_{YY})$, i.e. the two azimuthally symmetric normal components.

We can estimate the accuracy of the reconstructed tensors from the spatial variations of σ_{ZZ} at 4.9 GPa. Assuming the medium is an ideal fluid, one would expect that σ_{ZZ} to be flat in the region above the gasket hole. In practice, we observe spatial fluctuations characterized by a standard deviation ≈ 0.01 GPa; this is consistent with the expected accuracy based on frequency noise (Table 2.1). The errorbars in the reconstructed stress tensor are estimated using the aforementioned experimental accuracy.

Interestingly, the measured values for σ_{ZZ} differs from the ruby pressure scale by $\sim 10\%$. This discrepancy is likely explained by inaccuracies in the susceptibility parameters; in particular, the reported susceptibility to axial strain (i.e. β_1) contains an error bound that is also $\sim 10\%$. Other potential sources of systematic error include inaccuracies in our calibration scheme or the presence of plastic deformation.

Finally, we note that, in many cases, our reconstruction procedure yielded two degenerate solutions for the non-symmetric stress components; that is, while σ_{ZZ} and $\sigma_\perp$ have a unique solution, we find two different distributions for σ_{XX}, σ_{XY}, etc. This degeneracy arises from the squared term in the splitting parameter, $\Pi_{\perp,i} = 2\sqrt{\Pi_{x,i}^2 + \Pi_{y,i}^2}$, and the fact we measure only six of the eight observables. In Fig. 2.9 and Fig. 2.10 (and Fig. 2.2(b)), we show the solution for the stress tensor that is more azimuthally symmetric, as physically motivated by our geometry.

2.7.5 Finite element simulations of the stress tensor

Using equations from elasticity theory under the finite element approach, a numerical simulation was coded in ABAQUS for the stress and strain tensor fields in the diamond anvil cell. The diamond anvil cell is approximately axially symmetric about the diamond loading axis, in this case the crytallographic (111) axis (i.e. the Z axis). This permits us to improve simulation efficiency by reducing the initially 3D tensor of elastic moduli to the 2D axisymmetric cylindrical frame of the diamond as follows. Initially, the tensor can be written in 3D with cubic axes $c_{11} = 1076$ GPa, $c_{12} = 125$ GPa, $c_{44} = 577$ GPa. Next, we rotate cubic axes such that the (111) direction is along the Z axis of the cylindrical coordinate system. Finally, the coordinate system is rotated by angle θ around the Z axis and the elastic constants are averaged over 360° rotation. The resulting elasticity tensor in the cylindrical coordinate system is

$$\begin{bmatrix} 1177.5 & 57.4 & 91 & 0 \\ 57.4 & 1211.6 & 57.4 & 0 \\ 91 & 57.4 & 1177.5 & 0 \\ 0 & 0 & 0 & 509.2 \end{bmatrix} \text{[GPa]}.$$

The geometry of the anvil and boundary conditions (Fig. 2.11) are as follows:

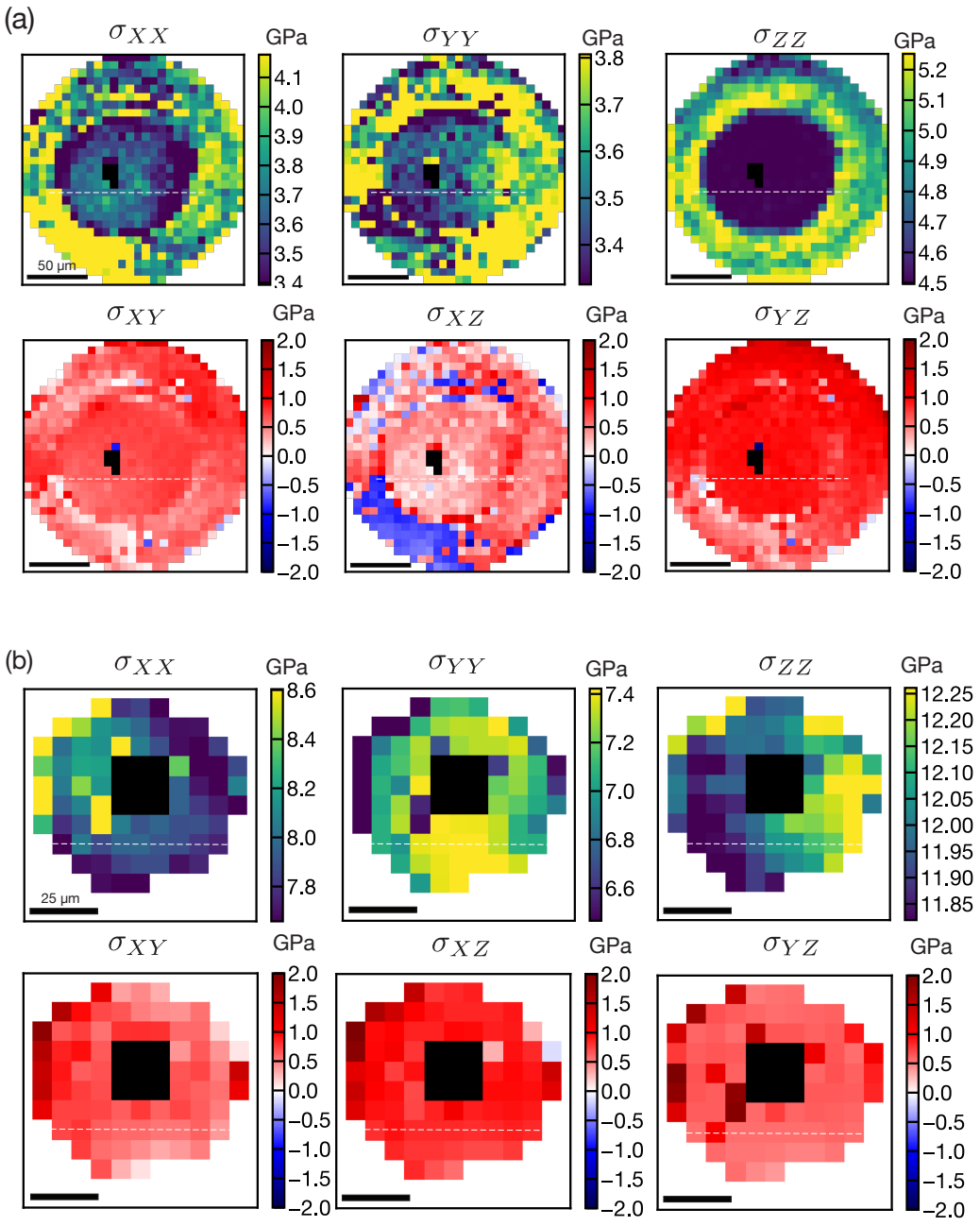

Figure 2.9: Stress tensor reconstruction of (111)-cut diamond at (a) 4.9 GPa and (b) 13.6 GPa. In the former case, we reconstruct both the inner region in contact with the fluid-transmitting medium, and the outer region in contact with the gasket. In the latter case, we reconstruct only the inner region owing to the large stress gradients at the contact with the gasket; note that the black pixels in the center indicates where the spectra is obscured by the ruby flourescence. Both pressures exhibit inward concentration of the normal lateral stress (σ_{XX} and σ_{YY}). In contrast, the normal loading stress is uniform for the lower pressure and spatially varying at the higher pressure, indicating that the pressure medium has solidified.

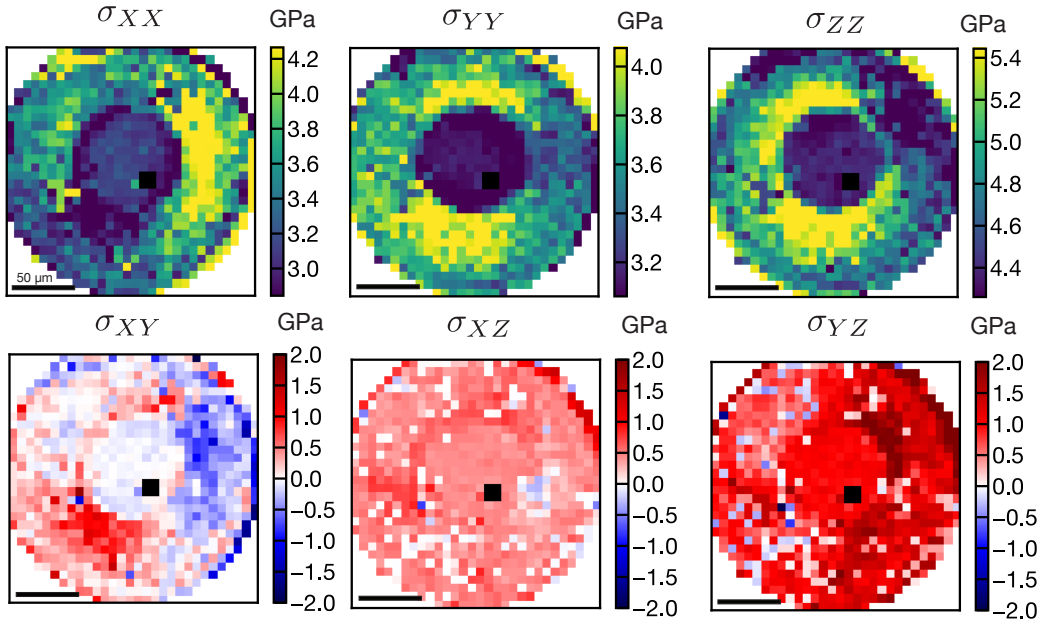

Figure 2.10: Stress tensor reconstruction of (110)-cut diamond at 4.8 GPa pressure. Analogous to the (111)-cut at low pressure, we observe an inward concentration of lateral stress and a uniform loading stress in the fluid-contact region.

1. The top surface of the anvil is assumed to be fixed. The distribution of stresses or displacements along this surface does not affect our solution close to the diamond culet line AB.

2. The normal stress σ_{ZZ} along the line AB is taken from the experimental measurements (Fig. 2.2(a) and 2.12). The pressure-transmitting medium/gasket boundary runs along the innermost 47 μm of this radius.

3. Along the pressure-transmitting medium/anvil boundary ($r \leq 47\ \mu m$) and also at the symmetry axis $r = 0$ (line AE) shear stress σ_{RZ} is zero. Horizontal displacements at the symmetry axis are also zero.

4. Normal and shear contact stresses along all other contact surfaces are determined from the best fit to the mean in-plane stress distribution $\sigma_{\perp} = 0.5(\sigma_{RR} + \sigma_{\Theta\Theta})$ measured in the experiment (Fig. 2.2(a) and Fig. 2.12). We chose to fit to $\sigma_{\perp}$ rather than to other measured stresses is because it has the smallest noise in experiment. With this, the normal stress on the line BD with the origin at point B is found to be

$$\sigma_c = 3.3 \times 10^5 x^4 - 7.5 \times 10^4 x^3 + 4.5 \times 10^3 x^2 - 10^2 x + 4.1, \tag{2.26}$$

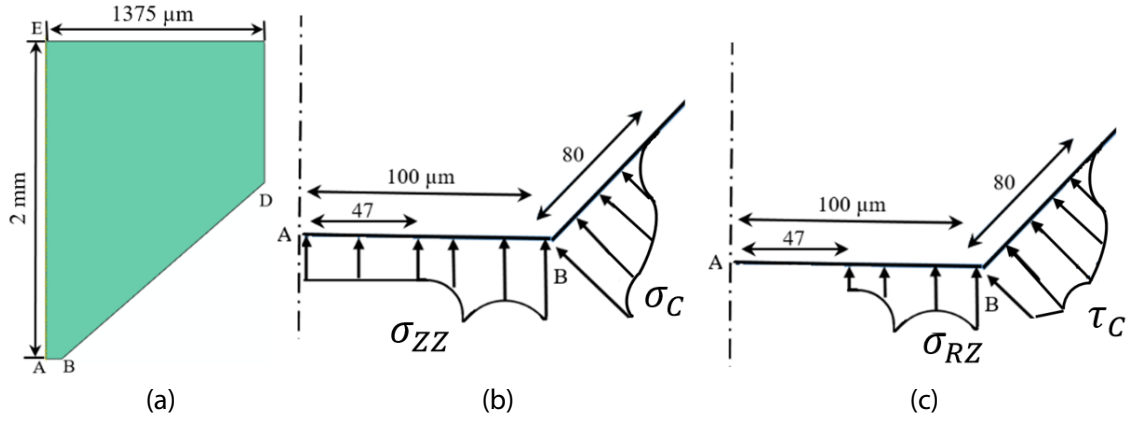

Figure 2.11: (a) Diamond geometry, (b) anvil tip with distribution of the applied normal stress, (c) distribution of the applied shear stress. Normal stress σ_{ZZ} at the culet and zero shear stress σ_{RZ} along the pressure-transmitting medium/anvil boundary ($r \leq 47$ μm) are taken from experiment. Normal and shear contact stresses along all other contact surfaces are determined from the best fit of the mean in-plane stress distribution $\sigma_\perp = 0.5(\sigma_{RR}+\sigma_{\Theta\Theta})$ to experiment (Fig. 2.2(a) and Fig. 2.12).

where σ_c is in units of GPa, and the position x along the lateral side is in units of mm. The distribution of the normal stresses is shown in Fig. 2.11(b) and Fig. 2.13.

5. At the contact surface between the gasket and the anvil, a Coulomb friction model is applied. The friction coefficient on the culet is found to be 0.02 and along the inclined surface of the anvil (line BD) is found to vary from 0.15 at point B to 0.3 at 80 μm from the culet. The distribution of shear stresses is shown in Fig. 2.11(c) and Fig. 2.13.

6. Other surfaces not mentioned above are stress-free.

The calculated distributions of the stress tensor components near the tip of the anvil are shown in Fig. 2.14.

2.8 Iron dipole reconstruction

In this section, we discuss the study of the pressure-induced $\alpha \leftrightarrow \epsilon$ transition in iron. In particular, we provide the experimental details, describe the model used for fitting the data, and outline the procedure to ascertain the transition pressure.

For this experiment, the DAC is prepared with a rhenium gasket preindented to 60 μm thickness and laser drilled with a 100 μm diameter hole. We load a $\sim$ 10 μm iron pellet, extracted from a powder (Alfa Aesar Stock No. 00737-30), and a ruby microsphere for

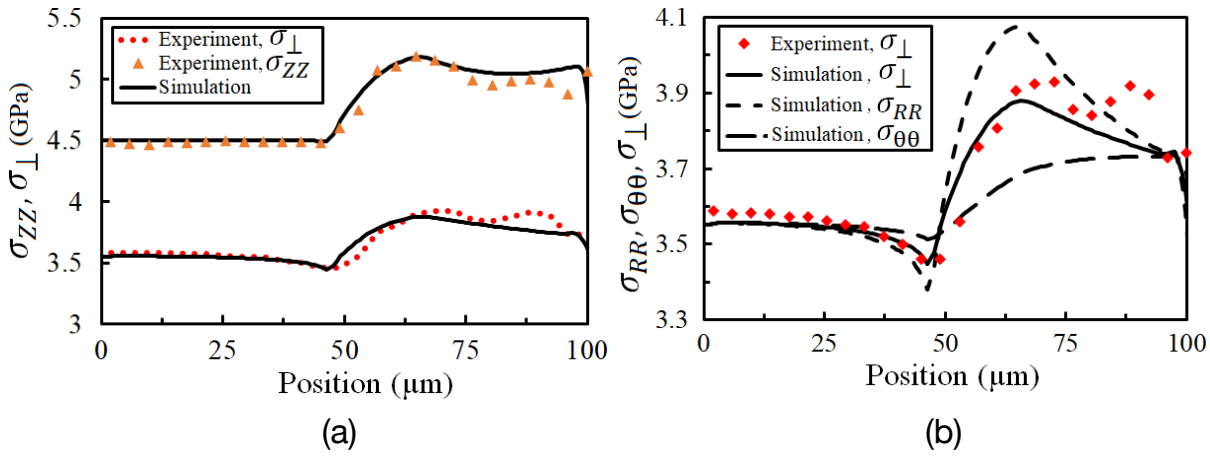

Figure 2.12: (a) Distribution of applied normal stress σ_{ZZ} and the mean in-plane stress $\sigma_\perp$ along the culet surface of the diamond from the experiment and FEM simulations. (b) Distribution of the mean in-plane stress $\sigma_\perp$ (experimental and simulated) as well as the simulated radial σ_{RR} and circumferential $\sigma_{\Theta\Theta}$ stresses along the culet surface of the diamond. Simulations conducted and analyzed by Mehdi Kamrani and Valery Levitas.

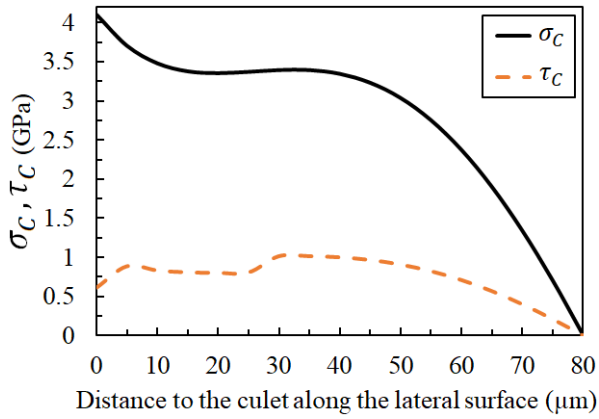

Figure 2.13: Distribution of applied normal and shear stress along the lateral surface of the diamond determined from the best fit of the mean in-plane stress distribution $\sigma_\perp$ to experiment (Fig. 2.2(a) and Fig. 2.12). Simulations conducted and analyzed by Mehdi Kamrani and Valery Levitas.

pressure calibration. A solution of methanol, ethanol and water (16:3:1 by volume) is used as the pressure-transmitting medium.

The focused laser is sequentially scanned across a 10×10 grid corresponding to a ∼

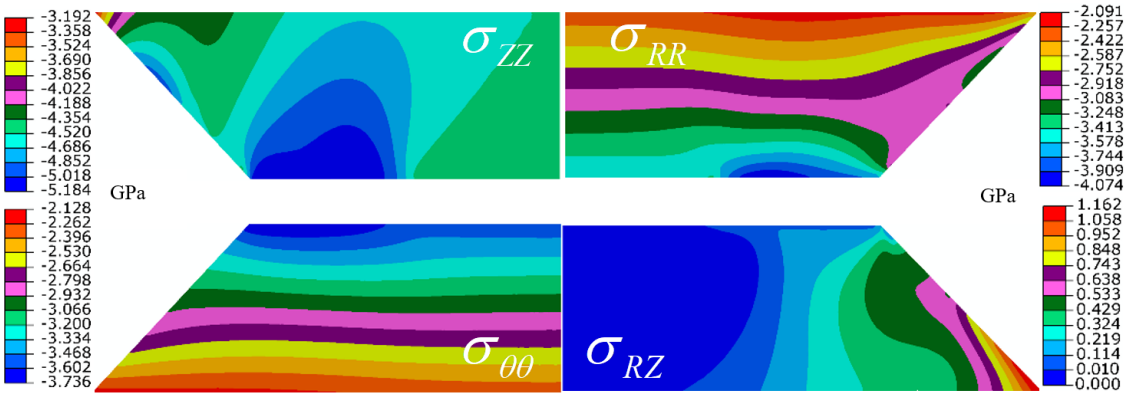

Figure 2.14: Calculated distributions of the components of stress tensor in the anvil for $r < 150$ and $z < 475$ μm. Simulations conducted and analyzed by Mehdi Kamrani and Valery Levitas.

30×30 μm area of the NV layer in the vicinity of the iron pellet, taking an ODMR spectrum at each point. The energy levels of the NV are determined by both the magnetic field and the stress in the diamond. Owing to their different crystallographic orientations, the four NV orientations in general respond differently to these two local parameters. As a result, for each location in the scan, eight resonances are observed.

A large bias magnetic field ($\sim$ 180 G), not perpendicular to any of the axes, is used to suppress the effect of the transverse stress in the splitting for each NV orientation. However, the longitudinal stress still induces an orientation-dependent shift of the resonances which is nearly constant across the imaging area, as measured independently (Fig 2.7(c)).

By analyzing the splittings of the NV resonances across the culet, we can determine the local magnetic field and thereby reconstruct the dipole moment of the iron pellet.

To estimate the error in pressure, a ruby fluorescence spectrum was measured before and after the ODMR mapping, from which the pressure could be obtained [77]. The pressure was taken to be the mean value, while the error was estimated using both the pressure range and the uncertainty associated with each pressure point.

2.8.1 Extracting Splitting Information

The eight resonances in a typical ODMR spectrum are fit to Gaussian lineshapes to extract the resonance frequency (Fig 2.15(a)). Resonances are paired as in Fig. 1.4(a): from outermost resonances to innermost, corresponding to NV orientations with the strongest magnetic field projection to the weakest, respectively. Once identified, we calculate the splitting and magnetic field projection for each NV orientation.

We note that there are two regimes where our spectra cannot confidently resolve and

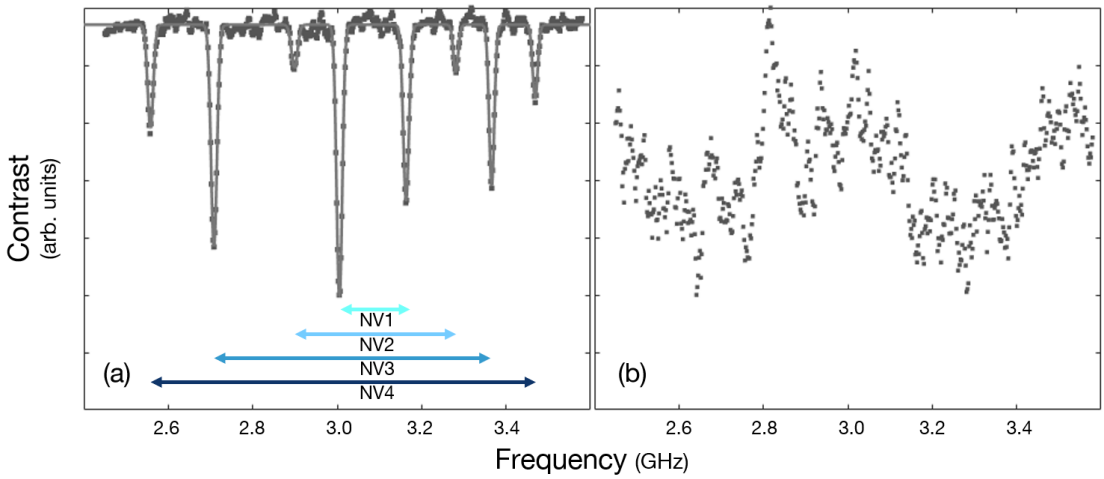

Figure 2.15: (a) Example of a typical spectrum with a fit to eight free Gaussians. Resonance pairs are identified as in Fig. 1.4(a): NV4 has the strongest magnetic field projection and NV1 has the weakest. (b) Example spectrum for which resonances are broadened and shifted. In this case we cannot correlate any resonances in the spectrum to specific NV orientations.

identify all the eight resonances. First, at high pressure, the resonance contrast for some NV orientations is diminished, possibly due to a modification of the frequency response of the microwave delivery system. Second, close to or on top of the iron pellet, the resonances are broadened; we attribute this to the large magnetic field gradients (relative to the imaging resolution) caused by the sample. The resulting overlap in spectral features obfuscates the identity of each resonance (Fig. 2.15(b)). In both cases, we fit and extract splittings only for the orientations we could identify with certainty.

2.8.2 Point Dipole Model

We model the magnetization of our pellet sample as a point dipole at some location within the sample chamber. The total magnetic field is then characterized by the external applied field, $\boldsymbol{B}_0$, the dipole of the sample, $\boldsymbol{d}$, and the position of the dipole, $\boldsymbol{r}$. Because of the presence of a large applied field, we observe that the magnetization of the sample aligns with $\boldsymbol{B}_0$, and thus, we require only the strength of the dipole to characterize its moment, $\boldsymbol{d} = D\hat{B}_0$. We expect the external magnetic field and the depth of the particle to remain nearly constant at different pressures. This is indeed borne out by the data, see Sec. 2.8.4. As a result, we consider the external magnetic field $\boldsymbol{B}_0 = (-23(7), -160(1), 92(2))$ G and depth of the iron pellet $r_Z = -5(1)$ μm to be fixed.

Due to the dipole of the iron pellet, the magnetic field across the NV layer at position $\boldsymbol{x}$

is given by:

$$\boldsymbol{B}(\boldsymbol{x}) = \boldsymbol{B}_0 + \frac{\mu_0}{4\pi}\frac{1}{|\boldsymbol{x}|^3}\left(3\hat{x}(\boldsymbol{d}\cdot\hat{x}) - \boldsymbol{d}\right), \tag{2.27}$$

where hats represent unit vectors. At each point, the local field induces a different splitting, $\Delta^{(i)}$, to the 4 NV crytallographic orientations $i \in \{1,2,3,4\}$, measured by diagonalizing the Hamiltonian $H = D_{gs}S_z^2 + B_z^{(i)}S_z + B_\perp^{(i)}S_x$, where $B_z = |\boldsymbol{B}\cdot\hat{z}^{(i)}|$ is the projection of $\boldsymbol{B}$ onto the axis of the NV, and $B_\perp^{(i)} = \sqrt{|\boldsymbol{B}|^2 - (B_z^{(i)})^2}$, its transverse component. D_{gs} is the zero field splitting of the NV. For each choice of D, r_X and r_Y, we obtain a two dimensional map of $\{\Delta^{(i)}\}$. Performing a least squares fit of this map against the experimental splittings determines the best parameters for each pressure point. The error in the fitting procedure is taken as the error in the dipole strength D.

2.8.3 Determining Transition Pressure

Although the $\alpha \leftrightarrow \epsilon$ structural phase transition in iron is a first order phase transition, we do not observe a sharp change in the dipole moment of the sample, observing instead a cross-over between the two magnetic behaviors. We attribute this to the non-hydrostatic behavior of the sample chamber at high pressures. As a result, different parts of the iron pellet can experience different amounts of pressure and, thus, undergo a phase transition at different applied pressures. The measured dipole moment should scale with the proportion of the sample that has undergone the phase transition. This proportion, $p(P)$, should plateau at either 0 or 1 on different sides of the phase transition, and vary smoothly across it. To model this behavior we use a logistic function:

$$p(P) = \frac{1}{e^{B(P-P_c)}+1}\ . \tag{2.28}$$

The dipole strength is then given by:

$$D = p(P)D_\alpha + [1-p(P)]D_\epsilon\ , \tag{2.29}$$

where D_α (D_ϵ) is the dipole moment of the sample in the α (ϵ) structural phase and $1/B$ corresponds to the width of the transition, thus its uncertainty.

2.8.3.1 Large error bar in the 11 GPa decompression point

During the decompression, around 11 GPa, we observed a significant drift of the pressure during measurement of the ODMR spectra. Unfortunately, the starting pressure was close to the transition pressure, and the drift in pressure led to a very large change in the pellet's dipole moment throughout the scanning measurement. This is clear in the measured data, Fig. 2.16, with the top-half of the map displaying a significantly larger shift with respect to the bottom-half.

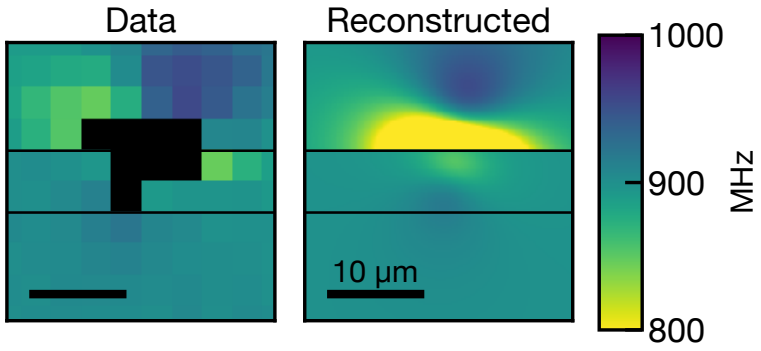

Figure 2.16: Measured map of the splittings of one of the NV orientations (left). Near the top of the plot we observe a much stronger splitting compared to the bottom of the plot. Throughout the measurement, the shift in the pressure induced a shift in the dipole moment of the sample. We consider 3 different regions (seperated by horizontal lines) corresponding to 3 different dipole strengths. The reconstructed map of the splittings is shown on the right in agreement with the data. From the center and the spread of dipole strengths, we extract the dipole moment and its error. Black bar corresponds to 10 μm.

To extract the drift in the dipole moment, we divide the two-dimensional map into three different regions, each assumed to arise from a constant value of the dipole moment of the pellet. By fitting to three different dipole moments (given a fixed position, r_X and r_Y) we obtain an estimate of the drift of the dipole moment that allows us to compute an errorbar of that measurement. The estimated dipole moment at this pressure point is taken as the midpoint of the three extracted values, $\frac{D_{max}+D_{min}}{2}$, while the error is estimated by the range, $\frac{D_{max}-D_{min}}{2}$.

2.8.4 Fitting to external magnetic field and depth

In this section we present additional data where we have allowed both the external magnetic field and the depth of the iron pellet to vary in the fitting procedure. The result of the fitting procedure is summarized in Fig. 2.17.

In particular, we expect the external magnetic field and the depth of the pellet to remain constant at different pressures. Indeed, we observe this trend in the extracted parameters, Fig. 2.17(a), (b). Using the mean and standard deviation, we estimate these values and their errors, quoted in Sec. 2.8.2.

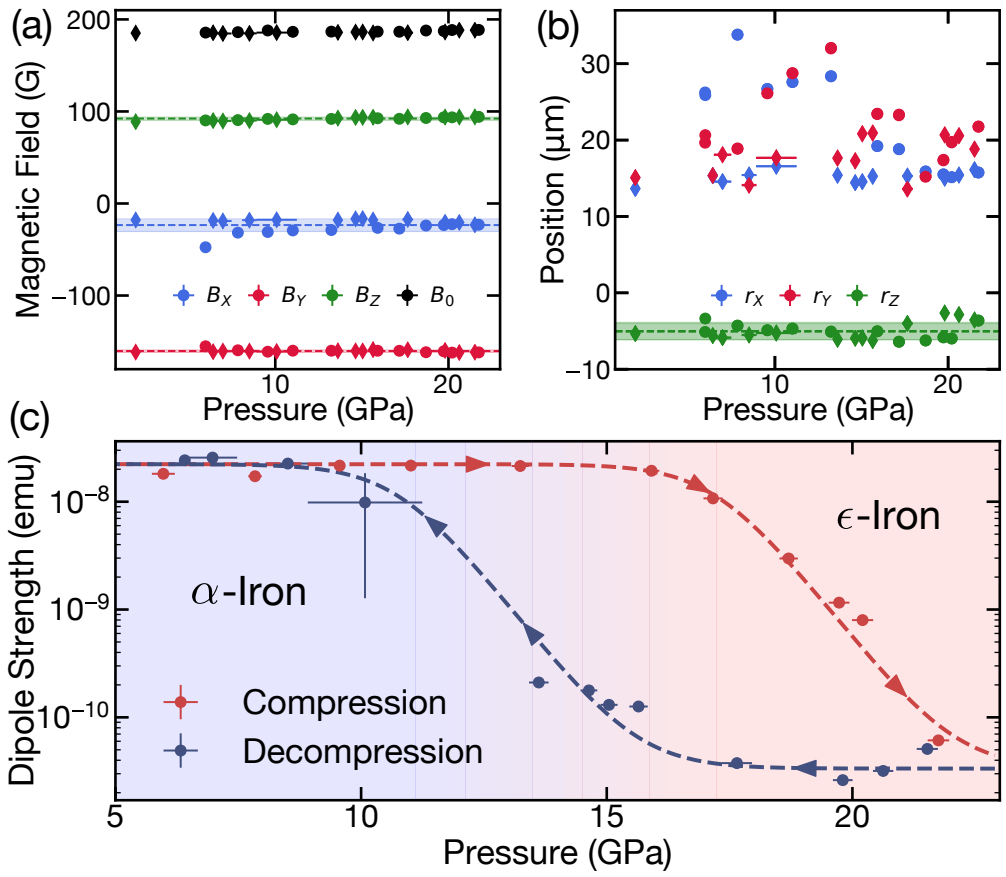

Figure 2.17: Result of fitting procedure when the external magnetic field and the depth of the iron pellet is allowed to vary at each pressure. (a)[(b)] External magnetic field [position of the pellet] extracted as a function of pressure (circles correspond to compression while diamonds correspond to decompression). Across the entire range of pressures, the extracted external magnetic field and the depth of the iron pellet is approximately constant. In the final fitting procedure, these values are fixed to their extracted mean (dashed lines). Shaded regions correspond to a standard deviation above and below the mean value. (c) Dipole strength of the iron pellet, extracted when all seven parameters $(B_X, B_Y, B_Z, D, r_X, r_Y, r_Z)$ are fitted. The resulting transitions occur at 17.2 GPa and 10.8 GPa for compression and decompression, respectively. Comparing with the width of the transition (1.3 GPa), these values are in excellent agreement with those presented in Section 2.4.1.

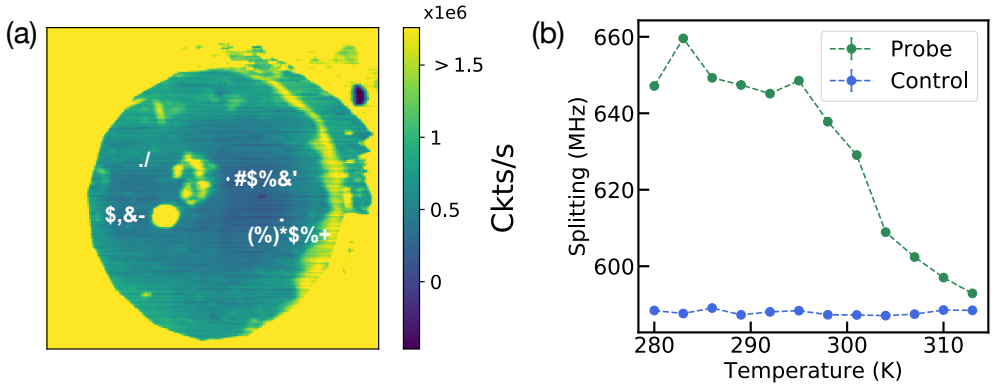

Figure 2.18: (a) The protocol for obtaining P-T phase map of Gd relies on monitoring the ODMR spectrum versus temperature and pressure at a point of interest (probe) near the sample. To verify that the observed signal is from the Gd flake, one can perform the same measurement on a control point further away from the sample. (b) The difference in the splitting between the probe and control points isolates the magnetic field generated by the Gd sample, allowing us to monitor the magnetic behavior of the sample.

2.9 Gadolinium

2.9.1 Experimental detail

We use a custom-built closed cycle cryostat (Attocube attoDRY800) to study the P-T phase diagram of Gd. The DAC is placed on the sample mount of the cryostat, which is incorporated with a heater and a temperature sensor for temperature control and readout.

For this experiment, we use beryllium copper gaskets. The Gd sample is cut from a 25 μm thick Gd foil (Alfa Aesar Stock No. 12397-FF) to a size of $\sim 30\,\mu\text{m} \times 30\,\mu\text{m}$ and loaded with cesium iodide (CsI) as the pressure-transmitting medium. A single ruby microsphere loaded into the chamber is used as a pressure scale.

For each experimental run, we start with an initial pressure (applied at room temperature 300 K) and cool the cell in the cryostat. Due to contraction of the DAC components with decreasing temperature, each run of the experiment traverses a non-isobaric path in P-T phase space, Fig. 2.19(a). Using fiducial markers in the confocal scans of the sample chamber, we track points near and far from the Gd sample throughout the measurement. By performing ODMR spectroscopy at these points for each temperature, we monitor the magnetic behavior of the sample. More specifically, comparing the spectra between the close point (probe) against the far away one (control), Fig. 2.18, enables us to isolate the induced field from the Gd sample.

2.9.2 Fitting phase transition

There are three different transitions we which to locate in the study of the Gd's P-T phase diagram: a magnetic transition from PM dhcp to FM dchp; structural phase transitions, either hcp $\rightarrow$ dhcp or Sm-type $\leftrightarrow$ dhcp; and a magnetic phase transition from PM Sm-type to AFM Sm-type.

In order to extract the transition temperature of the paramagnet to ferromagnet transition from our data, we model the magnetization of our sample near the magnetic phase transition using a regularized mean field theory.

The magnetism of gadolinium is well-described by a three dimensional Heisenberg magnet of core electrons [255]. In the presence of an external magnetic field, the free energy near the critical point is expanded in even powers of the magnetization with a linear term that couples to the external magnetic field:

$$f = -Bm + \frac{\alpha}{2}(T - T_{\mathrm{C}})m^2 + \frac{\beta}{4}m^4, \tag{2.30}$$

where m is the magnetization, B is the external magnetic field, α and β the expansion coefficients, T the temperature, and T_{C} the transition temperature. In this treatment, we implicitly assume that α and β do not vary significantly with pressure and thus can be taken to be constant across paths in P-T phase space. The magnetization m_{min} is then obtained by minimizing the free energy.

Because our observation region extends far away from the transition, we observe a plateauing of the splittings that emerges from the microscopics of Gd. Using R as the regularization scale and $\tilde{A}$ as the maximum magnetization of the sample we propose the simple regularization scheme:

$$m(T, P) = \tilde{A}\frac{m_{\mathrm{min}}}{m_{\mathrm{min}} + R}. \tag{2.31}$$

The splitting of the NV group, up to some offset, is proportional to the magnetization of the sample. This proportionality constant, A, captures he relation between magnetization and induced magnetic field, the geometry of sample relative to the measurement spot, as well as the susceptibility of the NV to the magnetic field. The splitting of the NV is then given by:

$$\Delta = A\frac{m_{\mathrm{min}}}{m_{\mathrm{min}} + R} + c \tag{2.32}$$

where we incorporated $\tilde{A}$ into A as well. Normalizing α and β with respect to B, we obtain six parameters that describe the magnetization profile, directly extracting T_{C}.

In the case of the first order structural phase transitions, similar to that of iron, we take the susceptibility to follow a logistic distribution. We model the observed splitting as:

$$\Delta = \frac{A}{e^{B(T-T_{\mathrm{C}})} + 1} + c \tag{2.33}$$

Fitting to the functional form provides the transition temperature T_{C}. Error bar is taken as largest between $1/B$ and the fitting error.

In the case of the paramagnetic to antiferromagnetic transition, we use the mean field susceptibility across the phase transition of the system. The susceptibility across such transition is peaked at the transition temperature:

$$\chi(T) \propto \begin{cases} \dfrac{1}{T-\theta_p} & T > T_c \\ \\ C\dfrac{3L'(H/T)}{T-\theta_p 3L'(H/T)} & T < T_c \end{cases} \tag{2.34}$$

where C is chosen to ensure continuity of χ, $L'(x)$ is the derivative of the Langevin function $L(x)$at, H is a meaasure of the applied field, and θ_p is the assymptotic Curie point. Finally, we fit the observed splitting to:

$$\Delta = A\chi(T; T_c, H, \theta_p) + c \tag{2.35}$$

where, as before, A captures both the geometric effects, as well as the response of the chosen NV group to the magnetic field.

2.9.3 Additional data

In this section we present the data for the different paths taken in P-T phase and the resulting fits. Table 2.2 summarizes the observations for all experimental runs. Fig. 2.19 contains the data used in determining the linear pressure dependence of the hcp phase. Fig. 2.20 comprises the data used in determining the transition to the dhcp phase, either via the FM hcp to PM dhcp transition, Fig. 2.20(b), or via the difference in susceptibilities between PM Sm-type and PM dhcp of Gd, Fig. 2.20(c) and d. We emphasize that in the blue path, we begin the experiment below 2 GPa and thus in the hcp structure, while for the orange and green, we begin above 2 GPa, so we expect the system to be in Sm-type. Finally, Fig. 2.21 contains the data where we observe a change in the susceptibility of Gd that occurs at the purported Sm-type PM to AFM transition.

2.9.4 Recreating the P-T phase diagram of Gd

The rich magnetic behavior of Gd is partially dependent on its structural phases, captured in the sequence: hexagonal closed packed (hcp) to Samarium (Sm) type at ~ 2 GPa, and then to double hexagonal closed packed (dhcp) at ~ 6 GPa. In particular, while the paramagnetic (PM) phase of hcp orders to a ferromagnet (FM), the PM phase of Sm-type orders to an antiferromagnet (AFM) [165]. Similarly, dhcp undergoes a PM to magnetically ordered phase transition.

For experimental runs with initial pressures < 2 GPa (runs 1-3, 5-9, 11-13, 17-19), we observe a PM $\leftrightarrow$ FM phase transition in hcp Gd. In agreement with previous studies, we see a linear decrease of the Curie temperature with increasing pressure up to ~ 4 GPa [157,

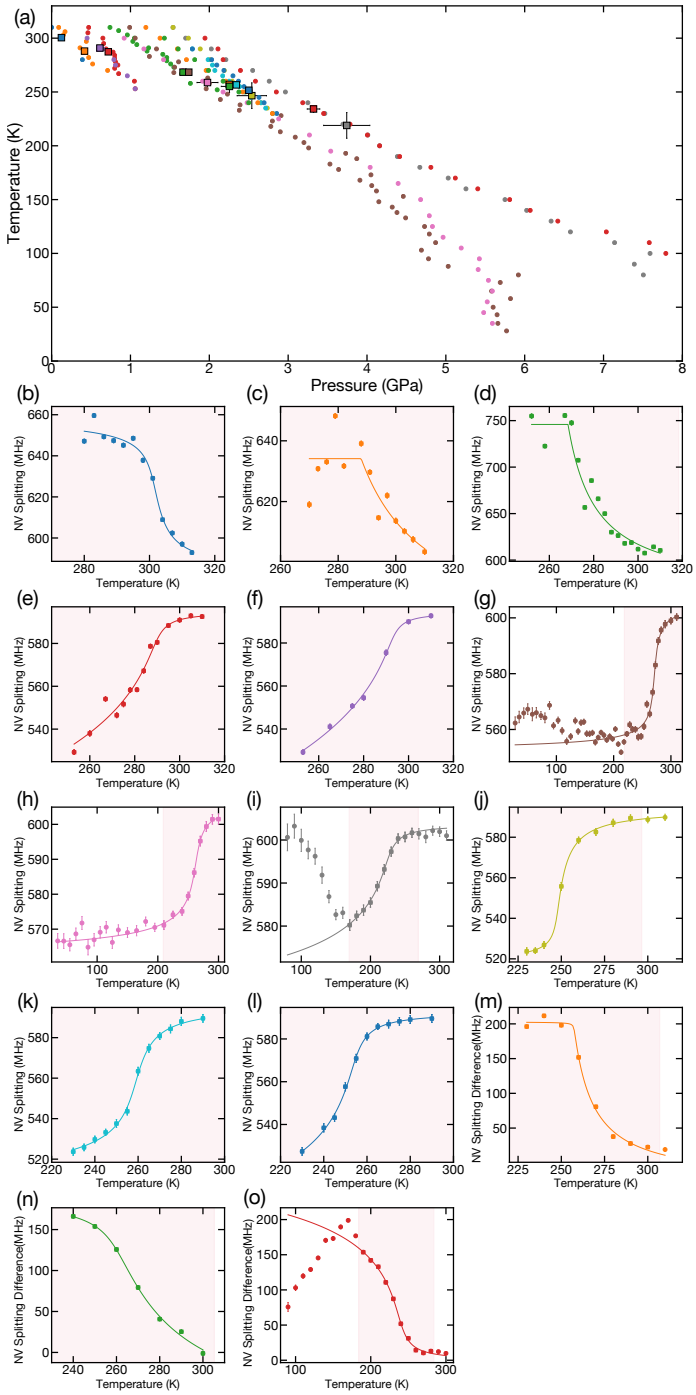

Figure 2.19: (a) Paths in the P-T phase space that inform about the hcp PM phase to the hcp FM phase. (b-o) Measured NV splitting and corresponding fit. The resulting transition temperatures are highlighted in (a) with squares. Shaded region corresponds to the part of the spectrum fitted.

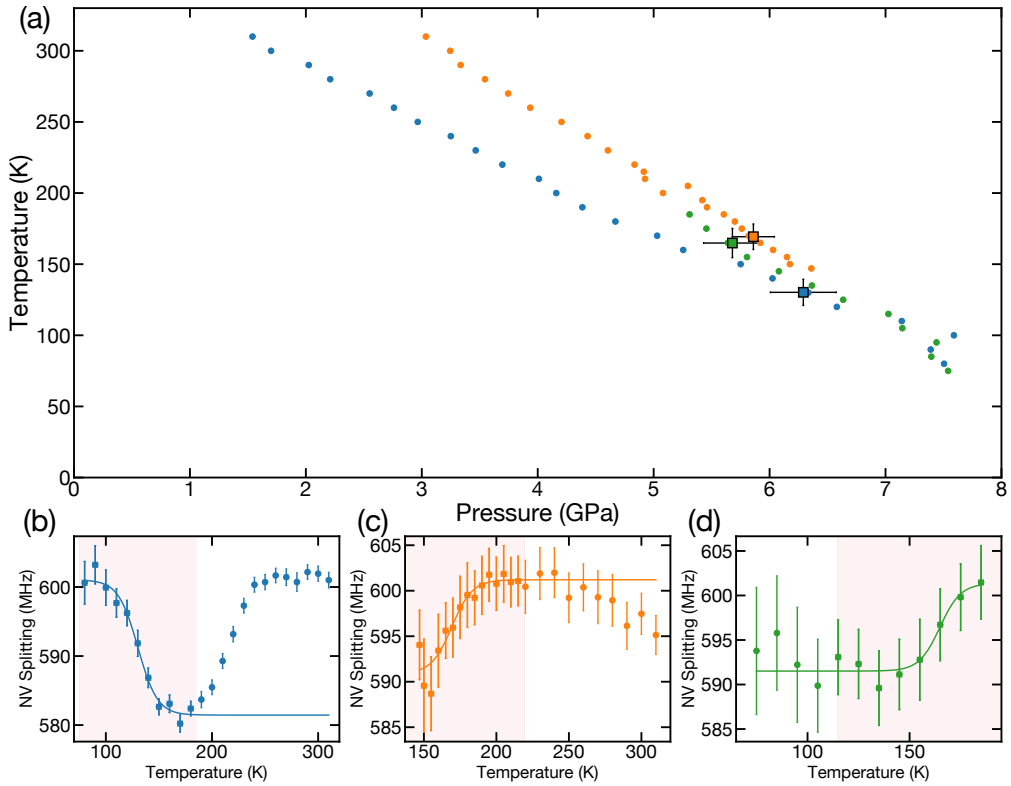

Figure 2.20: (a) Paths in the P-T phase space that inform about the transition to the PM dhcp phase. (b-d) Measured NV splitting and corresponding fit. The resulting transition temperatures are highlighted in (a) with squares. We interpret (b) as a transition from FM hcp to PM dhcp, while (c),(d) as a transition from PM Sm-type to PM dhcp. Shaded region corresponds to the part of the spectrum fitted.

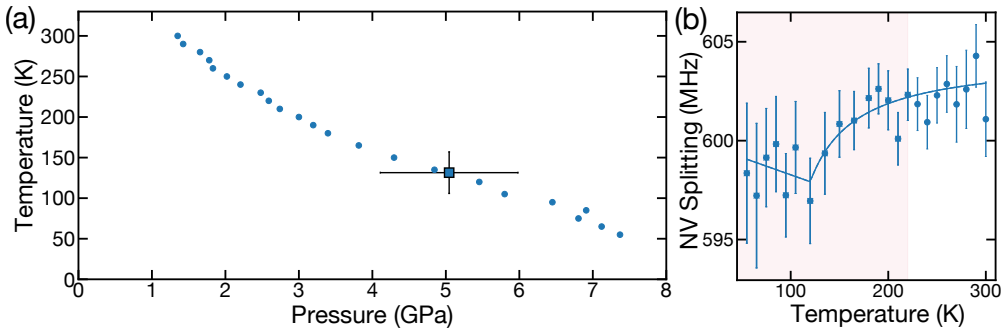

Figure 2.21: (a) Path in the P-T phase space where a signal consistent with the purported AFM transition in Sm-type Gd is seen (b). Shaded region corresponds to the part of the spectrum fitted.

Run	Direction	Phase transition	Remarks, visible in Fig.
1	Heat-up	hcp (FM) $\longrightarrow$ hcp (PM)	New sample, Fig. 2.19(b)
2	Cool-down	hcp (PM) $\longrightarrow$ hcp (FM)	Fig. 2.19(c)
3	Cool-down	hcp (PM) $\longrightarrow$ hcp (FM)	Fig. 2.19(d)
4	Cool-down	No observation	Probably starting in Sm due to large initial pressure
5	Cool-down	hcp (PM) $\longrightarrow$ hcp (FM)	New sample, Fig. 2.19(e)
6	Heat-up	hcp (FM) $\longrightarrow$ hcp (PM)	Fig. 2.19(f)
7	Cool-down	hcp (PM) $\longrightarrow$ hcp (FM)	Fig. 2.19(g)
8	Heat-up	hcp (FM) $\longrightarrow$ hcp (PM)	Fig. 2.19(h)
9	Cool-down	hcp (PM) $\longrightarrow$ hcp (FM) $\longrightarrow$ dhcp (PM)	Fig. 2.19(i), 2.20(b)
10	Cool-down	Weak evidence for Sm (PM) $\longrightarrow$ Sm (AFM)	Probably starting in Sm due to metastability, Fig. 2.21(b)
11	Cool-down	hcp (PM) $\longrightarrow$ hcp (FM)	New sample, Fig. 2.19(j)
12	Heat-up	hcp (FM) $\longrightarrow$ hcp (PM)	Fig. 2.19(k)
13	Cool-down	hcp (PM) $\longrightarrow$ hcp (FM)	Fig. 2.19(l)
14	Cool-down	Weak evidence for Sm (PM) $\longrightarrow$ dhcp (PM)	Probably starting in Sm due to large initial pressure
15	Cool-down	Weak evidence for Sm (PM) $\longrightarrow$ dhcp (PM)	Probably starting in Sm due to metastability, Fig. 2.20(c)
16	Heat-up	Weak evidence for dhcp (PM) $\longrightarrow$ Sm (PM)	Fig. 2.20(d)
17	Cool-down	hcp (PM) $\longrightarrow$ hcp (FM)	New sample, Fig. 2.19(m)
18	Heat-up	hcp (FM) $\longrightarrow$ hcp (PM)	Fig. 2.19(n)
19	Cool-down	hcp (PM) $\longrightarrow$ hcp (FM) and start of transition to dhcp (PM)	Fig. 2.19(o)

Table 2.2: Summary of all experimental runs in the P-T phase diagram, indexing either a decrease or increase in temperature during this path, and the observed phase transitions. Each group of runs, between double lines in the table, corresponds to a different sample.

233, 155]. Notably, prior studies have shown a structural transition from hcp to Sm-type at 2 GPa [233, 287, 12], which is believed to be "sluggish" [165, 233]. This is indeed consistent with our observation that the linear dependence of the Curie temperature persists well into the Sm-type region, suggesting the existence of both structural phases over our experimental timescales.

Furthermore, in run 9 (Table 2.2 and Fig. 2.21(a),(b)), we observe a complete loss of FM signal when pressures exceed $\sim$ 6 GPa at $\sim$ 150 K, in good agreement with the previously reported phase transition from hcp (FM) to dhcp (PM) structure [287, 233]. Upon performing a similar path in P-T space (run 19), we observe the same behavior. In contrast to the previous slow hcp to Sm-type transition, we believe that the equilibrium timescale for the hcp (FM) to dhcp (PM) transition is much faster at this temperature.

After entering the dhcp structure (run 9), we no longer observe a clear FM signal from the sample even after heating to 315 K and depressurizing < 0.1 GPa. This can be explained by the retention of dhcp or Sm-type structure in the sample. Previous studies, suggesting that the Sm-type phase in Gd is metastable up to ambient pressure and temperature [165], corroborate that our sample is likely still in the Sm-type structural phase. It is not too surprising, that by continuing to cool down and walking along a slightly different P-T path, we observe only a small change in the NV splitting at $\sim$ 150 K and $\sim$ 5 GPa as we cross the purported Sm-type PM to AFM phase boundary (run 10 in Table 2.2)[287, 165, 233].

Moreover, the metastable dynamics of hcp to Sm-type transitions are strongly pressure and temperature dependent, suggesting that different starting points (in the P-T phase diagram) can lead to dramatically different behaviors. Indeed, by preparing the sample above 2 GPa at room temperature (run 4), we no longer detect evidence for a ferromagnetic Curie transition, hinting the transition to the Sm-type structure. Instead, we only observe a small change in the NV splitting at $\sim$ 6 GPa and $\sim$ 170 K, which could be related to the presence of different paramagnetic susceptibilities of the Sm-type and dhcp structural phases. Interestingly, by cycling temperature across the transition (run 14-16 in Table 2.2), we observe negligible hysteresis, suggesting fast equilibration of this structural transition.

2.9.5 Noise spectroscopy

In order to perform magnetic noise spectroscopy of Gd at temperatures ranging from 273 K to 340 K, we attach a small chunk of Gd foil (100 μm $\times$ 100 μm $\times$ 25 μm) close to a microwave wire on a Peltier element with which we tune the temperature. Instead of mm-scale diamonds as before, we use nano-diamonds (*Adamas*, $\sim$ 140 nm average diameter) drop-cast onto the Gd foil to minimize the distance to the surface of our sample.

With no external field applied, all eight resonances of the NVs inside the nano-diamonds are found within our resolution to be at the zero-field splitting D_{gs} for either para- and ferromagnetic phase of Gd, leading to a larger resonance contrast since we can drive all NVs with the same microwave frequency. Measuring the NV's spin relaxation time T_1 under these circumstances is equivalent to ascertaining the AC magnetic noise at $\sim$ 2.87 GHz.

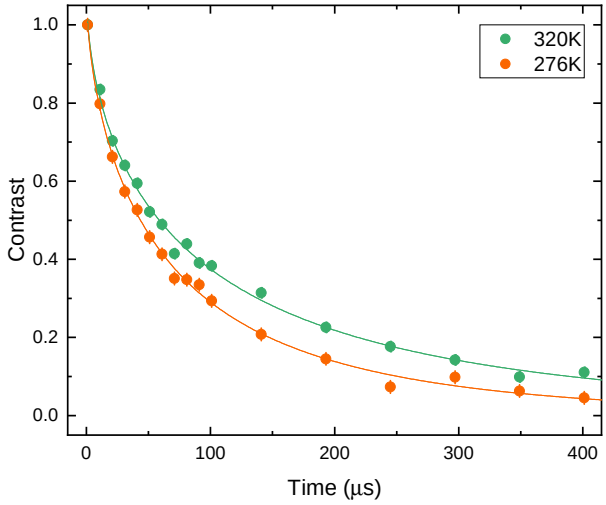

Figure 2.22: Plots of T_1 measurements below and above the magnetic phase transition in Gd. The green (orange) curve was measured at 320 K (276 K) and yields $T_1 = 91\pm4$ μs (66 ± 3 μs), indicating a clear reduction of the spin polarization lifetime in the ferromagnetic phase. A stretched exponential function with exponent $\alpha = 0.6$ (0.65) was used for fitting.

For this purpose, we utilize the following pulse sequence to measure T_1. First, we apply a 10 μs laser pulse to intialize the spin into the $|m_s = 0\rangle$ state. After laser pumping, we let the spin state relax for a variable time τ, before turning on a second laser pulse to detect the spin state (signal bright). We repeat the exact same sequence once more, but right before spin detection, an additional NV π-pulse is applied to swap the $|m_s = 0\rangle$ and $|m_s = \pm1\rangle$ populations (signal dark). The difference between signal bright and dark gives us a reliable measurement of the NV polarization (Fig. 2.4(d) top inset) after time τ. The resulting T_1 curve exhibits a stretched exponential decay $\propto e^{-(\tau/T_1)^\alpha}$, with $\alpha \sim 0.65$ (Fig. 2.22).

By sweeping the Peltier current over a range of ~ 3.5 A, we adjust the temperature of the sample from 273 K to 340 K, therefore determining the temperature dependence of T_1.

This procedure is performed on two different nano-diamonds on top of the Gd flake to confirm that the signal is not an artifact. Furthermore, this is contrasted with an additional measurement at a nano-diamond far away from the Gd foil, exhibiting no temperature dependence of T_1.

2.9.6 Theoretical analysis of T_1

The depolarization time T_1 of NV centers shows a distinct drop when we decrease the temperature T to across the ferromagnetic phase transition of Gd, Fig. 2.4(d). Assuming that

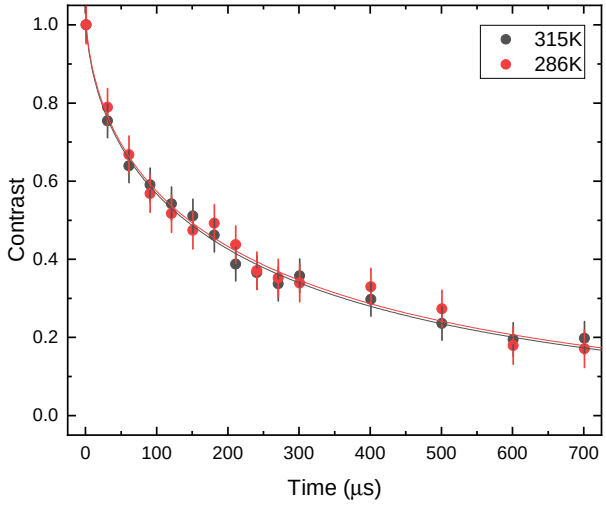

Figure 2.23: Plots of T_1 measurements away from the Gd flake at 315 K (grey curve) and 286 K (red curve). The resulting spin polarization lifetimes $T_1 = 243\pm14$ μs (315 K) and 247 ± 20 μs (286 K) are the identical within the errorbar.

Johnson noise is the main contribution, because we are working at a fixed small transition frequency ($\omega \sim 2.87$ GHz) and in the thermal limit ($\hbar\omega \ll k_B T$), we can consider the DC limit. In this case, we have $T_1 \propto \rho(T)/T$, where $\rho(T) = 1/\sigma(T)$ is the DC resistivity [7]. Importantly, previously measurements of the resistivity curve for Gd show a kink at T_C, with a sharper temperature dependence below T_C [249, 159]. However, this sudden change in slope is insufficient to explain our observations of T_1; in particular, given the magnitude of the resistivity, the change in temperature dominates the T_1 behavior. This implies that T_1 should increase in the ferromagnetic phase if the sole contribution is bulk Johnson noise, whereas observations indicate otherwise.

A hint to the resolution of this puzzle comes from two observations. First, NV centers drop-cast onto Gd samples are very close to the sample, and hence far more sensitive to the surface than the bulk. Second, the surface of Gd is well known to show a higher ferromagnetic transition temperature than the bulk; the drop in T_1 starts at a larger temperature ($\approx$ 300 K) compared to the bulk $T_C \approx 292$ K. These observations strongly suggest that the NV is detecting a large drop of surface resisitivity as we lower T across the surface critical temperature, and this dominates over the small drop of bulk resistivity in the observed behavior.

In order to quantitatively estimate the relative contribution of the surface to the bulk, we write down, following Ref. [7], the contribution to the noise for a single two-dimensional

layer at a distance z from the probe for a sample with conductivity $\sigma(T)$

$$\frac{1}{T_1} \propto N(\omega) = \frac{k_B T \mu_0^2 \sigma(T)}{16\pi z^2} \ . \tag{2.36}$$

Here we have assumed that the optical conductivity has a smooth dc limit (true for typical metals) and taken the extreme thermal limit to neglect the small frequency dependence of σ. Gd has a hcp structure with $c \approx 2a$, so we approximate the sample as being composed of decoupled two-dimensional layers and add their individual contributions to the noise. If the distance from the surface to the probe is d, the surface thickness is D (infinite bulk thickness), and the surface and bulk conductivity are denoted by σ_s and σ_b respectively, then we have:

$$\frac{1}{T_1} \propto T\left[\int_d^{d+D} dz\ \frac{\sigma_s(T)}{z^2} + \int_{d+D}^{\infty} dz\ \frac{\sigma_b(T)}{z^2}\right] = T\sigma_s(T)\left(\frac{1}{d} - \frac{1}{d+D}\right) + \frac{T\sigma_b(T)}{d+D} \ . \tag{2.37}$$

Eq. (2.37) makes it explicit that when D/d is an $\mathcal{O}(1)$ number (i.e. the surface thickness is of the order of sample-probe distance) the surface and bulk contributions are comparable. On the other hand, if $D/d \ll 1$, the bulk noise dominates. For our drop-cast nano-diamonds on the surface of Gd, we can estimate $D \approx 10$ nm, given the distinct surface signatures in the density of states even 6 layers deep [255]. We also estimate the average distance as approximately half the radius of a nano-diamond, $d \approx 50$ nm. Therefore, we see that, for our samples, a large rise in surface conductivity can cause a significant increase in magnetic noise, even if the bulk conductivity remains roughly constant across the transition to the ferromagnetic phase. Hence, we conjecture that an enhanced surface conductivity below the surface critical temperature $T_{c,s}$ is responsible for the observed drop in T_1.

The sharp drop of surface resisitivity below the surface ordering temperature can be due to several reasons. It can be caused by the critical behavior of surface magnetism, or a different electron-magnon coupling on the surface because the surface electrons have more localized wave-functions. Here, we provide one consistent picture for the drop in surface resisitivity in terms of a distinct surface criticality relative to the bulk.

From Ref. [67, 159, 249] we know that both the bulk residual resistivity and the phonon contribution to the resistivity is quite small, and electron scattering below the bulk T_{C} is dominated by magnetic excitations. Since $T_{\mathrm{C}} = 292$ K is much larger than the Debye temperature $\Theta_D \approx 170$ K [43, 159], the phonon contribution to scattering is expected to be linear in T near T_{C}. Above T_{C}, the slope $d\rho/dT$ for Gd is very small. Hence the majority of scattering below T_{C} takes place due to magnetic correlations, which, below T_{C}, changes resistivity by $d\rho/dT \propto t^{2\beta-1}$ where $t = |T_{\mathrm{C}} - T|/T_{\mathrm{C}}$ [109]. β can be significantly different from 1, leading to a cusp in $\rho(T)$ at T_{C}. For the bulk, we can write:

$$\rho_b(T) = \rho_b(T_{\mathrm{C}}) - \alpha_{ph}\left(\frac{T_{\mathrm{C}} - T}{T_{\mathrm{C}}}\right) - \alpha_{mag}\left(\frac{T_{\mathrm{C}} - T}{T_{\mathrm{C}}}\right)^{2\beta}\Theta(T_{\mathrm{C}} - T) \tag{2.38}$$

Above T_{C}, the singularity in $d\rho/dT$ is of the form $t^{-\alpha}$. However, for both Heisenberg and Ising universality classes of ferromagnetic transitions, α is close to zero ($\alpha \approx -0.1$), and the

surface enhancement of the surface density of states is negligible. Therefore, for $T > T_{\mathrm{C}}$ we assume that the surface conductivity is identical to the bulk conductivity. Moreover, the scattering from uncorrelated core-spins should be constant at high temperatures away from T_{C}, so the slope $d\rho/dT$ is entirely from phonons for $T \gg T_{\mathrm{C}}$. Using this relation, we can estimate $\alpha_{ph} \approx 27\ \mu\Omega$cm using the data for T between 350 and 400 K [159]. Using the data for ρ at $T = 280$ K in Ref. [249] to extract α_{mag} and $\beta \approx 0.35$ for the three dimensional Heisenberg model, which is believed to describe quite well the ordering of local moments in Gd [255], we obtain α_{mag}:

$$\rho_b(T) - \rho_b(T_{\mathrm{C}}) = -4\ \mu\Omega\mathrm{cm} = -\alpha_{ph}\left(\frac{12}{292}\right) - \alpha_{mag}\left(\frac{12}{292}\right)^{0.7} \implies \alpha_{mag} \approx 27\ \mu\Omega\mathrm{cm} \quad (2.39)$$

This gives the bulk resistivity as a function of temperature, but it does not replicate the experimental observations, purple line in Fig. 2.24. We now postulate a similar critical behavior at the surface but with surface critical exponent β_s for the magnetization. On a two-dimensional surface, the Mermin-Wagner theorem forbids the spontaneous breaking of a continuous spin-rotation symmetry at a non-zero temperature [183]. For a surface ferromagnetic phase transition, we must have theory with reduced symmetry. Given the easy axis anisotropy in Gd [249, 255], the surface magnetic phase transition is plausibly in the Ising universality class, with $\beta_s = 0.125$ [183]. Therefore, on the surface, we have:

$$\rho_s(T) = \rho_s(T_{c,s}) - \alpha_{ph,s}\left(\frac{T_{c,s} - T}{T_{c,s}}\right) - \alpha_{mag,s}\left(\frac{T_{c,s} - T}{T_{c,s}}\right)^{0.25}\Theta(T_{c,s} - T) \quad (2.40)$$

In absence of evidence otherwise, we take $\alpha_{ph,s} = \alpha_{ph}$ (same value as in the bulk). However, $\alpha_{mag,s}$ can be significantly enhanced relative to the bulk value. This can be due to several reasons. The surface electrons can be more localized than the bulk, therefore increasing the electron core-spin coupling. Further, the surface local moments can have a larger net spin S relative to the bulk which orders more slowly. Since the electron-spin scattering cross-section is proportional to $S(S+1)$ [109], a fully polarized core 4f state with $S = 7/2$ will have a larger scattering rate with an itinerant electron compared to a partially polarized state with $S < 7/2$. The exact value of $\alpha_{mag,s}$ thus depends on delicate surface physics; here we treat it as a free parameter. Fig. 2.24 shows a good fit to our data with the estimates $\alpha_{mag,s} = 7\alpha_{mag} \approx 189\ \mu\Omega$cm, surface thickness $D = 10$ nm $\approx 17c$, and sample-probe distance $d = 50$ nm (we have used an overall proportionality factor for the fit).

We note that spin-fluctuations in Gd can also cause cause the NV polarization to relax. Although such fluctuations are negligible in the paramagnetic phase as our sample-probe distance is much larger than the lattice spacing [7], gapless critical fluctuations and spin-wave modes can indeed have a larger contribution to magnetic noise. However, the magnon contribution is related to magnon occupancies and decreases with decreasing temperature [59], implying that T_1 should increase as one lowers temperature in the ferromagnetic phase. This is inconsistent with the behavior we observe. Bulk critical spin-fluctuations should make the largest contribution at T_{C}, which is also not observed. An even more involved

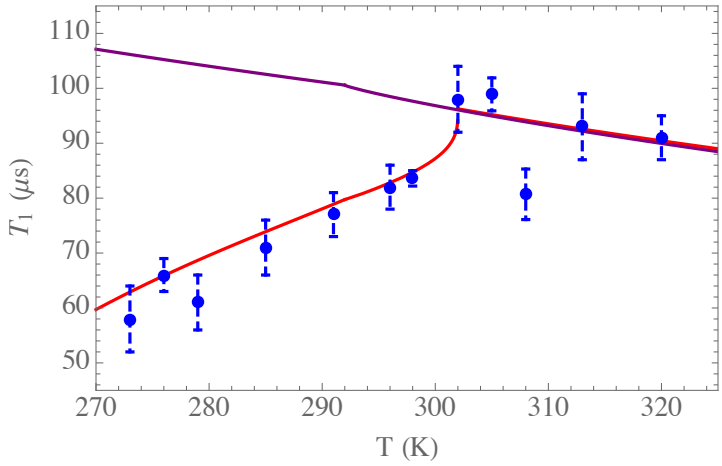

Figure 2.24: The purple curve shows T_1 taking only the bulk contribution to Johnson noise into account. The red curve shows T_1 taking both surface and bulks contribution into account, with $T_C = 292$ K and $T_{c,s} = 302$ K. The blue dots are experimental data.

theoretical analysis is required to rule out critical surface spin-fluctuations. This analysis is left for future work.

2.10 Conclusion

In this Chapter, we have developed a hybrid platform that integrates quantum sensors into diamond anvil cells. While our work utilizes NV centers, the techniques developed here can be readily extended to other atomic defects. For instance, recent developments on all-optical control of silicon-vacancy centers in diamond may allow for microwave-free stress imaging with improved sensitivities [22]. In addition, one can consider defects in other anvil substrates beyond diamond; indeed, recent studies have shown that moissanite (6H silicon carbide) hosts optically active defects that show promise as local sensors [22]. In contrast to millimeter-scale diamond anvils, moissanite anvils can be manufactured at the centimeter-scale or larger, and therefore support larger sample volumes that ameliorate the technical requirements of many experiments.

For the first time, the full stress tensor can be mapped across the sample and gasket as a function of pressure. Further stress characterization of other fluids and solids may provide insights into mechanical phenomena such as viscous flow, plastic deformation, and pressure-dependent yield strength. Crucially, such information is challenging to obtain via either numerical finite-element simulations or more conventional experimental methods and may ultimately allow control of the deviatoric- as well as normal-stress conditions in high pressure experiments [106]. In Chapter 3, we utilize this stress sensing modality to image

the shear stresses on a pressurized sample of chrysotile serpentine, which provides unique insights into the dynamics of amorphization.

In the case of magnetometry, the high sensitivity and close proximity of our sensor enables one to probe signals that are beyond the capabilities of existing techniques (Fig. 2.1(d)); these include for example, nuclear magnetic resonance (NMR) at picoliter volumes [174] and single grain remnant magnetism [123], as well as phenomena that exhibit spatial textures such as magnetic skyrmions [91] and superconducting vortices [320]. In Chapter 4, we utilize this magnetic imaging modality to observe a pressure-induced magnetic transition in a micron-scale grain of pyrrhotite.

Finally, the suite of sensing capabilities previously demonstrated for NV centers (i.e. electric, thermal, gyroscopic precession etc.) can now straightforwardly be extended to high pressure environments, opening up an enormous new range of experiments for quantitatively characterizing materials at such extreme conditions which can test, extend and validate first-principles theory. In Chapters 5 and 6, we explore the feasibility of NV-based electric field sensing using a range of microwave and optical spectroscopic techniques, and we theoretically apply these insights to the study of polar and dielectric materials.

Chapter 3

Amorphization of Serpentine: Acoustic Emissions and Stress Imaging

3.1 Introduction

In the previous Chapter, we experimentally realized a high pressure sensing platform based on fluorescent spin defects through a series of proof-of-concept demonstrations. In the next two Chapters, we utilize this platform to investigate two applications of scientific interest. Both of these applications are relevant to the study of high pressure mineralogy, where the micron-scale resolution of our sensor is naturally suited to relevant length scales in terrestrial rocks and meteorites.

The first of these applications, and the subject of this Chapter, relates to a longstanding question in geoscience: what causes earthquakes observed more than 100 km inside Earth [49, 262, 113]? At these pressure-temperature conditions, minerals are known to deform through ductile flow, as opposed to brittle fracturing. A proposed resolution invokes the amorphization transformation observed in mantle minerals, which is characterized by brittle-like failure and the release of acoustic energy [179, 235, 81, 293, 124]. We experimentally investigate this transformation in chrysotile serpentine ($(Mg, Fe)_3Si_2O_5(OH)_4$) up to 26 GPa via two complementary modalities. Firstly, utilizing a phase-calibrated network of piezoelectric transducers, we identify focal mechanisms from nano-seismic acoustic emissions and observe significant shear components during all events, consistent with deep seismicity. Concurrent x-ray diffraction measurements link these acoustic emissions to amorphization. Secondly, using an NV center-based sensing platform, we perform *in situ* stress imaging and find that shear stresses accumulate and dissipate immediately before and after acoustic events, a hallmark of brittle failure.

In this work, we study amorphization in chrysotile serpentine, an abundant mineral in the subducting slabs where deep earthquakes are observed. Using a two-pronged approach,

we characterize the acoustic emissions and the local stress state on both compression and decompression. Focal mechanisms for acoustic emissions are determined from first motions of the acoustic traces and show that shear – not volumetric – displacements are generated by high-pressure transformation. Second, using nitrogen vacancy (NV) color center, a novel platform for high pressure sensing, we directly image the stress in the confining diamonds at the diamond-sample interface. Crucially, stress maps show an accumulation and relaxation of shear stresses, analogous to brittle failure mechanisms. X-ray diffraction confirms structural changes to be coincident with acoustic emissions.

3.2 Acoustic emissions

In the first study, we directly measure acoustic emissions using a diamond anvil cell instrumented with four displacement sensors (Figure 3.1). Three of the sensors are in the plane of the sample, perpendicular to the loading axis, and a fourth sensor is placed on the bottom of the diamond cell, off center of the symmetry (loading) axis of the cell. Sampling at 0.1-40 MHz, first motions from over 450 acoustic emissions were collected up to 26 GPa at 300 K (Figure 3.1).

First motion amplitude varied between 0.3 and 3 mV (corresponding to Angstrom-scale displacements) depending on the strength of the acoustic emission and the quality of coupling between the sensors and the diamond cell. Durations of first motions are proportional to sample diameter (1.2 µs and 1.7 µs for 90 µm and 140 µm respectively). These timescales indicate that ruptures traverse the sample chamber at 1/3 of shear velocity (∼2.2 µm/ns in chrysotile serpentine at ambient pressure) [273]. These velocities are consistent with expected nucleation and growth rates of a new phase in a high pressure medium, as well as observations of brittle-like failure observed on other systems (e.g. Si, $MgGeO_4$) [293, 300, 219, 220].

All signals had 2-3 traces indicate tensional first motions (trace moving to positive voltages), with 1-2 in-plane traces indicating compressional first motions (trace moving to negative voltages). Compressional and tensional first motions of the sensors are used along with sensor location to determine focal mechanisms (Fig. 3.1). The complexity of the diamond cell, and the scarcity of sensors necessitates the assumption of double-couple sources, precluding the determination of Compensated Linear Vector Dipole (CLVD) components of the focal mechanism. The observed focal mechanisms rule out completely volumetric (i.e., isotropic) sources.

Acoustic emissions appear in clusters, with a typical pressure step yielding several acoustic emissions within hundreds of microseconds to seconds of each other. Figure 3.2 shows a subset of our emissions over a ∼100 ms timespan, with a mix of first motion types active concurrently, and repetition of first motion types on timescales of 3-5 ms. First motions of the acoustic events were similar enough to sort into groups in all experiments (see color-coded traces in Figure 3.2).

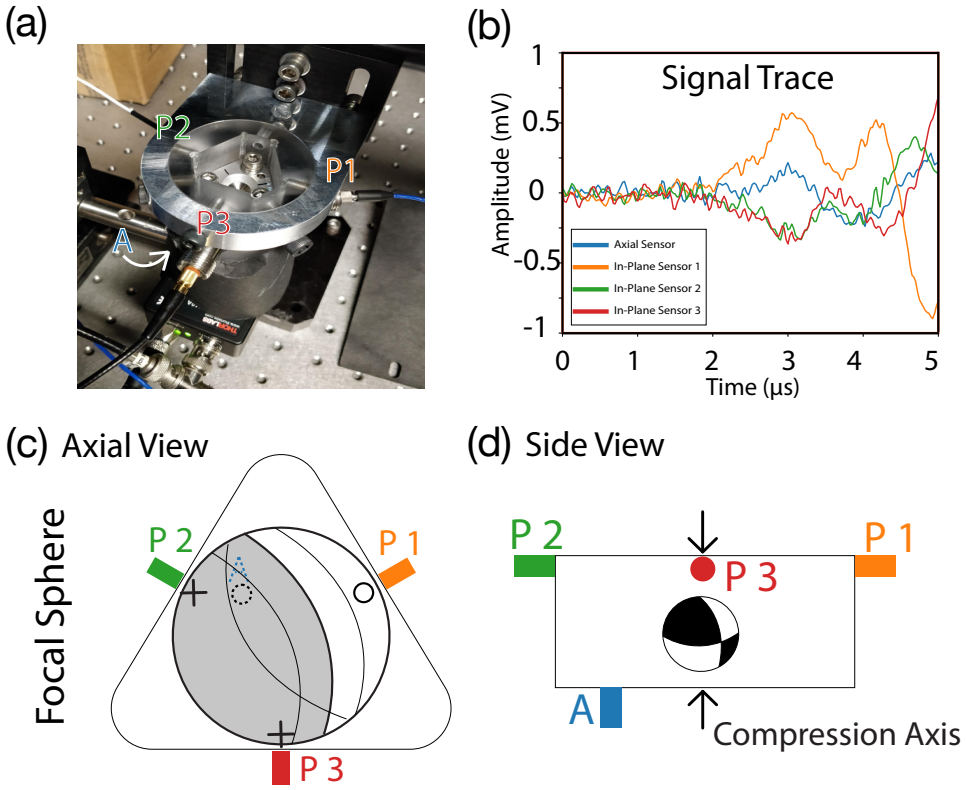

Figure 3.1: Example traces and seismic source diagram for Serpentine at high pressure. (a) A photograph of the experimental setup with labels for the sensors shown color-coded with their respective traces. (b) An example first motion signal trace representative of the signal quality across all data sets. (c) Top-down illustration of a focal sphere projection. In-Plane sensors P1,2, and 3 and Axial Sensor A are shown in their relative positions and are color coordinated to the traces they record. All sensors are coupled orthogonally to the triangular pressure cell, with P1, P2, and P3 organized radially, and the Axial sensor attached to the bottom, near the compression axis. The axial sensor and its polarity observation are shown in dashed lines to indicate they are observing from the opposite side of the diamond cell as the In-plane sensors. Each sensor shows a black plus sign if the trace indicated the sample was in compression, and a hollow circle if the trace indicated the sample was in tension. Due to scarcity of sensors, the proposed focal spheres are only roughly constrained, with several degrees of uncertainty in the nodal lines of these spheres. Additional possible nodal lines are shown with thin black lines. (d) An illustrated side view looking along in-plane sensor 3 is shown in the right. An example focal mechanism appropriate for the first motion is shown in the cross sectional plane, approximately in the location of the sample chamber. The axis of compression is shown with black arrows. Additional possible nodal lines are omitted to improve legibility. Data collected and analyzed by Thomas Smart and Jes Parker.

Cross correlations between first motions allowed us to identify different source types, with first motions of the same type exhibiting high correlation coefficients ($> 95\%$) indicative of similar slip mechanisms [245]. The wavelengths observed here correspond to the resonance of the sample chamber, however, making distinction of rupture zones within the sample chamber is beyond the resolution of the present measurements. As a cross-check, correlation between signals of different first motion types, or signals from different sample loadings, yielded values of $40 - 80\%$ further confirming that they have different sources. First motion amplitudes are also strongly correlated between signals of mutual first motion type, demonstrating similar energy during rupture and suggesting similar rupture area during failure. These lines of evidence strongly suggest that signals sharing a first motion type come from repeating events along a single rupture or system of related ruptures, as suggested by other high-pressure rupture systems [300].

3.3 Concurrent x-ray diffraction

Acoustic emissions were collected concurrently with X-ray diffraction on compression between 8-24 GPa, and then on decompression, all at 300 K. Diffraction peaks broaden and disappear on compression, demonstrating that the high-pressure transformation of serpentine is amorphization, with partial re-emergence of several of the diffraction peaks on decompression (Fig. 3.3) following previous observations [235]. Disappearing diffraction peaks ($[00l]$ peaks), associated with the interlayer spacing between serpentine sheets, are attributed to the collapse of hydrogen bonds as seen during the amorphization of other hydrous materials [246, 248]. Re-emerging $[hk0]$ peaks are associated with the magnesium-silicate sheets, showing that the integrity of the serpentine layers is partially preserved through the amorphization process. Crucially, this precludes a thermal disordering such as that expected from frictional melting, and indicates that the amorphization remains in the solid-state. Solid-state amorphization is a well-known metastable transformation at high pressures, generally facilitated by high shear stresses and often – though not always – reversible (e.g. SiC, $AlPO_4$) [200, 189, 178].

3.4 Stress sensing

Finally, using nitrogen vacancy (NV) centers, we study the changes in the culet stress across several acoustic emission events to unearth the microscopic mechanisms driving amorphization. The NV center, a quantum defect in diamond, has shown promise as a robust and versatile high-pressure sensor whose spin-1 ground state can be spectroscopically interrogated using optically detected magnetic resonance (ODMR) to image the crystal stress *in situ* [148, 197, 352]. In this experiment, we study the NV group aligned along the surface normal $\hat{Z}$) of the diamond culet to measure the symmetry preserving (primarily σ_{ZZ} and $\sigma_{\perp}$) normal stress and symmetry breaking (primarily σ_{RZ}) shear stress. While it is nontriv-

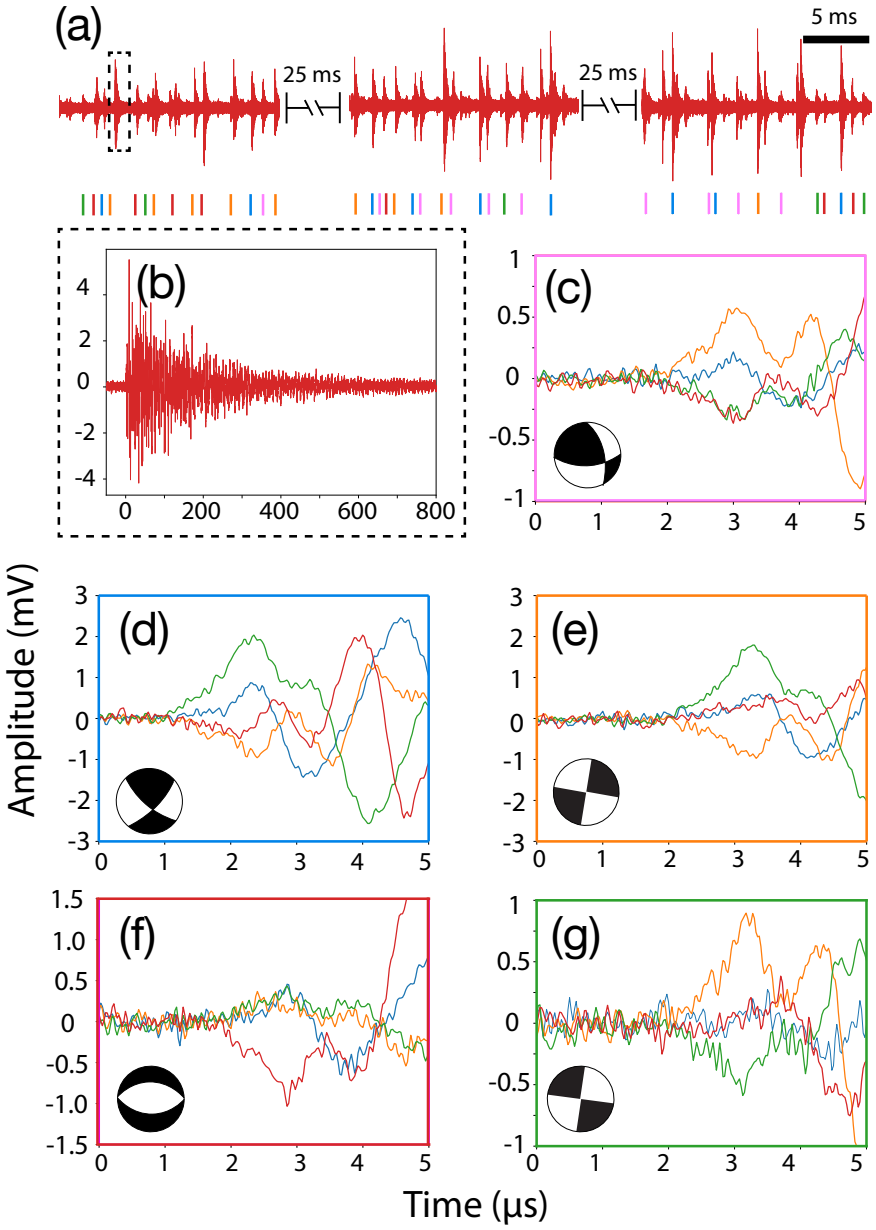

Figure 3.2: Acoustic emission cluster plotted with example first motions. (a) Exemplary acoustic emission cluster at 12 GPa. Beneath each waveform in the cluster we show a colored bar displaying the first motion type observed for the waveform. (b) An exemplary acoustic waveform shows the millisecond timescales typical of our signals. (c)-(g) Example traces of each of the first motion types are shown color coordinated to the colored bars under the emission cluster. First motions types are shown with their focal mechanisms as insets as in the side view shown in Figure 3.1. Signals of a given first motion type occur successively with minimum lag times of 3-5 milliseconds. First motions were not discernible for signals with amplitudes too small to distinguish them from background noise or signals that truncated the coda of an earlier signal. Data collected and analyzed by Thomas Smart and Jes Parker.

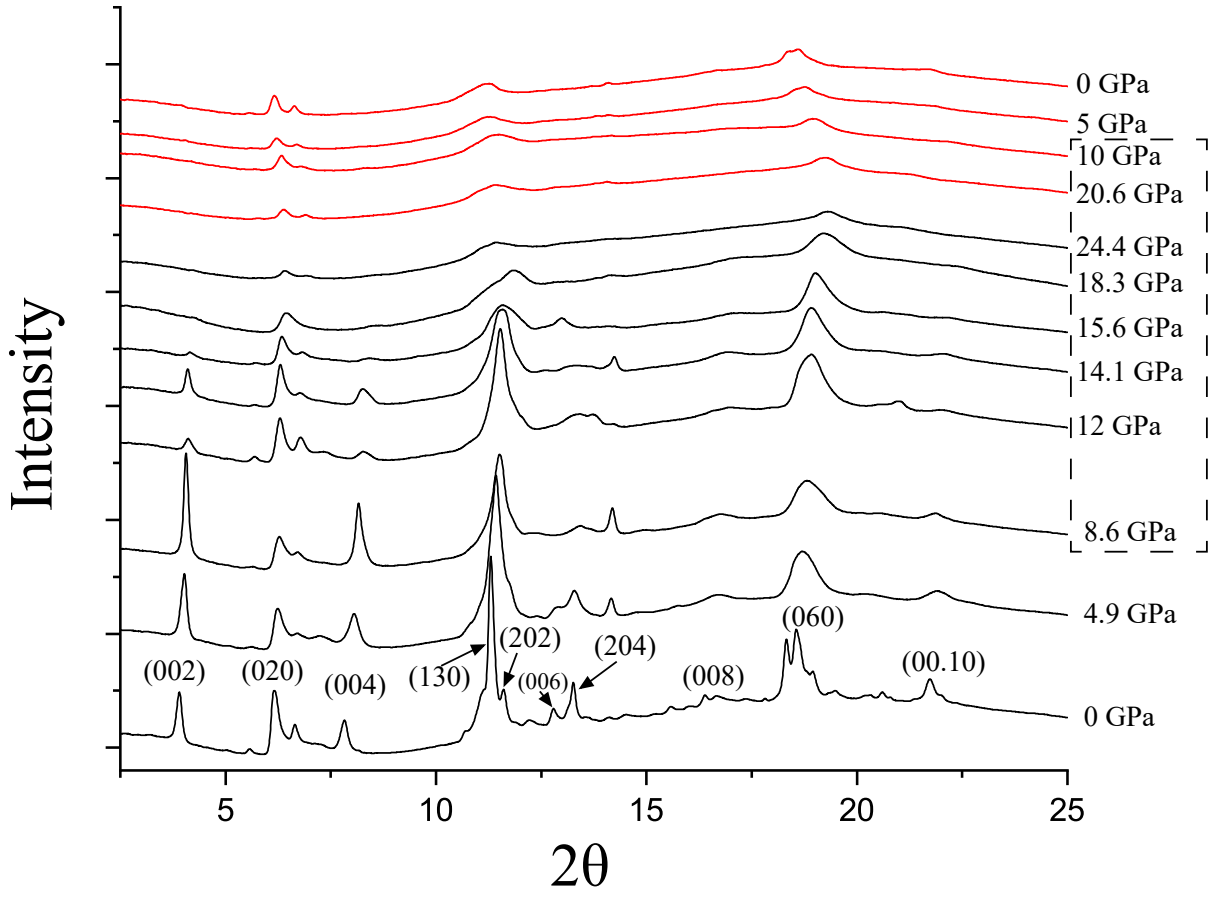

Figure 3.3: X-ray diffraction intensity versus 2 theta for Serpentine on compression and decompression between 0 and 24.4 GPa. The pressure for each diffraction pattern is listed on the right, with pressure steps that yielded acoustic emissions outlined by the dashed box. Patterns taken on decompression are shown in red. Miller indices are shown for the ambient pressure above the ambient pressure diffraction pattern. Data collected and analyzed by Thomas Smart.

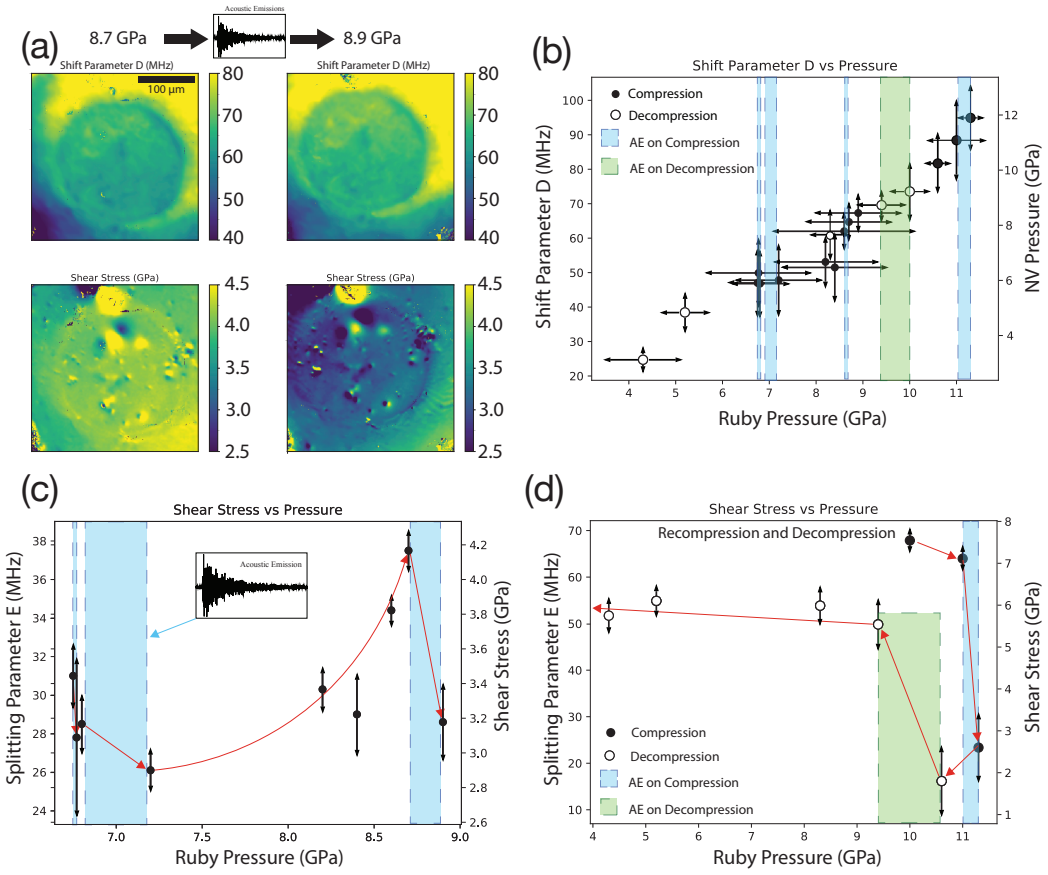

Figure 3.4: (a) Example map of shear stresses taken at 8.7 GPa on compression. Large circular feature is the sample chamber and is surrounded by the rhenium gasket. The dipoles visible in the sample are magnetic noise introduced by magnetite impurities in the natural serpentine sample. (b) Shifting parameter D vs pressure measured by ruby florescence. Open circles represent data taken on compression and closed circles represent data taken on decompression. Arrows shown represent the range of values in pressure and D values that we observe, measured from several points across the sample chamber. We expect that the uncertainty in our fits for the shift parameter D are .03 MHz which is smaller than the symbols shown. Uncertainties of pressure from Ruby fluorescence are 0.05-0.1 GPa. Blue and green rectangles represent pressure steps where we observed acoustic emissions during increase (or decrease) of pressure. (c)-(d) We show shear stresses vs pressure as determined by ruby fluorescence. Data are from the same experiment as those shown in (a) and (b). Red arrows show the chronological sequence of data points and guide the eye through the accumulation and dissipation of shear stresses. Blue and green rectangles represent pressure steps where we observed acoustic emissions during increase (or decrease) of pressure. Uncertainties in the measured shear stresses are estimated to be $\sim$0.03 GPa.

ial to constrain all components of the stress tensor within the sample from those measured within the diamond anvil, the components $\{\sigma_{ZZ}, \sigma_{RZ}, \sigma_{\Theta Z}\}$ are continuous across the sample-diamond interface. We can define our reported shear stresses as $\sigma_{\text{shear}} \equiv \sqrt{\sigma_{RZ}^2 + \sigma_{\Theta Z}^2}$, with σ_{RZ} and $\sigma_{\Theta Z}$ being the radial and azimuthal shear stresses at the diamond-sample interface, respectively.[1]

We monitor for acoustic emissions on compression and decompression, and after every incremental modulation of pressure we collect a map of stresses (Fig. 3.4). The symmetry-preserving stresses follows expectations for a quasi-hydrostatic environment (Fig. 3.4(b)), showing a linear correlation with pressure as measured by ruby fluorescence. The occurrence of acoustic emission within the sample does not perturb the linearity of the symmetry preserving stresses, indicating that they play a negligible role in the instabilities that lead to acoustic emission.

On compression, we observe an accumulation in shear stress, which persists until it is dissipated concurrently with acoustic emission (Figure 3.4(c)-(d)). The peak shear stress observed is interpreted to be the effective shear strength of the material. The relaxation in shear stresses is consistent with volume collapse during the disordering of the interlayer spacing of the serpentine during amorphization as observed in the XRD data. Shear stresses are often invoked as the mechanism for solid-state amorphization, whereby a meta-stable material pressurized beyond its equilibrium phase boundary overcomes kinetic hinderances and transforms [124, 200, 178]. Our work demonstrates the link between shear stresses and solid state amorphization, and crucially, is the first to image the local shear stress field in the sample that lead to these crystalline instabilities.

On decompression we observe a pronounced increase in σ_{shear} coincident with AE on, further demonstrating the reversibility of the structural instabilities that lead to acoustic emissions. Here we infer a volume expansion of the serpentine as it re-crystallizes and presses against the confining diamond anvils.

3.5 Experimental details

We compress natural Serpentine (60% clino- 40% ortho-chrysotile, determined by x-ray diffraction) collected in Marin, California, in diamond anvil cells to 26 GPa and 300 K. Spring steel or rhenium gaskets pre-indented to 40-60 µm thick and drilled with holes 100-150 µm in diameter were used in all experiments and samples were prepared following Ref. [300]. Pressure was determined using the standard ruby fluorescence technique [78].

Acoustic emissions (AE) were recorded with 1-4 Glaser-type conical displacement sensors (model KRNBB-PC) following Ref. [229]. The sensors have a near-flat frequency response from ∼0.1-5 MHz. The built-in preamps were powered with 24VDC, resulting in a sensitivity on the order of 1 V/nm when coupled to steel. Three sensors are prepared around the three edges of the upper diamond cell plate, and a fourth sensor is attached from the bottom,

[1] Due to an abuse of notation, the σ_{shear} defined here is a different quantity from that defined in Chapter 4.

off center of the symmetry axis of the diamond cell. A custom clamp was machined from a 2-inch thick polycarbonate cylinder in order to provide an impedance mismatch strong enough to dampen ringing within the system and hold the diamond cells and sensors in place during the acoustic experiments. AE signals arrive coincidentally at the sensors within $\sim$0.1 µs; assuming wave speeds of mm/µs, this suggests that the sensors are equidistant from the sample chamber within $\sim$0.1 mm. For all measurements performed concurrently with x-ray diffraction measurements, AE signals were digitized on an oscilloscope (Tektronix MSO 2104B); all other AE experiments were digitized at 40 MHz using an Elsys TraNET EPC digitizer and TranAX 4.0 recording software. The Merrill-Basset DACs often produced highly broadband signals, with signal to noise ratios (SNR) >2 up to the Nyquist frequency of 20 MHz and SNR>10 up to 4 MHz. Synchotron X-ray diffraction was performed at beamline 12.2.2 of the Advanced Light Source at Lawrence Berkeley National Laboratory, using an X-ray wavelength of 0.4959 nm, and a distance from the sample to the detector of 330 cm.

3.5.1 Acoustic Calibration and Control Tests

We calibrated the sensors using two approaches that provide a known acoustic source for comparison with signals observed from the serpentine samples: firstly, glass capillaries were broken between the diamond anvils used for the high-pressure experiments to ensure that the signals for this calibration use the same ray paths as acoustic emissions produced during the experiment. Secondly, pin drop calibrations were performed by dropping a stainless steel 38mm long, 0.7mm diameter sewing needle onto the backside of the diamond anvil from a height of 5mm. Pin drop calibrations were performed before and after the collection of acoustic emissions from the sample to account for any deviation in the sensor-to-cell mechanical coupling. Calibration tests give a step-like acoustic pulse, with all traces moving in the same direction, as expected for a single force source transmitted through symmetric paths [229, 230]. Thus, despite the complex geometry and multiple impedance mismatches along the ray path, the system maintains the linearity required for first motions analysis of experimental signals. The calibration results also reveal that a useable Greens function cannot be extracted because deconvolution of the calibration source is non-unique, and that a modeling-based determination of the full acoustic response of the diamond cell is beyond the scope of this work. Therefore, we cannot invert for a full moment tensor, thus precluding determination of the CLVD component. Control tests were performed on our experimental setups to pressures of 30-40 GPa, well beyond the pressure limit of our experiments. We used both spring steel and Rhenium gaskets for these tests, and blank gaskets (with and without holes), 4:1 Methanol:ethanol mixture, and PbCl2 as the control test media. Typically, the diamond cell's pressure transmitting screws are equipped with Belleville spring washers to control compression. However, when equipped with these springs, rubbing between the washers yielded acoustic signals that triggered our sensors, and therefore Belleville washers were omitted in our experiments. Noise from outside the sample chamber is spectrally distinct (10's-100kHz versus 1-5MHz of the signals from our samples) and exhibits time delays more than the 10-20 ns required to traverse the sample chamber.

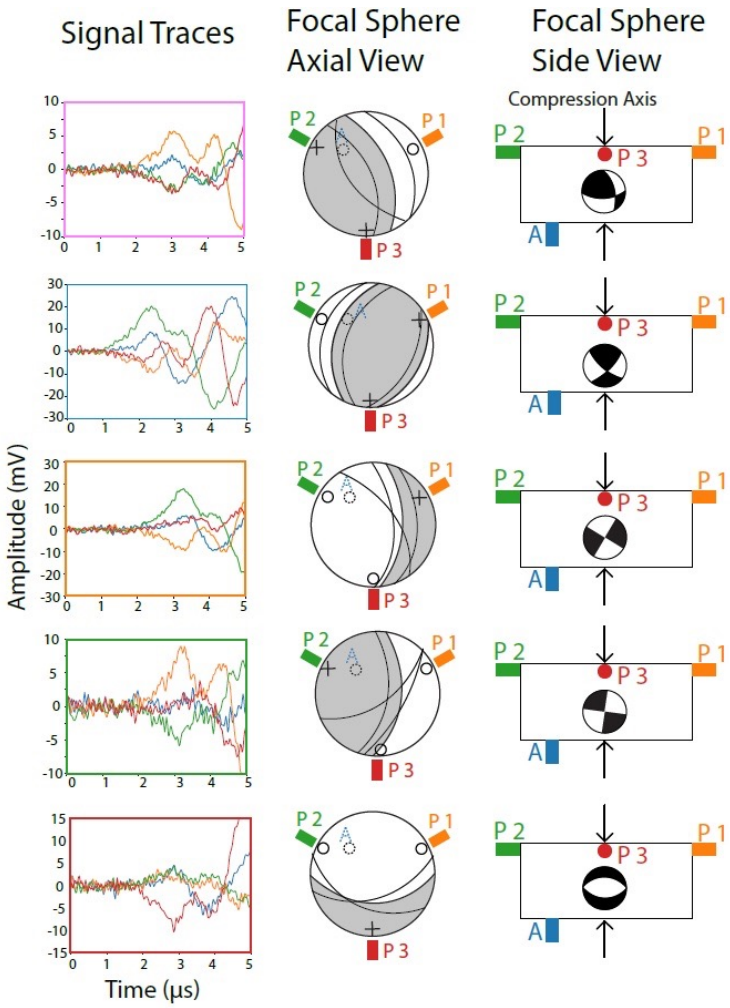

Figure 3.5: First motion types with their respective focal spheres are shown. As in Figure 3.1, Signal Trace) shows an example first motion signal trace is shown. this signal is representative of the average signal quality across our data set. Focal sphere, Axial View) Shows a top-down illustration of a focal sphere projection. In-Plane sensors P1,2, and 3 and Axial Sensor A are shown in their relative positions and are color coordinated to the traces they record. All sensors are coupled orthogonally to the triangular pressure cell, with P1, P2, and P3 organized radially, and the Axial sensor attached to the bottom, near the compression axis. The axial sensor and its polarity observation are shown in dashed lines to indicate they are observing from the opposite side of the diamond cell as the In-plane sensors. Each sensor shows a black plus sign if the trace indicated the sample was in compression, and a hollow circle if the trace indicated the sample was in tension. Due to scarcity of sensors, the proposed focal spheres are only roughly constrained, with several degrees of uncertainty in the nodal lines of these spheres. Side View) An illustrated side view looking along in-plane sensor 3 is shown in the right. An example focal mechanism appropriate for the first motion is shown in the cross-sectional plane, approximately in the location of the sample chamber. The axis of compression is shown with black arrows. Data collected and analyzed by Thomas Smart and Jes Parker.

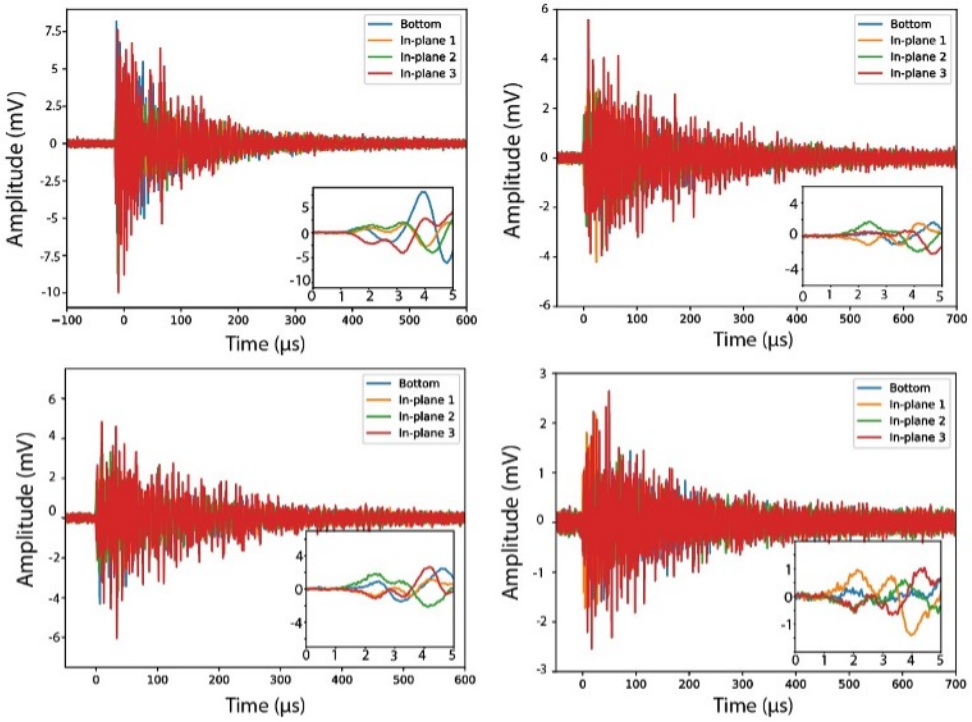

Figure 3.6: Four example acoustic emission signals and their first motions (inserts) are shown. These are 4 signals each with different first-motion character and are average signals that represent the quality of our data well. Duration of the full acoustic waveforms are proportional to first-motion amplitude in all experiments demonstrating that our system has a high Q factor. Signal durations vary between 0.05-1 ms, longer than the resonances expected from our sample chamber (10^{-7}-10^{-6} s), though in accord with expected resonance times of the experimental apparatus [300, 234]. Peak waveform amplitudes vary between 1 and 15 mV. Data collected and analyzed by Thomas Smart and Jes Parker.

3.6 Possibilities and limitations for frictional heating during deformation of Serpentine

Though we do not observe evidence of melting, the sample may be transiently heating due to feedback loops between plastic work and rheologic weakening of the material causing localized heating along shear zones [124, 272]. Previous work observed serpentine to remain acoustically active at pressures and temperatures exceeding 25 GPa and 900 K, indicating the failure mechanism responsible for acoustic emission is somewhat tolerant of high temperature [235]. Heat in this case must dissipate quickly enough between successive failures for the serpentine remain solid and regain material strength needed for subsequent failure [231]. Ambient pressure thermal diffusivity of serpentine (0.005-0.01 cm^2/s or 0.5-1 $\mu m^2/s$) suggests that it would take ∼25-50 µs for heat in the center of the sample to diffuse to the serpentine/diamond interface, where the relatively high mass and heat conductivity of the diamonds act as heatsinks [118, 76]. These 10s of microsecond timescales are easily accommodated within the observed minimum lag time between signals (see Figure 3.2).

While our experiments show that frictional heating is not observed in these laboratory scale experiments, it is possible that melting plays a role when scaled to larger length scales. Figure 3.7 shows a comparison between the time/distance relations of acoustic transit and thermal diffusion. Acoustic transit times are typically km/s (µm/ns), while typical thermal diffusivity in rocks is mm^2/s ($\mu m^2/\mu s$). While at shorter length scales, the two curves converge at nanometer distances and picosecond timescales, at larger distances, acoustic transits are orders of magnitude faster than thermal diffusion. Therefore, at larger distances, if crystal-structural instability initiates fracture or other rapid deformation in nature, frictional heating may potentially cause melting subsequent to the failure, potentially obscuring the evidence of the initial instability. That is to say, failure due to shear-induced solid-state amorphization and frictional melting are not mutually exclusive. This has bearing not only for faulting at crustal pressures (e.g. generation of pseudotachylites in shear zones) but in deep seismicity as well where localized shear zones generate feedback loops between material strength and frictional heating (and possibly melting) to drive material failure [124, 341, 18].

3.7 Stress measurements

Here, we provide a brief summary of the experimental apparatus, measurement protocol and data fitting procedure relevant to the current study.

3.7.1 Sample preparation

We directly procured Type Ib HPHT diamond anvils with [111] crystal cut culet from Syntek Co. Ltd. We performed $^{12}C^+$ ion implantation (CuttingEdge Ions, LLC) at 12 keV with 2.25×10^{11} ions/cm^2 and at 30 keV with 6.75×10^{11} ions/cm^2 to generate vacancies up to

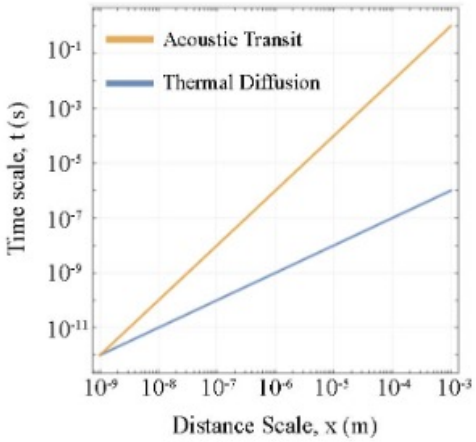

Figure 3.7: Comparison of the acoustic transit and thermal diffusion timescales in a typical rock, by distance. Calculation by Thomas Smart.

50 nm from the surface of the diamond anvil. We used SRIM [363] to determine the required energy and dosage of the ions for creating vacancies. In the final step, the anvil was vacuum annealed to created a shallow layer of NV centers.

3.7.2 Experimental apparatus

The NV measurements were performed on a home-built widefield fluorescence microscope. We use 2 W 532 nm laser (Coherent Verdi V-2) as our excitation beam. A laser speckle reducer (Optotune LSR-3005-6D-VIS) is used to suppress the spatial coherence in the laser beam in order to enhance image clarity. The diffuse laser beam is collimated using with an aspheric lens and directed at the sample using a dichroic mirror (AVR Optics FF556-SDi01-25x36). The NV fluorescence is transmitted through the dichroic and focused on an EMCCD camera (Princeton Instruments ProEM-HS: 512BX3). Microwaves for ODMR are synthesized by a RF signal generator (Stanford Research Systems SG384) and subsequently amplified using an RF amplifier (Minicircuits ZHL-16W-43S+). Similar to previous work [148], the amplified microwaves are applied at the sample region using a platinum foil. Continuous wave optically detected magnetic resonance (ODMR) spectra are collected by measuring the fluorescence while synchronously chirping the frequency of the applied microwaves.

3.7.3 Magnetite contamination

The dipoles visible in the E-splitting maps are due to impurities of magnetite in the sample chamber (presence of magnetite in the sample is confirmed through x-ray diffraction of the natural serpentine powder). The splitting of the NV spectra is sensitive to magnetic fields

(via the Zeeman effect) and therefore can be used to image local magnetic fields in the sample.

3.8 Conclusion

In this Chapter, we have demonstrated the use of NV center-based stress imaging to elucidate the crystalline-to-amorphous transition in a mantle mineral. The observed accumulation and dissipation of shear stresses before and after acoustic emissions is a characteristic feature of brittle-like failure which was elusive in previous laboratory experiments. Crucially, this phenomenon is only observed in the shear stress and not the hydrostatic pressure, suggesting that the unique ability of the NV center-based sensing platform to distinguish individual stress tensor components plays a key role in our measurement.

Chapter 4

Magnetic Transition in a Single Grain of Pyrrhotite

4.1 Introduction

Having utilized our NV center-based sensing platform to elucidate the evolution of stresses associated with a crystal structural transformation, we next apply our sensor to *magnetic* transitions under pressure. To this end, we consider a key question in the study of Martian paleomagnetism: why does Earth exhibit a global magnetic field, but Mars does not? Intriguingly, the strong crustal magnetization first measured during the Mars Global Surveyor mission in 1996 suggests that this was not always the case [6]. A glimpse into this magnetic history comes from young impact basins (Hellas, Argyre, and Isidis) on the Martian crust, where an absence of magnetization suggests that shock demagnetization may have occurred after the cessation of an ancient dynamo [204, 331]. This hypothesis has motivated several experiments characterizing magnetic rocks and minerals under the pressure conditions expected during impact cratering. However, owing to sample size constraints imposed by high pressure instrumentation, conventional sensors have difficulty resolving magnetism at geologically relevant pressures. In this Chapter, we overcome these challenges by utilizing our high pressure sensing platform based on NV centers, enabling magnetic imaging with micron-scale resolution at gigapascal pressure. We demonstrate the utility of this tool by probing the pressure-induced ferrimagnetic-to-paramagnetic transition in $4C$ monoclinic pyrrhotite (Fe_7S_8), an iron sulfide mineral found in Martian meteorites as well as chondritic meteorites and terrestrial rocks. By leveraging the NV center's exquisite magnetic sensitivity, we probe the saturation isothermal remanent magnetization (SIRM) of a single micrometer-scale pyrrhotite grain under two rounds of compression and decompression. We find that the SIRM decays by three orders of magnitude by the highest pressure of 6.5 GPa and completely revives upon decompression, in contrast to previous works that observe irreversible loss of magnetic remanence. Furthermore, we find reproducible pressure hysteresis of the SIRM, suggestive of a first-order transition. Finally, we demonstrate imaging of both normal

and shear stresses near the sample. Our findings have implications for the interpretation of shock demagnetization and broadly demonstrate the utility of NV center sensing for high pressure rock and mineral magnetism.

Monoclinic $4C$ pyrrhotite is believed to contribute significantly to Martian crustal magnetization [278, 355].[1] Neutron diffraction and Mössbauer spectroscopy reveal a pressure-driven ferrimagnetic-to-paramagnetic transition, providing a candidate mechanism for shock demagnetization [329, 182, 277]. In spite of this motivation, conventional sensors struggle to resolve magnetism within high pressure instrumentation, where sample sizes are constrained to be small relative to the pressure cell dimensions and thus the subtraction of undesirable background magnetism is challenging. To maximize the signal-to-background ratio, packed volumes of powder samples are typically used, which introduces heterogeneities in grain sizes and applied stresses [277, 38, 36, 37, 119].[2] The subsequent averaging over stress and grain size distributions using this approach introduces systematic uncertainties that may contribute to the large spread of transition pressures previously reported in literature [207].[3] Indeed, the detailed evolution of high pressure phase transitions—including their critical pressure, hysteresis, and reversibility—is known to be sensitive to stress gradients and deviatoric stresses [26, 199].

To overcome these challenges, we utilize a sensing platform based on NV centers implanted $\sim 500\,\mathrm{nm}$ from the surface of a diamond anvil. We utilize the magnetic field-dependent fluorescence of the NV centers to image stray fields from the sample of interest [123, 148, 197, 352, 86, 308]. Crucially, embedding NV centers into a diamond anvil cell enables *in situ* magnetometry at gigapascal pressure under both compression and decompression [148, 197]. In comparison to induction coil techniques, the NV-based system enhances magnetic moment sensitivity by several orders of magnitude, enabling the imaging of ferromagnetic grains at the micrometer scale. Furthermore, the sensitivity of NV centers to stresses enables imaging of all six unique components of the stress tensor, allowing for quantitative characterization of the applied stress tensor environment [148].

4.2 Methods and system characterization

4.2.1 Description of sample

Pyrrhotite ($Fe_{1-x}S$, $0 < x < 0.125$) is found in a variety of crystal structures. Of these, the monoclinic $4C$ phase is the only equilibrium phase which retains a spontaneous magnetization, exhibiting ferrimagnetism due to its ordered array of Fe vacancies [333]. The pyrrhotite sample in this work is sourced from a single crystal whose structural, magnetic,

[1] We note that besides monoclinic pyrrhotite, hexagonal pyrrhotite in a metastable ferrimagnetic state has been proposed to carry remanence in meteorite samples [278].

[2] Additional subtleties arise in dynamic loading experiments, where ambient magnetic fields and applied stresses are not straightforward to control [206, 208].

[3] We note that the pyrrhotite phase composition and domain sizes of samples examined in previous works may also contribute to the spread of transition pressures.

and electronic properties have been previously characterized [333, 334]. X-ray diffraction reveals that the crystal is pure monoclinic $4C$ pyrrhotite without any other structural phases such as hexagonal pyrrhotite. Its bulk chemical composition, as determined through electron microprobe analysis, is $Fe_{6.78\pm0.12}S_8$, which is within the stability field of the monoclinic $4C$ phase [334]. No impurities, such as nickel, were detected. Low-temperature remanence experiments reveal a sharp Besnus transition at 32 K, further corroborating the presence of the monoclinic $4C$ phase [334].

Pieces of the single crystal of pyrrhotite (MSM17591) were ground using a mortar and pestle to obtain fragments between 15-50 µm. This grinding was conducted under ethanol to retard oxidation as in the sieving procedure of [347]. The resulting silt-sized particles were pulsed by a 1 T field using an ASC pulse magnetizer in the Berkeley paleomagnetism lab. Two pulses were applied as the first pulse may result in grain rotation with the second pulse assuring saturation.

4.2.2 High pressure experimental setup

A schematic of our experiment is shown in Figure 4.1. We load a nonmagnetic steel diamond anvil cell, described in [311], with two opposing diamond anvils of culet diameter 350 µm compressing a rhenium gasket preindented to 50 µm. A $\sim$ 15 µm-diameter grain of pyrrhotite is placed onto the diamond anvil culet in addition to a ruby microsphere (pressure scale). The sample chamber, defined by a 120 µm-diameter laser-drilled hole in the rhenium gasket, is filled with solid cesium iodide to provide a quasi-hydrostatic pressure environment [54]. Microwave excitation is applied with a 4 µm-thick platinum foil compressed between the gasket and diamond anvil pavilion facets.

4.2.3 Quantum diamond microscope

Operation of our high pressure sensing platform based on NV centers has been previously described both in the context of rock magnetism [123] and high pressure [148, 197]. We briefly review the operational procedure here, emphasizing unique characteristics of the current implementation.

At the heart of the system is an ensemble ($\sim$1 part-per-million density) of NV centers prepared in a thin layer from the diamond anvil surface. Each of these atomic-scale defects harbors an electronic spin ground state whose spin sublevels are sensitive to local changes in applied stress and magnetic fields. These sublevels can be optically initialized and read out with laser light. One can probe these sublevels through optically detected magnetic resonance spectroscopy, which measures the spin-dependent fluorescence intensity as the frequency of an applied microwave field is swept across the NV center spin resonances. We excite the NV centers using a 532 nm laser and collect their fluorescence onto a charge-coupled-device (CCD) camera, which allows us to image two-dimensional magnetic field maps directly below the sample with micrometer resolution. The laser can be substituted with a white light source, allowing for reflected light microscopy which colocalizes the magnetic images with

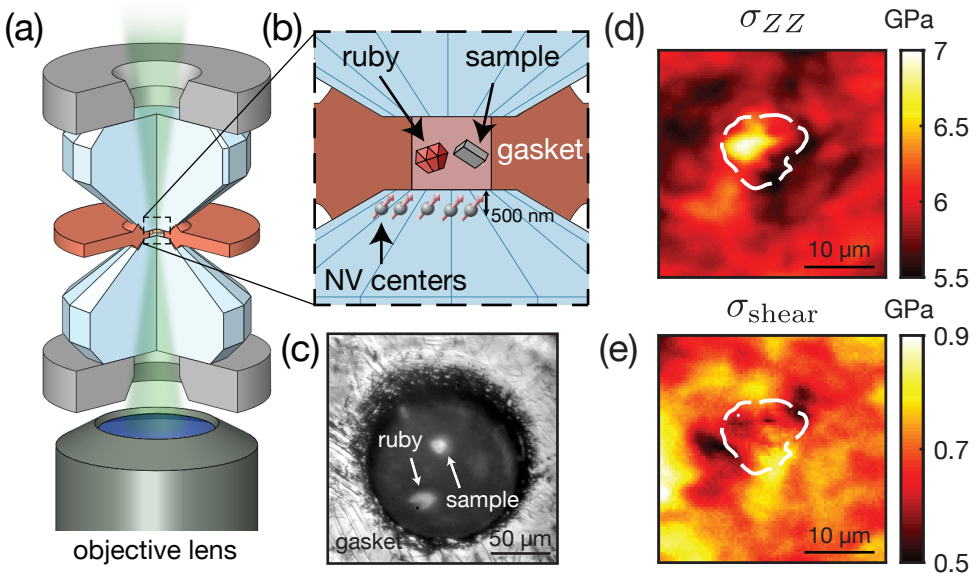

Figure 4.1: Experimental setup. (a) Schematic of the high pressure setup. Two opposing diamond anvils are compressed between cubic boron nitride backing plates (gray). NV centers are interrogated by a 532 nm laser; the resulting fluorescence is imaged onto a charge-coupled-device camera. (b) The sample chamber, defined by a laser-drilled hole in the rhenium gasket, contains a ruby microsphere, a single pyrrhotite grain, and a cesium iodide pressure-transmitting medium. NV centers are prepared ~ 500 nm below the sample chamber. (c) Reflected light image of the sample chamber viewed through the bottom anvil. (d)-(e) Stress maps near the pyrrhotite sample (dashed white outline) measured at $P_{\mathrm{ruby}} = 5.8$ GPa. Both the normal stress along the loading axis, σ_{ZZ}, and the shear stress, $\sigma_{\mathrm{shear}} \equiv \sqrt{\sigma_{XZ}^2 + \sigma_{YZ}^2 + \sigma_{XY}^2}$, reveal micron-scale gradients that highlight the complexity of the applied stress environment.

the sample. An applied external magnetic field ($B_{\text{ext}} \sim 50\,\text{G}$) spectroscopically separates the NV center resonances in order to decouple their response to magnetism and stress [148].[4]

4.2.4 Characterizing magnetic sensitivity

We begin by characterizing the magnetic sensitivity of our high pressure sensing platform under a fixed magnetic field. The image area-normalized magnetic sensitivity ranges from 8-14 $\mu\text{T} \cdot \mu\text{m}/\sqrt{\text{Hz}}$ over the studied pressures under both compression and decompression. We note that this range is within the 1-100 $\mu\text{T} \cdot \mu\text{m}/\sqrt{\text{Hz}}$ sensitivities reported in previous NV center implementations at ambient pressure which can resolve magnetic sources down to $10^{-16}\,\text{Am}^2$ [123].

4.3 Results

Sensitivity in hand, we begin measuring the SIRM of pyrrhotite under pressure. At low pressures, we observe shifts of all eight NV resonances near the pyrrhotite grain owing to its stray magnetic field. As we increase pressure, the resonance shifts sharply diminish, reflecting a reduction in the SIRM. This trend continues up to the highest pressure of $P_{\text{ruby}} = 6.5$ GPa, whereby the SIRM has reduced by over three orders of magnitude.

To quantify this phase transition, we reconstruct the full vector magnetic field produced from the pyrrhotite sample at the NV center layer. We compare the experimentally determined field distribution to the expected distribution from a single magnetic point source. At the highest pressures where multiple magnetic sources are resolvable (e.g. Fig. 4.2(c)), the same procedure is applied to the source with the largest magnitude.[5] Through this procedure, we extract the SIRM as a function of applied pressure (Fig. 4.2). Fitting to a logistic function, we find that the transition occurs at a critical pressure of $P_{\text{c, compress}} = 4.45 \pm 0.05$ GPa with a transition width of $\Delta P = 0.24 \pm 0.05$ GPa (Fig. 4.2(d)). Crucially, the high pressure sensing platform can be operated under both compression *and* decompression, which allows us to probe hysteresis under pressure. Indeed, as the applied pressure is decreased, we observe a complete revival of the SIRM at low pressure, in contrast to previous reports observing irreversible loss of the SIRM upon quenching. We find $P_{\text{c, decompress}} = 2.9 \pm 0.2$ GPa, while $\Delta P = 0.7 \pm 0.2$ GPa.

In addition to probing pressure hysteresis, the diamond anvil cell enables the ability to cycle pressure multiple times without degradation of the apparatus. To this end, we repeat the experiment using the same grain of pyrrhotite and nominally identical experimental conditions. As shown in Fig. 4.2(e), in run 2, while the critical pressures under compression and decompression do not change appreciably compared to run 1, the transition widths are markedly different.

[4] We note that the applied field is much smaller than the measured coercive field at all pressures [119]

[5] Due to the saturated response at some pixels, upward continuation to isolate the dipolar component of the multipole distribution was not feasible.

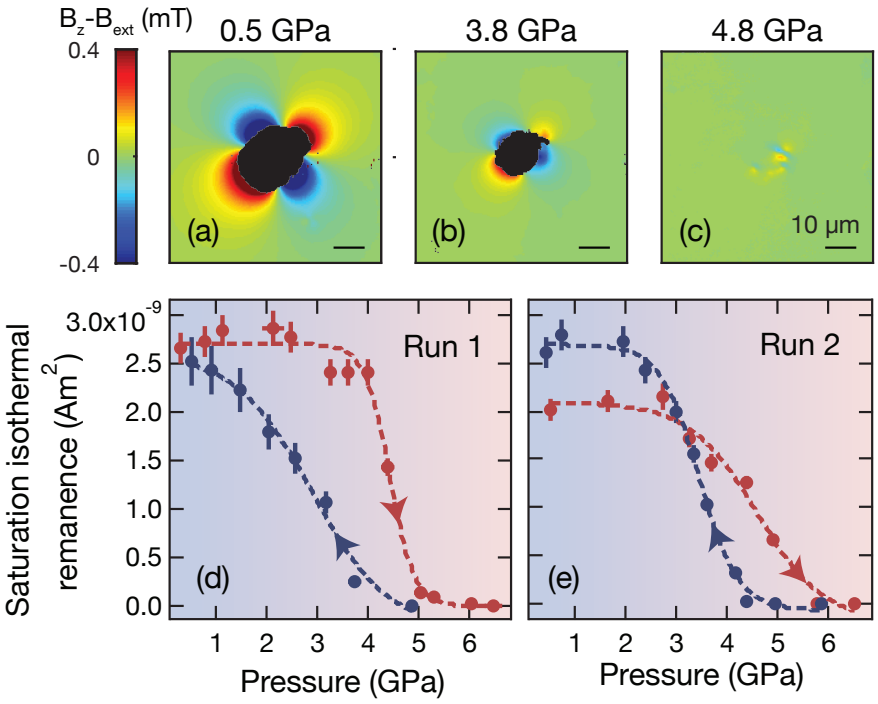

Figure 4.2: Magnetic sensing at high pressure. (a)-(c) Magnetic maps of the stray field produced by the pyrrhotite sample under pressure and an applied field, $B_{\text{ext}} \sim 50$ G. Maps correspond to the field projection along a particular (100) crystallographic orientation, which is 54° from the culet normal direction. Black pixels correspond to areas where the NV response is indeterminate due to exceedingly large field gradients. As pressure increases, the stray fields produced by the sample are diminished, corresponding to a reduction in the SIRM. (d)-(e) Measured SIRM at room temperature under both compression (red dashed lines) and decompression (blue dashed lines).

A few remarks are in order. Firstly, the hysteresis between the critical pressures observed under compression and decompression is the hallmark of a first-order magnetic transition and suggests coupling to a structural phase transition.[6] We note that a structural transition was previously reported in x-ray diffraction measurements at a commensurate pressure (6.2 GPa); future studies performing simultaneous NV and x-ray diffraction measurements may help elucidate whether these two transitions relate to each other [172, 322]. The presence of a structural transition would also be consistent with the observed variation in transition widths under compression and decompression, as well as from run to run; the detailed evolution of high pressure structural phase transitions is known to be sensitive to the distribution of

[6] As a point of nomenclature, we note that this pressure hysteresis under compression/decompression is distinct from the phenomenon of magnetic hysteresis under magnetic field reversal.

Run number	M_0 (10^{-9} Am^2)	P_c (GPa)	ΔP (GPa)
1 (compression)	2.71 ± 0.06	4.45 ± 0.05	0.24 ± 0.05
1 (decompression)	2.6 ± 0.2	2.9 ± 0.2	0.7 ± 0.2
2 (compression)	2.1 ± 0.1	4.6 ± 0.2	0.7 ± 0.2
2 (decompression)	2.70 ± 0.05	3.45 ± 0.04	0.38 ± 0.04

Table 4.1: Summary of SIRM data

normal and shear stresses, which varies over the course of the experiment due to plastic deformation of the sample and gasket [26]. Secondly, we note the transition widths are much sharper than in previous static high pressure measurements [277, 38, 36, 37, 119]. We attribute this to the unique ability to distinguish magnetism from a single grain; compared to measurements of powder samples that must average the magnetic response over both domain sizes and the stress distribution within the sample chamber, the single grain in this experiment is well-defined in size and experiences significantly minimized stress gradients, thus sharpening the apparent transition. Thirdly, the observed critical pressure is notably higher than previous reports, which may be attributed to the crystallinity and phase purity of the sample; the absence of structural defects commonly enhances the pressure required to initiate phase transitions [199].

Finally, we demonstrate a method to image normal and shear stresses near the sample. While reconstruction of all six unique components of the stress tensor has been previously demonstrated at gigapascal pressure using NV centers, here we propose and demonstrate a truncated sensing protocol to measure a subset of these components entirely by reanalyzing magnetic measurements taken for the SIRM study [148]. We depict exemplary results in Figure 4.1(d) and 4.1(e) at $P_{\text{ruby}} = 5.8\,\text{GPa}$. The normal stress along the loading axis, σ_{ZZ}, is consistent with the independently determined pressure in the sample chamber (via ruby fluorescence) yet concentrated near the center of the sample. The shear stress, defined here as $\sigma_{\text{shear}} \equiv \sqrt{\sigma_{XZ}^2 + \sigma_{YZ}^2 + \sigma_{XY}^2}$, reveals distinct gradients from the loading stress despite the presence of a relatively soft pressure-transmitting medium.[7] The ability to image both normal and shear stresses with micron-scale resolution provides a detailed glimpse into the applied stress environment that may help elucidate the complex interplay between stress gradients and the microstructural evolution of high pressure phase transitions.

4.4 SIRM summary

We fit to a logistic function of the form:

[7] Due to an abuse of notation, the σ_{shear} defined here is a distinct quantity from that defined in Chapter 3.

$$M(p) = \frac{M_0}{1 + \exp\left(\frac{p - P_c}{\Delta P}\right)}, \tag{4.1}$$

where M is the magnitude of the SIRM, M_0 is the SIRM at zero pressure, P_c is the measured critical pressure, and ΔP is the transition width.

4.5 Truncated stress sensing protocol

4.5.1 Stress coupling

The NV coupling to stress has been previously stated in Section 1.1.4. We note that the basis vectors $\{\hat{x}, \hat{y}, \hat{z}\}$ ($\{\hat{X}, \hat{Y}, \hat{Z}\}$) correspond to an individual NV center's local frame (cubic crystal frame); in particular, $\hat{z}$ is oriented in the direction of the NV bond and determines the NV's quantization axis, and $\hat{x}$ is defined such that the xz-plane contains one of the carbon-vacancy bonds. In the diamond lattice, there are four possible quantization axes, i.e. $\hat{z} \in \{111, 1\bar{1}\bar{1}, \bar{1}\bar{1}1, \bar{1}1\bar{1}\}$ in crystallographic notation.

The stress maps presented in Fig. 4.1 are determined by measuring Π_z for the four distinct NV orientations. While these measurements alone are insufficient to reconstruct the full stress tensor, they allow us to uniquely determine the isotropic stress, $\sigma_{\text{iso}} \equiv \frac{1}{3}(\sigma_{XX} + \sigma_{YY} + \sigma_{ZZ})$, and the average shear stress, $\sigma_{\text{shear}} \equiv \sqrt{\sigma_{XZ}^2 + \sigma_{YZ}^2 + \sigma_{XY}^2}$. To see this, let us explicitly write Π_z with respect to the stress tensor in the *cubic frame* for the four NV orientations:

$$\begin{aligned}
\Pi_z^{[111]} &= \frac{1}{3}(2\alpha_1 + \beta_1)(\sigma_{XX} + \sigma_{YY} + \sigma_{ZZ}) + \frac{2}{3}(\beta_1 - \alpha_1)(\sigma_{XZ} + \sigma_{YZ} + \sigma_{XY}) \\
\Pi_z^{[1\bar{1}\bar{1}]} &= \frac{1}{3}(2\alpha_1 + \beta_1)(\sigma_{XX} + \sigma_{YY} + \sigma_{ZZ}) + \frac{2}{3}(\beta_1 - \alpha_1)(-\sigma_{XZ} + \sigma_{YZ} - \sigma_{XY}) \\
\Pi_z^{[\bar{1}\bar{1}1]} &= \frac{1}{3}(2\alpha_1 + \beta_1)(\sigma_{XX} + \sigma_{YY} + \sigma_{ZZ}) + \frac{2}{3}(\beta_1 - \alpha_1)(-\sigma_{XZ} - \sigma_{YZ} + \sigma_{XY}) \\
\Pi_z^{[\bar{1}1\bar{1}]} &= \frac{1}{3}(2\alpha_1 + \beta_1)(\sigma_{XX} + \sigma_{YY} + \sigma_{ZZ}) + \frac{2}{3}(\beta_1 - \alpha_1)(\sigma_{XZ} - \sigma_{YZ} - \sigma_{XY})
\end{aligned}$$

By inspection, the first term is constant for the four orientations, while the second term has a mean of zero (across the four orientations) and a constant variance. This leads to the following relations:

$$\bar{\Pi}_z = (2\alpha_1 + \beta_1)\sigma_{\text{iso}} \tag{4.2}$$

$$\delta\Pi_z = \frac{2}{3}|\beta_1 - \alpha_1|\sigma_{\text{shear}} \tag{4.3}$$

where $\bar{\Pi}_z$ and $\delta\bar{\Pi}_z$ are the mean and standard deviation of the four shifting parameters, respectively.

We note that the above relations can also be motivated from a symmetry perspective. In particular, as average quantities of the four orientations, $\bar{\Pi}_z$ and $\delta\Pi_z$ are invariant under any permutation of the four crystallographic axes, i.e. they belong to the A_1 irreducible representation of the T_d point group. Moreover, $\bar{\Pi}_z$ is a linear function of the stress components. At this order, the only combination of stress components that belongs to the A_1 irreducible representation is the isotropic stress, $\sigma_{XX} + \sigma_{YY} + \sigma_{ZZ}$. The remaining terms in $\delta\Pi_z$ are shear terms, which belong to the T_2 irreducible representation. At quadratic order, the only combination of these terms which belongs to A_1 irreducible representation, and hence can contribute to the variance $(\delta\Pi_Z)^2$, is $\sigma_{XZ}^2 + \sigma_{YZ}^2 + \sigma_{XY}^2$.

4.5.2 Stress measurement

To determine Π_z from all four NV orientations, we rely on the same external magnetic field used to measure the SIRM which spectroscopically distinguishes all eight NV resonances. The average spectroscopic position of each pair of resonances is taken to be $D_{\text{gs}} + \Pi_z$. This analysis neglects corrections due to transverse magnetic fields which are suppressed at linear order. From this, σ_{shear} is straightforwardly deduced by calculating the standard deviation of the four resonances, as derived in the previous section. To distinguish the normal stress along the loading axis, σ_{ZZ}, from the isotropic pressure, we fix σ_{ZZ} near the ruby microsphere to equal P_{ruby} (as expected for an ideal pressure-transmitting medium) and take the ratio $\sigma_{ZZ}/(\sigma_{XX}+\sigma_{YY})$ to be approximately constant over tens of microns, as observed in Ref. [148].

4.6 Conclusion

In summary, we report SIRM of $4C$ monoclinic pyrrhotite under multiple rounds of compression and decompression up to 6.5 GPa. To our knowledge, we report the first observation of pressure hysteresis in this mineral, indicating the presence of a first-order transition. The observed SIRM revival upon decompression stands in stark contrast to previous reports of irreversible SIRM loss and calls for a nuanced understanding in the interpretations of shock demagnetization. Specifically, while conventional wisdom holds that meteorites experiencing sufficiently large shock pressure will not retain remanence from pyrrhotite [278], we have demonstrated an SIRM counterexample to this mantra.

More broadly, we show that the magnetic sensitivity and imaging capability of the NV center combined with the gigapascal pressures of the DAC enables the exploration of geological phenomena previously inaccessible to existing techniques. In particular, the capability to perform magnetic imaging opens the door to the localization of micron-scale ferromagnetic sources in geological samples and their evolution under pressure.

Chapter 5

Electric Field Sensing Single Localized Charges

5.1 Introduction

In the previous Chapters, we utilized NV centers in diamond to explore the structural and magnetic properties of materials under pressure. Sensing these signals relies on an exhaustive understanding of the NV response to physics within the diamond itself. In this Chapter, we step away from *external* stimuli and turn our attention to the local *internal* environment surrounding our solid-state spin defects. This is especially germane to the case of defect ensembles which can exhibit a complex interplay between interactions, internal fields and lattice strain. We demonstrate that local electric fields dominate the magnetic resonance behavior of NV ensembles at low magnetic field. We introduce a simple microscopic model that quantitatively captures the observed spectra for samples with NV concentrations spanning over two orders of magnitude. Motivated by this understanding, we propose and implement a novel method for the nanoscale localization of individual charges within the diamond lattice; our approach relies upon the fact that the charge induces an NV dark state which depends on the electric field orientation.

A tremendous amount of recent effort has focused on the creation and control of nanoscale defects in the solid-state [8, 290]. The spectral properties of these defects often depend sensitively on their environment. On the one hand, this sensitivity naturally suggests their use as nanoscale quantum sensors of *external* signals. On the other hand, accurately quantifying these signals requires the careful characterization of *internal* local fields. Here, we focus on the NV center in diamond [85, 290]. The electronic spin associated with the NV center is sensitive to a broad range of external signals, from magnetic and electric fields to pressure, temperature and gyroscopic precession [226, 213, 324, 1, 98, 88, 89, 83, 196, 9]. Isolated single NVs have been used to explore phenomena in biology [290, 191, 228], materials science [194, 263, 95, 92, 130], and fundamental physics [336, 35, 144].

More recently, many-body correlations have emerged as a powerful resource for enhancing

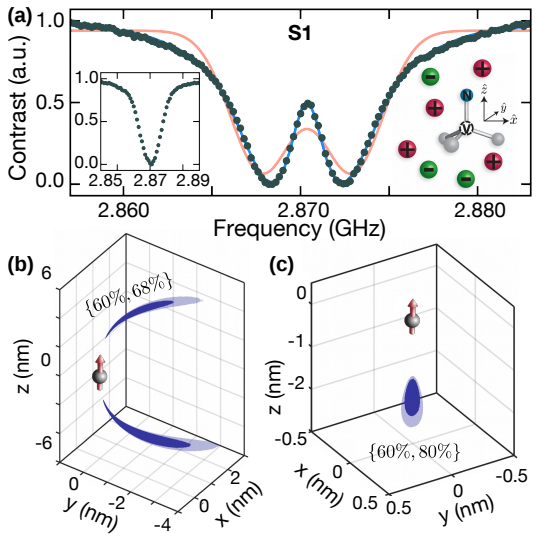

Figure 5.1: Typical optically-detected magnetic resonance (ODMR) spectrum of an electron-irradiated and annealed Type-Ib diamond sample (S1) at zero magnetic field. The spectrum exhibits heavy tails which cannot be reproduced by either a double Lorentzian or Gaussian (orange fit) profile. The blue theory curve is obtained via our microscopic charge model. (Left inset) A typical zero-field spectrum for a single NV center shows only a single resonance. (Right inset) Schematic depicting an equal density of positive (e.g. N^+) and negative (e.g. NV) charges, which together, create a random local electric field at each NV center's position. (b) Nanoscale localization ($\sim$5 nm) of a single positive charge via dark-state spectroscopy of an isolated NV center. The shaded regions indicate the probable location of the charge with darker indicating a higher likelihood. Percentages shown correspond to the confidence intervals of the dark/light region, respectively. (c) Analogous localization of a more proximal charge defect ($\sim$2 nm) for a different NV center.

the sensitivity of interacting spin ensembles [338, 299, 171, 51, 360]. To this end, a number of studies have explored and leveraged the properties of high-density NV systems [2, 309, 210, 1, 307, 265, 164, 25, 195, 163, 346, 27, 123]. The local environment in such systems is substantially more complex than that of isolated NVs; this arises from a competition between multiple effects, including: lattice strain, paramagnetic impurities, charge dynamics, and NV-NV dipolar interactions. While the presence of an applied external magnetic field can suppress some of these effects, it significantly limits the scope of sensing applications such as zero-field nuclear magnetic resonance spectroscopy [340, 319]. Thus, characterizing and understanding the spectral properties of NV ensembles at zero field is crucial to utilizing these systems as quantum sensors.

In this Chapter, we present three main results. First, we demonstrate that the characteristic splitting of the NV's magnetic resonance spectrum (Fig. 5.1a), observed in ensemble NV experiments [132, 191, 29, 88, 150, 112, 362, 298, 5, 190, 193, 44, 281, 161, 298, 223, 60,

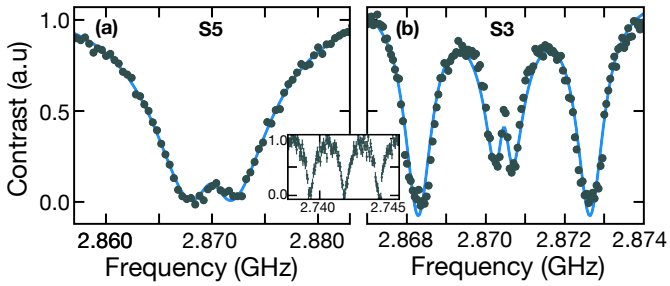

Figure 5.2: ODMR spectra at zero magnetic field for (a) a Type-Ib untreated diamond sample (S5) and (b) a Type-IIa electron-irradiated and annealed sample (S3). The spectra portray the two qualitative regimes one expects based upon the average electric field strength as shown schematically in the right panel of Fig. 5.3d. The blue theory curve is obtained via our microscopic charge model. (inset) The spectrum for S3 at a magnetic field ≈ 45 G exhibits three identical hyperfine resonances.

198, 308], originates from its local electric environment [215]; this contrasts with the conventional picture that strain dominates the zero-field properties of these systems. Second, we introduce a charge-based model (Fig. 5.1a, right inset) that quantitatively reproduces the observed ODMR spectra for samples spanning two orders of magnitude in NV density. Third, our model suggests the ability to directly *image* the position of individual charges inside the diamond lattice. To this end, we propose and implement a novel method that localizes such charges to nanometer-size volumes (Fig. 5.1b,c). The essence of our approach is to leverage the interplay between the polarization of the applied microwave field and the orientation of the local electric field.

5.2 Magnetic spectra of NV ensembles

The NV center has a spin triplet ground state ($|m_s = \pm 1, 0\rangle$), which can be initialized and read out via optical excitation and coherently manipulated using microwave fields [224]. In the absence of any external perturbations, the $|m_s = \pm 1\rangle$ states are degenerate and separated from $|m_s = 0\rangle$ by $D_{\rm gs} = (2\pi) \times 2.87$ GHz (Fig. 5.3a).

This leads to the usual expectation of a single resonance peak at $D_{\rm gs}$, consistent with experimental observations of isolated NVs (Fig. 5.1a, inset). However, for high-density NV ensembles, one observes a qualitatively distinct spectrum, consisting of a pair of resonances centered at $D_{\rm gs}$ (Fig. 5.1a, sample S1). This spectrum poses a number of puzzles: First, the line-shape of each resonance is asymmetric and cannot be captured by either a Gaussian or Lorentzian profile. Second, the central feature between the resonances is sharper than the inhomogenous linewidth. Third, despite the presence of a strong *splitting*, there exists almost no *shift* of the NV's overall spectrum.

These generic features are present in diamond samples with NV and P1 (nitrogen impu-

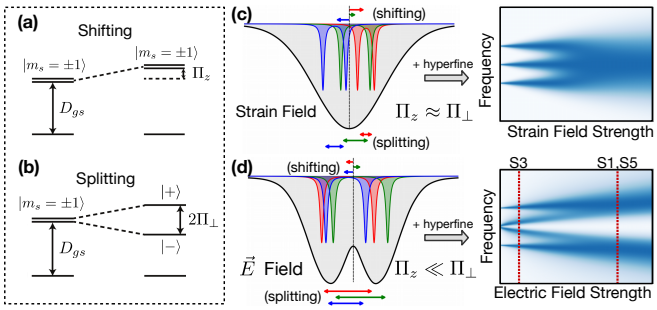

Figure 5.3: Both strain and electric fields lead to (a) shifting Π_z and (b) splitting $2\Pi_\perp$ of the $|m_s = \pm 1\rangle$ manifold. (c) When averaged over an ensemble of NV centers, random local strain fields lead to a single broad spectral feature (at large strain). (d) In contrast, random local electric fields lead to two distinct spectral regimes: at small electric fields, the center hyperfine resonance splits, leading to a total of four resolvable features (S3); at large electric field, one obtains the characteristic split resonance seen in typical high density NV ensembles (S1, S5).

rity) densities spanning over two orders of magnitude. Fig. 5.2 demonstrates this ubiquity. In particular, it depicts the spectrum for two other samples: one with a significantly lower NV concentration (Fig. 5.2a, sample S5) and a second with significantly lower concentrations for both NVs and P1s (Fig. 5.2b, sample S3). In this latter case, the P1 density is low enough that the hyperfine interaction between the NV's electronic spin and its host ^{14}N nuclear spin can be resolved. Normally, this hyperfine splitting would simply result in three identical resonances split from one another by $A_{zz} = (2\pi) \times 2.16$ MHz [301] (Fig. 5.2, inset). However, as shown in Fig. 5.2b, one finds that the central hyperfine resonance is split in direct analogy to the prior spectra.

The most distinct of the aforementioned features – a split central resonance – has typically been attributed to the presence of lattice strain [29, 88, 150, 112, 362, 298, 5, 190, 193, 44, 281, 161, 298, 223, 60, 198, 308]. Such strain can indeed lead to a coupling between the $|m_s = \pm 1\rangle$ states, and thus split their energy levels. However, a more careful analysis reveals an important inconsistency. In particular, given the measured strain susceptibility parameters [29], for each individual NV, any strain-induced splitting should be accompanied by a comparable shift of the overall spectrum (Fig. 5.3). Ensemble averaging then naturally leads to a spectrum that exhibits *only* a single broadened resonance (Fig. 5.3c).

5.3 Microscopic charge model

In contrast, we demonstrate that all of the observed features can be quantitatively explained via a microscopic model based upon randomly positioned charges inside the diamond lattice. The physical intuition underlying this model is simple: each (negatively charged) NV center

Sample	ρ_c (ppm)	ρ_{NV} (ppm)	ρ_s (ppm)	Γ (MHz)
Ib treated (S1)	1.35(5)	1-10	70(5)	1.16(2)
Ib treated (S2)	1.7(1)	1-10	100(5)	0.78(3)
IIa treated (S3)	0.06(2)	0.01-0.1	12(3)	0.26(2)
Ib untreated (S4)	3.6(4)	0.001-0.01	90(20)	1.0(1)
Ib untreated (S5)	0.9(2)	0.001-0.01	130(30)	3.3(1)
IIa untreated (S6)	0.05(1)	0.001-0.01	16(2)	0.08(3)

Table 5.1: Summary of the measured and extracted parameters for each diamond sample. ρ_c and Γ are directly extracted from our microscopic model, while ρ_s is independently measured at high magnetic fields and ρ_{NV} is estimated from fluorescence counts.

plays the role of an electron acceptor, and charge neutrality implies that there must be a corresponding positively charged electron donor (typically thought to be N^+, a positively charged P1 center).

Such charges produce an electric field that also (like strain) couples the $|m_s = \pm 1\rangle$ states, leading to the splitting of the resulting eigenstates. Crucially, however, the NV's susceptibility to transverse electric fields (which cause splitting) is $\sim$50 times larger than its susceptibility to axial electric fields (which cause shifting) [254, 41]. This implies that even upon ensemble averaging, the electric-field-induced splitting remains prominent (Fig. 5.3d).

Qualitative picture in hand, let us now introduce the details of our microscopic model. In particular, we consider each NV to be surrounded by an equal density, ρ_c, of positive and negative charges [1]. These charges generate a local electric field at the position of the NV center and couple to its spin via the Hamiltonian:

$$\begin{aligned} H =& \left(D_{gs} + \Pi_z\right) S_z^2 + \left(\delta B_z + A_{zz} I_z\right) S_z + \\ & \Pi_x (S_y^2 - S_x^2) + \Pi_y (S_x S_y + S_y S_x). \end{aligned} \tag{5.1}$$

Here, $\hat{z}$ is the NV-axis, $\hat{x}$ is defined such that one of the carbon-vacancy bonds lies in the x-z plane (Fig. 5.1a, right inset), $\vec{S}$ are the electronic spin-1 operators of the NV, $\vec{I}$ are the nuclear spin-1 operators of the host ^{14}N,[2] and δB_z represents a random local magnetic field (for example, generated by nearby paramagnetic impurities). Note that we absorb the gyromagnetic ratio into δB_z. The two terms $\Pi_{\{x,y\}} = d_\perp E_{\{x,y\}}$ and $\Pi_z = d_\parallel E_z$ characterize the NV's coupling to the electric field, $\vec{E}$, with susceptibilities $\left\{d_\parallel, d_\perp\right\} = \{0.35, 17\}$ Hz cm/V [254].

In order to obtain the spectra for a single NV, we sample $\vec{E}$ and δB_z from their random distributions and then diagonalize the Hamiltonian. Moreover, to account for the natu-

[1] We assume that the charges are independently positioned in three dimensions

[2] We note that the the hyperfine interaction in the Hamiltonian is obtained under the secular approximation.

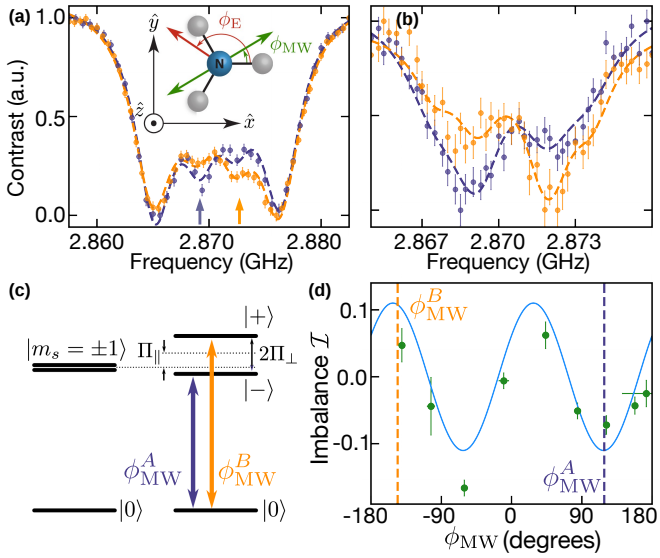

Figure 5.4: Charge localization via dark-state spectroscopy. (a) Single NV ODMR spectra (untreated Type-Ib diamond) for two different microwave polarizations, ϕ_{MW}, depicting the reversal of the split-peak imbalance. The data correspond to the localized charge shown in Fig. 5.1b. (inset) Top view through the NV-axis ($\hat{z}$), where ϕ_E and ϕ_{MW} are defined with respect to $\hat{x}$ (along a carbon-vacancy bond). (b) Analogous split-peak imbalance data corresponding to the localized charge shown in Fig. 5.1c. (c) By changing the microwave polarization, ϕ_{MW}, one can directly control the coupling strength between the $|0\rangle$ and $|\pm\rangle$ states. (d) Measuring the change in the imbalance as a function of ϕ_{MW} allows one to extract the orientation of the electric field. Dashed lines indicate the polarizations plotted in (a).

ral linewidth of each resonance, we include an additional Lorentzian broadening with full-width-half-maximum, Γ. Averaging over this procedure yields the ensemble spectrum. The distribution of $\vec{E}$ is determined by the random positioning of the aforementioned charges. The distribution of δB_z is determined by the local magnetic environment, which depends sensitively on the concentration of spin defects (Table 5.1).

In samples S1 and S5 (Type-Ib diamond), δB_z is dominated by the dipolar interaction with a high-density P1 spin bath, whose concentration, ρ_{s}, is independently characterized. Meanwhile, in sample S3 (Type-IIa diamond), the P1 density is over two orders of magnitude smaller, leading to a δB_z that is dominated by interactions with ^{13}C nuclei (with a natural abundance of 1.1%); despite this difference in microscopic origin, one can also characterize the effect of this nuclear spin bath using an effective density, ρ_s. For each sample, using this independently characterized ρ_{s}, we then fit the experimental spectrum by varying ρ_{c} and Γ . We find excellent agreement for all three samples (Fig. 5.1, 5.2) despite their vastly different defect concentrations (Table 5.1).

A few remarks are in order. First, the presence of local electric fields suppresses the

effect of magnetic noise when $\delta B_z \ll \Pi_\perp = \sqrt{\Pi_x^2 + \Pi_y^2}$. This is precisely the origin for both the sharpness of the inner central feature seen in Fig. 5.1a, as well as the narrowness of the inner hyperfine resonances seen in Fig. 5.2b. Second, in samples where the electric field dominates, the long-range, power-law nature of the electric field leads to a particularly heavy tailed spectrum. Third, the extracted charge density, ρ_c, is consistent with the estimated NV density, ρ_{NV}, for all "treated" (electron-irradiated and annealed) samples (S1-S3). This agrees with our previous physical intuition: NVs behave as electron acceptors while P1s behave as electron donors. Interestingly, this simple picture does not directly translate to "untreated" samples (S4-S6) where the observed charge density is significantly larger than ρ_{NV} (Table 5.1); one possible explanation is that such samples harbor a higher density of non-NV charged defects (e.g. vacancy complexes [73]).

5.4 Nanoscale imaging of a single charge

Our microscopic model suggests that in samples where one can resolve single NV centers, it should be possible to directly probe the *local* charge environment. However, one expects a key difference in contrast to ensemble measurements: for a single NV, the electric field has a definite orientation with respect to the NV axes (Fig. 5.4a diagram).

Crucially, this orientation (namely, the angle, ϕ_E, in the NV's transverse plane) dictates the way in which the electric field mixes the original $|m_s = \pm 1\rangle$ states into bright and dark states:

$$|\pm\rangle = \frac{1}{\sqrt{2}} \left(|m_s = +1\rangle \mp e^{-i\phi_E} |m_s = -1\rangle \right). \tag{5.2}$$

Applying a linearly polarized microwave field will then drive transitions between the $|m_s = 0\rangle$ state and the $|\pm\rangle$ states. However, the relative strength of the two transitions depends on both ϕ_E and the polarization of the microwave field, ϕ_{MW} (Fig. 5.4c). Thus, one generally expects the measured amplitudes of the corresponding resonances to be different. These expectations are indeed borne out by the data (Fig. 5.4a,b).[3] We note that this observed imbalance in the inner hyperfine resonances for a *single* NV is naturally averaged out in an ensemble measurement.

Our detailed understanding of this spectroscopy for a single NV suggests a novel method to extract the full vector electric field and to localize the position of the corresponding charge. In particular, by measuring the imbalance as a function of ϕ_{MW}, one can extract the electric field orientation, ϕ_E. More specifically, we define the imbalance, $\mathcal{I} \equiv \frac{A_+ - A_-}{A_+ + A_-}$, where $A_\pm$ are the amplitudes of the $|m_s = 0\rangle \leftrightarrow |\pm\rangle$ resonances and derive:

$$\mathcal{I} \sim -\cos(2\phi_{MW} + \phi_E). \tag{5.3}$$

Thus, $\phi_E = 124(5)^\circ$ can be extracted as the phase offset in Fig. 5.4d. In combination with the observed splitting and shifting of the inner resonances, $\Pi_z = 30(50)$ kHz, $\Pi_\perp = 650(10)$

[3] We measure the ODMR spectra of 68 single NV centers in an untreated Type-Ib sample, and find four that exhibit a significant electric-field-induced splitting with amplitude difference at zero magnetic field.

kHz, one can fully reconstruct the local electric field vector [343]. We do not observe any changes to this field over the course of the experiment (months) and find that it varies for different NV centers. This suggests that it originates from a stationary local charge environment. Moreover, charge neutrality and a low defect density suggest that the electric field is generated by a single positive charge, which we can then localize to within a nanoscale volume (Fig. 5.1b,c).

5.5 Materials and Methods

5.5.1 Sample details

The six diamond samples used in this work are all sourced from Element Six. Three of them have been treated (electron irradiation at Prism Gem and vacuum annealing) to increase NV density. The details are listed in Table 5.1.

5.5.2 Experimental apparatus

We conduct single and ensemble NV measurements in a scanning confocal microscope equipped with controllable magnetic field and microwave delivery (Fig. 5.5). A 532 nm laser beam (Coherent Compass 315M) shuttered by an acousto-optic modulator (AOM, Gooch & Housego AOMO 3110-120) is used for both ground state preparation and spin state detection. An objective lens focuses the beam to a diffraction limited spot size. We use an oil immersion objective lens (Nikon Plan Fluor 100x, NA 1.49) for resolving single NV centers or an air objective lens (Olympus LUCPLFLN, NA 0.6) for ensemble measurements. The combined action of an X-Y galvanometer (Thorlabs GVS212) and a $4f$ telescope provides the ability to scan the sample at the focal plane of the objective lens. A piezo mount for the objective lens serves to move the scanning plane in the longitudinal direction for depth scans.

The fluorescence photons collected by the objective lens are separated from the excitation beam path by a dichroic mirror (Semrock FF552-Di02). The coupling of the fluorescence beam to a single mode fiber serves as an effective pinhole for the confocal microscope. The fiber shuttles the fluorescence photons to a single photon counting module (SPCM, Excelitas SPCM-AQRH-64-FC) or avalanche photodiode (Thorlabs APD410A). We use a Data Aquisition card (DAQ) for fluorescence measurements and subsequent data processing (National Instruments USB 6343).

A microwave source (Stanford Research Systems SG384) in combination with a 16W amplifier (Mini-Circuits ZHL-16W-43+) serves to generate signals for spin state manipulation. For ensemble measurements, microwave signals are delivered using a coplanar waveguide (CPW) deposited on a coverslip. For single NV experiments, a 46 AWG magnet wire taped to a rotation mount (Thorlabs RSP05) is used (Fig. 5.5 inset). The magnet wire is adjusted to sit parallel to, and approximately 550 μm above, the focal plane of the objective lens. By rotating the wire using the mount, we effectively change the polarization of the microwaves

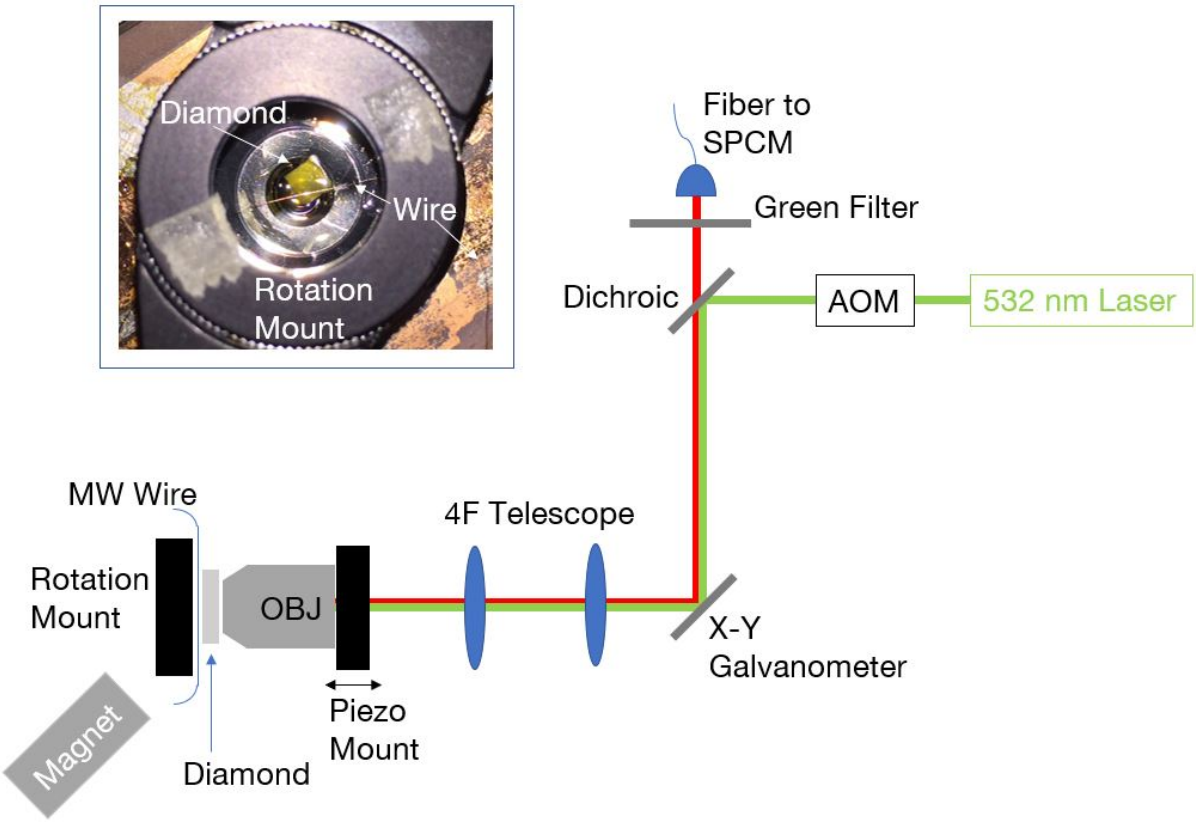

Figure 5.5: Experimental Apparatus: A 532 nm laser shuttered by an AOM light switch excites the NVs, both for state preparation and read-out. A $4f$ telescope permits the galvonometer to scan the surface of the diamond and a piezo-mounted objective controls the depth of the focal plane. The objective lens focuses the excitation beam and collects fluorescence. Microwave fields are delivered by a magnet wire (as pictured) or a coplanar waveguide. Inset: Magnet wire stretched onto an optical rotation mount hovers over the surface of the diamond

at the site of the single NV center of interest. The calculation of the polarization angle in the NV center frame is discussed later in the Section **Microwave Angle Projection**.

5.5.3 Pulse sequence for measuring magnetic resonance spectra of NVs

To measure the optically detected magnetic resonance (ODMR) spectra of NVs, we first use a 10 μs 532 nm laser pulse to initialize the spin triplet ground states to $m_s = 0$ (Fig. 5.6). After turning off the laser for 1 μs to allow the excited state population to decay, we apply a microwave π pulse and sweep its frequency. Our π pulse length is chosen as 2-6 μs for measurements on Type-Ib diamonds and 8-10 μs for Type-IIa diamonds to avoid power broadening. At the end, we apply another 10 μs laser pulse to detect the NV spin state by collecting the resulting fluorescence photons (Signal). In addition, we collect the photon counts at the end of the initialization laser pulse (Reference), and normalize the measured contrast.

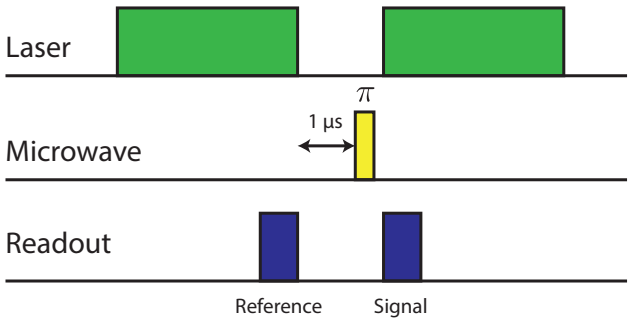

Figure 5.6: Pulse sequence for ODMR measurement.

5.5.4 Isolating single NVs

The diamond sample used for single NV experiments is sample S4 (untreated type Ib). We found a region of the sample where we could isolate single NVs as confirmed by a $g^{(2)}$ measurement (Fig. 5.7).

5.6 Charge model and ensemble spectrum

In this section, we provide additional details regarding our charge model. This includes an analysis of the electric and magnetic field distributions, as well as an explanation of our fitting procedure for the ensemble spectra and the estimation of error bars.

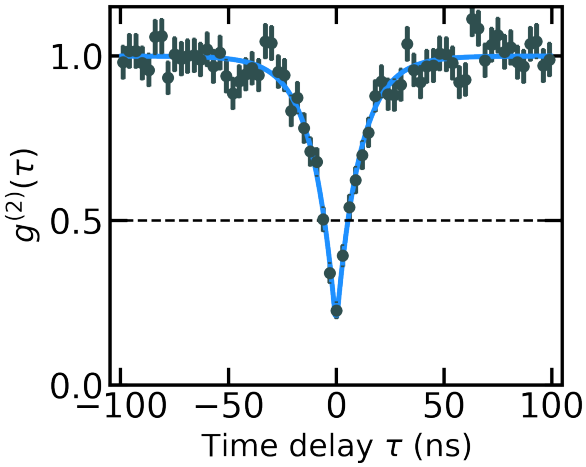

Figure 5.7: $g^2(\tau)$ measurement on NV1: the extracted $g^2(0) = 0.17^{+0.05}_{-0.03} < 0.5$ definitively confirms it is a single NV center.

5.6.1 Electric field distribution

In our model, we consider each NV to be surrounded by an equal density, ρ_c, of positive and negative point-like charges. We simulate the positions of these charges by randomly placing a large number ($N_{\text{charge}} \sim 100$) of points within a spherical volume. The radius of the sphere, R, is determined so that the average density of the charges matches ρ_c; in particular, this implies

$$R = \left(\frac{3}{4\pi} \frac{N_{\text{charge}}}{(2\rho_c) n_0} \right)^{\frac{1}{3}}, \tag{5.4}$$

where $n_0 = 1.76 \times 10^{-4}$ $(\text{ppm}\cdot\text{nm}^3)^{-1}$ is a conversion factor relating the number density (in ppm) to the volume density, and $2\rho_c$ is the combined density of positive and negative charges.

Based on the charge positions, we calculate the electric field at the center of the sphere (the NV's location):

$$\vec{E} = \sum_i \frac{q_i}{4\pi\epsilon_0\epsilon_r} \frac{\hat{r}_i}{r_i^2}, \tag{5.5}$$

where $\epsilon_r = 5.7$ is the relative permittivity of diamond[343], $|q_i|$ is the charge of an electron, and the sign of q_i is chosen to be positive or negative with equal probability. Sampling over the charge positions, $\{\vec{r}_i\}$, yields a distribution for $\vec{E}$. We are particularly interested in the transverse component, $E_\perp$, which couples ~ 50 times stronger to the NV, i.e. $\Pi_\perp = d_\perp E_\perp$. The probability distribution, $\text{P}(\Pi_\perp)$, for various densities is shown in Fig. 5.8. The peak of this distribution is approximately 0.56 $\text{MHz}/\text{ppm}^{2/3}$, where the scaling factor can be understood from dimensional analysis.

5.6.2 Magnetic field distribution

Our model further assumes that each NV is surrounded by magnetic impurities, which give rise to a local magnetic environment. For Type-Ib diamond, the dominant impurities are the electronic spins associated with P1 centers. For Type-IIa diamond, the leading contribution comes from the nuclear spins associated with ^{13}C (1.1% natural abundance).

In both cases, we model the effect of the magnetic impurities as a dipolar interaction between the NV and a bath of electronic spins $\left(s = \frac{1}{2}\right)$ at density ρ_s:

$$H_{\text{dipolar}} = \sum_i -\frac{J_0}{r_i^3}\left(3(\hat{S}\cdot\hat{r}_i)(\hat{P}_i\cdot\hat{r}_i) - \hat{S}\cdot\hat{P}_i\right). \tag{5.6}$$

Here $\{\vec{r}_i\}$ are the positions of the magnetic impurities, $\hat{S}$, $\hat{P}_i$ are the spin operators for the NV and impurities, respectively, and $J_0 = (2\pi)52$ MHz·nm^3. Under the secular approximation, this interaction further simplifies to

$$H_{\text{dipolar}} = \delta B_z\, S_z\ , \quad \delta B_z = \sum_i -\frac{J_0}{r_i^3}\left(3\hat{n}_i^z - 1\right) p_i\ , \tag{5.7}$$

where $\hat{n}_i^z = \hat{z}\cdot\hat{r}_i$, and $p_i = \pm 1/2$ are the spins of the magnetic impurities at the mean-field level.

A few remarks are in order. First, the interaction for nuclear spins is $\sim$ 2600 times weaker than J_0. Without loss of generality, we can account for this difference by treating

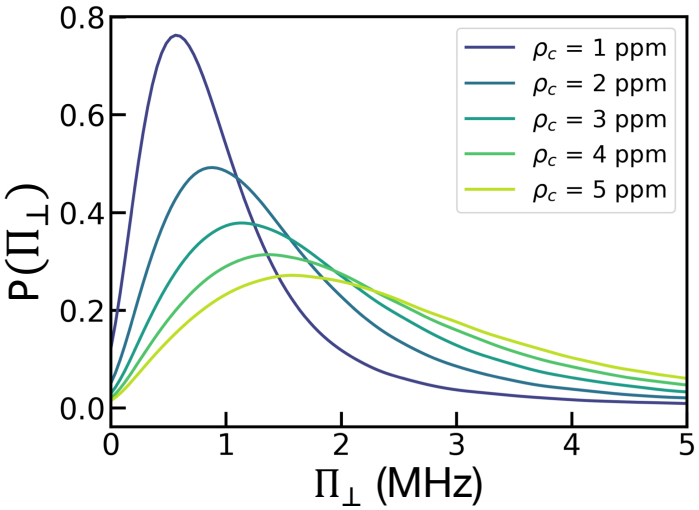

Figure 5.8: Distributions for the transverse electric field component, $\Pi_\perp = d_\perp E_\perp$, at various charge densities. The distributions were generated by the charge sampling procedure described in the text.

the nuclear spins as effective electronic spins with a rescaled density. This allows us to characterize the magnetic environment of all samples by the same parameter, ρ_s, regardless of whether the spins are nuclear or electronic. Second, the ^{13}C nuclear spins give rise to an additional interaction via the Fermi contact term [301]. Because directly accounting for this is difficult, we approximate its effect as an extra contribution to ρ_s. The resulting spectra are in quantitative agreement with the experimental data at high magnetic field (Fig. 5.9,5.10), validating this approximation.

Analogous to the random charges, we sample the positions of the magnetic impurities, $\{\vec{r}_i\}$, from a sphere whose radius matches the average spin density, ρ_s (Eq. 5.4). We further sample the spin configuration of the impurities from a uniform distribution, i.e. $\mathrm{P}(p_i = \frac{1}{2}) = \mathrm{P}(p_i = -\frac{1}{2}) = \frac{1}{2}$. Inserting $\{\vec{r}_i\}$ and $\{p_i\}$ into Eq. 5.7 allows us to calculate δB_z.

5.6.3 Fitting procedure and error estimation

Our fitting procedure for each ensemble sample consists of two steps. First, we fit a spectrum taken at high magnetic field, where the effects of electric fields are highly suppressed and the broadening is primarily due to magnetic noise (Figs. 5.9 and 5.10, left column). This allows us to independently characterize the magnetic spin density, ρ_s. Second, we fit a spectrum at zero applied field by taking into account the effects of both electric field and magnetic field noise. For these latter fits, we use the previously determined magnetic spin density ρ_s, but add additional free parameters for the charge density ρ_c and a natural linewidth Γ (Figs. 5.9 and 5.10, right column).

More specifically, we simulate the high-field spectra by sampling over the positions $\{\vec{r}_i\}$ and spins $\{p_i\}$ of the magnetic impurities. For each configuration, we calculate the NV's resonance frequencies using the full Hamiltonian of the system, Eq. 5.1. Repeating this procedure for ~ 5000 realizations, we obtain a histogram of resonance energies, which corresponds to an ensemble-averaged spectrum. We generate such spectra for a range of ρ_s and fit each to the high-field measurement. The free parameters for these fits are the center frequency, vertical offset, and overall amplitude. We characterize ρ_s by calculating the least-square residuals between our simulated spectra and the experimental data (Figs. 5.9 and 5.10, left column). In particular, we identify ρ_s that minimizes the residual as the best-fit parameter and estimate the error on this value as the range of ρ_s whose residuals lie within 10% of the minimum.

The fitting procedure for the zero-field spectra follows in close analogy, except we now average over both the charge distribution and the magnetic impurity distribution. In particular, we sample the positions of the charges and calculate the electric field at the NV center for over ~ 5000 realizations. For each charge realization, we then add magnetic noise by sampling over the positions and spins of the magnetic impurities and calculating the shift in resonance frequencies due to δB (additional ~ 5000 realizations). Lastly, we incorporate a natural linewidth for each resonance by convolving the distribution of resonance frequencies with a Lorentzian profile characterized by a full-width-half-maximum Γ. This linewidth accounts for broadening that is independent from the charge environment or static magnetic

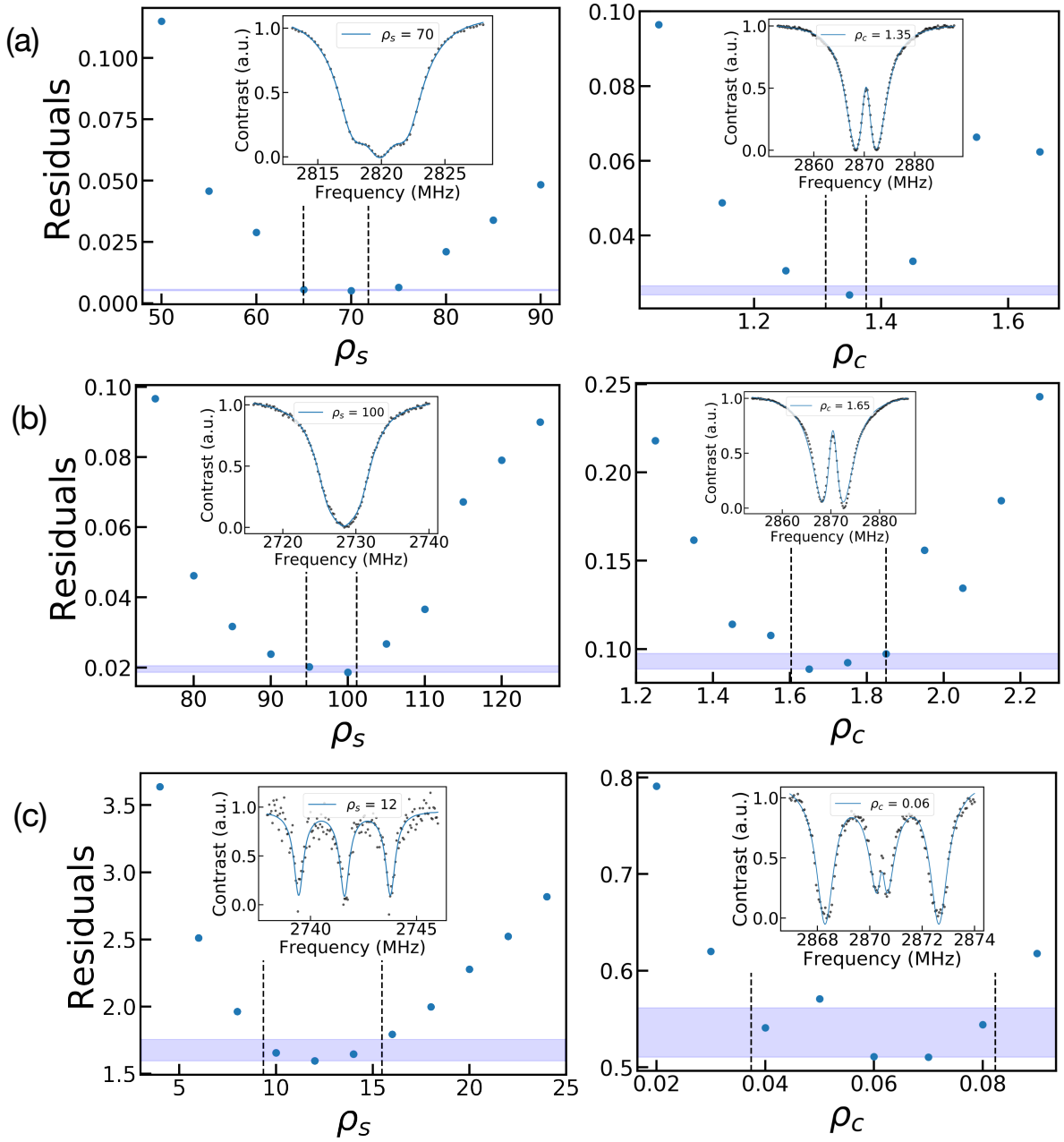

Figure 5.9: Ensemble fitting procedure applied to the treated samples: (a) Ib treated (S1), (b) Ib treated (S2), and (c) IIa treated (S3). The main plots show the least-square residuals as a function of ρ_s (left) and ρ_c (right) under large ($\sim$ 25-50 G) and zero applied field, respectively. We identify the best-fit values for ρ_s, ρ_c based on the minimum residual, and we estimate their error from the range of paremeters whose residuals lie within 10% of the minimum (blue shaded regions). The insets depict the best-fit spectra (blue curve), along with the experimental data (black points).

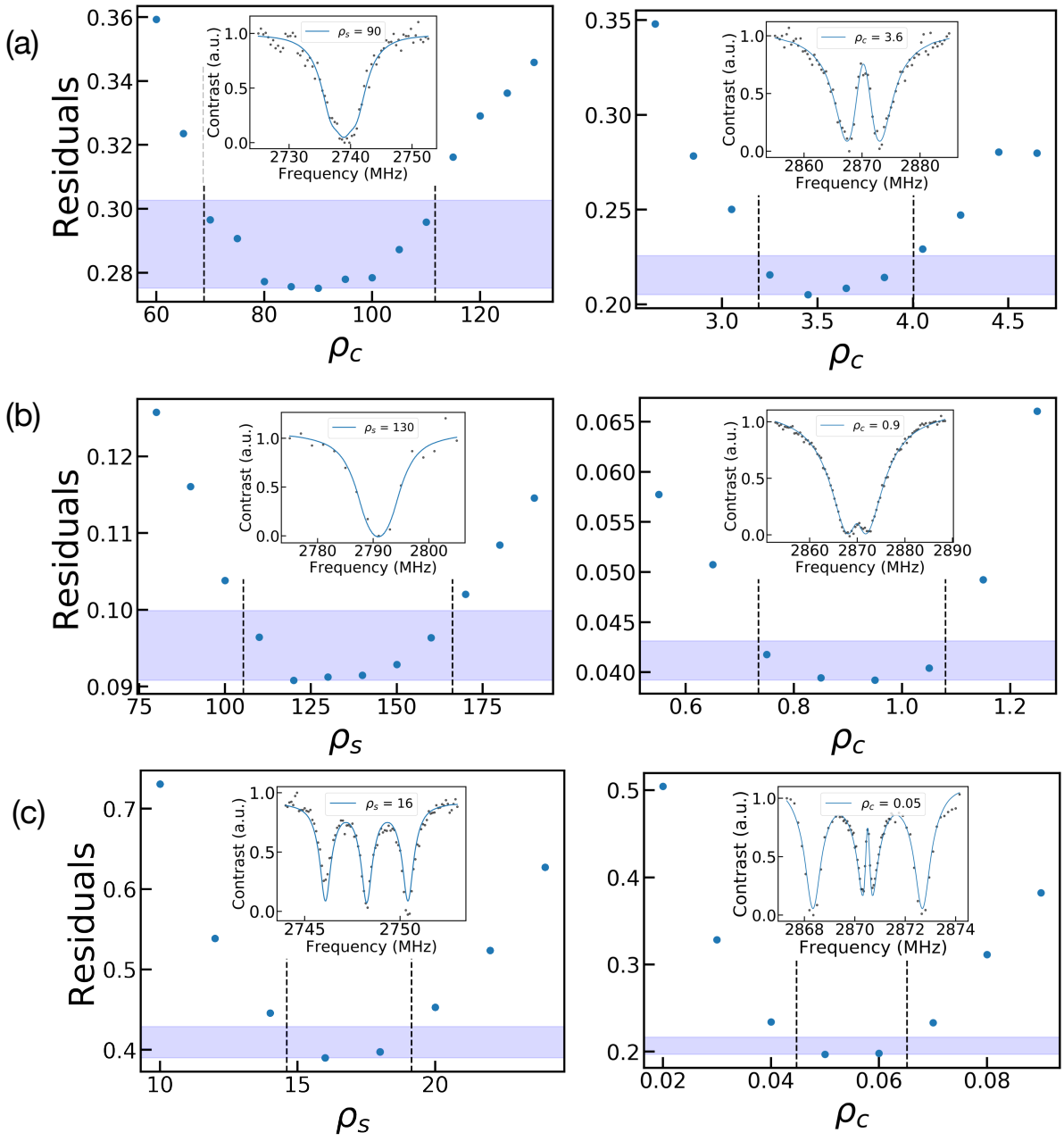

Figure 5.10: Fitting procedure applied to the untreated samples: (a) Ib untreated (S4), (b) Ib untreated (S5), and (c) IIa treated (S6). See caption of Fig. 5.9 for description.

fields. For example, it would include contributions from power broadening, fluctuating fields in the environment (i.e. $T_{2,\mathrm{echo}}$), and strain-induced broadening.

To characterize charge environment, we fit the zero-field spectra as a function of ρ_c while fixing the magnetic noise (ρ_s) from the results of the high-field measurements. For each value of ρ_c, we optimize with respect to the natural linewidth Γ, the center frequency, overall amplitude, and vertical offset. These results are shown in the right column of Figs. 5.9 and 5.10. As before, we estimate the error on ρ_c from the 10% interval of the residuals, while for Γ we take the standard error estimated by the fitting routine.

All simulated spectra agree quantitatively with the experimental data, and the extracted ρ_s, ρ_c and Γ are listed in Table 5.1. We note that for one of the six samples (S5), the linewidth contribution from δB_z is on the same order as Γ. Since we assume δB_z is the dominant source of noise in the high field spectra when extracting ρ_s, the magnetic impurity density for this sample may not be precise.

5.7 Charge localization using single NVs

In this section, we discuss the details associated with the charge localization based on a single NV. We consider the derivation of the imbalance and relate it to the electric field orientation and the microwave polarization. We note that the imbalance of the resonances is strong evidence for the presence of a nearby charge, as most other interactions would not modify the transition amplitudes differentially with respect to linearly polarized microwave fields.

To extract the position of the charge, we first calculate the polarization of the microwave field in the reference frame of the NV, ϕ_MW (Fig. 5.8a inset). By varying ϕ_MW, and measuring the imbalance one can directly extract the transverse orientation of the electric field ϕ_E. Combined with the observed splitting $2\Pi_\perp$ and shifting Π_z we can fully determine the local electric field vector and localize the corresponding charge. These procedures are detailed below.

5.7.1 Derivation of the Imbalance

In order to quantitatively extract the orientation of the electric field ϕ_E, we introduce the notion of imbalance as the difference in the weights of the resonances in the observed spectra. This imbalance $\mathcal{I}$ is directly related to ϕ_MW and the transverse orientation of the electric field ϕ_E.

We begin by focusing our attention to the states with ^{14}N nuclear spin $m_I = 0$ (two inner resonances). In the presence of an electric field, these states are described by the Hamiltonian:

$$H = (D_{gs} + \Pi_z)S_z^2 + \Pi_x(S_y^2 - S_x^2) + \Pi_y(S_xS_y + S_yS_x). \tag{5.8}$$

One finds that the electric field couples only the $|m_s = \pm 1\rangle$ states, leading to the new eigenstates:

$$|+\rangle = \frac{1}{\sqrt{2}}\left(|m_s = +1\rangle - e^{-i\phi_E}|m_s = -1\rangle\right) \tag{5.9}$$

$$|-\rangle = \frac{1}{\sqrt{2}}\left(e^{i\phi_E}|m_s = +1\rangle + |m_s = -1\rangle\right) \tag{5.10}$$

with energy splitting $2\Pi_\perp = 2\sqrt{\Pi_x^2 + \Pi_y^2}$.

The magnetic resonance spectrum is obtained by driving transitions from the $|m_s = 0\rangle$ state to the $|\pm\rangle$ states using a linearly polarized microwave field. The matrix elements associated with these transitions are

$$\mathcal{M}_\pm = \langle 0|\, S_x \cos\phi_{\mathrm{MW}} + S_y \sin\phi_{\mathrm{MW}}\, |\pm\rangle \tag{5.11}$$

$$= \frac{1}{2}\left[e^{-i\phi_{\mathrm{MW}}} \mp e^{i(\phi_E + \phi_{\mathrm{MW}})}\right] \tag{5.12}$$

where ϕ_{MW} is the direction of microwave polarization. This results in two resonances with amplitudes, $A_\pm \equiv |\mathcal{M}_\pm|^2$:

$$A_\pm = \frac{1}{2} \mp \frac{1}{2}\cos(2\phi_{\mathrm{MW}} + \phi_E). \tag{5.13}$$

By defining the imbalance $\mathcal{I} \equiv \frac{A_+ - A_-}{A_+ + A_-}$, we recover Eq. 5.2:

$$\mathcal{I} = -\cos(2\phi_{\mathrm{MW}} + \phi_E). \tag{5.14}$$

We note that the imbalance reverses direction for $\phi_{\mathrm{MW}} \to \phi_{\mathrm{MW}} + 90^\circ$ and that, for certain microwave angles, the amplitude of one resonance can fully vanish.

For completeness, we also derive the imbalance of the outer ^{14}N hyperfine states, which correspond to $m_I = \pm 1$. The derivation follows the same logic as above, except the Hamiltonian is now

$$H = (D_{gs} + \Pi_z)S_z^2 + \Pi_x(S_y^2 - S_x^2) + \Pi_y(S_xS_y + S_yS_x) \pm 2A_{zz}S_z. \tag{5.15}$$

The eigenstates $|\pm\rangle$ are split by $2\sqrt{A_{zz}^2 + \Pi_\perp^2}$. For $m_I = 1$, one finds

$$|+\rangle = \frac{1}{\sqrt{1+\xi^2}}\left(|+1\rangle - \xi e^{-i\phi_E}|-1\rangle\right) \tag{5.16}$$

$$|-\rangle = \frac{1}{\sqrt{1+\xi^2}}\left(\xi e^{i\phi_E}|+1\rangle + |-1\rangle\right) \tag{5.17}$$

where

$$\xi = \frac{A_{zz}}{\Pi_\perp}\left(\sqrt{1 + \left(\frac{\Pi_\perp}{A_{zz}}\right)^2} - 1\right) \tag{5.18}$$

An analogous expression holds for $m_I = -1$. In both cases, the amplitudes of the $|m_s = 0\rangle \leftrightarrow |\pm\rangle$ resonances are

$$A_\pm = \frac{1}{\sqrt{1+\xi^2}} \left(1 + \xi^2 \mp 2\xi \cos(2\phi_{\mathrm{MW}} + \phi_E)\right). \tag{5.19}$$

This leads to an imbalance:

$$\mathcal{I} = \frac{-2\xi \cos(2\phi_{\mathrm{MW}} + \phi_E)}{1+\xi^2}. \tag{5.20}$$

Thus, the imbalance of the outer resonances follows the same phase dependence as the inner resonances, but the maximum imbalance depends on the ratio $\Pi_\perp / A_{zz}$. In particular, in the limit $\Pi_\perp \gg A_{zz}$, $\xi \approx 1$ and a fully dark state is still possible; whereas, for $\Pi_\perp \ll A_{zz}$, the maximum imbalance is reduced to $\mathcal{I}_{\max} \approx \Pi_\perp / A_{zz}$.

The resulting dependence on ϕ_{MW} and ϕ_E does not change if we include the interaction with a nearby ^{13}C (within the secular approximation), since it interacts with the NV in a similar fashion to ^{14}N hyperfine.

5.7.2 Microwave Angle Projection

We define $(\hat{X}, \hat{Y}, \hat{Z})$ as our lab frame shown in Fig. 5.11a and the NV frame $(\hat{x}, \hat{y}, \hat{z})$ as shown in Fig. 5.1a left inset. These two frames are related by the crystallographic axes of the sample. We approximate the microwave delivery wire to be infinitely long, with an angle ϕ_{Wire} with respect to $\hat{X}$, and an in-plane distance r away from the NV. We extract ϕ_{Wire} and r from an image of the sample geometry (Fig. 5.5 inset). The height h of the wire's plane above the NV is assumed to be 550 ± 100 μm given the thickness of the diamond 500 μm, the wire diameter 40 μm, and an intentional air gap to avoid contact to the sample (~ 30 μm). The wire carries a current which generates a linearly polarized microwave field at the location of the NV (Fig. 5.11) whose transverse projection ϕ_{MW} drives the $|m_s = 0\rangle \leftrightarrow |\pm\rangle$ transition. ϕ_{MW} is fully determined by the values $\{\phi_{\mathrm{Wire}}, h, r\}$. To estimate error in each realization of ϕ_{Wire}, we use a Monte Carlo method assuming a $\pm 10^\circ$ tilting of the wire out of the plane.

5.7.3 Single Charge Localization

We search through 68 single NVs and find four exhibiting a significant imbalance in the zero-field spectrum consistent with a nearby charge, from which we analyze two in this work (referred to as NV1 and NV2). Because these spectra can also be affected by the presence of a nearby strongly-coupled ^{13}C, we apply a bias B_z field, which suppresses the effect of the electric field and identifies the source of the splitting. The zero- and high-field spectra for these two NVs are shown in Fig. 5.12. For NV1, we find three resonances spaced $\sim$2.16 MHz apart, a signal associated exclusively with ^{14}N hyperfine. In contrast, for NV2 we observe four resonances, indicating the additional presence of a strongly-coupled ^{13}C. We fit the spectrum of NV2 to extract the ^{13}C hyperfine coupling strength $\approx 1.65(7)$ MHz. To confirm the charge origin, we then measure the full imbalance curve using dark-state spectroscopy.

Sample name	Synthesis	[N] (ppm)	Electron irradiation dose	Energy (MeV)	Anneal temperature (°C)	Spectrum
Ib treated (S1)	HPHT	$\lesssim$200	2×10^{18} cm^{-2}	2	800	Fig. 5.9a, Fig. 5.1a
Ib treated (S2)	HPHT	$\lesssim$200	1×10^{17} cm^{-2}	14	400; 800; 1200	Fig 5.9b
IIa treated (S3)	CVD	$\lesssim 1$	1×10^{17} cm^{-2}	2	700; 875	Fig. 5.9c, Fig. 5.2a
Ib untreated (S4)	HPHT	$\lesssim$200	n/a	n/a	n/a	Fig. 5.10a
Ib untreated (S5)	HPHT	$\lesssim$200	n/a	n/a	n/a	Fig. 5.10b, Fig. 5.2b
IIa untreated (S6)	CVD	$\lesssim$1	n/a	n/a	n/a	Fig. 5.10c

Table 5.2: Details of all samples in this Chapter. All samples are sourced from Element Six. [N] is specified by the manufacturer.

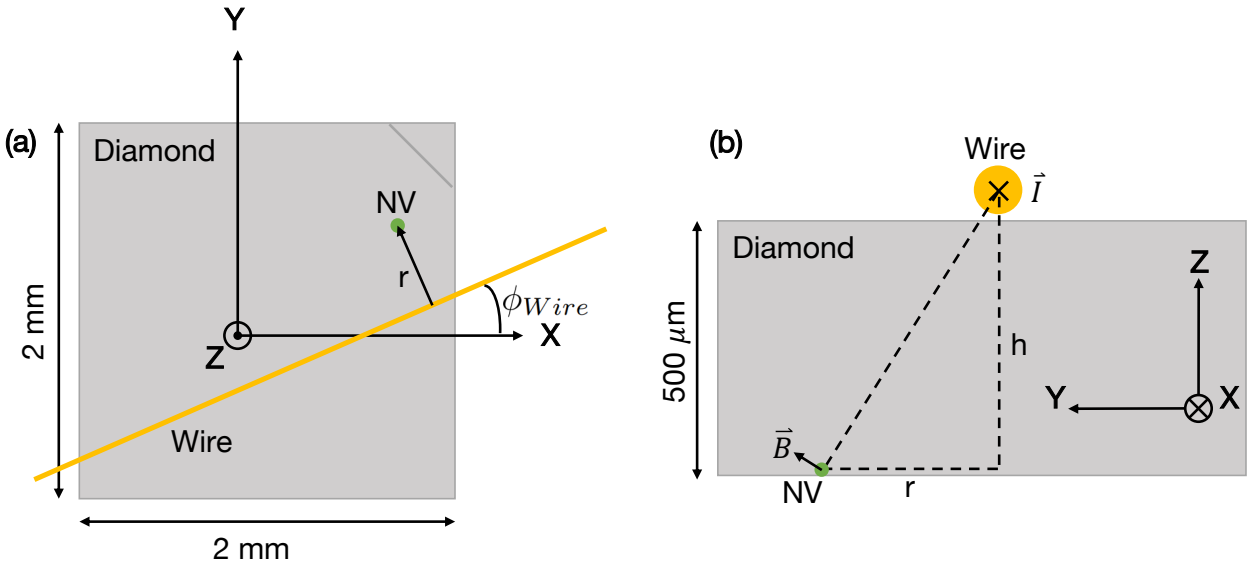

Figure 5.11: a) Top view of lab frame, $\hat{X}$, $\hat{Y}$, and $\hat{Z}$ axes are defined as shown. Wire is displayed at an angle ϕ_{Wire} relative to X, and r is the distance between the wire and the NV. b) Side view of lab frame. With $\phi_{\text{Wire}} = 0$, when the oscillating current $\vec{I}$ flows in the direction shown, we calculate the direction of the magnetic field vector $\vec{B}$ at a height h below the wire as shown.

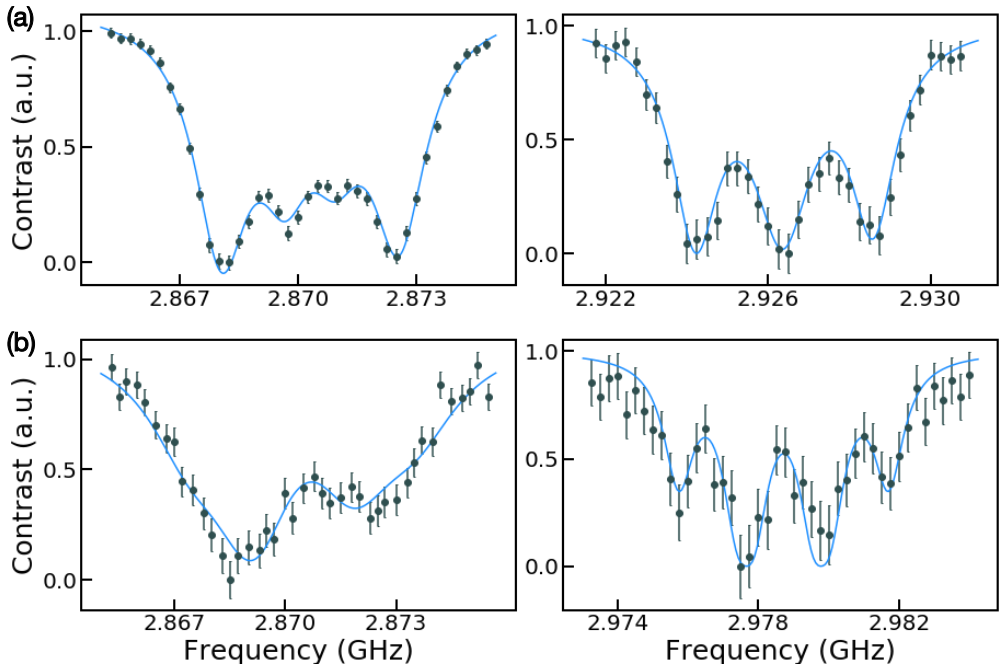

Figure 5.12: Spectra taken with and without a magnetic field applied along the NV z-axis. a) Left: zero-field spectrum for NV1 with microscopic model fit; Right: spectrum with an applied magnetic field and a fit to 3 Lorentzians. b) Left: zero-field spectrum for NV2 with microscopic model fit; Right: spectrum with an applied magnetic field. The fit function is two sets of three Lorentzians. The Lorentzians in each set are separated by the ^{14}N hyperfine splitting. The sets are split from each other by a fit parameter for the ^{13}C hyperfine interaction.

For NV1, we can clearly resolve the four resonances. The information about the imbalance is encoded into the amplitude of the inner two resonances. To estimate these amplitudes we measure only six spectral data points for each ϕ_{MW} (Fig. 5.13): two data points closely spaced at the location of each of the two inner resonances and two data points far from the resonances (measurement of the baseline contrast) . The imbalance extracted with this method is shown in Fig. 5.4d, from which we extract $\phi_E = 124(5)^\circ$.

For NV2, since we cannot clearly resolve the four resonances due to the presence of the nearby ^{13}C, we estimate imbalance by integrating the area on either side of the fit center frequency (Fig. 5.14 a). The imbalance curve is shown in Fig. 5.14b, from which we extract $\phi_E = 236(15)^\circ$.

We note that the amplitudes of these curves are much smaller than unity. This discrepancy from our simple theoretical model can also be explained by a few possibilities. First, our methods do not directly probe the weight of the transitions. Second, due to the intrinsic linewidth and power broadening, the inner and outer resonances overlap, which precludes

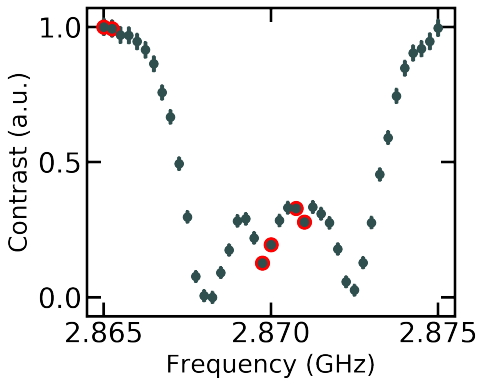

Figure 5.13: Position of the six frequencies (red) considered when computing the imbalance. Instead of measuring full-spectra, we take data points closely spaced at the location of each of the two inner resonances and two data points far from the resonances, so as to measure the baseline signal.

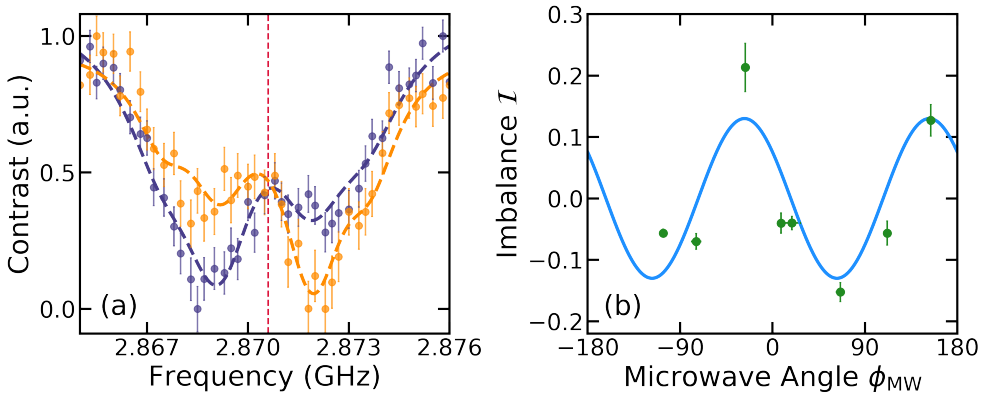

Figure 5.14: a) Two spectra from NV2 with fit from the microscopic model at different values of ϕ_{MW}. The dashed vertical line indicates the fit center frequency (2.8706 GHz). We estimate the imbalance by compare the integral on either side of the center frequency. b) Resultant imbalance sinusoid, from where we extract $\phi_E = 236(15)^\circ$.

isolating any single transition. Third, a dynamic charge bath may generate a background spectrum that is not included in our model.

In order to localize the charge, we also need to extract the charge-induced splitting $\Pi_\perp$ and shifting Π_z. In direct analogy to the treatment of ensembles, we fit the full zero-field single NV spectra using our microscopic model to extract these parameters as follows:

1. The spectra depend on five physical parameters: the three components of the electric field $\vec{E}$, the density of magnetic defects ρ_s, and the natural linewidth Γ. We also include a global amplitude scaling factor and background offset.

2. To account for the magnetic noise distribution, we follow a prescription similar to the previous magnetic field distribution section. We begin by considering the distribution of magnetic field for ρ_s which yields a probability distribution for measuring a particular value of δB_z. We then discretize over δB_z and for each possible value, perform steps 3-5. Each of the resulting spectra is weighted by the probability of measuring δB_z.

3. We solve the full Hamiltonian of the system (including ^{13}C and ^{14}N hyperfine interactions where applicable) to find the positions of the resonances.

4. We generate a spectrum by weighting each resonance by its transition amplitude with the $|m_s = 0\rangle$ state. We compute the wright by fixing the microwave direction in the $\hat{x}$ axis and computing $|\langle 0| S_x |\pm\rangle|^2$.

5. We broaden each resonance by a Lorentzian distribution with full-width-half-maximum of Γ.

6. We use a least-squares regression method on steps 1-5 over the seven fitting parameters, reproducing the experimental spectra.

Note, in order to determine Π_z, we use the ensemble-averaged $D_{\text{gs}} = 2870.25(5)$ MHz from the adjacent region of the same diamond containing a high density of NVs as a reference value (Figure 5.10a).

From the fits (Figure 5.4a,b) we extract the shifting and splitting due to the electric field:

$$\text{NV1:} \quad \Pi_z = (30 \pm 50) \text{ kHz} \quad , \quad \Pi_\perp = (650 \pm 10) \text{ kHz} \tag{5.21}$$

$$\text{NV2:} \quad \Pi_z = (270 \pm 70) \text{ kHz} \quad , \quad \Pi_\perp = (850 \pm 80) \text{ kHz} \, . \tag{5.22}$$

Using the susceptibilities [254], we extract the electric field vectors at the position of the single NVs:

$$\text{NV1:} \quad (E_x, E_y, E_z) = (-2.1 \pm 0.2, \ 3.2 \pm 0.2, \ 9 \pm 14) \text{ MV/m} \tag{5.23}$$

$$\text{NV2:} \quad (E_x, E_y, E_z) = (-2.8 \pm 1.1, \ -4.1 \pm 0.8, \ 77 \pm 20) \text{ MV/m} \, . \tag{5.24}$$

The parameters of the electric field uniquely determine the position of the positive single fundamental charge (Fig. 5.1b and 5.1c). The confidence intervals can be estimated using a Monte Carlo method.

5.8 Conclusion

While it is abundantly asserted in the literature that the zero-field spectral features of NV ensembles owe to lattice strain, here, we demonstrate that such spectra are in fact dominated by the effect of local electric fields. Using a microscopic charge model, we quantitatively capture the magnetic resonance spectra of NV ensembles for defect concentrations spanning two orders of magnitude. Moreover, we introduce a method to image the spatial location of individual charges near a single NV center with nanoscale precision.

These results open the door to a number of intriguing future directions. First, although we observe charge densities that are consistent with the NV density in all treated samples (and thus consistent with a picture for charge neutrality), we find a deviation from this understanding for untreated samples which exhibit an anomalously large charge density. Further study is necessary to reveal the precise nature of these additional charges [215]. Second, our results provide an improved understanding of NV ensembles at low magnetic fields; this is of particular relevance to the sensing of electric fields, lattice strain and gyroscopic precession, as well as to studies of magnetically sensitive quantum materials. Third, the charge-induced suppression of δB_z suggests the possibility of enhancing the NV's resilience to magnetic noise. Finally, understanding the local charge environment of single NV centers could provide insights into the optical spectral diffusion observed at low temperatures [63, 166]. In the next Chapter, we apply our model of the local charge environment from this Chapter to elucidate low temperature optical spectra and use this understanding to propose a high sensitivity electrometry protocol.

Chapter 6

Electric Field Sensing Proposals

6.1 Introduction

In the previous Chapter, we described the effect of the local charge environment on the NV center $^3A_2$ ground state. In this Chapter, we expand on this work in two directions: firstly, we extend our understanding to the ^3E excited state and show how this understanding naturally leads to an electric field sensing protocol with a hundredfold enhancement in sensitivity compared to state-of-the-art electrometers. Secondly, we theoretically propose an NV-based electric noise sensing protocol for polar and dielectric materials which provides unique information about their phases and collective excitations.

6.2 Electric field sensing using the ^3E excited state

Working with NV ensembles, we demonstrate that a detailed understanding of the *internal* electric field environment enables enhanced sensitivity in the detection of *external* electric fields. We follow this logic along two complementary paths. First, using excitation tuned near the NV's zero-phonon line, we perform optically detected magnetic resonance (ODMR) spectroscopy at cryogenic temperatures in order to precisely measure the NV center's excited-state susceptibility to electric fields. In doing so, we demonstrate that the characteristically observed contrast inversion arises from an interplay between spin-selective optical pumping and the NV centers' local charge distribution. Second, motivated by this understanding, we propose and analyze a method for optically-enhanced electric-field sensing using NV ensembles; we estimate that our approach should enable order of magnitude improvements in the DC electric-field sensitivity.

The precision measurement of electric fields remains an outstanding challenge at the interface of fundamental and applied sciences [136, 169, 149, 79, 34]. Leading electric field sensors are often based upon nanoelectronic systems [292, 323, 170, 327], electromechanical resonators [65, 48], or Rydberg-atom spectroscopy [105, 102, 192]. While such techniques of-

fer exquisite sensitivities, their versatility can be limited by intensive fabrication, calibration or operation requirements.

More recently, quantum sensors based on solid-state spin defects have emerged as localized probes [23, 88, 317, 348], offering nanoscale spatial resolution and the ability to operate under a wide variety of external conditions [16, 324, 86, 197, 352, 148, 191, 290]. The spin sub-levels of such defects are naturally coupled to magnetic fields [317, 148, 187], but exhibit comparatively weak susceptibilities to electric fields [328]. To this end, a tremendous amount of effort has focused on developing techniques to improve spin-defect-based electrometry [88, 60, 237, 180, 103, 156, 19, 177, 17, 356].

Broadly speaking, these efforts can be divided into two categories: (i) leveraging orbital states (as opposed to spin states), which exhibit significantly stronger coupling to electric fields, or (ii) utilizing high-density ensembles, which enhances the sensitivity as $\sim 1/\sqrt{N}$, the standard quantum limit [121]. Each of these approaches, however, faces its own obstacles. In the first case, accurate measurements of the electronic susceptibilities have proven challenging due to the deleterious effects of local charge traps observed in single defect experiments [315, 3, 30, 282, 342, 250, 243, 247, 356, 52]. In the latter case, higher densities exacerbate inhomogeneous broadening, which can ultimately overwhelm any statistical improvement in sensitivity.

In this work, we propose and analyze a technique, inspired by atomic saturation spectroscopy, designed to mitigate these challenges [176, 289, 289]. In particular, we focus on dense ensembles of nitrogen vacancy (NV) color centers in diamond—a spin defect which can be optically polarized and coherently manipulated via microwave fields [85, 290]. The essence of our approach is to apply *resonant* optical excitation to polarize a subgroup of an inhomogeneously broadened ensemble, and to probe the ground-state properties of this subgroup using optically detected magnetic resonance (ODMR). In doing so, we observe an unusual spectral feature — inverted-contrast peaks [14, 13] — which are significantly narrower than the magnetic spectra obtained via conventional, *off-resonant* ODMR (Fig. 6.1); crucially, this feature reveals an underlying correlation between the excited- and ground-state energy levels, which arises from the presence of internal electric fields within the diamond lattice [241, 42, 184].

Investigating these correlations yields three main results. First, we develop a microscopic model for the charge-induced, electric field environment that quantitatively reproduces all features of the resonant ODMR spectra [Fig. 6.1(a)]. Second, we demonstrate the first zero-field, *ensemble*-based method to determine the NV's excited-state susceptibilities, yielding the transverse and longitudinal susceptibilities as $\chi_\perp^{\mathrm{e}} = 1.4 \pm 0.1$ MHz/(V/cm) and $\chi_\parallel^{\mathrm{e}} = 0.7 \pm 0.1$ MHz/(V/cm), respectively. Third, based on our microscopic insights, we propose and analyze an electrometry protocol that combines resonant optical excitation [13] with the excited-state's strong electric-field susceptibility to enable a significant improvement in expected sensitivity. In particular, at low temperatures ($\lesssim 45$K) we estimate a DC sensitivity of $\eta \approx 1.3 \pm 0.3$ mV/cm/$\sqrt{\mathrm{Hz}}$, representing a two order of magnitude improvement compared

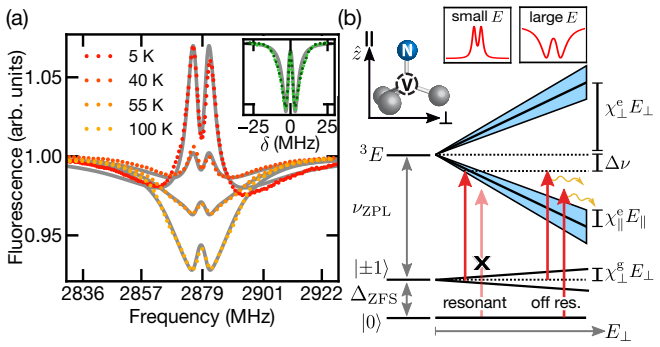

Figure 6.1: (a) Resonant ODMR at varying temperatures with drive detuning $\Delta\nu \approx 156$ GHz below the ZPL. For $T \lesssim 45$ K, where the optical transition linewidth is smaller than $\Delta_{\rm ZFS}$ [114], we observe the emergence of sharp positive-contrast peaks [14]. Our numerical charge-based model (gray lines) quantitatively reproduces the experimental spectra. (Inset) The lineshape of the off-resonant ODMR as a function of δ, the microwave detuning from $\Delta_{\rm ZFS}$, at room temperature (dark green) and 5 K (light green) exhibits no temperature dependence. Resonant and off-resonant ODMR were performed at 0 magnetic field. Error bars are smaller than the marker size. (b) NV level structure in the presence of internal electric fields. The wavelength of the ZPL transition is approximately 637.2 nm, and resonant (off-resonant) ODMR is performed with an excitation wavelength of $636 - 639$ nm (532 nm). The perpendicular field, $E_\perp = \sqrt{E_x^2 + E_y^2}$, splits the ^3E manifold, while the parallel field, $E_\parallel = E_z$, shifts it (shaded blue region); the ^3E fine structure (not shown) is much smaller than these effects. Only perpendicular fields, which split $|m_s = \pm1\rangle$ by $\chi^{\rm e}_\perp E_\perp$, strongly affect the ground state [328]. Internal electric fields determine whether a given NV is: (i) *resonantly* driven (favored at small E), resulting in positive-contrast peaks, or (ii) *off-resonantly* driven (favored at large E), resulting in a negative contrast ODMR lineshape.

to the best known NV methods [60].[1]

6.2.1 Inverted ODMR contrast

6.2.1.1 Overview

The NV center hosts an electronic spin-triplet ground state, where, in the absence of perturbations, the $|m_s = \pm1\rangle$ sublevels are degenerate and sit $\Delta_{\rm ZFS} = 2.87$ GHz above the $|m_s = 0\rangle$ state [Fig. 6.1(b)]. In high-density NV ensembles, this degeneracy is lifted most strongly by the local charge environment which directly couples the $|m_s = \pm1\rangle$ sublevels; this leads to

[1]We would also like to point out that our protocol's *DC* sensitivity compares favorably to the best reported NV-ensemble based *AC* sensing method [237]. In particular, assuming equal illumination volumes, our DC sensitivity is one order of magnitude better than the AC sensitivity reported in [237] (e.g. the adjusted AC sensitivity of [237] for an illumination volume of $\sim 0.1\text{mm}^3$ would be $10\text{mV/cm}/\sqrt{\text{Hz}}$).

typical ground-state ODMR spectra which exhibit a pair of heavy-tailed resonances centered around Δ_{ZFS} [inset, Fig. 6.1(a)] [241].[2]

Such ODMR spectra are usually obtained using continuous-wave *off-resonant* optical excitation, in which the NV center is initialized and read out with laser frequency detuned far above the zero-phonon line (ZPL), ν_{ZPL} [Fig. 6.1(b)]. During such off-resonant excitation, the $|m_s = \pm 1\rangle$ states fluoresce less brightly than the $|m_s = 0\rangle$ state. Moreover, in the absence of microwave excitation, the NV population accumulates in the $|m_s = 0\rangle$ state, owing to the spin-selective branching ratio of the singlet-decay channel. Applying resonant microwave excitation thus drives the population from the (brighter) $|m_s = 0\rangle$ state to the (dimmer) $|m_s = \pm 1\rangle$ states. This leads to the typically observed negative-contrast ODMR feature [inset, Fig. 6.1(a)]. We note that for off-resonant driving, identical spectra are observed at both room temperature and cryogenic conditions [inset, Fig. 6.1(a)].

In contrast, continuous-wave ODMR spectra taken with an optical drive near resonance with the ZPL exhibit a marked temperature dependence characterized by two principal features [Fig. 6.1(a)]. Most prominently, for temperatures $\lesssim 45$ K, the resonances *invert*, becoming a pair of narrow, positive-contrast peaks [14]. The entire spectrum, however, does not invert: Rather, these sharp peaks sit inside a broad envelope of negative contrast which is relatively temperature independent.

To understand the coexistence of these features, one must consider the interplay between resonant optical pumping and the local charge environment [14, 241]. Under resonant optical excitation, only one of the ground-state sublevels is driven to the excited state [Fig. 6.1(b)], while the other sublevels are optically dark and hence accumulate population. Microwave excitation drives population back into the resonant sublevel, leading to an increase in floures-cence — i.e. a positive-contrast ODMR feature [Fig. 6.2(a)]. This resonant pumping mech-anism is highly dependent on temperature: it can only occur if the thermally-broadened optical transition linewidth is smaller than Δ_{ZFS}, a situation that arises for $T \lesssim 45$ K [114].

The above picture is complicated by the presence of internal electric fields, which perturb the NV's excited-state energy levels, leading to a distribution of optical resonance conditions within the NV ensemble. In particular, perpendicular electric fields (relative to the NV axis) split both the excited-state manifold and the ground-state $|m_s = \pm 1\rangle$ sublevels [Fig. 6.1(b)].[3] Crucially, this *correlates* the optical resonance condition and the ground-state splitting. Indeed, for relatively small optical detunings (Fig. 6.1), the resonance condition is generally satisfied by NVs subject to weak local electric fields; hence, the positive-contrast feature

[2]Lattice strain effects have also been shown to lead to a split resonance in single NV centers [184]. However, typical strain fields result in *both* a shifting and splitting of the resonance. In ensembles, this naturally leads to a *single* broad peak instead of the observed split resonance [241]. In the case of electric fields, due to the large anisotropy between the transverse and longitudinal susceptibilities, local charges generically *split* the $|m_s = \pm 1\rangle$ sub-levels without significant *shifting*.

[3]We define a resonant configuration, at a given detuning, as a combination of transverse and longitudinal electric fields which cause the NV's ground to excited state transition to be resonantly driven by the optical excitation. Note that the resonance condition does not depend on the direction of the transverse component of the field in the plane perpendicular to the NV axis.

is relatively sharp and narrowly split. Meanwhile, the off-resonant pumping mechanism is more likely for NVs subject to large electric fields, resulting in a broad, negative-contrast background [Fig. 6.1(a)]. It is the superposition of these two features that gives rise to the unusual lineshapes observed in Fig. 6.1(a).

6.2.1.2 Microscopic model

Let us now turn our heuristic understanding into a quantitative microscopic model which takes into account: (*i*) the electric field distribution, (*ii*) the excited state resonance condition, and (*iii*) the ODMR lineshape for individual NV centers under resonant and off-resonant conditions.

To begin, we consider the internal electric field distribution $P(\vec{E})$ arising from randomly placed elementary charges at an overall density ρ. Physically, we expect these charges to consist primarily of the NV centers themselves (which are electron acceptors) and their corresponding donors — hence, $\rho \approx 2\rho_{\mathrm{NV}}$, where ρ_{NV} is the NV defect density [241]. As the angular distribution of $\vec{E}$ is fully symmetric, it suffices to consider the distribution for the electric field strength, $P(E)$. In Section 6.2.6, we demonstrate via Monte Carlo simulations that this distribution may be approximated by the analytic expression,

$$P_E(\tilde{E})\, d\tilde{E} = \frac{4\pi}{\tilde{E}^{5/2}} \exp\left\{-\frac{4\pi}{3\tilde{E}^{3/2}}\right\} d\tilde{E}. \tag{6.1}$$

Here, $\tilde{E} = E/E_{\mathrm{ref}}$ is a dimensionless electric field, where $E_{\mathrm{ref}} = (2\rho)^{2/3}/(4\pi\epsilon_0\epsilon_r)$ is approximately the electric field strength of the nearest charge, ϵ_0 is the vacuum permittivity, and ϵ_r is the relative permittivity of diamond, which we take to be 5.7 [39].

Second, we consider the optical resonance condition given by the energy levels of the ^{3}E excited state. In particular, we assume that electric fields, which couple directly to the orbital degree of freedom, dominate over hyperfine effects, including spin-orbit coupling and spin-spin interactions (see Section 6.2.10) [224]. It is thus sufficient to model the excited state as two branches (upper and lower) of states, whose energies relative to ν_{ZPL} are given by [224, 82]

$$\Delta\nu_{\mathrm{U,L}}(\vec{E}) = \chi^{\mathrm{e}}_{\parallel} E_{\parallel} \mp \chi^{\mathrm{e}}_{\perp} E_{\perp} \tag{6.2}$$

Note that in our notation positive detuning is *below* the ZPL. The resonance condition for a given NV center optically excited with a laser detuning $\Delta\nu$ is then given by the function,

$$D_R(\vec{E}, \Delta\nu) = [\Theta(\gamma_{\mathrm{e}}/2 - |\delta_{\mathrm{U}}|/2) + \Theta(\gamma_{\mathrm{e}}/2 - |\delta_{\mathrm{L}}|/2)] \tag{6.3}$$

$$\delta_{\mathrm{U,L}} = \Delta\nu - \Delta\nu_{\mathrm{U,L}}(\vec{E})\ , \tag{6.4}$$

where γ_{e} is the single-NV linewidth of the optical transition and Θ is the Heaviside step function. In particular, $D_R(\vec{E}, \Delta\nu)$ is 1 on resonance and 0 otherwise.

Finally, we model the ground-state ODMR of each *single* NV using a primitive lineshape. This lineshape, denoted $\Lambda(\omega; E_\perp)$, is parameterized by the perpendicular electric field $E_\perp$,

which determines the splitting between the $|m_s = \pm 1\rangle$ sublevels. It also incorporates two forms of broadening: (i) magnetic broadening arising from nearby spins (e.g. nitrogen defects and ^{13}C nuclear spins), and (ii) non-magnetic broadening, which includes microwave power broadening and strain. The explicit form of $\Lambda(\omega; E_\perp)$ is provided in Section 6.2.6.

Putting all this together, we now determine the *ensemble* resonant ODMR. This consists of two separate contributions. The first is due to resonantly driven NVs and is given by integrating over primitive lineshapes whose associated electric field matches resonance condition:

$$S_{\mathrm{R}}(\omega; \Delta\nu) = \int dE\ P(E) \int \sin(\theta) d\theta \Lambda(\omega; E_\perp) D_R(\vec{E}, \Delta\nu)\ , \tag{6.5}$$

where $\vec{E} = (E_\perp, E_\parallel) = (E\sin\theta, E\cos\theta)$. An analogous expression (see Section 6.2.6) describes the contribution due to off-resonantly driven NV centers. Adding these two cases together with a relative contrast factor, ϵ_C, yields the full spectrum:

$$S_{\mathrm{tot}}(\omega; \Delta\nu) = \epsilon_C S_{\mathrm{R}}(\omega; \Delta\nu) - S_{\mathrm{OR}}(\omega; \Delta\nu). \tag{6.6}$$

The sign of ϵ_C determines whether the resonantly driven NV centers exhibit positive or negative contrast, while its magnitude depends on the details of the resonant optical pumping mechanism.

Using the above model, we perform numerical simulations of both resonant and off-resonant ODMR spectra for a range of temperatures. While our simulations depend on several input parameters, the most physically relevant of these are constrained by independent analysis. In particular, we determine the charge density $\rho \approx 15 \pm 2$ ppm by fitting the *off-resonant* ODMR spectra to our charge-based model [inset, Fig. 6.1(a)] [241]; this suggests an NV density of $\rho_{\mathrm{NV}} \approx \rho/2 \approx 8$ ppm, which is consistent with prior density estimates for this sample [2]. In addition, as we discuss at length in the following section, we determine the excited state electric-field susceptibilities from independent measurements of resonant ODMR as function of optical detuning. The remaining temperature-dependent fit parameters, related to linewidth broadening and relative ODMR contrast, are provided in Section 6.2.9.

The resulting lineshapes shown in Fig. 6.1(a) are in excellent agreement with the experimental data across all temperatures. Notably, even at high temperatures where the striking positive-contrast peak is absent, the resonant experimental spectra remain qualitatively distinct from the off-resonant spectra, yet are correctly captured by our lineshape simulations.

6.2.2 Excited State Electric-field Susceptibilities

Interestingly, the correlation between the positive-contrast peaks and the optical resonance condition inspires a means of determining the *excited-state* electric-field susceptibilities from *ground-state* ODMR spectroscopy. In particular, as shown in Fig. 6.2(a), we perform ODMR measurements of the inverted-contrast feature as a function of the optical detuning. By

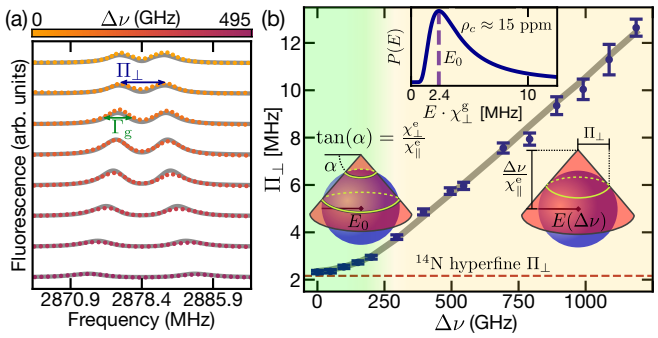

Figure 6.2: (a) Resonant ODMR spectra as a function of the detuning below ZPL, $\Delta\nu$, taken under a 20 G magnetic field perpendicular to the NV axis at 8 K. The positive-contrast peaks in the spectra are characterized by a splitting, $\Pi_\perp$, and a linewidth Γ_g. Gray lines correspond to our numerical model. Error bars are smaller than the marker size. (b) $\Pi_\perp$ as a function of $\Delta\nu$. In the small detuning region (light green), the highest-probability electric-field sphere (blue) intersecting the resonant cone (red) is of radius E_0 (in fact, the highest-probability electric-field sphere (i.e. that of radius E_0) will actually intersect the resonant cone twice, leading the to the expectation of *two* resonant peaks). However, the width of $P(E)$ around E_0 broadens these features, resulting a single, slightly asymmetric peak. In the large detuning region (light yellow), the radius of the highest-probability sphere that interesects the cone depends linearly on $\Delta\nu$. The red dashed line indicates the limit to $\Pi_\perp$ imposed by the hyperfine interaction. By fitting our numerical model to this data (gray line), we extract the excited-state electric-field susceptibilities. (upper inset) The probability distribution $P(E)$ exhibits a peak at E_0, which is determined by the charge density.

tracking how the splitting, $\Pi_\perp$, of the positive-contrast feature changes as a function of $\Delta\nu$, we fully determine the excited-state susceptibilities, $\chi^{\mathrm{e}}_\parallel$ and $\chi^{\mathrm{e}}_\perp$ [Fig. 6.2(b)]. At its core, this ability to independently extract the susceptibilities stems from the fact that Fig. 6.2(b) exhibits two distinct regimes: at small detunings, $\Pi_\perp$ exhibits a suppressed dependence on $\Delta\nu$, while at large detunings, $\Pi_\perp$ exhibits a linear dependence.

Let us now explain the origin of these two regimes. The splitting, $\Pi_\perp$, of the positive-contrast ODMR feature is controlled by: (i) the optical resonance condition and (ii) the distribution of electric fields. We focus on resonance with the lower branch, which is dominant resonant pumping mechanism for optical detunings below the ZPL (see Section 6.2.5). This resonance condition (equation (6.2)) can be rearranged to obtain

$$E_z - \frac{\Delta\nu}{\chi^{\mathrm{e}}_\parallel} = -\frac{\chi^{\mathrm{e}}_\perp}{\chi^{\mathrm{e}}_\parallel}\sqrt{E_x^2 + E_y^2}, \tag{6.7}$$

which defines a "resonant cone" in electric field space with apex at $E_z = \Delta\nu/\chi^{\mathrm{e}}_\parallel$ [Fig. 6.2(b)]. On the other hand, the electric-field distribution is spherically symmetric and peaked at a characteristic electric field, $E_0 \cdot \chi^{\mathrm{g}}_\perp \approx 2.4$ MHz, set by ρ [inset, Fig. 6.2(b)].

For a given detuning, this provides a geometric interpretation for determining the electric field configurations most likely to match the resonance condition; in particular, these config-

urations are set by the highest-probability sphere that intersects the resonant cone [yellow circles in Fig. 6.2(b)]. At small detunings, this sphere is always at radius E_0, implying that $\Pi_\perp \sim E_0$ can only weakly depend on the detuning. At large detunings, the sphere of radius E_0 no longer intersects the cone, and instead, the highest-probability intersecting sphere is the inscribed sphere [Fig. 6.2(b)]. The size of the inscribed sphere grows linearly with the detuning, and thus so does $\Pi_\perp$.

As a result of these two regimes, $\Pi_\perp(\Delta\nu)$ in Fig. 6.2(b) has both a slope, m_Π, and an elbow, at $\Delta\nu = \Delta\nu^*$. From this information alone, we can analytically estimate $\chi^{\mathrm{e}}_\parallel$ and $\chi^{\mathrm{e}}_\perp$. In particular, setting $\alpha = \tan^{-1}(\chi^{\mathrm{e}}_\perp/\chi^{\mathrm{e}}_\parallel)$ be the exterior angle of the resonant cone, we obtain

$$\sin(\alpha) = m_\Pi \cdot \Delta\nu^*/(E_0\chi^{\mathrm{g}}_\perp) \tag{6.8}$$

$$\frac{\chi^{\mathrm{e}}_\parallel}{\chi^{\mathrm{g}}_\perp} = \cos(\alpha)\Delta\nu^*/(E_0\chi^{\mathrm{g}}_\perp). \tag{6.9}$$

We estimate $\Delta\nu^* = 200$ GHz and $m_\Pi = 10^{-5}$ from Fig. 6.2(b) and $E_0\chi^{\mathrm{g}}_\perp = 2.4$ MHz from the off-resonant spectra [Fig. 6.1(b), inset]. This yields $\chi^{\mathrm{e}}_\perp \approx 1.2$ MHz/(V/cm) and $\chi^{\mathrm{e}}_\parallel \approx 0.8$ MHz/(V/cm).

To refine these estimates and corroborate our geometric interpretation, we simulate the full resonant ODMR lineshape as a function of optical detuning and fit the simulated $\Pi_\perp$ to the experimental data. Unlike the analytic estimates above, this model takes into account all resonant electric-field configurations. To perform the fits, we fix all parameters of our microscopic model except for the susceptibilities (see Section 6.2.7 for details). The best-fit susceptibilties are given by $\chi^{\mathrm{e}}_\perp = 1.4 \pm 0.1$ MHz/(V/cm) and $\chi^{\mathrm{e}}_\parallel = 0.7 \pm 0.1$ MHz/(V/cm) [gray line in Fig. 6.2(b)], which agree within error bars with the analytic estimates.

These results represent a refinement over previous measurements of the excited state susceptibilities via single NV Starks shifts, which are strongly distorted by photo-ionized charge traps [315, 3, 30]. In contrast, ensemble measurements appear to be insensitive to the effects of charge traps [328, 60, 237]; indeed, assuming their positions are random, charge traps would contribute to the effective charge density but would not systematically bias the ensemble Stark shift.[4]

Beyond allowing us to extract the susceptibilities, our numerical model fully reproduces the detuning-dependent experimental data [Fig. 6.2(a)]. In particular, the model quantitatively recovers two characteristic features of these spectra: a decrease in the overall fluorescence and an increase in the linewidth Γ_{g}, for increasing $\Delta\nu$. Physically, fluorescence declines with $\Delta\nu$ because the larger electric fields required for resonance are less likely. The dependence of Γ_{g} on $\Delta\nu$ is more subtle and is discussed in Section 6.2.8.

[4]We note, however, that photo-ionization effects could cause the charge density to depend on excitation wavelength, although we do not observe this in our measurements [3, 216].

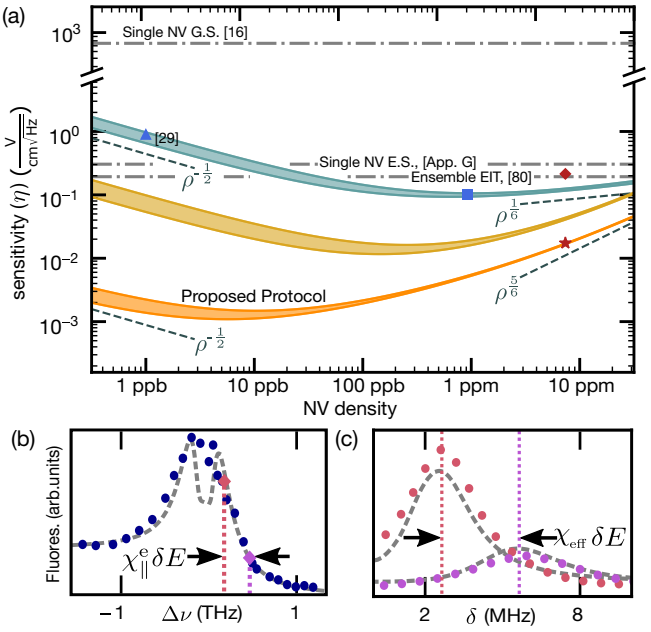

Figure 6.3: (a) Comparison of sensitivities for various NV-based DC electric field sensing methods. Teal region: estimated sensitivity using established NV ensemble electrometry techniques at an illumination volume of 0.1 mm^3. The light-blue triangle marks the sensitivity achieved in [60]; the light-blue square marks the optimal sensitivity for this method based on our scaling arguments. Additional demonstrations of NV electrometry include [237, 295, 147, 294, 203]. Orange (yellow) region: estimated sensitivity for our optically-enhanced protocol assuming an excited-state broadening of 10 GHz (100 GHz), an illumination volume of 0.1 mm^3 (0.015 mm^3), and a temperature of $\lesssim$ 45 K ($\lesssim$ 100 K). Red star (diamond): estimated sensitivity for our sample at low temperature (for the microwave-free variant of our protocol at 300 K). For our sample, we take the paramagnetic broadening to be the experimentally measured value $\sim$ 1.7 MHz (see Section 6.2.10). For all other other sensitivity estimates, we use a density-dependent model for the paramagnetic ODMR linewidth, assuming a natural abundance of ^{13}C [97, 28]. Dashed lines indicate asymptotic scaling of sensitivities. (b) Measured fluorescence as a function of $\Delta\nu$ (blue dots) and simulated fluorescence (dashed lines, see Section 6.2.10 for details). An external field of strength δE results in a change in overall fluorescence. (c) Measured peak shift of the resonant ODMR spectra (pink, purple dots) and simulated peak shift (dashed lines) for an external field of strength δE.

6.2.3 Optically Enhanced Electrometry

Our understanding of the interplay between internal electric fields and resonant excitation suggests a protocol for DC electric field sensing using NV ensembles. The protocol is premised on the fact that an external electric field parallel to the NV axis induces an overall shift of the excited-state levels. In effect, this is equivalent to changing the optical detuning, which we have already observed has two primary consequences: (i) it alters the splitting of the inverted-contrast peaks [Fig. 6.3(c)], and (ii) it changes the density of resonant configurations and therefore the overall fluorescence [Fig. 6.3(b)] [5].

To leverage these effects for electrometry, we propose the following protocol. First, apply a bias electric field parallel to one of the NV orientations to spectrally isolate its excited state.[6] Second, perform resonant ODMR with fixed laser detuning below the peak of the ZPL such that positive-contrast peaks are clearly observed. Because overall fluorescence decreases with detuning, the optimal choice is the *smallest* detuning such that the positive contrast peaks disperse linearly with an applied field [see Section 6.2.10, Fig 6.9(a)]. Finally, monitor the fluorescence at a fixed microwave drive frequency that maximizes the slope of the inner edge of one of the resonant ODMR peaks. Unless otherwise stated, we assume operating temperatures of $\lesssim 45$ K throughout our discussion, as required for the occurrence of positive-contrast peaks.

Unlike typical NV electric field sensing methods, our protocol is sensitive to fields *parallel* to the NV axis and insensitive to perpendicular fields. Intuitively, the insensitivity to perpendicular fields owes to the random orientation of internal electric fields. To illustrate this, consider the level shift induced by a small perpendicular field $\delta E_\perp$ oriented in the $\hat{x}$ direction and assume internal perpendicular fields are randomly oriented in the xy plane with strength E_0. The ensemble-average level shift, $\delta\nu$, of the lower branch is then given by

$$\delta\nu/\chi_\perp^{\mathrm{e}} = \frac{1}{2\pi}\int d\theta \sqrt{E_0^2 + \delta E_\perp^2 + 2\delta E_\perp E_0 \cos\theta} - E_0 \tag{6.10}$$

$$\sim O(\delta E_\perp^2/E_0), \tag{6.11}$$

which vanishes at leading order in $\delta E_\perp$.

We now evaluate the sensitivity of our protocol to parallel fields. We first estimate the sensitivity owing to the peak shift alone [317]:

$$\eta_\Pi = P_\Pi \frac{\Gamma_{\mathrm{g}}}{\chi_{\mathrm{eff}} C_0 C_{\mathrm{r}}} \cdot \frac{1}{\sqrt{R}}, \tag{6.12}$$

where Γ_{g} is the linewidth of the positive-contrast peak, $P_\Pi \approx 0.77$ is a numerical factor associated with the lorentzian lineshape, $C_0 \approx 0.21$ is the inherent ODMR contrast, R is the total photon count rate, and $C_{\mathrm{r}} \approx 0.55$ is the ratio of resonant fluorescence to total

[5] Interestingly, the first of these effects has also been explored in the context of a complementary MW-free magnetometry protocol [13]

[6] In Section 6.2.10, we show that the necessary fields are similar in scale to those required in [60].

fluorescence. Note that $\chi_{\text{eff}} \approx 0.41\chi_{\perp}^{\text{g}}$ is an effective susceptibility (right inset, Fig. 6.3) related to the slope of $\Pi_{\perp}$ with respect to $\Delta\nu$ [Fig. 6.2(b)]. Similarly, we estimate the sensitivity due to overall fluorescence variation:

$$\eta_{\text{F}} = P_{\text{F}} \frac{\Gamma_{\text{e}}}{\chi_{\parallel}^{\text{e}} C_{\text{r}}} \cdot \frac{1}{\sqrt{R}}, \tag{6.13}$$

where Γ_{e} is the linewidth of the optical transition and $P_{\text{F}} \approx 0.39$ is a numerical lineshape factor determined from experimental data (see Section 6.2.10). The change in fluorescence due to both these mechanisms may be combined, leading to an overall sensitivity: $1/\eta = 1/\eta_{\Pi} + 1/\eta_{\text{F}}$ (see Section 6.2.10).

For our current sample, one finds a sensitivity, $\eta = 18 \pm 4$ mV/cm/$\sqrt{\text{Hz}}$, assuming an illumination volume of 0.1 mm^3 [60]. This represents a 5× improvement over established NV electrometry techniques (Fig. 6.3). The enhancement in sensitivity derives primarily from three factors: (i) a larger photon count rate due to resonant scattering, (ii) an improvement in contrast, and (iii) the ability to constructively combine the signal from peak-shifting and fluorescence variation.

The sensitivity of our protocol can be further improved by optimizing the NV density. As in our numerical model, let us assume that the total charge density is twice the NV density. At low densities, η_{Π} and η_{F} are limited by the intrinsic broadening of resonant ODMR and the optical transition, respectively. By increasing density, both sensitivities improve according to the standard quantum limit, $\eta \propto 1/\sqrt{\rho_{\text{NV}}}$ — the usual motivation for performing ensemble sensing (Fig. 6.3). However, at sufficiently high densities, the broadening due to internal electric fields becomes larger than the intrinsic broadening and the sensitivity degrades (Fig. 6.3);[7] intuitively, this occurs because the NV ensemble is primarily sensing electric fields within the diamond lattice rather than the external signal. In particular, we show in Section 6.2.10 that the sensitivity degrades upon increasing density as $\eta \sim \rho_{\text{NV}}^{5/6}$ (Fig. 6.3). Conversely, the sensitivity improves rapidly upon decreasing density until one reaches the crossover density between the intrinsically-broadened and charge-broadened regimes.

Interestingly, this crossover density is naturally different for η_{Π} and η_{F}. In particular, the non-charge-induced broadening of the *ground-state* ODMR linewidth is often limited to $\sim$ 200 kHz by the ^{13}C nuclear spin bath (although isotopically purified samples can exhibit narrower linewidths, changing the crossover density; this is discussed in more detail in Section 6.2.10) [266, 24, 97]. This implies that η_{Π} is optimal at NV densities of $\sim$ 30 ppb. On the other hand, these same magnetic fields only weakly affect the excited state. Rather, the non-charge-induced broadening of the excited-state, whose origin is less well understood, has been empirically observed to be $\sim$ 10 GHz [31, 4].[8] This yields an optimal NV density

[7] Other perturbations to the NV level structure, such as strain and magnetic fields, can exacerbate ensemble broadening. For this discussion, we restrict attention to the ideal limit where there is minimal charge ($\rho_c = 2\rho_{\text{NV}}$) and there are no other significant density dependent sources of inhomogenous broadening.

[8] We emphasize that here we are referring to ensemble broadening; single NVs can exhibit nearly lifetime-limited excited state linewidths [332, 315, 71, 63]

for η_F of ~ 7 ppb.

Putting everything together, we obtain an optimal total sensitivity of $\eta = 1.3 \pm 0.3$ mV/cm/$\sqrt{\text{Hz}}$ at an NV density ~ 10 ppb (Fig. 6.3, Table 6.2). This represents a two order of magnitude enhancement compared state-of-the-art NV methods (though these do not require cryogenic temperatures [60]).

A few remarks are in order. First, while our sensitivity estimates assume an optically-thin sample, comparable sensitivities may be achieved at larger optical depths by monitoring, for example, transmission amplitude instead of fluorescence [4]. Second, monitoring resonant fluorescence variation alone via resonant excitation — without performing ODMR — already provides a significant electric field sensitivity, yielding a microwave-free version of our protocol. Since this microwave-free protocol does not require one to track the positive-contrast ODMR feature, it can also be applied at room temperature [Fig. 6.1(a)]. Assuming a thermally broadened linewidth of ~ 2 THz at 300 K yields a sensitivity of ≈ 300 mV/cm/$\sqrt{\text{Hz}}$ (Fig. 6.3); this is comparable to the best reported NV sensitivities at room temperature. Relatedly, our protocol may be extended to radiofrequency electrometry through Fourier analysis of the time-dependent fluorescence [297].

6.2.4 Experimental Setup

The experimental apparatus is illustrated in Fig. 6.4(a). A resonant (636-639 nm, 0.2 mW) or off-resonant (532 nm, ~ 1 mW) laser light is focused with a 0.5 numerical-aperture, 8 mm focal length aspheric lens onto the surface of a (111)-cut diamond housed in a continuous-flow cryostat (Janis ST-500). Fluorescence was collected using the same lens, spectrally filtered (within $650 - 800$ nm), and detected with a Si photodiode. Microwaves were delivered by a 75 μm diameter copper wire running across the surface of the diamond. The temperature was measured with a diode located at the base of the cryostat's sample holder.

The diamond used in this work, labeled S2 in [2], was grown under high-pressure-high-temperature conditions (HPHT) and initially contained ~ 100 ppm of substitutional nitrogen. It was then irradiated with 3 MeV electrons at a dose of 10^{19} cm^{-2} in order to produce a uniform distribution of vacancies, and subsequently annealed at 1050 °C for two hours in order to facilitate the formation of NV centers by mobilizing the vacancies. After this treatment, the sample contains ~ 16 ppm of NV^- and ~ 50 ppm of unconverted substitutional nitrogen or NV^0 based on ZPL intensity measurements [2]. We note that this estimate of the NV density is $\sim 2\times$ larger than that of the charge-based model (see subsection 6.2.1.2).

6.2.5 Detuning Above ZPL

Shown in Fig. 6.5 is the dependence of the resonant ODMR lineshapes for a wide range optical detunings. For drives below ZPL, the positive-contrast peaks are clearly visible and are described quantitatively by our microscopic model (see section 6.2.1). In contrast, for drives above ZPL, the positive-contrast peaks disappear with increasing detuning. We conjecture that this disappearance is related to the fact that the resonance condition is most

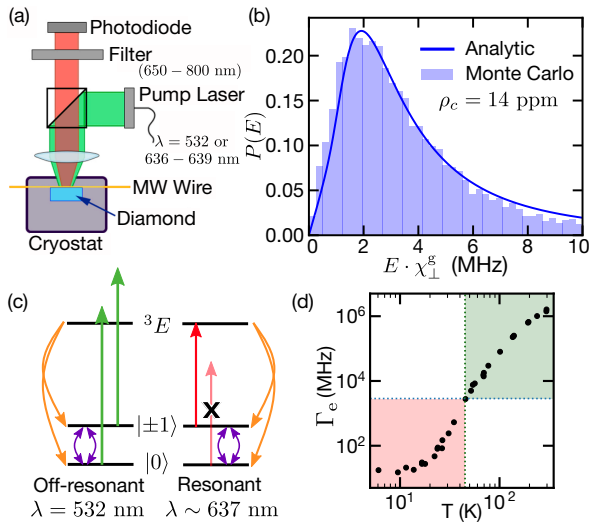

Figure 6.4: (a) Experimental setup. Both green and red lasers can be used for NV excitation. (b) Comparison of analytic (solid line) and Monte Carlo (histogram) models of $P(E)$. They are in close agreement, particularly near the peak of $P(E)$. (c) Off-resonant (left) and resonant (right) excitation schemes. Under resonant excitation, an effective dark state ($|0\rangle$ above) results in *increased* fluorescence on microwave resonance. (d) Optical transition linewidth (Γ_e) as a function of temperature. Data reproduced from [114]. In the green-shaded region, $\Gamma_e > \Delta_{ZFS}$ and no inverted contrast is observed; in the red-shaded region $\Gamma_e < \Delta_{ZFS}$ and resonant excitation yields inverted contrast ODMR.

likely to be met by the *upper branch* of the ^3E manifold at these detunings, but this branch is itself within the phonon-sideband of the lower branch. Hence, excited states of the upper branch will have shorter lifetimes than their lower branch counterparts, possibly rendering the linewidth of the associated optical transitions too large for the positive-contrast feature to emerge.

6.2.6 Additional Details of the Resonant ODMR Model

In this section, we elaborate on four aspects of our microscopic model of resonant ODMR. First, we demonstrate that the electric field distribution arising from randomly placed charges can be accurately modeled by the analytic expression equation (6.1). Second, we discuss the single-NV primitive lineshape, $\Lambda(\omega; E_\perp)$, used in our analysis. Third, we provide the explicit expression for the off-resonant contribution to the resonant ODMR lineshape, S_{OR}. Finally, we extend our model to account for the background fluorescence of resonant ODMR, yielding the prediction of Fig. 6.3(b).

Electric field distribution: At its core, our microscopic model proposes that the NV is affected by internal electric fields arising from randomly placed point charges in the diamond

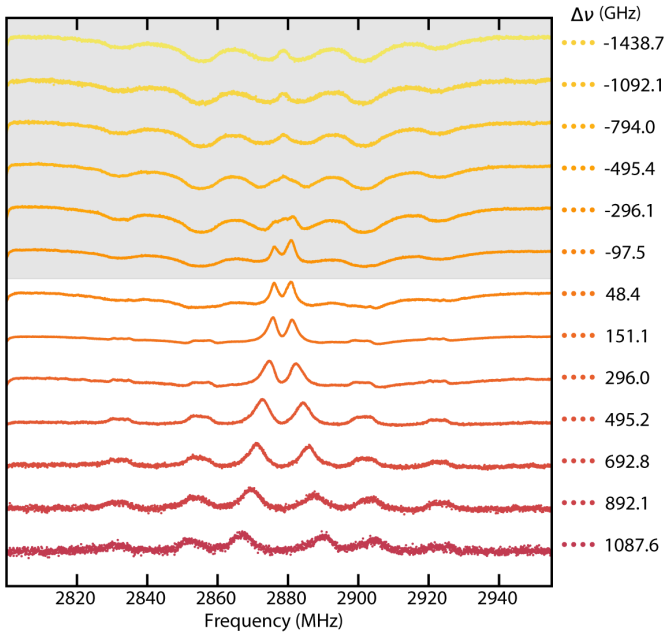

Figure 6.5: Resonant ODMR spectra at varying optical detuning; shaded background corresponds to detunings above ZPL, while white background corresponds to detunings below ZPL. The spectra were taken with a 20 G magnetic field applied in the plane of the (111)-cut diamond (i.e. perpendicular to one NV axis). Smaller peaks, split $\gtrsim 20$ MHz from the center frequency, correspond to microwave resonance with other NV groups. Other presentations of these spectra restrict focus to the central group at detunings below ZPL.

lattice. To determine the electric field distribution, we numerically sampled random spatial configurations for ~ 100 charges at a given density ρ and computed their net electric field at an arbitrary spatial point corresponding to the location of the NV. Empirically, we found that these Monte Carlo results were well approximated by Eq. (6.1), especially near the peak of the distribution, which is most relevant for our susceptibility analysis [Fig. 6.4(b)]. Incidentally, Eq. (6.1) corresponds to the electric field distribution owing to the nearest (single) charge at a renormalized density 2ρ; however, we consider this a mathematical coincidence. For our purposes, it is relevant only that Eq. (6.1) provides a convenient analytic expression to approximate the full electric field distribution generated by Monte Carlo simulations

Primitive lineshape: The single-NV ODMR lineshape Λ depends on an magnetic broadening parameter κ_{B}, arising from local magnetic fields, and a non-magnetic broadening parameter κ_0, due to microwave power broadening and strain. The difference between the two forms of broadening is that magnetic broadening adds in quadrature with the electric field splitting, while non-magnetic broadening is treated as an overall convolution. We model both forms of broadening as a Lorentzian distribution, where κ is the full-width-half-maximum (FWHM). Finally, we take into account the effective magnetic field, $\mu_B g_e B_{\mathrm{I}} \in$

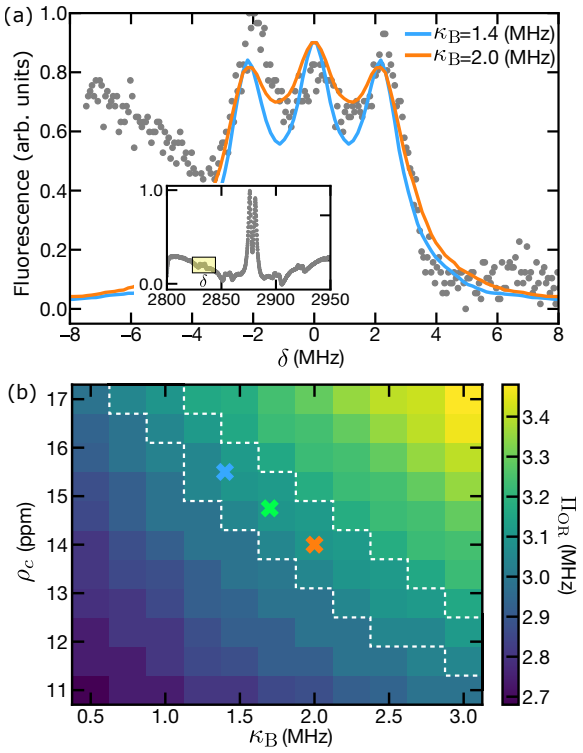

Figure 6.6: (a) Resonant ODMR spectrum with optical drive detuned 190 GHz below ZPL and magnetic field applied in the plane of the (111)-cut diamond. We focus on the lineshape of an NV sub-ensemble experiencing a large magnetic field projection along its axis. Solid blue and orange traces are triple-Lorentzian lineshapes with widths 1.4 MHz and 2.0 MHz respectively; these are used to constrain the magnetic broadening, κ_B. (inset) The full resonant ODMR spectrum. The peaks shown in the main panel are located in highlighted box. (b) Predicted off-resonant ODMR splitting as a function of charge density ρ and κ_B. The white-dashed contour indicates the region for which the predicted splitting value is consistent with the room-temperature spectrum [Fig. 6.1(a), inset]. This region, coupled with the extracted range for κ_B, is used to constrain the acceptable values of ρ. We extract susceptibilities for three pairs (ρ, κ_B), indicated by the colored x-markers, spanning this range.

$\{0, \pm 2.16 \text{ MHz}\}$ owing to the three distinct ^{14}N nuclear states, i.e. $m_I = 0, \pm 1$. Altogether, the explicit form for $\Lambda(\omega; E_\perp)$ is given by

$$\Lambda(\omega; E_\perp) = \int d\omega' \Lambda_{\mathrm{B}}(\omega; E_\perp) \frac{\frac{\kappa_0}{2}}{\pi\left[(\omega-\omega')^2 + (\frac{\kappa_0}{2})^2\right]}, \tag{6.14}$$

where

$$\Lambda_{\mathrm{B}}(\omega; E_\perp) = \begin{cases} 0 & |\omega| \leq \chi_\perp^{\mathrm{g}} E_\perp \\ \sum_{B_{\mathrm{I}}} \frac{\frac{\kappa_{\mathrm{B}}}{2}|\omega|}{\pi\sqrt{\omega^2-(\chi_\perp^{\mathrm{g}} E_\perp)^2}\left(\left(|\mu_B g_e B_{\mathrm{I}}| - \sqrt{\omega^2-(\chi_\perp^{\mathrm{g}} E_\perp)^2}\right)^2 + (\frac{\kappa_{\mathrm{B}}}{2})^2\right)} & |\omega| > \chi_\perp^{\mathrm{g}} E_\perp \end{cases}$$

is the lineshape with magnetic broadening alone.

Off-resonant contribution: The expression for the off-resonant contribution to the resonant ODMR spectra is structurally identical to the resonant case. The essential difference lies in replacing the kernel defining the resonant condition, D_{R}, with a new kernel that quantifies the degree of *off-resonant* driving. Specifically, the off-resonant kernel, D_{OR}, can take three values: 0 if the optical drive is below both branches, 1 if it is between the two branches, and 2 if it is above both branches; this is because the phonon sidebands of each excited state branch can contribute to the off-resonant cross-section. Formalizing this physical picture, we obtain,

$$S_{\mathrm{OR}}(\omega; \Delta\nu) = \int dE\ P(E) \times \int \sin(\theta) d\theta \Lambda(\omega; \sin(\theta)E) D_{\mathrm{OR}}(\vec{E}, \Delta\nu), \tag{6.15}$$

$$D_{\mathrm{OR}}(\vec{E}, \Delta\nu) = \left[\Theta(\delta_U - \gamma_{\mathrm{e}}/2) + \Theta(\delta_L - \gamma_{\mathrm{e}}/2)\right]. \tag{6.16}$$

Total fluorescence: The total fluorescence is determined by the fraction of resonant and off-resonant configurations. These fractions are given by

$$F_{\mathrm{R}}(\Delta\nu) = \frac{1}{\mathcal{N}} \int dE\ P(E) \times \int \sin(\theta) d\theta D_R(\vec{E}, \Delta\nu) \tag{6.17}$$

$$F_{\mathrm{OR}}(\Delta\nu) = \frac{1}{\mathcal{N}} \int dE\ P(E) \times \int \sin(\theta) d\theta D_{OR}(\vec{E}, \Delta\nu)\ , \tag{6.18}$$

where $\mathcal{N}$ is the total number of configurations. The total fluorescence is a weighted sum of these two contributions:

$$R(\Delta\nu) \propto \epsilon_{\mathrm{R}} F_{\mathrm{R}}(\Delta\nu) + F_{\mathrm{OR}}(\Delta\nu)\ , \tag{6.19}$$

where ϵ_R is the enhancement factor of the resonant mechanism. From single NV experiments, we estimate $\epsilon_R \approx 10^5$ [276]. Up to overall rescaling, we can then calculate the predicted fluorescence as a function of detuning; this exhibits good agreement with the background fluorescence as shown in Fig. 6.3(b).

6.2.7 Estimating Susceptibilities

We extract the excited-state electric field susceptibilities by fitting our model to the measured splitting of the positive-contrast peak, $\Pi_\perp$, as a function optical detuning, $\Delta\nu$. Here, we provide additional details on this procedure, including error estimation and the determination of model parameters, i.e. the charge density and broadening parameters.

To begin, we determine $\Pi_\perp$ as a function of detuning from the experimentally measured ODMR spectra [Fig. 6.2(a)]. In particular, we identify the frequency of the local maximum, $\omega_\pm$, associated with each positive-contrast peak and compute $\Pi_\perp = \frac{1}{2}(\omega_+ - \omega_-)$. The uncertainty on these estimates arises from shot noise in the resonant ODMR spectra, which causes the frequency of maximum florescence to vary between successive measurements. To determine this uncertainty, we perform a Monte Carlo simulation of Lorentzian lineshapes with Gaussian noise, whose strength is determined from the experimental data, and sample the frequency of local maximum; this yields the error bars shown in Fig. 6.2(b) and 6.7(a).

We next determine the three parameters required in our resonant ODMR model (see section 6.2.1.2) other than the susceptibilities through the following independent calibration steps:

1. Magnetic broadening, κ_B: We measure the resonant ODMR spectrum of an NV subensemble with a significant magnetic field projection along its axis [Fig 6.6(a)]. Since this magnetic field suppresses electric field noise, the dominant source of remaining noise is due to inhomogeneous magnetic fields. Fitting this spectrum to three Lorentzians yields an magnetic linewidth $\kappa_B = 1.7 \pm 0.3$ MHz [Fig. 6.6(a)].

2. Charge density, ρ: We measure a room-temperature, off-resonant ODMR spectrum without a bias magnetic field. The characteristic splitting observed in this spectrum is fit to our model of randomly placed charges, leading to a charge-density estimate of $\rho = 15 \pm 2$ ppm.

3. Non-magnetic broadening, κ_0: We perform a Lorentzian fit to the positive-contrast features of an ODMR spectrum measured with optical excitation near the zero-phonon-line ($\Delta\nu \lesssim 1$ GHz). This spectrum is chosen because it has minimal broadening due to electric fields. We subtract κ_B from the extracted linewidth and assume the remaining broadening arises from non-magnetic sources (e.g. microwave power broadening); this yields $\kappa_0 \approx 1$ MHz. We note that this parameter has only a minor effect on the susceptibility estimates.

Finally, we extract the susceptibility parameters by fitting our model to the empirical values for $\Pi_\perp$ as a function of $\Delta\nu$. In particular, we calculate the least-square error of the

data compared to the predicted splittings from our resonant ODMR model, with $\chi_\perp^e$ and $\chi_\parallel^e$ as the only free parameters [Fig. 6.7(a)][9]. We find the χ^2-error is minimized at $\{\chi_\perp^e, \chi_\parallel^e\} = \{1.43, 0.68\}$ MHz/(V/cm) with a reduced-χ^2 value of $\chi_\nu^2 = 0.87$ (with 15 observations and 2 fit parameters). By linearizing our model around the fitted values, we determine the 2σ confidence region of the susceptibility estimates [Fig. 6.7(b)] and estimate uncertainties of $\sim 5\%$ for $\chi_\perp^e$, and $\sim 15\%$ for $\chi_\parallel^e$. We also estimate systematic errors by repeating the analysis with the values ρ and κ_B indicated in Fig 6.6(b). This is shown in Fig. 6.7(b) and leads to a systematic error of $\sim 5\%$ for $\chi_\perp^e$, and $\sim 15\%$ for $\chi_\parallel^e$. Summing in quadrature, we have a total error estimate of $\sim 7\%$ for $\chi_\perp^e$ and $\sim 21\%$ for $\chi_\parallel^e$.

A few additional remarks are in order. First, we note that our procedure, by focusing on the splitting of the ODMR spectra, depends primarily on the magnitude of the most-probable electric field (i.e. E_0) and not on the details of the full distribution. Second, in principle ρ may depend on the temperature, optical excitation frequency, and excitation power, which would invalidate our assumption that ρ can be determined from off-resonant room-temperature ODMR [30, 3, 216]. However, even if we relax this assumption, the optical transition linewidth provides an additional, independent constraint on the charge-density and susceptibilities. By demanding that $(\rho, \chi_\parallel^e, \chi_\perp^e)$ simultaneously recover $\Pi_\perp(\Delta\nu)$ and the excited state linewidth, we find $\rho = 15^{+7}_{-3}$, where the super- (sub-) script indicates the upper (lower) bound. The systematic errors on the extracted susceptibilities concordantly increase to $\sim 10\%$ and $\sim 30\%$ for $\chi_\perp^m$ and $\chi_\parallel^m$ respectively. Therefore, the essentials of our analysis and conclusions do not depend on an assumption of consistent ρ (although our observations support this conclusion for ensemble measurements).

6.2.8 Resonant ODMR Linewidth

The positive-contrast features shown in Fig. 6.2(a) exhibit not only a splitting $\Pi_\perp$ which depends on the optical detuning, but also a linewidth Γ_g which systematically increases with detuning (Fig. 6.8). Qualitatively, this effect can be understood as arising from the *tail* of the electric field distribution: If the electric field distribution decays very slowly, Γ_g will be large since many nearly equal probability electric-field spheres will intersect the resonant cone at different values of $E_\perp$.

While our microscopic model accounts for this general trend, it does not accurately predict the precise form of Γ_g vs. $\Delta\nu$ (Fig. 6.8). Interestingly, this discrepancy suggests that our microscopic model is missing subtle aspects of the electric field distribution at large strengths / short distances. More formally, the trend that Γ_g increases with $\Delta\nu$ (Fig. 6.8)

[9] In the vicinity of the positive-contrast peaks, the off-resonant configurations only contribute a flat background, and can hence be neglected in our fitting procedure. This eliminates ϵ_C and off-resonant linewidths as free parameters and thus simplifies the model we use to extract the susceptibilities. To check this approximation, we also extract the susceptibilities using the ϵ_C and off-resonant linewidths extracted from the 5 K spectrum (Table 6.1) and find that they are within statistical error of those determined from our simpler estimation procedure.

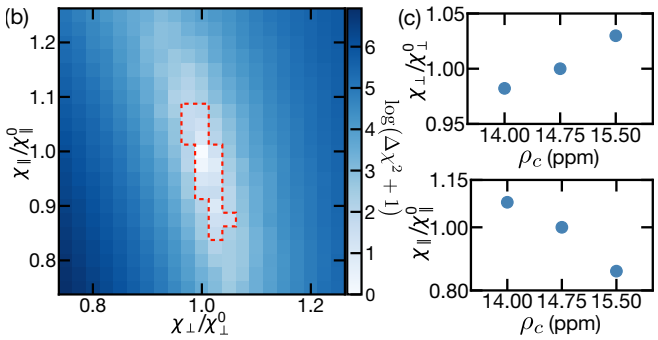

Figure 6.7: (a) Experimental $\Pi_\perp$ (dark blue) and model (gray) as functions of $\Delta\nu$. The fit yields $\chi^2_\nu = 0.87$ (b) $\Delta\chi^2$ as a function of $\chi^{\rm e}_\parallel$ and $\chi^{\rm e}_\perp$. The red-dashed contour denotes the 2σ confidence region. (c) $\chi^{\rm e}_\perp$ and $\chi^{\rm e}_\parallel$ as functions of ρ. This quantifies the main source of systematic error in our analysis. Errors are relative to $\{\chi^0_\perp, \chi^0_\parallel\} = \{1.43, 0.68\}$ MHz/(V/cm)

indicates the relative decay rate of the electric-field distribution *decreases* at larger values of E. This is characteristic of a polynomially decaying tail: if $P(E) \sim 1/(E/E_0)^q$ then $\frac{d(\log(P(E)))}{dE} = -q/E$, so the tail decays more slowly at larger E resulting in larger $\Gamma_{\rm g}$. Indeed, one possible direction for future research is to quantitatively extract $\frac{d(\log(P(E))}{dE}$ from $\Gamma_{\rm g}(\Delta\nu)$ at large $\Delta\nu$. This could yield insight into the underlying short-range physics controlling the tail of the electric field distribution, such as whether charges are more likely to be localized in the vicinity of the NV center.

6.2.9 Temperature Dependent Spectra

Our procedure for fitting the temperature-dependent ODMR spectra, shown in Fig. 6.1(a), relies on the same resonant ODMR model, susceptibility parameters, and charge density as in the previous sections. In addition, we find it necessary to vary (i) the ODMR contrast ratio and (ii) broadening parameters at each temperature. Here, we discuss the physical origin of the temperature dependence of these parameters.

Contrast: We attribute the change in contrast to the the fact that increasing temperature broadens the optical transition linewidth, which in turn reduces the density of resonant configurations at a given optical detuning, effectively reducing ϵ_C. Indeed, we find qualitatively that ϵ_C decreases with temperature, though we do not attempt to develop a quantitative model for it.

Broadening: Experimentally, we observe that off-resonant dips in the ODMR spectrum exhibit larger broadening than the positive-contrast peaks (see Fig. 6.1(a)). We conjecture two possible causes of this additional broadening. First, there may be different degrees of *light-narrowing* in the resonant and off-resonant configurations. Light-narrowing arises because resonantly driven transitions experience a greater rate of optical pumping than transitions to the phonon-sideband, and hence have a different effective linewidth. In this setting, a

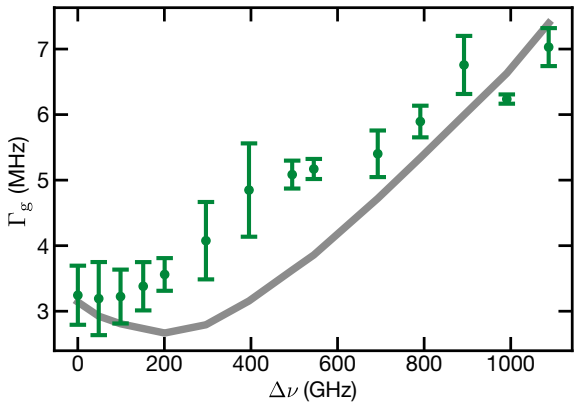

Figure 6.8: Resonant ODMR linewidth Γ_g as a function optical detuning. Error bars reflect the difference in the FWHM of Lorentzian fits of the left and right peaks of experimental data. The same analysis applied to the spectra generated by our model yields the gray curve. Although the model accounts for the general trend of increasing Γ at large detuning, there are clear qualitative differences between the experiment and theory. Most notably, the experiment is broader at moderate detunings ($200 - 600$ GHz) than the model would suggest. This could be because the true electric field distribution decays more slowly than the random charge model predicts. The effects of strain may also partially account for the discrepancy.

greater rate of optical pumping actually *reduces* the effective linewidth [167]. Second, power broadening itself may not be well described by a convolution with a Lorentzian; indeed we find that this is the case even for *off-resonant* ODMR spectra under higher microwave power. Intuitively, large electric fields alter the matrix elements between ground-state sublevels, causing the degree of power-broadening to be electric field strength dependent. To account for this, we treat the off-resonant magnetic broadening parameter, κ_B^{OR}, as a free parameter and find that its best-fit value is comparable to the non-magnetic broadening. We emphasize that this is a convenient way to account for the dependence of power broadening on electric field strength and does not constitute a meaningful estimate of the true broadening due to magnetic fields.

We note that both of these issues are artifacts of working in a microwave power-broadened regime, which is the case for the present temperature-dependent data. For extraction of susceptibilities, ODMR measurements were performed with 100 $\times$ lower microwave power, where these effects are suppressed.

6.2.10 Sensitivity Estimates

Here, we provide additional details for estimating the sensitivity of our resonant electric-field sensing protocol. The estimates are calibrated based on the sample measured in this work,

Temp. [K]	κ_0^{R} [MHz]	$\kappa_{\mathrm{B}}^{\mathrm{R}}$ [MHz]	κ_0^{OR} [MHz]	$\kappa_{\mathrm{B}}^{\mathrm{OR}}$ [MHz]	ϵ_C [1]
5	2.0	4.0	20.0	27.0	10^4
40	2.0	4.0	16.0	16.0	$4 \cdot 10^3$
55	2.0	4.0	12.0	15.0	$-1.7 \cdot 10^3$
100	2.0	4.0	9.0	8.0	$-1.7 \cdot 10^3$

Table 6.1: Summary of parameters used to fit the temperature dependent ODMR spectra [Fig. 1(a)]. The linewidth parameters for resonant configurations are roughly consistent with the more carefully estimated parameters used for susceptibility extraction; the off-resonant linewidth parameters, however, are significantly altered by power-broadening, as we discuss in Section 6.2.9. In particular, $\kappa_{\mathrm{B}}^{\mathrm{OR}}$ should not be interpreted as an accurate estimate of the magnetic broadening; instead, we regard it as a phenomenological parameter that controls the amount of broadening which "adds in quadrature" to the electric field [see equation (6.2.6)]. The value of ϵ_C at 5 K is roughly consistent with an estimate based on ϵ_R. Qualitatively, ϵ_C decreases with increasing temperature because the density of resonant states decreases.

and then extrapolated to other densities using scaling arguments.

Let us begin by recalling that the sensitivity for an electric-field dependent count rate $R(\delta E)$ is given by

$$\frac{1}{\eta} = \frac{dR}{d(\delta E)}\bigg|_{\delta E=0} \frac{1}{\sqrt{R(0)}}, \tag{6.20}$$

$$\tag{6.21}$$

or equivalently,

$$\frac{1}{\eta} = \frac{d\log(R)}{d(\delta E)}\bigg|_{\delta E=0} \cdot\sqrt{R(0)}\ . \tag{6.22}$$

In our sensing protocol, the fluorescence rate is determined by two effects: (i) the shift of the positive-contrast peaks, and (ii) the change in overall fluorescence. These effects contribute independently to the total signal, such that $R(\delta E) = R_{\mathrm{F}}(\delta E) \cdot R_{\Pi}(\delta E)$, where R_{F} and R_{Π} capture the dependence of fluorescence on optical detuning and microwave frequency, respectively. The total sensitivity is then

$$\frac{1}{\eta} = \left[\frac{d\log(R_{\Pi})}{d(\delta E)} + \frac{d\log(R_{\mathrm{F}})}{d(\delta E)}\right]_{\delta E=0} \cdot \sqrt{R(0)}\ , \tag{6.23}$$

which leads to the equation stated in Section 6.2.3:

$$\frac{1}{\eta} = \frac{1}{\eta_\Pi} + \frac{1}{\eta_\mathrm{F}} \ . \tag{6.24}$$

For simplicity, we define $R \equiv R(0)$. The sensitivities can be decomposed as

$$\eta_\Pi = P_\Pi \frac{\Gamma_\mathrm{g}}{\chi_\mathrm{eff} C_0 C_\mathrm{r}} \cdot \frac{1}{\sqrt{R}} \ , \tag{6.25}$$

$$\eta_\mathrm{F} = P_\mathrm{F} \frac{\Gamma_\mathrm{e}}{\chi_\parallel^\mathrm{e} C_\mathrm{r}} \cdot \frac{1}{\sqrt{R}} \ , \tag{6.26}$$

where Γ (P) is the linewidth (lineshape factor) associated with the ground and excited states, R is the count rate, C_0 is the maximum CW contrast of the resonant ODMR peaks, C_r is the ratio of photons resulting from resonant fluorescence to total fluorescence, and $\{\chi_\mathrm{eff}, \chi_\parallel^\mathrm{e}\}$ are the effective ground- and excited-state susceptibilities, respectively.

For our estimates, we assume the ground state ODMR lineshape is Lorentzian, such that $P_\Pi \approx 0.77$, and we use the excited-state susceptibility determined in our work: $\chi_\parallel^\mathrm{e} = 0.7$ MHz/(V/cm); moreover, we determine $\chi_\mathrm{eff} \approx 0.41$ and $P_\mathrm{F} \approx 0.39$ from our model [Fig. 6.9(a)] and from experimental data [Fig. 6.3(b)], respectively. The remaining parameters are discussed below.

6.2.10.1 Parameter calibration

Linewidths: We model the ODMR and optical transition linewidths as containing both an intrinsic broadening and an electric-field induced broadening:

$$\Gamma_\mathrm{g,e} = \Gamma_\mathrm{g,e}^0(\bar{\rho}) + \Gamma_\mathrm{g,e}^E \cdot \bar{\rho}^{2/3} \ , \tag{6.27}$$

where $\bar{\rho}$ is a normalized NV density, $\bar{\rho} = \rho_\mathrm{NV}/\rho_\mathrm{NV}^0$. The ground state intrinsic broadening, $\Gamma_\mathrm{g}^0(\bar{\rho})$, is typically dominated by paramagnetic impurities and is modeled by [97]

$$\Gamma_\mathrm{g}^0 = (A_{^{13}\mathrm{C}}[^{13}\mathrm{C}]) + A_{\mathrm{N}^0}[\mathrm{N}^0])^{-1} \cdot \frac{1}{\pi}, \tag{6.28}$$

where $[^{13}\mathrm{C}], [\mathrm{N}^0]$ represent the concentrations of ^{13}C and uncharged substitutional nitrogen defects, respectively. From [97] we obtain $A_{^{13}\mathrm{C}} \approx 0.1\ \mathrm{ms}^{-1}\mathrm{ppm}^{-1}$ and $A_{\mathrm{N}^0} \approx 101\ \mathrm{ms}^{-1}\mathrm{ppm}^{-1}$. For impurity concentrations, we assume a natural abundance of ^{13}C (1.1% or 11000 ppm) and that $[\mathrm{N}^0] = 0.3 \cdot [\mathrm{NV}^{-1}]$ — i.e., a 30% conversion ratio, which is among the best typically observed [28]. Since the intrinsic excited-state broadening is less well-understood, and certainly not limited by paramagnetic impurities, we adopt the simple density-independent model $\Gamma_\mathrm{e}^0 \approx 10$ GHz [32, 4]. Finally, we calibrate the charge-induced linewidths against our sample ($\rho_\mathrm{NV}^0 \approx 8$ ppm), yielding $\Gamma_\mathrm{g}^E \approx 3.7$ MHz and $\Gamma_\mathrm{e}^E \approx 10^6$ MHz. We note that here, and throughout our sensitivity estimates, we will assume that the charge environment consists

primarily of other uniformly distributed NVs and charge donors, such that $\rho = 2\rho_{\mathrm{NV}}$ (see subsection 6.2.1.2).

Fluorescence rate: The overall fluorescence rate contains contributions from the resonant and off-resonant configurations. The former is proportional to the density of resonant configurations, and therefore is inversely proportional to the optical transition linewidth. Thus, the fluorescence from resonant configurations R_R can be modeled as

$$R_R = rR_0, \quad r = \frac{\Gamma^{\mathrm{ref}}}{\Gamma_{\mathrm{e}}^0 + \Gamma_{\mathrm{e}}^E \bar{\rho}^{2/3}} \ , \tag{6.29}$$

where R_0 is the fluorescence rate for a single, off-resonantly driven NV orientation, r is the fluorescence enhancement factor for resonant configurations, and κ^{ref} is a density-independent prefactor. To determine Γ^{ref}, we compare the resonant fluorescence at the optimal detuning to the off-resonant fluorescence for detunings far above the ZPL [Fig. 6.9(b)]. This yields $r \approx 2$, corresponding to $\Gamma^{\mathrm{ref}} \approx 2 \cdot 10^6$ MHz; for an optimal sample, we estimate that r can reach $r \approx 100$ at ~ 10 ppb.

To determine the overall count rate, we take into account the fact that our sensing protocol includes signals from one resonant NV orientation and three off-resonant orientations. This is because the bias electric field required to lift the excited-state degeneracy pushes the excited state of three orientations below the excited state of the target orientation, so they are excited by the off-resonant mechanism. In particular, assuming a (111)-cut diamond, the fluorescence rate due to off-resonant orientations is $R_{\mathrm{OR}} = 5/3 \ R_0$ [10]. In combination, the total count rate is

$$R = R_0(r + 5/3) \ . \tag{6.30}$$

We note that R_0 depends on the specific optical setup (e.g. illumination volume, laser power, and collection efficiency). We determine this constant for a similar setup as described in [60] [11]. The final count rate for our sample and for an optimal sample are reported in Table 6.2.

Finally, for the room-temperature sensitivity estimate (Fig. 6.3), we additionally adjust R to account for the decrease in the Debye-Waller factor with temperature. We estimate the Debye-Waller factor decreases by 35% at 300K compared to 5K, degrading the sensitivity by $\sim 50\%$ [268, 175].

Contrast: We first estimate the maximum CW contrast of the positive-contrast peaks, $C_0 \approx 0.21$, from the experimental data [Fig. 6.9(c)] [12]. However, of the total counts, only the resonant fraction, C_{r}, contributes to sensing. Therefore, the actual contrast of the resonant

[10] The factor of 5/3 arises because the three off-resonant groups are not perpendicular to the laser polarization [29].

[11] In particular, we rescale their reported count rate by the ratio of our sample's NV density to their sample's density and correct for a difference in laser polarization. We also divide by 8, since only one NV crystallographic orientation will be used in the sensing protocol.

[12] For a (111)-cut diamond, $C_0 = 8/3 \ C_{\mathrm{exp}}$, where C_{exp} is the experimentally observed contrast. This factor is also related to the laser polarization [29]

DC Electrometry Method		ρ_{NV} (ppm)	T (K)	$\Delta\nu_{op}$ (GHz)	Γ (MHz)	P	χ (Hz cm/V)	R (counts/s)	C	η (V/cm$\sqrt{\text{Hz}}$)
Single NV - G.S. [88]		-	$\lesssim 300$	-	0.05	0.77	17	100	0.3	760
Single NV - E.S. [64]		-	$\lesssim 4$	-	13	0.77	$7.0 \cdot 10^5$	2500	1	0.29
EIT Ensemble [4]		0.03	$\lesssim 30$	-	1.0	0.77	9.8	$3.2 \cdot 10^{14}$	0.022	0.20
Off-res. Ensemble [60]		1	$\lesssim 300$	-	1.0	0.77	17	$5.0 \cdot 10^{14}$	0.02	0.10
Res. Ensemble (Our sample)	F	8	$\lesssim 200$	200	10^6	0.39	$7.0 \cdot 10^5$	$2.4 \cdot 10^{15}$	0.54	0.021
	$\Pi_\perp$		$\lesssim 45$		3.9	0.77	6.97	$2.4 \cdot 10^{15}$	0.11	0.077
	Total		$\lesssim 45$		-	-	-	-	-	0.017
Res. Ensemble (Low-density sample)	F	0.01	$\lesssim 55$	2.3	$2.1 \cdot 10^4$	0.39	$7.0 \cdot 10^5$	$6.9 \cdot 10^{13}$	0.98	0.0014
	$\Pi_\perp$		$\lesssim 45$		0.25	0.77	6.97	$6.9 \cdot 10^{13}$	0.21	0.016
	Total		$\lesssim 45$		-	-	-	-	-	0.0013
Res. Ensemble ($[^{12}C] = 99.995\%$)	F	0.002	$\lesssim 55$	0.8	$1.4 \cdot 10^4$	0.39	$7.0 \cdot 10^5$	$3.1 \cdot 10^{13}$	0.98	0.0015
	$\Pi_\perp$		$\lesssim 45$		0.017	0.77	6.97	$3.1 \cdot 10^{13}$	0.21	0.0016
	Total		$\lesssim 45$		-	-	-	-	-	$8 \cdot 10^{-4}$

Table 6.2: Summary of DC NV electrometry protocols and their associated sensitivities, assuming an illumination volume of ~ 0.1 mm^3 (for ensemble techniques). For our protocol (lower section), we provide both the sensitivity owing to the peak shift (η_Π) and the sensitivity owing to the change in overall fluorescence (η_F). All sensitivities are given by $\eta = P\frac{\Gamma}{C\chi\sqrt{R}}$, where P is a lineshape dependent prefactor, C is the contrast (i.e. $C = C_0 C_r$ for η_Π, and $C = C_r$ for η_F), χ is the relevant susceptibility, and Γ is the relevant linewidth (i.e. $\Gamma = \Gamma_g$ for η_Π, and $\Gamma = \Gamma_e$ for η_F). The ^{12}C concentration assumed for an isotopically purified sample is estimated from [97]. For reference [60], we report the sensitivity that would obtained at optimal NV densities (by rescaling the linewidth and counts according to our scaling formulae). The parameter $\Delta\nu$ refers to the optimal optical detuning below the ZPL for our electrometry protocol [Fig. 6.9(a)]

ODMR peaks is $C = C_0 C_\mathrm{r}$; meanwhile, for sensing via direct variation in fluorescence (η_F), the relevant contrast is C_r. For a (111)-cut sample, we have

$$C_\mathrm{r} = \frac{r}{(r + 5/3)} \ , \tag{6.31}$$

where r is the resonant enhancement factor defined in (6.29).

Bias electric field: In addition to the sensitivity estimates provided in the manuscript, we estimate the bias field required to spectrally isolate the crystallographic orientation used in our sensing protocol [Fig. 6.9(d)]. Given a bias field parallel to one of the NV groups, three other groups will actually be shifted by the electric field *below* the target group since $\chi^\mathrm{e}_\perp \approx 2\chi^\mathrm{e}_\parallel$. Therefore, we determine this bias field by demanding the lowest-energy NV group parallel to the bias field is at least $\Gamma_\mathrm{e}/2$ above the lowest three NV groups.

6.2.10.2 Scaling with density

Here, we determine how sensitivity degrades in the high-density regime. We consider an ideal limit for which there is minimal charge broadening, i.e. $\rho \equiv \rho = 2\rho_\mathrm{NV}$ and no density-dependent broadening other than internal electric-fields. As discussed above, in the charge-dominated regime the ODMR and optical transition linewidths ($\Gamma_\mathrm{g}, \Gamma_\mathrm{e}$) are proportional to the average electric field strength, which scales as $\rho_\mathrm{NV}^{2/3}$. In this regime, we also have $r \propto \rho^{-2/3}$ and $r \ll 5/3$, implying $C_\mathrm{r} \propto \rho^{-2/3}$ and $R \sim \rho$. Thus the sensitivity scaling at high-densities is given by

$$\eta \propto \frac{\Gamma}{C_\mathrm{r}\sqrt{R}} \propto \frac{\rho^{2/3}}{\rho^{-2/3}\sqrt{\rho}} = \rho^{5/6} \tag{6.32}$$

as plotted in Fig. 6.3. The scaling for typical electrometry protocols may be similarly determined. In this case, all photons are scattered off-resonantly and C_r is no longer relevant in the sensitivity expressions. Then

$$\eta \sim \frac{\rho^{2/3}}{\sqrt{\rho}} = \rho^{1/6} \tag{6.33}$$

as shown in Fig. 6.3.

6.2.10.3 Isotopically Purified Samples

We note that for isotopically purified samples the relative contributions of η_F and η_Π may be comparable (see Tab. 6.2). To illustrate this, let us consider the sensitivity of NV electrometry protocols assuming a ^{13}C concentration of 50 ppm ([^{12}C] = 99.995% purified) as utilized in recently optimized samples [97, 28]; indeed, such isotopically purified samples have been of tremendous recent interest for applications to precision metrology [97]. Assuming an excited state broadening of 10 GHz, we find that $\eta_\mathrm{F} = 1.4 \cdot 10^{-3}\mathrm{V/cm}\sqrt{\mathrm{Hz}}$ and $\eta_\Pi = 1.8 \cdot 10^{-3}\mathrm{V/cm}\sqrt{\mathrm{Hz}}$ at the optimal NV density $\rho_\mathrm{NV} \approx 2$ ppb.

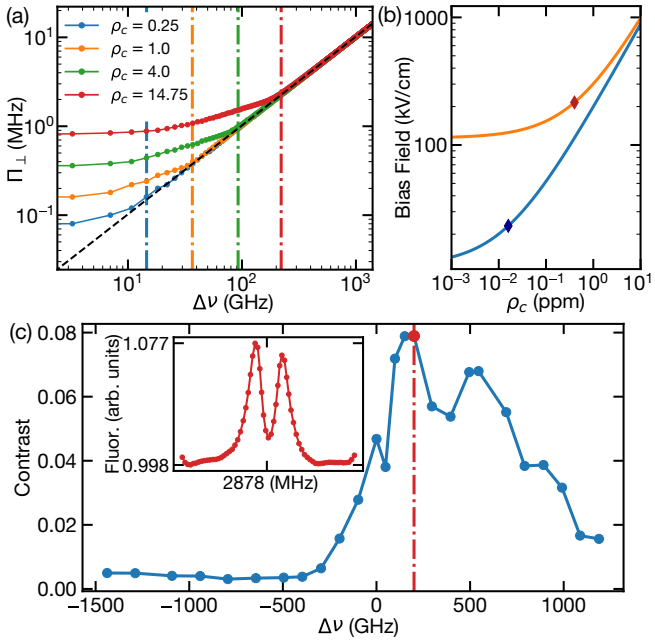

Figure 6.9: (a) $\Pi_\perp$ as a function of $\Delta\nu$ for various ρ. Dash-dot vertical lines indicate the optimal operating $\Delta\nu$ for our sensing proposal. In particular, we choose the smallest $\Delta\nu$ for which $\Pi_\perp$ depends linearly on $\Delta\nu$. This maximizes χ_{eff} and the resonant fluorescence. (b) Fluorescence as a function of $\Delta\nu$ from experiment (brown) and theory (solid blue). The dash-dot vertical line indicates the optimal operating $\Delta\nu$ for our sample. We estimate $\Gamma_e \approx 1$ THz, ignoring asymmetry (dashed orange lines). (c) Contrast of resonant ODMR (with a 20 G applied magnetic field perpendicular to the NV axis) as a function of $\Delta\nu$. The red marker and dash-dot line indicates the contrast at the optimal operating detuning. Since magnetically split groups provide additional background for the central peak, the maximum CW ODMR contrast C_0 is a factor 8/3 larger than what is observed (see Section 6.2.10.1) [29]. (inset) Experimental resonant ODMR at the optimal operating $\Delta\nu$. (d) Electric field bias required for our sensing procedure as a function of ρ assuming $\kappa_e^0 = 10$ GHz (blue) and $\kappa_e^0 = 100$ GHz (orange). The blue and red diamonds mark the bias field required at optimal NV densities.

6.2.10.4 ^{3}E Fine Structure

Our sensitivity model assumes that electric-field induced splitting dominates the ^{3}E fine structure. Under this assumption, it is sufficient to consider two three-fold degenerate orbital degrees of freedom in determining the resonance conditions. However, this assumption breaks down when the splitting due to internal electric fields of the diamond becomes comparable to the intrinsic hyperfine effects of the ^{3}E manifold, whose typical magnitude is $\sim$ 5GHz [224]. Based on our extracted susceptibilities, we estimate this occurs for NV densities $\lesssim$ 2ppb. For densities below this threshold, it is still possible to perform resonant sensing using individual sublevels; in particular, one should probe a pair of sublevels ($E_{x,y}$ or $E_{1,2}$) which are linearly sensitive to electric fields [224]. In this regime, the sensitivity would be determined entirely by the change in overall fluorescence, i.e. η_{F}.

6.2.11 Theoretical Estimates of Susceptibilities

In this section, we discuss the physical origin of the NV's electric field susceptibility in both the ground and excited state, and compare the measured susceptibility parameters to theoretical estimates (Table 6.3).

6.2.11.1 Excited state

While it is well understood that the orbital doublet nature of the excited state allows for a linear Stark shift, the microscopic origin of this shift can in principle be explained by two different mechanisms [224]. One mechanism, the electronic effect, is based on the polarization of the NV's electronic wavefunction. The second mechanism, the ionic effect, consists of the relative displacement of the ions and is thus closely related to piezoelectricity. The two effects are indistinguishable from a group theoretic perspective and, in general, both will contribute to the total susceptibility. Below we estimate the susceptibilities based on the electronic effect and find good agreement with the measured values (Table 6.3). On the other hand, the ionic effect was previously estimated with *ab initio* simulations and was found to be on the same order of magnitude [224]. Thus, a more precise calculation of the excited susceptibilities should take into account both effects.

To estimate the electronic effect, we consider the molecular model of the defect center, in which the NV's single-particle orbitals are constructed from non-overlapping atomic orbitals, $\{\sigma_1, \sigma_2, \sigma_3, \sigma_N\}$, centered on the three carbon ions and the nitrogen ion, respectively [82, 224]. In particular, the single-particle orbitals are given by

$$e_x = \frac{1}{\sqrt{6}}\left(2\sigma_1 - \sigma_2 - \sigma_3\right) \tag{6.34}$$

$$e_y = \frac{1}{\sqrt{2}}\left(\sigma_2 - \sigma_3\right) \tag{6.35}$$

$$a_1 = \frac{1}{\sqrt{3+\lambda^2}}\left(\sigma_1 + \sigma_2 + \sigma_3 + \lambda\sigma_N\right) \ , \tag{6.36}$$

	$\chi_\perp$ (Hz cm/V)	$\chi_\parallel$ (Hz cm/V)
E.S. measured (this work)	$1.4 \pm 0.1 \times 10^6$	$0.7 \pm 0.1 \times 10^6$
E.S. electronic effect	1.6×10^6	0.6×10^6
G.S. measured [328]	17 ± 2.5	0.35 ± 0.02
G.S. spin-spin effect	76	0

Table 6.3: Comparison between measured susceptibilities and theoretical estimates. Details of the theoretical estimates are provided in this work and accompanying references.

where σ_1 is the carbon orbital that lies in the xy plane, and $\lambda \approx 0.7$ is determined from density functional theory (DFT) calculations [117][13] These orbitals are combined to form the ${}^3A_2$ ground state

$$|A_2\rangle = \frac{1}{\sqrt{2}} \left(|e_x e_y\rangle - |e_y e_x\rangle \right) \tag{6.37}$$

and the two ${}^3E$ excited states

$$|X\rangle = \frac{1}{\sqrt{2}} \left(|a_1 e_x\rangle - |e_x a_1\rangle \right) \tag{6.38}$$

$$|Y\rangle = \frac{1}{\sqrt{2}} \left(|a_1 e_y\rangle - |e_y a_1\rangle \right). \tag{6.39}$$

From first-order perturbation theory, the electric field susceptibility is determined by the permanent dipole of the excited state. For the transverse susceptibility, it is sufficient to calculate the dipole moment along the x-axis, which is diagonal in the $\{|X\rangle, |Y\rangle\}$ basis:

$$d_\perp = -e \langle X | \, x_1 + x_2 \, | X \rangle \ , \tag{6.40}$$

where $x_{1,2}$ are the single particle positions and e is the elementary charge. In the single-particle basis, this reduces to

$$|d_\perp| = e \langle e_x | \, x \, | e_x \rangle \tag{6.41}$$

$$\approx \frac{e}{2} \langle \sigma_1 | \, x \, | \sigma_1 \rangle \ , \tag{6.42}$$

[13] We note that there is a fourth state with the same symmetry properties as a_1 (i.e. transforms according to the totally symmetric A_1 irreducible representation), but it is higher in energy than the other three and therefore not relevant for this discussion [224].

where we have approximated the full integral by assuming non-overlapping atomic orbitals. For the longitudinal direction, the relevant term is the relative dipole moment between between the ground and excited state. This is given by

$$d_{\parallel} = -e\left[\langle X|\, z_1 + z_2\, |X\rangle - \langle A_2|\, z_1 + z_2\, |A_2\rangle\right] \tag{6.43}$$

$$= -e\left[\langle a_1|\, z\, |a_1\rangle - \langle e_x|\, z\, |e_x\rangle\right] \tag{6.44}$$

$$\approx \frac{e\lambda^2}{3+\lambda^2}\left[\langle \sigma_1|\, z\, |\sigma_1\rangle - \langle \sigma_N|\, z\, |\sigma_N\rangle\right]. \tag{6.45}$$

Inserting orbital expectation values from DFT calculations, we obtain $|d_{\perp}| \approx e(0.67\ \mathbf{r}A)$ and $d_{\parallel} \approx e(0.26\ \mathbf{r}A)$ [117, 86]. This yields susceptibility estimates of $\{\chi_{\perp}^{\mathrm{e}}, \chi_{\parallel}^{\mathrm{e}}\} = \{1.6, 0.6\}$ MHz/(V/cm), in good agreement with the values measured in this work (Table 6.3).

6.2.11.2 Ground state

The ground state of the NV center is an orbital singlet, leading to the naive expectation that a linear Stark effect is disallowed. This, however, contradicts experimental observation of $\{\chi_{\perp}^{\mathrm{g}}, \chi_{\parallel}^{\mathrm{g}}\} = \{17, 0.35\}$ Hz/(V/cm) [328]. The conventional explanation is that the ground state inherits a permanent dipole moment from the excited state due to spin-orbit coupling [88, 84]. While such coupling is indeed present, its magnitude is likely insufficient to account for the measured transverse field susceptibility. More recently, it was suggested that the ground state transverse susceptibility arises from the interplay between electric fields and the dipolar spin-spin interaction [84]. In particular, the effect is as follows: At first order in perturbation theory, the ground state wavefunction is mixed with the excited state by the presence of an electric field; this perturbation then couples to the ground-state spin degrees of freedom via the dipolar spin-spin interaction. Below we estimate the magnitude of the effect (which was not reported in [84]) and find good agreement with the known ground state transverse susceptibility (Table 6.3). We also hasten to emphasize that this effect only occurs to leading order for transverse electric fields, which naturally explains the 50-fold anisotropy between $\chi_{\perp}^{\mathrm{g}}$ and $\chi_{\parallel}^{\mathrm{g}}$.

As in the case of the excited state, it is sufficient to consider the transverse susceptibility for a field along the x-axis. At first order in perturbation theory, an electric field $\vec{E} = E_{\perp}\hat{x}$ mixes the ground state $|A_2\rangle$ with the excited state $|Y\rangle$:

$$|A_2'\rangle = |A_2\rangle + \frac{E_{\perp}}{\nu_0} d_{\perp}' |Y\rangle\,, \tag{6.46}$$

where e is the elementary charge, and $\nu_0 \approx 1.9$ eV is the energy splitting between the ground and excited state. $d_{\perp}'$ is the dipole moment associated with the transition between the states,

$$d_{\perp}' = -e\,\langle A_2|\, x_1 + x_2\, |X\rangle\,. \tag{6.47}$$

In the single-particle basis, this becomes

$$|d'_\perp| = e \langle e_x | x | a_1 \rangle \tag{6.48}$$

$$\approx \frac{3e}{\sqrt{6(3+\lambda^2)}} \langle \sigma_1 | x | \sigma_1 \rangle . \tag{6.49}$$

Based on DFT results, we estimate $|d'_\perp| \approx e(0.88\ \mathbf{r}A)$ [117, 84].

To determine the effect on the ground-state spin degrees of freedom, it is then necessary to consider the dipolar spin-spin interaction, given by

$$H_{ss} = \eta \frac{3(\boldsymbol{S}\cdot\hat{r}_{12})(\boldsymbol{S}\cdot\hat{r}_{12}) - \boldsymbol{S}\cdot\boldsymbol{S}}{r_{12}^3} , \tag{6.50}$$

where $\eta = \frac{\mu_0 \mu_B^2 g^2}{8\pi h}$, μ_B is the Bohr magneton, $g_e \approx 2$ is the NV gyromagnetic ratio, $\boldsymbol{S}$ are spin-1 operators, and $\vec{r}_{12}$ is the relative displacement between the two particles. In the absence of an external perturbation, the orbital degrees of freedom are integrated with respect to the ground-state wavefunction $|A_2\rangle$, and the only non-vanishing term is the ground-state splitting, $H^0_{ss} = \Delta_{\mathrm{ZFS}} S_z^2$. For the perturbed wavefunction $|A'_2\rangle$, there is an additional non-vanishing term, corresponding to a ground-state Stark shift:

$$H'_{ss} = \Delta_{\mathrm{ZFS}} S_z^2 + \Pi_\perp (S_y^2 - S_x^2). \tag{6.51}$$

The magnitude of $\Pi_\perp$ is given by

$$\Pi_\perp = 2\frac{E_\perp}{\nu_0} |d'_\perp| D_E \tag{6.52}$$

with

$$D_E = \eta \langle A_2 | \frac{x_{12}^2 - y_{12}^2}{r_{12}^5} | Y \rangle \tag{6.53}$$

$$= \eta \langle a_1 e_y | \frac{x_{12}^2 - y_{12}^2}{r_{12}^5} \left(|e_x e_y\rangle - |e_y e_x\rangle \right) . \tag{6.54}$$

Assuming non-overlapping orbitals, this simplifies to

$$D_E \approx \frac{2\eta}{\sqrt{6(3+\lambda^2)}} \left(\langle \sigma_1 \sigma_2 | \frac{x_{12}^2 - y_{12}^2}{r_{12}^5} | \sigma_1 \sigma_2 \rangle + \langle \sigma_2 \sigma_3 | \frac{x_{12}^2 - y_{12}^2}{r_{12}^5} | \sigma_2 \sigma_3 \rangle \right) . \tag{6.55}$$

We further approximate the two-particle integrals with the semiclassical position of each particle individually [84, 86]:

$$\langle \sigma_1 \sigma_2 | \frac{x_{12}^2 - y_{12}^2}{r_{12}^5} | \sigma_1 \sigma_2 \rangle \approx \frac{\left(\langle x \rangle_1 - \langle x \rangle_2\right)^2 - \left(\langle y \rangle_1 - \langle y \rangle_2\right)^2}{\left(\langle r \rangle_1 - \langle r \rangle_2\right)^5} = \frac{1}{2\left(\langle r \rangle_1 - \langle r \rangle_2\right)^3} = \frac{1}{6\sqrt{3}\langle x \rangle_1^3} \tag{6.56}$$

$$\langle \sigma_2 \sigma_3 | \frac{x_{12}^2 - y_{12}^2}{r_{12}^5} | \sigma_2 \sigma_3 \rangle \approx \frac{\left(\langle x \rangle_2 - \langle x \rangle_3\right)^2 - \left(\langle y \rangle_2 - \langle y \rangle_3\right)^2}{\left(\langle r \rangle_2 - \langle r \rangle_3\right)^5} = \frac{1}{\left(\langle r \rangle_1 - \langle r \rangle_2\right)^3} = \frac{1}{3\sqrt{3}\langle x \rangle_1^3} , \tag{6.57}$$

where $\langle\cdot\rangle_i = \langle\sigma_i|\cdot|\sigma_i\rangle$ and in the final expressions we utilized the triangular symmetry of the carbon orbitals. This leads to

$$D_E \approx \frac{\mu_0 \mu_B^2 g_e^2}{8\pi h\sqrt{2(3+\lambda^2)}} \frac{1}{\langle x\rangle_1^3}. \tag{6.58}$$

Altogether, this predicts a susceptibility of $\chi_\perp^{\mathrm{e}} \approx 76$ Hz/(V/cm), which is within a factor of 5 of the measured value.

Crucially, the spin-spin effect also provides a group theoretic explanation for the large anisotropy between the ground state transverse and longitudinal susceptibilities. In particular, the longitudinal dipole moment between the ground and excited states,

$$d'_\parallel = -e\,\langle A_2|\, z_1 + z_2\,|X\rangle\,, \tag{6.59}$$

vanishes due to symmetry, implying that *only* a transverse electric field can mix the ground and excited states to leading order. We thus postulate that the relatively strong transverse susceptibility arises from the proposed spin-spin effect, while the weak longitudinal effect arises from entirely different physical origin, e.g. based on spin-orbit coupling or the ionic (piezoelectric) effect.

6.2.12 Conclusion

Our work opens the door to a number of intriguing future directions. First, in combination with recent work on diamond-surface-termination [252, 70], our protocol's enhanced sensitivities may help to mitigate the deleterious effects of surface screening, which currently limit the NV's ability to detect external electric fields [46, 306, 236]. Second, our spectroscopy tools are generically applicable to characterizing the charge environment in defect systems. In particular, non-linear Stark shifts, consistent with the presence of local charges, have been observed in a multitude of defects, including: boron-vacancy in h-BN, chromium in diamond, and both silicon-vacancy and divacancies in 4H-SiC [250, 126, 286, 243, 282, 342, 247, 52]. These non-linear Stark effects hinder the accurate experimental determination of susceptibilities, making it challenging to assess the potential of such defect systems for quantum metrology. Finally, our sensitivity scaling analysis suggests that for any defect ensemble exhibiting charge-dominated, inhomogeneous broadening, one can dramatically optimize electric-field sensitivities by carefully tuning the defect density. Such enhanced sensitivities could enable the observation of new quantum transport phenomena [33, 253] as well as mesoscopic quantum thermodynamics studies [242].

6.3 Electric noise sensing for polar and dielectric materials

Having investigated the effect of electric fields on both the ground and excited state manifolds of the NV center, we are equipped to utilize this sensitivity for sensing applications. In this

section, we theoretically propose an electric noise sensing protocol and calculate the expected signal from polar and dielectric materials. We show that polarization fluctuations from this class of materials encode a wealth of information about the associated phases and collective excitations that are difficult to glean through other methods.

6.3.1 Motivation

A qubit sensor with an electric dipole moment acquires an additional contribution to its depolarization rate when it is placed in the vicinity of a polar or dielectric material as a consequence of electrical noise arising from polarization fluctuations in the material. Here, we characterize this relaxation rate as a function of experimentally tunable parameters such as sample-probe distance, probe-frequency, and temperature, and demonstrate that it offers a window into dielectric properties of insulating materials over a wide range of frequencies and length scales. We discuss the experimental feasibility of our proposal and illustrate its ability to probe a variety of phenomena, ranging from collective polar excitations to phase transitions and disorder-dominated physics in relaxor ferroelectrics. Our proposal paves the way for a novel table-top probe of polar and dielectric materials in a parameter regime complementary to existing tools and techniques.

Polar and dielectric materials exhibit a plethora of interesting correlated physics [72, 186, 335, 96] and are emerging as key components in next-generation solid-state technologies [325, 153, 214, 56, 221]. As a consequence, a multitude of techniques for probing them have been developed, ranging from different forms of microscopy and spectroscopy to electrical transport (Fig. 6.10b) [227, 269, 133, 131, 345, 128, 258]. While these methods have led to incredible scientific progress, several outstanding questions, such as the origin of polar instabilities in ultra-thin ferroelectric films [221] and the structure of polar domains in relaxor ferroelectrics [314], remain formidable challenges. In part, this is due to the difficulty of probing the near-equilibrium polar dynamics of thin samples over a wide range of length and time scales simultaneously [221] — which at present requires the use of high-intensity synchrotron light sources. As such, developing a table-top probe with the requisite frequency and spatial resolution would naturally complement existing experimental probes of polar and dielectric materials.

The advent of nanoscale quantum sensors, typically based upon atomic-scale impurities embedded in insulating materials, provides an avenue for developing such a probe. Such sensors are often excellent AC electrometers and magnetometers; they can probe a wide range of frequencies and can locally image both static configurations and dynamic fluctuations of electromagnetic fields with nanoscale resolution [75, 129, 91, 148, 41, 241]. Indeed, a number of theoretical proposals and pioneering experiments have utilized their magnetic field sensing capabilities to probe spin dynamics and electrical current fluctuations in solid-state systems [185, 53, 7, 280, 108, 288, 201, 291, 19, 310, 101, 361, 227, 279, 271, 337, 283, 354, 59, 57, 90, 110, 111, 232, 148, 58].

In this section, we show that the *electrical* sensing capabilities of single-qubit sensors can be used to probe the near-equilibrium physics of polar and dielectric materials, even in

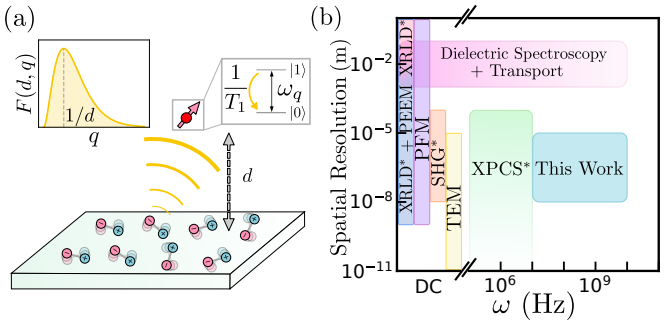

Figure 6.10: (a) Schematic of qubit sensing experiment. A probe qubit (top right), with splitting ω_q, is a distance d away from a polar or dielectric material. Fluctuations in the material's dipoles lead to electrical noise at the location of qubit causing the qubit to relax from $|1\rangle$ to $|0\rangle$ at a rate $1/T_1$. The qubit is sensitive to fluctuations at frequency ω_q and wavevectors near $1/d$ (see filter on top left). (b) Regimes of applicability of qubit sensors and other probes including microscopy techniques [atomic-force, piezoresponse-force, and transmission electron microscopy (AFM, PFM, and TEM)], spectroscopy techniques [x-ray photon correlation, x-ray linear dichroism, and second harmonic generation spectroscopy (XPCS, XRLD, and SHG)] and electrical transport techniques [227, 269, 133, 131, 345, 128, 258]. Techniques that often require high intensity light sources are marked with a $*$.

the thin-film context. In particular, we demonstrate that the relaxation rate of a qubit in the presence of electrical noise arising from such materials encodes the material's dielectric properties at frequencies set by the energy splitting of the qubit and wave vectors set by the qubit-sample distance. Hence, by tuning these two parameters, such qubit sensors can non-invasively and wirelessly probe polar and dielectric materials on frequency scales between 10 MHz $-$ 10 GHz down to nanometer length scales and over a wide range of temperatures, 1 K - 600 K [21, 324, 205]. To highlight the utility of these sensors, we demonstrate how they can (i) detect the presence of exotic collective excitations in polar fluids, (ii) characterize paraelectric-to-ferroelectric phase transitions that underlie polar instabilities, and (iii) probe local polar dynamics in relaxor ferroelectrics. Finally, we illustrate the feasibility of qubit sensing via numerical estimates for the relaxation rate of a nitrogen-vacancy (NV) center in diamond placed near a polar material (strontium titanate).

6.3.2 Qubit Relaxometry Protocol

Our experimental proposal is depicted schematically in Fig. 6.10a wherein we envision an isolated impurity qubit sensor placed a distance d away from a polar or dielectric material. This qubit is a two-level system with a ground state $|0\rangle$ split in energy from an excited state $|1\rangle$ by $\hbar\omega_q$ and its quantum state can be initialized, measured, and manipulated optically. Moreover, we consider qubits with an electric dipole moment $\hat{\mathbf{d}} = d_\perp(\sigma_x\hat{x} + \sigma_y\hat{y})$ and a

magnetic moment $\hat{\boldsymbol{\mu}} = \mu_z \sigma_z \hat{z}$, where $\boldsymbol{\sigma}$ are the Pauli matrices, which specifies their coupling to electromagnetic fields as $H_{\text{q-EM}} = \hat{\mathbf{d}}\cdot\mathbf{E} + \hat{\boldsymbol{\mu}}\cdot\mathbf{B}$. As a result, electric fields $\mathbf{E}$ drive transitions between $|0\rangle$ and $|1\rangle$ and magnetic fields $\mathbf{B}$ can be utilized to control their frequency splitting. When placed close to a polar or dielectric material, electrical noise emanating from the material will couple the two states of the qubit and cause the qubit, initialized in its excited state, to naturally relax to a thermal equilibrium set by the ambient temperature, T. The rate of this relaxation can be expressed in terms of a time-scale, T_1, and can be computed from Fermi's Golden Rule as:

$$\frac{1}{T_1} = \frac{d_\perp^2}{2} \coth\left(\frac{\beta\omega_q}{2}\right) \int_{-\infty}^{\infty} dt\ \langle [E_-(t), E_+(0)]\rangle e^{i\omega_q t} \tag{6.60}$$

where the electrical noise is quantified via the auto-correlation function $\langle [E_-(t), E_+(0)]\rangle$ with $E_\pm = E_x \pm iE_y$, $\beta = 1/k_B T$, and $\langle \cdots \rangle$ denotes thermal averaging. Intuitively, Eq. (6.60) expresses that only electrical noise at a frequency resonant with the splitting of the qubit contributes to its relaxation rate.

To understand how the relaxation rate is connected to the dielectric properties of the underlying material, we note that electrical noise arises due to thermal or quantum fluctuations of the material's polarization density, $\mathbf{P}$. The fluctuations at frequency, ω, and wavevector, $\mathbf{q}$, can be quantified by the retarded polarization correlation function $\chi_{\alpha\beta}(\omega, \mathbf{q}) = i\int_0^\infty dt\, e^{i\omega t}\langle [P_\alpha^\dagger(t, \mathbf{q}), P_\beta(0, \mathbf{q})]\rangle$ $(\alpha, \beta = x, y, z)$ which determines the dielectric tensor of the material, $\varepsilon_{\alpha\beta}(\omega, \mathbf{q})$, and thus encodes its electrical response [141, 127].[14] By utilizing these correlation functions, we can formalize the relationship between fluctuations of polarization in the material and electrical noise at the qubit. For simplicity, we assume that the material is a stack of N, weakly inter-correlated, two-dimensional (2D) monolayers spaced apart by a distance w (modeling a thin-film) and is both translationally and rotationally invariant (see Appendix A for generalizations). From Maxwell's equations, polarization fluctuations of this sample propagate to electrical noise as:

$$\langle [E_-(t), E_+(0)]\rangle = \mu_0^2 \int \frac{d\omega\ d^2\mathbf{q}}{(2\pi)^3}\ F(d, q)\mathcal{C}(\omega, \mathbf{q}) e^{-i\omega t} \tag{6.61}$$

where $\mathcal{C}(\omega, \mathbf{q}) = \text{Im}\left[\chi_{+-}(\omega, \mathbf{q}) + \chi_{-+}(\omega, \mathbf{q}) + 4\chi_{zz}(\omega, \mathbf{q})\right]$, and

$$F(d, q) = \sum_{j=0}^{N-1} q^2 e^{-2q(d+jw)}/16$$

filters polarization fluctuations at different wavevectors. Crucially, $F(d, q)$ is sharply peaked at $q = 1/d$ and so the qubit will only be affected by fluctuations in the polarization around

[14] To be precise, we write the retarded polarization correlation function as $\chi_{\alpha\beta}(\mathbf{q}, \omega) = \hat{q}_\alpha \hat{q}_\beta \chi_L(\mathbf{q}, \omega) + (\delta_{\alpha\beta} - \hat{q}_\alpha \hat{q}_\beta)\chi_T(\mathbf{q}, \omega)$ and decompose the dielectric function as $\varepsilon_{\alpha\beta}(\mathbf{q}, \omega) = \hat{q}_\alpha \hat{q}_\beta \varepsilon_L(\mathbf{q}, \omega) + (\delta_{\alpha\beta} - \hat{q}_\alpha \hat{q}_\beta)\varepsilon_T(\mathbf{q}, \omega)$. Then $\frac{\varepsilon_L(\mathbf{q},\omega)-1}{4\pi\varepsilon_L(\mathbf{q},\omega)} = \chi_L(\mathbf{q}, \omega)$ and $\frac{\varepsilon_T(\mathbf{q},\omega)-1}{4\pi} = \chi_T(\mathbf{q}, \omega)$ [141, 127].

this wavevector. By combining Eqs. (6.60) and (6.61), we find that:

$$\frac{1}{T_1} = \frac{d_\perp^2 \mu_0^2}{2} \coth\left(\frac{\beta\omega_q}{2}\right) \int \frac{d^2\mathbf{q}}{(2\pi)^2} F(d,q)\mathcal{C}(\omega_q, \mathbf{q}) \tag{6.62}$$

Therefore, by tuning the frequency splitting of the qubit ω_q and the qubit-sample distance d, one can effectively reconstruct the functional form of $\mathcal{C}(\omega, \mathbf{q})$.[15] Thus, measuring the qubit's relaxation rate gives one access to the dielectric properties of a proximate material.

A few remarks are in order. First, we note that existing qubit sensing setups have demonstrated the capability to tune a probe qubit's frequency between 10 MHz − 10 GHz, qubit-sample distances down to ~ 10 nm, and temperatures between $1-600$ K [244, 45, 212]. The parameter regimes accessible by qubit sensors and other equilibrium/near-equilibrium probes of polar and dielectric materials are depicted in Fig. 6.10b [227, 269, 133, 131, 345, 128, 258] which highlights the complementary nature of our probe to existing experimental techniques.[16] Second, we note that the frequency scales accessible to qubit sensors are small relative to the excitation energy scales of typical materials ($\sim$ eV). As a result, they will be sensitive to gapless or weakly gapped polar excitations.

6.3.3 Applications

The ability to probe such excitations naturally enables qubit sensors to address questions about polar and dielectric materials relevant to both fundamental and applied science. We examine in detail three such questions.

6.3.3.1 Collective modes in neutral polar fluids

While the existence of "plasmon" collective modes, arising from long-range Coulomb interactions between charged electrons in metals, has been well established [284], the conclusive observation of their dipolar analogues—"dipolarons"—has remained an outstanding challenge [270, 20, 55]. Dipolarons in a 2D dipolar fluid with density, n_d, molecular mass, m, and dipole moment, $\boldsymbol{\mu}$, are predicted to be gapless [270] with an unusual dispersion $\omega_d^2(\mathbf{q}) = v^2q^2 + 2\pi n_d q(\mathbf{q}\cdot\boldsymbol{\mu})^2/m$, which is anisotropic due to the directional dependence of the dipolar interaction. Dispersion in hand, we can predict the frequency and distance scaling of the relaxation rate $1/T_1$ of a nearby qubit. In particular, for a general polar mode with dispersion $\omega(\mathbf{q})$ and gap ω_0, the polarization correlations take the form

[15] We remark that, in principle, by changing the orientation of the qubit sensor, one can extract not only $\mathcal{C}(\omega,\mathbf{q}) = \mathrm{Im}\left[\chi_{+-}(\omega,\mathbf{q}) + \chi_{-+}(\omega,\mathbf{q}) + 4\chi_{zz}(\omega,\mathbf{q})\right]$, but also $\mathrm{Im}\left[\chi_{+-}(\omega,\mathbf{q})\right], \mathrm{Im}\left[\chi_{-+}(\omega,\mathbf{q})\right]$, and $\mathrm{Im}\left[\chi_{zz}(\omega,\mathbf{q})\right]$ individually.

[16] We remark that, because we are interested in probing *near-equilibrium* dynamics, we do not depict time-resolution accessible via pump-probe techniques.

$\chi_{-+}(\omega, \mathbf{q}) \sim (\omega - \omega(\mathbf{q}) + i0^+)^{-1}$ and hence $1/T_1$ is given by:[17]

$$\frac{1}{T_1} \sim \coth\left(\frac{\beta\omega_q}{2}\right) \times \left[e^{-2q_{res}d} q_{res}^2\right] \Theta(\omega_q - \omega_0) \tag{6.63}$$

where q_{res} satisfies $\omega(q_{\text{res}}) = \omega_q$. Thus, for gapless dipolarons in particular, the crossover from a linear to $q^{3/2}$ dispersion with increasing q manifests in a corresponding crossover in the frequency scaling of $1/T_1$ from $\omega_q e^{-2\omega_q d/v}$ to $\sim \omega_q^{1/3} e^{-2(\omega_q)^{2/3} d}$, and can serve as a smoking gun signature of these collective modes.

6.3.3.2 Para/ferroelectric phase transitions

The ability to probe low-energy polar excitations further enables qubit sensors to characterize phase transitions in polar and dielectric materials. While such transitions are well-understood in three dimensions (3D), their nature is unclear in 2D; coupling to additional low-energy modes, irrelevant in 3D, could dramatically alter the universal properties of the transition [257]. Furthermore, previous experiments aimed at fabricating thin-film ferroelectrics for device applications have encountered instabilities in the material's polarization, suspected to be intimately related to the stability of the 2D paraelectric to ferroelectric (PE/FE) phase transition [40]. Motivated by these outstanding questions, we make predictions for the behavior of $1/T_1$ across a continuous PE/FE phase transition.

The PE/FE transition is a structural phase transition accompanied by inversion symmetry breaking and a spontaneously generated polarization density. It can be visualized by considering an ionic crystal with alternating charges $\pm Q$ shown in both the PE and FE phase in Fig. 6.11(a, b) respectively. This transition is driven by the softening of transverse optical phonon modes which correspond to the relative displacement between the $\pm Q$ charges depicted. The mechanism underlying this softening is either thermal or quantum fluctuations depending on whether the transition is driven by temperature (a "thermal phase transition") or a separate tuning parameter λ (e.g. strain) at $T = 0$ (a "quantum phase transition") [284, 305]. If we assume that these phonon modes do not interact and have dispersion $\omega^2(\mathbf{q}) = c_s^2\mathbf{q}^2 + \omega_0^2$ with $\omega_0 \to 0$ at the transition, from Eq. (6.63) we find that once ω_0 is less than the frequency splitting of the qubit, the qubit sensor will detect its presence. Although interactions will dramatically affect the polarization correlations near the transition and hence the scaling of $1/T_1$, this simple analysis illustrates that qubit sensors are ideal for probing the critical physics around the transition. This motivates a more careful analysis of $1/T_1$ around a critical point by using dynamical scaling theories for both thermal and quantum transitions [284].

Around the critical point $\lambda = \lambda_c$, the static correlations of the polarization are set by a diverging correlation length $\xi \propto |\lambda - \lambda_c|^{-\nu}$, while dynamics are strongly constrained by symmetries. Since the polarization density is not conserved, the corresponding dynamics are

[17] We remark that this expression is only valid in the case of an isotropic dispersion but has been generalized in the supplementary material.

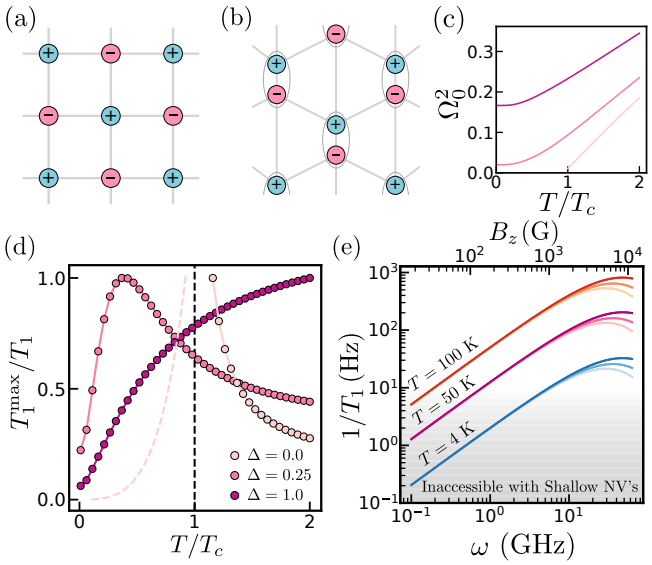

Figure 6.11: (a, b) Schematic of ionic crystal in the (a) PE phase and the (b) FE phase. (c, d) Behavior of $1/T_1$ across a relaxor ferroelectric for disorder $\Delta = 0.0, 0.25, 1.0$ (see Panel (d) for legend). The presence of disorder causes a polarization-carrying mode to open a gap which can drastically change the response of qubit sensors. (e) Numerical estimate for $1/T_1^{\text{sig}}$ compared to intrinsic relaxation rate of the NV qubit as a function of frequency, ω, and applied magnetic field, B_z. $1/T_1$ is depicted for temperatures $T = 4$ K, 50 K, 100 K (shown in blue, purple, and red respectively) and distances $d = 30, 50, 70$ nm (depicted as shading from dark to light). For all parameters shown, the relaxation rate is above experimental limits of $1/T_1$ determined in Ref. [143].

relaxational, characterized by a order-parameter relaxation rate Γ. A key difference between thermal and quantum phase transitions is how they behave upon changing T in the vicinity of the critical point. Thermal transitions are driven by T and hence both ξ and Γ scale as a power law of the distance from the critical point $t = (T - T_c)/T_c$. Consequently, we can conclude using the dynamic scaling theory of critical phenomena [137, 138, 139, 145] that:

$$\frac{1}{T_1} \sim \frac{2T}{d^{2+\eta-z}} \Psi_t \left(\omega d^z, \frac{\xi}{d} \right), \quad \xi \propto |t|^{-\nu} \tag{6.64}$$

where Ψ_t is a scaling function, η, ν, and z are critical exponents. If Ψ_t is smooth in the $\omega \to 0$ limit, then $1/T_1$ scales with qubit-sample distance as $d^{-2-\eta+z}$ at the critical point in stark contrast to the non-critical regime where it scales as $1/d^4$. A change in the distance dependence of T_1 is thus a tell-tale signature of approaching thermal criticality. In addition, a scaling analysis near T_c enables extracting critical exponents η, z and ν. On the other hand, if we tune to a quantum critical point ($\lambda = \lambda_c$) and raise T from 0 K, then the lack of any gap scale in the spectrum ($\omega_0 = 0$) implies that both the correlation length $\xi \sim c_s/T^{1/z}$

and relaxation rate $\Gamma \sim T$ are solely determined by temperature. This can be used to show that $1/T_1$ scales as a power law in T (rather than $T - T_c$), with a distinct distance dependence [285, 284]:

$$\frac{1}{T_1} \propto \begin{cases} T^{(2+\eta)/z} \log\left(\frac{c_s}{dT^{1/z}}\right), & d \ll \xi \\ T^{(-2+\eta)/z} d^{-4}, & d \gg \xi. \end{cases} \tag{6.65}$$

While the distance-scaling of $1/T_1$ informs us of whether we are in the critical regime, its temperature-scaling can be used to determine the critical exponents η and z. Finally, the dependence of the spectral gap $\omega_0 \propto |\lambda - \lambda_c|^{\nu z}$ on the tuning parameter λ, derived from low-T activated behavior of $1/T_1$, may be used to deduce the critical exponent, ν. Thus, all critical exponents for the quantum transition may be deduced by an analysis of the qubit's relaxation rate as a function of T, d and $\lambda - \lambda_c$.

6.3.3.3 Relaxor ferroelectrics

Up until this point, we have explored clean systems without quenched disorder. However, it is known that disorder can dramatically affect the behavior of low-dimensional materials [151]. A prototypical example is in relaxor ferroelectrics (relaxors), dielectric materials characterized by anomalously large internal polar fluctuations resembling "disorder broadened" critical correlations of phase transitions [69, 302, 66, 68, 330]. While a full microscopic description of relaxors remains elusive, their properties are often attributed to competition between the long-range dipolar interaction, which orders internal dipoles, and short-range disorder, which freezes them in a particular direction [134, 135, 330]. This competition is captured by a minimal classical model of dipoles arranged in a 2D lattice [135]:[18]

$$H = \sum_i \left[\frac{\Pi_i^2}{2M} + V(u_i) - h_i u_i\right] - \sum_{i<j} v_{ij} u_i u_j \tag{6.66}$$

where $\Pi_i = M\dot{u}_i$ is the conjugate momentum of the polarization-carrying displacement u_i chosen to be along the z-axis, M is the effective mass, v_{ij} is the dipolar interaction, h_i is a normally distributed random field with width Δ, and $V(u_i) = \frac{\kappa}{2}u_i^2 + \frac{\gamma}{4}u_i^4$ ($\kappa, \gamma > 0$) is an anharmonic potential. When our impurity qubit is far from the material ($d \gg \sqrt{A}$ where A is the area of a polar region), the qubit is insensitive to the local realization of h_i and encodes the disorder-averaged dynamics of the relaxor. Here, the polarization correlations take a damped harmonic form $\chi_{zz}(\omega, \mathbf{q}) = (M\Omega^2(\mathbf{q}) - M\omega^2 + i\omega\Gamma)^{-1}$ where $\Omega^2(\mathbf{q}) = \Omega_0^2 + (v_0 - v_\mathbf{q})$, $v_\mathbf{q}$ is the Fourier transformed dipolar interaction, $v_0 = \lim_{\mathbf{q}\to 0} v_\mathbf{q}$, Γ is a phenomenological damping, and Ω_0 is determined self-consistently in a mean-field analysis and is depicted in Fig. 6.11(c)

[18] Although such a model is known to be unable to capture the complex Vogel-Fuchler dynamics known to be associated with relaxor ferroelectrics, it has been shown to reproduce experimental measurements of the static structure factor.

in the clean, weak disorder, and strong disorder case ($\Delta = 0, 0.25, 1.0$, respectively) [134, 135, 330, 349, 100]. From the mode frequency Ω_0^2 at $\Delta = 0$, we can extract a critical temperature T_c defined as the temperature where the mode becomes massless. Mode frequency and critical temperature in hand, we numerically compute $1/T_1$ in a temperature range around $T = T_c$ and normalize $1/T_1$ by its maximum in that range, $1/T_1^{\max}$ (Fig. 6.11(d)). We find that, in the clean case $\Delta = 0$, the relaxation rate becomes sharply peaked at the location of the phase transition, whereas for weak disorder ($\Delta = 0.25$) the response broadens, reproducing our earlier intuition. For sufficiently large disorder, the peak is removed entirely and the relaxation rate increases monotonically on lowering T.

On the other hand, when our impurity qubit is sufficiently close to the material ($d \sim \sqrt{A}$), the qubit will be able to resolve the microscopic dynamics of individual polar domains and the assumption of translation invariance of Eq. 6.62 will no longer hold. Here we present a qualitative picture of the physics made accessible by spatio-temporally resolving these polar dynamics. Relaxor ferroelectrics are often modeled using polar nano-regions — static nanoscale polar domains with non-zero spontaneous polarization pinned by disorder [168, 259, 99]. The presence of these polar nano-regions with quenched fluctuations would imply a suppressed $1/T_1$ once the qubit is positioned proximal to such a region, and enhanced $1/T_1$ when the qubit is proximal to a domain wall. On the other hand, recent works have suggested a 'slush-water' picture of relaxors [314] characterized by coexisting static (ice-like) domains with frozen moments and dynamic (water-like) domains with fluctuating polarization; near an ice-like domain, $1/T_1$ would be suppressed, while near a water-like domain, $1/T_1$ would be an enhanced. By studying $1/T_1$ of an isolated qubit as a function of in-plane coordinates at a fixed distance $d \lesssim \sqrt{A}$, a spatially resolved map of the static and dynamic domains in an inhomogeneous sample could be obtained and aid in evincing a microscopic description of relaxors.

6.3.4 Experimental Realization and Feasibility

While our previous discussion has theoretically motivated the utility of qubit sensing in probing polar and dielectric materials, here we discuss a concrete realization of the qubit sensing setup and its feasibility. In particular, we envision utilizing the NV center in diamond: a point defect consisting of a nitrogen substitution adjacent to a lattice vacancy defect. The ${}^3A_2$ electronic spin manifold of the NV is modeled as a three-level system ($|0\rangle, |+\rangle$, and $|-\rangle$) and the degenerate $|\pm\rangle$ states are ideal for encoding the two-level qubit of our proposal [225]. Crucially, these degenerate states can be initialized and manipulated optically and read-out through state-dependent fluorescence [87]. Moreover, as required, electric fields drive transitions between these states with dipole moment $d_\perp = 17$ Hz $\cdot$ cm/V and magnetic fields control their splitting with a magnetic moment of $\mu_z = 2.8$ MHz/G [254, 87]. As a result, the energy separation of the NV states can be controlled by local magnetic fields and the qubit-sample distance can be controlled by, for example, placing a nano-diamond with a single NV on a scanning probe tip [19, 108, 361, 185], enabling a measurement of $1/T_1$ as a function of both frequency and distance.

To assess the feasibility of this proposal, we express the relaxation rate of the NV as $T_1^{-1} = (T_1^{\text{sig}})^{-1} + (T_1^{\text{int}})^{-1}$, where $(T_1^{\text{sig}})^{-1}$ accounts for the signal from the sample and $(T_1^{\text{int}})^{-1}$ accounts for intrinsic sources of relaxation from the diamond host; the latter quantity establishes a limit on the sensitivity of our sensing protocol. The magnitude of $(T_1^{\text{int}})^{-1}$ has been reported in shallow NV samples ($\sim$ 50 nm depth) as low as 10 Hz below 100 K [143].[19] The feasibility of our proposal can be established by comparing this noise floor to the expected signal magnitude in a paradigmatic setting: the ionic crystal model introduced earlier with a density ρ, lattice spacing a (See Fig. 6.11(a,b)), and polarization-carrying phonon mode with dispersion $\omega_d(\mathbf{q}) = \sqrt{c_s^2 q^2 + \omega_0^2}$ with c_s equal to the mode speed. In this case, $(T_1^{\text{sig}})^{-1}$ takes the form of Eq. 6.63 with a dimensionful multiplier $\mathcal{N} = (\pi/2c_s^2) \times (\mu_0^2 d_\perp^2 c^4/64\pi) \times [(Q^2/a^4) \times (\hbar/\rho)]$. Choosing material parameters $\{a, \rho, c_s, \omega_0, Q, w, N\} = \{0.3905 \text{ nm}, 183 \text{ amu}/a^2, 7.5 \cdot 10^3 \text{ m/s}, 0 \text{ GHz}, 9.66 \text{ e}, a, 300 \text{ layers}\}$, motivated from a representative dielectric material (thin-film strontium titanate) [359, 160, 350], we can now compare $(T_1^{\text{sig}})^{-1}$ as a function of frequency, distance, and temperature, to our noise floor, $(T_1^{\text{int}})^{-1}$ as depicted in Fig. 6.11(e). For the parameters chosen, the signal magnitude is found to be significantly larger than currently accessible NV intrinsic relaxation rates over a wide range of temperatures and frequencies.

We note that in our feasibility analysis, we assumed that excitations above the ground state are non-interacting and long-lived. While this assumption only holds in the limit of dilute excitations, we expect that the presence of interactions will enhance polarization fluctuations. Hence, our estimate is expected to be a lower bound on the relaxation rate and motivates the feasibility of our method generally. We also remark that we have neglected the contribution of magnetic noise, which induces decay from the NV's $|\pm 1\rangle$ states to $|0\rangle$. While this is appropriate when probing insulating materials because the relaxation rate due to magnetic noise generated from electrical dipoles is smaller than the electrical noise by a factor of $\mu_z^2 c_s^2/d_\perp^2 c^4 \sim 10^{-4} \ll 1$, it is not in general true for metals, where the relaxation rate will be dominated by current fluctuations of itinerant electrons.

6.3.5 Conclusions

In this work, we demonstrated that qubit sensors are a promising table-top tool for studying near-equilibrium dynamics in polar and dielectric materials and can probe even thin-film samples over a wide range of frequencies ($\sim$ 10 MHz $-$ 10 GHz) and temperatures ($1-600$ K) down to the nanometer scale. These capabilities make such sensors sensitive to low energy polar modes, enabling them to probe a variety of physical phenomena, ranging from collective polarization modes in long-range interacting systems, to paraelectric-to-ferroelectric phase transitions and disorder-induced phenomena in relaxor ferroelectrics. Complementary to existing techniques, the nanoscale spatial resolution of qubit sensors allows us to probe local

[19] While most previous reports focus on relaxation between the $|m_s = 0\rangle \Longleftrightarrow |m_s = \pm 1\rangle$ states, we note that our protocol is also affected by relaxation between $|m_s = +1\rangle \Longleftrightarrow |m_s = -1\rangle$ states which has been shown to be significant near surfaces [244].

dynamics in inhomogeneous materials. We briefly comment on a few open directions involving qubit electrometry. First, since previous work has demonstrated the sensing capabilities of impurity qubits at high pressures ($\sim \mathcal{O}(10)$ GPa), such qubits could naturally investigate the influence of stress and strain fields on the dynamics of polarization and could aid in characterizing strain-induced phase transitions [353, 251, 357]. In addition, as illustrated in Eq. (6.62), our qubit probe is more sensitive to surface physics at short sample-probe distances. Consequently, it can be used to resolve surface polarization dynamics, which can be distinct from the bulk [188]. The nanoscale resolution of the qubit is ideally suited to probe unconventional ferroelectricity in moiré materials, which typically have superlattice length scales of tens of nanometers [358, 351]. Finally, by using the electrical capabilities of qubit sensors, highlighted in this work, with the previously established magnetic capabilities, one may be able to probe the complex interplay between charge, polarization, and magnetization found in multiferroic materials [72].

Bibliography

[1] V M Acosta et al. "Broadband magnetometry by infrared-absorption detection of nitrogen-vacancy ensembles in diamond". In: *Applied Physics Letters* 97.17 (Oct. 2010), p. 174104.

[2] V M Acosta et al. "Diamonds with a high density of nitrogen-vacancy centers for magnetometry applications". In: *Physical Review B* 80.11 (Sept. 2009), p. 115202.

[3] V. M. Acosta et al. "Dynamic Stabilization of the Optical Resonances of Single Nitrogen-Vacancy Centers in Diamond". In: *Physical Review Letters* 108.20 (May 2012), p. 206401. ISSN: 0031-9007, 1079-7114. DOI: 10.1103/PhysRevLett.108.206401. URL: https://link.aps.org/doi/10.1103/PhysRevLett.108.206401 (visited on 10/13/2019).

[4] V. M. Acosta et al. "Electromagnetically Induced Transparency in a Diamond Spin Ensemble Enables All-Optical Electromagnetic Field Sensing". In: *Phys. Rev. Lett.* 110 (21 May 2013), p. 213605. DOI: 10.1103/PhysRevLett.110.213605. URL: https://link.aps.org/doi/10.1103/PhysRevLett.110.213605.

[5] VM Acosta et al. "Temperature dependence of the nitrogen-vacancy magnetic resonance in diamond". In: *Phys. Rev. Lett.* 104.7 (2010), p. 070801.

[6] M. H. Acuña et al. "Global Distribution of Crustal Magnetization Discovered by the Mars Global Surveyor MAG/ER Experiment". In: *Science* 284.5415 (1999), pp. 790–793. DOI: 10.1126/science.284.5415.790. eprint: https://www.science.org/doi/pdf/10.1126/science.284.5415.790. URL: https://www.science.org/doi/abs/10.1126/science.284.5415.790.

[7] Kartiek Agarwal et al. "Magnetic noise spectroscopy as a probe of local electronic correlations in two-dimensional systems". In: *Phys. Rev. B* 95 (15 Apr. 2017), p. 155107.

[8] Igor Aharonovich, Dirk Englund, and Milos Toth. "Solid-state single-photon emitters". In: *Nature Photonics* 10.10 (Oct. 2016), pp. 631–641.

[9] Ashok Ajoy and Paola Cappellaro. "Stable three-axis nuclear-spin gyroscope in diamond". In: *Physical Review A* 86.6 (Dec. 2012), p. 062104.

[10] Yuichi Akahama and Haruki Kawamura. "Pressure calibration of diamond anvil Raman gauge to 310GPa". In: *Journal of Applied Physics* 100.4 (2006), p. 043516. DOI: 10.1063/1.2335683. eprint: https://doi.org/10.1063/1.2335683. URL: https://doi.org/10.1063/1.2335683.

[11] Yuichi Akahama and Haruki Kawamura. "Pressure calibration of diamond anvil Raman gauge to 410 GPa". In: *Journal of Physics: Conference Series* 215 (Mar. 2010), p. 012195. DOI: 10.1088/1742-6596/215/1/012195. URL: https://doi.org/10.1088/1742-6596/215/1/012195.

[12] Jagannadham Akella, Gordon S. Smith, and Andrew P. Jephcoat. "High-pressure phase transformation studies in gadolinium to 106 GPa". In: *Journal of Physics and Chemistry of Solids* 49.5 (1988), pp. 573–576. ISSN: 0022-3697. DOI: https://doi.org/10.1016/0022-3697(88)90069-8. URL: http://www.sciencedirect.com/science/article/pii/0022369788900698.

[13] Rinat Akhmedzhanov et al. "Microwave-free magnetometry based on cross-relaxation resonances in diamond nitrogen-vacancy centers". In: *Physical Review A* 96.1 (July 2017), p. 013806. ISSN: 2469-9926, 2469-9934. DOI: 10.1103/PhysRevA.96.013806. URL: http://link.aps.org/doi/10.1103/PhysRevA.96.013806 (visited on 06/02/2020).

[14] Rinat Akhmedzhanov et al. "Optically detected magnetic resonance in negatively charged nitrogen-vacancy centers in diamond under resonant optical excitation at cryogenic temperatures". In: *Physical Review A* 94.6 (Dec. 2016), p. 063859. ISSN: 2469-9926, 2469-9934. DOI: 10.1103/PhysRevA.94.063859. URL: https://link.aps.org/doi/10.1103/PhysRevA.94.063859 (visited on 09/05/2019).

[15] Patricia Lebre Alireza and Gilbert George Lonzarich. "Miniature anvil cell for high-pressure measurements in a commercial superconducting quantum interference device magnetometer". In: *Rev. Sci. Instrum* 80.2 (Feb. 2009), p. 023906. DOI: 10.1063/1.3077303. URL: https://doi.org/10.1063/1.3077303.

[16] Robert Amsüss et al. "Cavity QED with magnetically coupled collective spin states". In: *Physical review letters* 107.6 (2011), p. 060502.

[17] Christopher P. Anderson et al. "Electrical and optical control of single spins integrated in scalable semiconductor devices". In: *Science* 366.6470 (2019), pp. 1225–1230. ISSN: 0036-8075. DOI: 10.1126/science.aax9406. URL: https://science.sciencemag.org/content/366/6470/1225.

[18] M Antolik, D Dreger, and B Romanowicz. "Finite fault source study of the great 1994 deep Bolivia earthquake". In: *Geophysical research letters* 23.13 (1996), pp. 1589–1592.

[19] Amila Ariyaratne et al. "Nanoscale electrical conductivity imaging using a nitrogen-vacancy center in diamond". In: *Nature communications* 9.1 (2018), p. 2406.

[20] G Ascarelli. "Collective modes in dipolar liquids—detection of dipolar plasmons". In: *Chemical Physics Letters* 39.1 (1976), pp. 23–26.

[21] T Astner et al. "Solid-state electron spin lifetime limited by phononic vacuum modes". In: *Nature Materials* 17.4 (Apr. 2018), pp. 313–317.

[22] Mete Atatüre et al. "Material platforms for spin-based photonic quantum technologies". In: *Nat. Rev. Mater.* 3.5 (2018), p. 38.

[23] David D. Awschalom et al. "Quantum technologies with optically interfaced solid-state spins". In: *Nature Photonics* 12.9 (Sept. 2018), pp. 516–527. ISSN: 1749-4893. DOI: 10.1038/s41566-018-0232-2. URL: https://www.nature.com/articles/s41566-018-0232-2 (visited on 06/16/2020).

[24] Gopalakrishnan Balasubramanian et al. "Ultralong spin coherence time in isotopically engineered diamond". In: *Nature Materials* 8.5 (May 2009), pp. 383–387. ISSN: 1476-1122, 1476-4660. DOI: 10.1038/nmat2420. URL: http://www.nature.com/articles/nmat2420 (visited on 03/07/2020).

[25] N Bar-Gill et al. "Solid-state electronic spin coherence time approaching one second". In: *Nature Communications* 4.1 (Apr. 2013), p. 1743.

[26] N. Von Barge and R. Boehler. "Effect of non-hydrostaticity on the $\alpha - \epsilon$ transition of iron". In: *High Pressure Research* 6.2 (1990), pp. 133–140. DOI: 10.1080/08957959008203204. eprint: https://doi.org/10.1080/08957959008203204. URL: https://doi.org/10.1080/08957959008203204.

[27] John F Barry et al. "Optical magnetic detection of single-neuron action potentials using quantum defects in diamond". In: *Proceedings of the National Academy of Sciences* 113.49 (Dec. 2016), pp. 14133–14138.

[28] John F. Barry et al. "Sensitivity optimization for NV-diamond magnetometry". In: *Reviews of Modern Physics* 92.1 (Mar. 2020), p. 015004. ISSN: 0034-6861, 1539-0756. DOI: 10.1103/RevModPhys.92.015004. URL: https://link.aps.org/doi/10.1103/RevModPhys.92.015004 (visited on 06/18/2020).

[29] Michael S J Barson et al. "Nanomechanical Sensing Using Spins in Diamond". In: *Nano Letters* 17.3 (Feb. 2017), pp. 1496–1503.

[30] L. C. Bassett et al. "Electrical Tuning of Single Nitrogen-Vacancy Center Optical Transitions Enhanced by Photoinduced Fields". In: *Phys. Rev. Lett.* 107 (26 Dec. 2011), p. 266403. DOI: 10.1103/PhysRevLett.107.266403. URL: https://link.aps.org/doi/10.1103/PhysRevLett.107.266403.

[31] A. Batalov et al. "Low Temperature Studies of the Excited-State Structure of Negatively Charged Nitrogen-Vacancy Color Centers in Diamond". In: *Physical Review Letters* 102.19 (May 2009), p. 195506. ISSN: 0031-9007, 1079-7114. DOI: 10.1103/PhysRevLett.102.195506.

[32] A. Batalov et al. "Temporal Coherence of Photons Emitted by Single Nitrogen-Vacancy Defect Centers in Diamond Using Optical Rabi-Oscillations". In: *Physical Review Letters* 100.7 (Feb. 2008), p. 077401. ISSN: 0031-9007, 1079-7114. DOI: 10.1103/PhysRevLett.100.077401. URL: https://link.aps.org/doi/10.1103/PhysRevLett.100.077401 (visited on 08/26/2019).

[33] Chinmay Belthangady et al. "Dressed-state resonant coupling between bright and dark spins in diamond". In: *Physical review letters* 110.15 (2013), p. 157601.

[34] Gilad Ben-Shach et al. "Detecting Majorana modes in one-dimensional wires by charge sensing". In: *Physical Review B* 91.4 (Jan. 2015), p. 045403. DOI: 10.1103/PhysRevB.91.045403. URL: https://link.aps.org/doi/10.1103/PhysRevB.91.045403 (visited on 06/16/2020).

[35] Hannes Bernien et al. "Heralded entanglement between solid-state qubits separated by three metres". In: *Nature* 497.7447 (2013), p. 86.

[36] Natalia S Bezaeva et al. "Demagnetization of terrestrial and extraterrestrial rocks under hydrostatic pressure up to 1.2 GPa". In: *Physics of the Earth and Planetary Interiors* 179.1-2 (2010), pp. 7–20. ISSN: 00319201. DOI: 10.1016/j.pepi.2010.01.004.

[37] Natalia S. Bezaeva et al. "Magnetic characterization of non-ideal single-domain monoclinic pyrrhotite and its demagnetization under hydrostatic pressure up to 2GPa with implications for impact demagnetization". In: *Physics of the Earth and Planetary Interiors* 257 (2016), pp. 79–90. ISSN: 0031-9201. DOI: https://doi.org/10.1016/j.pepi.2016.05.009. URL: https://www.sciencedirect.com/science/article/pii/S0031920116300693.

[38] Natalia S. Bezaeva et al. "Pressure demagnetization of the Martian crust: Ground truth from SNC meteorites". In: *Geophysical Research Letters* 34.23 (Dec. 2007), n/a–n/a. ISSN: 00948276. DOI: 10.1029/2007GL031501. URL: http://doi.wiley.com/10.1029/2007GL031501.

[39] S. Bhagavantam and D. a. a. S. Narayana Rao. "Dielectric Constant of Diamond". In: *Nature* 161.4097 (May 1948), pp. 729–729. ISSN: 1476-4687. DOI: 10.1038/161729a0. URL: https://www.nature.com/articles/161729a0 (visited on 03/26/2020).

[40] Lev Mikhailovich Blinov et al. "Two-dimensional ferroelectrics". In: *Physics-Uspekhi* 43.3 (2000), p. 243.

[41] M. Block et al. "Optically Enhanced Electric Field Sensing Using Nitrogen-Vacancy Ensembles". In: *Phys. Rev. Applied* 16 (2 Aug. 2021), p. 024024. DOI: 10.1103/PhysRevApplied.16.024024. URL: https://link.aps.org/doi/10.1103/PhysRevApplied.16.024024.

[42] Dolev Bluvstein, Zhiran Zhang, and Ania C Bleszynski Jayich. "Identifying and mitigating charge instabilities in shallow diamond nitrogen-vacancy centers". In: *Physical review letters* 122.7 (2019), p. 076101.

[43] V. Yu. Bodryakov, A. A. Povzner, and O. G. Zelyukova. "Magnetic contribution to the Debye temperature and the lattice heat capacity of ferromagnetic rare-earth metals (using gadolinium as an example)". In: *Physics of the Solid State* 41.7 (July 1999), pp. 1138–1143.

[44] E Bourgeois et al. "Photoelectric detection of electron spin resonance of nitrogen-vacancy centres in diamond". In: *Nature Communications* 6.1 (Oct. 2015), p. 8577.

[45] Jonathan D Breeze et al. "Continuous-wave room-temperature diamond maser". In: *Nature* 555.7697 (2018), pp. 493–496. ISSN: 1476-4687. DOI: 10.1038/nature25970. URL: https://doi.org/10.1038/nature25970.

[46] D. A. Broadway et al. "Spatial mapping of band bending in semiconductor devices using in situ quantum sensors". In: *Nature Electronics* 1.9 (Sept. 2018), pp. 502–507. ISSN: 2520-1131. DOI: 10.1038/s41928-018-0130-0. URL: https://www.nature.com/articles/s41928-018-0130-0 (visited on 03/16/2020).

[47] R Brout and H Thomas. "Molecular field theory, the Onsager reaction field and the spherical model". In: *Physics Physique Fizika* 3.6 (1967), p. 317.

[48] J Scott Bunch et al. "Electromechanical resonators from graphene sheets". In: *Science* 315.5811 (2007), pp. 490–493.

[49] J Byerlee. "Friction of rocks". In: *pure and applied geophysics* 116.4 (1978), pp. 615–626. ISSN: 1420-9136. DOI: 10.1007/BF00876528. URL: https://doi.org/10.1007/BF00876528.

[50] Jianming Cai, Fedor Jelezko, and Martin B. Plenio. "Hybrid sensors based on colour centres in diamond and piezoactive layers". In: *Nat. Commm.* 5 (June 2014). Article, p. 4065. URL: https://doi.org/10.1038/ncomms5065.

[51] Paola Cappellaro and Mikhail D Lukin. "Quantum correlation in disordered spin systems: Applications to magnetic sensing". In: *Physical Review A* 80.3 (2009), p. 032311.

[52] Charles F. de las Casas et al. "Stark tuning and electrical charge state control of single divacancies in silicon carbide". In: *Applied Physics Letters* 111.26 (Dec. 2017), p. 262403. ISSN: 0003-6951, 1077-3118. DOI: 10.1063/1.5004174. URL: http://aip.scitation.org/doi/10.1063/1.5004174 (visited on 10/05/2020).

[53] Francesco Casola, Toeno van der Sar, and Amir Yacoby. "Probing condensed matter physics with magnetometry based on nitrogen-vacancy centres in diamond". In: *Nat. Rev. Mater.* 3 (Jan. 2018). Review Article, p. 17088. URL: https://doi.org/10.1038/natrevmats.2017.88.

[54] A. Celeste, F. Borondics, and F. Capitani. "Hydrostaticity of pressure-transmitting media for high pressure infrared spectroscopy". In: *High Pressure Research* 39.4 (2019), pp. 608–618. DOI: 10.1080/08957959.2019.1666844. eprint: https://doi.org/10.1080/08957959.2019.1666844. URL: https://doi.org/10.1080/08957959.2019.1666844.

[55] A Chandra and B Bagchi. "Collective excitations in a dense dipolar liquid: How important are dipolarons in the polarization relaxation of common dipolar liquids?" In: *The Journal of chemical physics* 92.11 (1990), pp. 6833–6839.

[56] Sou-Chi Chang et al. "Theoretical Approach to Electroresistance in Ferroelectric Tunnel Junctions". In: *Phys. Rev. Applied* 7 (2 Feb. 2017), p. 024005. DOI: 10.1103/PhysRevApplied.7.024005. URL: https://link.aps.org/doi/10.1103/PhysRevApplied.7.024005.

[57] S Chatterjee et al. "Single-spin qubit magnetic spectroscopy of two-dimensional superconductivity". In: *Phys. Rev. Research* 4 (1 Jan. 2022), p. L012001. DOI: 10.1103/PhysRevResearch.4.L012001. URL: https://link.aps.org/doi/10.1103/PhysRevResearch.4.L012001.

[58] Shubhayu Chatterjee, Francisco Machado, and Norman Y. Yao. "Quantum noise spectroscopy of dynamical critical phenomena". In: *to appear* ().

[59] Shubhayu Chatterjee, Joaquin F. Rodriguez-Nieva, and Eugene Demler. "Diagnosing phases of magnetic insulators via noise magnetometry with spin qubits". In: *Phys. Rev. B* 99 (10 Mar. 2019), p. 104425. DOI: 10.1103/PhysRevB.99.104425. URL: https://link.aps.org/doi/10.1103/PhysRevB.99.104425.

[60] Edward H. Chen et al. "High-sensitivity spin-based electrometry with an ensemble of nitrogen-vacancy centers in diamond". In: *Phys. Rev. A* 95 (5 May 2017), p. 053417. DOI: 10.1103/PhysRevA.95.053417. URL: https://link.aps.org/doi/10.1103/PhysRevA.95.053417.

[61] K. Chen et al. "Surface- and pressure-induced bulk Kondo breakdown in SmB_6". In: *Phys. Rev. B* 97 (23 June 2018), p. 235153. DOI: 10.1103/PhysRevB.97.235153. URL: https://link.aps.org/doi/10.1103/PhysRevB.97.235153.

[62] Lilian Isabel Childress. "Coherent manipulation of single quantum systems in the solid state". PhD thesis. Harvard University, Massachusetts, Dec. 2007.

[63] Y Chu et al. "Coherent Optical Transitions in Implanted Nitrogen Vacancy Centers". In: *Nano Letters* 14.4 (Mar. 2014), pp. 1982–1986.

[64] Yiwen Chu. "Quantum optics with atom-like systems in diamond". PhD thesis. Harvard University, 2014.

[65] Andrew N Cleland and Michael L Roukes. "A nanometre-scale mechanical electrometer". In: *Nature* 392.6672 (1998), pp. 160–162.

[66] RE Cohen. "Relaxors go critical". In: *Nature* 441.7096 (2006), pp. 941–942.

[67] R. V. Colvin, Sam Legvold, and F. H. Spedding. "Electrical Resistivity of the Heavy Rare-Earth Metals". In: *Phys. Rev.* 120 (3 Nov. 1960), pp. 741–745.

[68] RA Cowley et al. "Relaxing with relaxors: a review of relaxor ferroelectrics". In: *Advances in Physics* 60.2 (2011), pp. 229–327.

[69] L Eric Cross. "Relaxor ferroelectrics". In: *Ferroelectrics* 76.1 (1987), pp. 241–267.

[70] Shanying Cui and Evelyn L Hu. "Increased negatively charged nitrogen-vacancy centers in fluorinated diamond". In: *Applied Physics Letters* 103.5 (2013), p. 051603.

[71] S. B. van Dam et al. "Optical coherence of diamond nitrogen-vacancy centers formed by ion implantation and annealing". In: *Physical Review B* 99.16 (Apr. 2019), p. 161203. DOI: 10.1103/PhysRevB.99.161203.

[72] S Das et al. "Observation of room-temperature polar skyrmions". In: *Nature* 568.7752 (2019), pp. 368–372.

[73] Gordon Davies. "Charge states of the vacancy in diamond". In: *Nature* 269.5628 (Oct. 1977), pp. 498–500.

[74] A.Th.A.M. de Waele and R. de Bruyn Ouboter. "Quantum-interference phenomena in point contacts between two superconductors". In: *Physica* 41.2 (1969), pp. 225–254. ISSN: 0031-8914. DOI: https://doi.org/10.1016/0031-8914(69)90116-5. URL: https://www.sciencedirect.com/science/article/pii/0031891469901165.

[75] C. L. Degen, F. Reinhard, and P. Cappellaro. "Quantum sensing". In: *Reviews of Modern Physics* 89.3, 035002 (July 2017), p. 035002. DOI: 10.1103/RevModPhys.89.035002. arXiv: 1611.02427 [quant-ph].

[76] PD Desai et al. *Thermophysical Properties of Selected Rocks.* Tech. rep. THERMOPHYSICAL and ELECTRONIC PROPERTIES INFORMATION ANALYSIS CENTER ..., 1974.

[77] A. Dewaele, P. Loubeyre, and M. Mezouar. "Equations of state of six metals above 94 GPa". In: *Phys. Rev. B* 70.094112 (Apr. 2004).

[78] Agnès Dewaele et al. "Compression curves of transition metals in the Mbar range: Experiments and projector augmented-wave calculations". In: *Physical Review B* 78.10 (2008), p. 104102.

[79] Rudra Sankar Dhar et al. "Direct nanoscale imaging of evolving electric field domains in quantum structures". In: *Scientific reports* 4 (2014), p. 7183.

[80] Ranga P. Dias and Isaac F. Silvera. "Observation of the Wigner-Huntington transition to metallic hydrogen". In: *Science* 355.6326 (2017), pp. 715–718. ISSN: 0036-8075. DOI: 10.1126/science.aal1579. eprint: https://www.science.org/doi/pdf/10.1126/science.aal1579. URL: https://www.science.org/doi/abs/10.1126/science.aal1579.

[81] David P Dobson et al. "The acoustic emissions signature of a pressure-induced polytypic transformation in chlorite". In: *American Mineralogist* 92.2-3 (2007), pp. 437–440.

[82] M. W. Doherty et al. "The negatively charged nitrogen-vacancy centre in diamond: the electronic solution". In: *New Journal of Physics* 13.2 (Feb. 2011), p. 025019. ISSN: 1367-2630. DOI: 10.1088/1367-2630/13/2/025019. URL: https://doi.org/10.1088%2F1367-2630%2F13%2F2%2F025019 (visited on 08/27/2019).

[83] Marcus W Doherty et al. "Electronic Properties and Metrology Applications of the Diamond NV- Center under Pressure". In: *Phys. Rev. Lett.* 112.4 (Jan. 2014), p. 047601.

[84] Marcus W Doherty et al. "Measuring the defect structure orientation of a single NV-centre in diamond". In: *New Journal of Physics* 16.6 (2014), p. 063067.

[85] Marcus W Doherty et al. "The nitrogen-vacancy colour centre in diamond". In: *Physics Reports* 528.1 (2013), pp. 1–45.

[86] Marcus W. Doherty et al. "Electronic Properties and Metrology Applications of the Diamond NV^- Center under Pressure". In: *Phys. Rev. Lett.* 112 (4 Jan. 2014), p. 047601. DOI: 10.1103/PhysRevLett.112.047601. URL: https://link.aps.org/doi/10.1103/PhysRevLett.112.047601.

[87] Marcus W. Doherty et al. "The nitrogen-vacancy colour centre in diamond". In: *Physics Reports* 528.1 (2013), pp. 1–45. ISSN: 0370-1573. DOI: https://doi.org/10.1016/j.physrep.2013.02.001.

[88] Florian Dolde et al. "Electric-field sensing using single diamond spins". In: *Nat. Phys.* 7.6 (2011), p. 459.

[89] Florian Dolde et al. "Nanoscale Detection of a Single Fundamental Charge in Ambient Conditions Using the NV- Center in Diamond". In: *Physical Review Letters* 112.9 (Mar. 2014), p. 097603.

[90] P E Dolgirev et al. "Characterizing two-dimensional superconductivity via nanoscale noise magnetometry with single-spin qubits". In: *Phys. Rev. B* 105 (2 Jan. 2022), p. 024507. DOI: 10.1103/PhysRevB.105.024507. URL: https://link.aps.org/doi/10.1103/PhysRevB.105.024507.

[91] Y Dovzhenko et al. "Magnetostatic twists in room-temperature skyrmions explored by nitrogen-vacancy center spin texture reconstruction". In: *Nat. Commm.* 9.1 (2018), p. 2712.

[92] Y Dovzhenko et al. "Magnetostatic twists in room-temperature skyrmions explored by nitrogen-vacancy center spin texture reconstruction". In: *Nature Communications* 9.1 (2018), p. 2712. ISSN: 2041-1723. DOI: 10.1038/s41467-018-05158-9. URL: https://doi.org/10.1038/s41467-018-05158-9.

[93] A Dréau et al. "Avoiding power broadening in optically detected magnetic resonance of single NV defects for enhanced dc magnetic field sensitivity". In: *Physical Review B* 84.19 (Nov. 2011), p. 195204.

[94] A. P. Drozdov et al. "Conventional superconductivity at 203 kelvin at high pressures in the sulfur hydride system". In: *Nature* 525 (Aug. 2015), p. 73. URL: https://doi.org/10.1038/nature14964.

[95] Chunhui Du et al. "Control and local measurement of the spin chemical potential in a magnetic insulator". In: *Science* 357.6347 (2017), pp. 195–198.

[96] K. Dunnett et al. "Dynamic Multiferroicity of a Ferroelectric Quantum Critical Point". In: *Phys. Rev. Lett.* 122 (5 Feb. 2019), p. 057208. DOI: 10.1103/PhysRevLett.122.057208. URL: https://link.aps.org/doi/10.1103/PhysRevLett.122.057208.

[97] A M Edmonds et al. "Generation of nitrogen-vacancy ensembles in diamond for quantum sensors: Optimization and scalability of CVD processes". In: *arXiv:2004.01746 [cond-mat, physics:quant-ph]* (Apr. 2020).

[98] RJ Epstein et al. "Anisotropic interactions of a single spin and dark-spin spectroscopy in diamond". In: *Nature physics* 1.2 (2005), p. 94.

[99] M Eremenko et al. "Local atomic order and hierarchical polar nanoregions in a classical relaxor ferroelectric". In: *Nature communications* 10.1 (2019), pp. 1–9.

[100] R. P. Erickson. "Long-range dipole-dipole interactions in a two-dimensional Heisenberg ferromagnet". In: *Phys. Rev. B* 46 (21 Dec. 1992), pp. 14194–14197. DOI: 10.1103/PhysRevB.46.14194. URL: https://link.aps.org/doi/10.1103/PhysRevB.46.14194.

[101] A. Ermakova et al. "Detection of a Few Metallo-Protein Molecules Using Color Centers in Nanodiamonds". In: *Nano Letters* 13.7 (2013). PMID: 23738579, pp. 3305–3309. DOI: 10.1021/nl4015233. eprint: https://doi.org/10.1021/nl4015233. URL: https://doi.org/10.1021/nl4015233.

[102] Adrien Facon et al. "A sensitive electrometer based on a Rydberg atom in a Schrödinger-cat state". In: *Nature* 535.7611 (July 2016), pp. 262–265. ISSN: 1476-4687. DOI: 10.1038/nature18327. URL: https://www.nature.com/articles/nature18327 (visited on 11/24/2019).

[103] Abram L Falk et al. "Electrically and mechanically tunable electron spins in silicon carbide color centers". In: *Physical review letters* 112.18 (2014), p. 187601.

[104] Gregory Falkovich. *Fluid Mechanics*. 2nd ed. Cambridge University Press, 2018. DOI: 10.1017/9781316416600.

[105] Haoquan Fan et al. "Atom based RF electric field sensing". In: *Journal of Physics B: Atomic, Molecular and Optical Physics* 48.20 (Sept. 2015), p. 202001. ISSN: 0953-4075. DOI: 10.1088/0953-4075/48/20/202001. URL: https://doi.org/10.1088%2F0953-4075%2F48%2F20%2F202001 (visited on 03/10/2020).

[106] Biao Feng, Valery I Levitas, and Russell J Hemley. "Large elastoplasticity under static megabar pressures: Formulation and application to compression of samples in diamond anvil cells". In: *Int. J. Plasticity* 84 (2016), pp. 33–57.

[107] Yejun Feng, D M Silevitch, and T F Rosenbaum. "A compact bellows-driven diamond anvil cell for high-pressure, low-temperature magnetic measurements". In: *Rev. Sci. Instrum* 85.3 (Mar. 2014), p. 033901. DOI: 10.1063/1.4867078. URL: https://doi.org/10.1063/1.4867078.

[108] Aurore Finco et al. "Imaging non-collinear antiferromagnetic textures via single spin relaxometry". In: *Nature Communications* 12.1 (2021), p. 767. ISSN: 2041-1723. DOI: 10.1038/s41467-021-20995-x. URL: https://doi.org/10.1038/s41467-021-20995-x.

[109] Michael E. Fisher and J. S. Langer. "Resistive Anomalies at Magnetic Critical Points". In: *Phys. Rev. Lett.* 20 (13 Mar. 1968), pp. 665–668.

[110] B. Flebus et al. "Proposal for dynamic imaging of antiferromagnetic domain wall via quantum-impurity relaxometry". In: *Phys. Rev. B* 98 (18 Nov. 2018), p. 180409. DOI: 10.1103/PhysRevB.98.180409. URL: https://link.aps.org/doi/10.1103/PhysRevB.98.180409.

[111] Benedetta Flebus. "Chemical potential of an antiferromagnetic magnon gas". In: *Phys. Rev. B* 100 (6 Aug. 2019), p. 064410. DOI: 10.1103/PhysRevB.100.064410. URL: https://link.aps.org/doi/10.1103/PhysRevB.100.064410.

[112] J. Forneris et al. "Mapping the Local Spatial Charge in Defective Diamond by Means of N-V Sensors—A Self-Diagnostic Concept". In: *Phys. Rev. Applied* 10 (1 July 2018), p. 014024. DOI: 10.1103/PhysRevApplied.10.014024. URL: https://link.aps.org/doi/10.1103/PhysRevApplied.10.014024.

[113] Cliff Frohlich. *Deep earthquakes*. Cambridge university press, 2006.

[114] Kai-Mei C. Fu et al. "Observation of the Dynamic Jahn-Teller Effect in the Excited States of Nitrogen-Vacancy Centers in Diamond". In: *Physical Review Letters* 103.25 (Dec. 2009), p. 256404. ISSN: 0031-9007, 1079-7114. DOI: 10.1103/PhysRevLett.103.256404. URL: https://link.aps.org/doi/10.1103/PhysRevLett.103.256404 (visited on 08/27/2019).

[115] Roger R. Fu et al. "High-Sensitivity Moment Magnetometry With the Quantum Diamond Microscope". In: *Geochemistry, Geophysics, Geosystems* 21.8 (2020). DOI: https://doi.org/10.1029/2020GC009147.

[116] Adam Gali, Maria Fyta, and Efthimios Kaxiras. "Ab initio supercell calculations on nitrogen-vacancy center in diamond: Electronic structure and hyperfine tensors". In: *Phys. Rev. B* 77 (15 Apr. 2008), p. 155206. DOI: 10.1103/PhysRevB.77.155206. URL: https://link.aps.org/doi/10.1103/PhysRevB.77.155206.

[117] Adam Gali, Maria Fyta, and Efthimios Kaxiras. "Ab initio supercell calculations on nitrogen-vacancy center in diamond: Electronic structure and hyperfine tensors". In: *Physical Review B* 77.15 (2008), p. 155206.

[118] Zachary M Geballe and Raymond Jeanloz. "Origin of temperature plateaus in laser-heated diamond anvil cell experiments". In: *Journal of applied physics* 111.12 (2012), p. 123518.

[119] S A Gilder et al. "Anatomy of a pressure-induced, ferromagnetic-to-paramagnetic transition in pyrrhotite: Implications for the formation pressure of diamonds". In: *Journal of Geophysical Research* 116.B10 (Oct. 2011), B10101. ISSN: 0148-0227. DOI: 10.1029/2011JB008292. URL: http://doi.wiley.com/10.1029/2011JB008292.

[120] E. Gilioli. "High pressure and multiferroics materials: a happy marriage." In: *IUCrJ* 1.Pt 6 (1 Nov. 2014), pp. 590–603. ISSN: 2052-2525. DOI: 10.1107/S2052252514020569.

[121] Vittorio Giovannetti, Seth Lloyd, and Lorenzo Maccone. "Quantum-enhanced measurements: beating the standard quantum limit". In: *Science* 306.5700 (2004), pp. 1330–1336.

[122] Gaétan Giriat et al. "Turnbuckle diamond anvil cell for high-pressure measurements in a superconducting quantum interference device magnetometer". In: *Rev. Sci. Instrum* 81.7 (2010), p. 073905. DOI: 10.1063/1.3465311. URL: https://doi.org/10.1063/1.3465311.

[123] David R Glenn et al. "Micrometer-scale magnetic imaging of geological samples using a quantum diamond microscope". In: *Geochem. Geophys.* 18.8 (2017), pp. 3254–3267.

[124] Narayama Golding et al. "Plastic faulting in ice". In: *Journal of Geophysical Research: Solid Earth* 125.5 (2020), e2019JB018749.

[125] J. P. Goss et al. "The Twelve-Line 1.682 eV Luminescence Center in Diamond and the Vacancy-Silicon Complex". In: *Phys. Rev. Lett.* 77 (14 Sept. 1996), pp. 3041–3044. DOI: 10.1103/PhysRevLett.77.3041. URL: https://link.aps.org/doi/10.1103/PhysRevLett.77.3041.

[126] Andreas Gottscholl et al. "Initialization and read-out of intrinsic spin defects in a van der Waals crystal at room temperature". en. In: *Nature Materials* 19.5 (May 2020), pp. 540–545. ISSN: 1476-4660. DOI: 10.1038/s41563-020-0619-6. URL: https://www.nature.com/articles/s41563-020-0619-6 (visited on 10/15/2020).

[127] Christopher G Gray and Keith E Gubbins. *Theory of Molecular Fluids: Volume 1: Fundamentals*. Oxford University Press, 1984.

[128] Jonas Grigas. *Microwave Dielectric Spectroscopy of Ferroelectrics and Related Materials*. CRC Press, June 2019. DOI: 10.1201/9780203747186. URL: https://doi.org/10.1201/9780203747186.

[129] M. S. Grinolds et al. "Nanoscale magnetic imaging of a single electron spin under ambient conditions". In: *Nat Phys* 9.4 (Apr. 2013), pp. 215–219. ISSN: 1745-2473. URL: http://dx.doi.org/10.1038/nphys2543.

[130] Isabell Gross et al. "Real-space imaging of non-collinear antiferromagnetic order with a single-spin magnetometer". In: *Nature* 549.7671 (2017), p. 252.

[131] G. Grübel, A. Madsen, and A. Robert. "X-Ray Photon Correlation Spectroscopy (XPCS)". In: *Soft Matter Characterization*. Springer Netherlands, 2008, pp. 953–995. DOI: 10.1007/978-1-4020-4465-6_18. URL: https://doi.org/10.1007/978-1-4020-4465-6_18.

[132] A Gruber et al. "Scanning Confocal Optical Microscopy and Magnetic Resonance on Single Defect Centers". In: *Science* 276.5321 (June 1997), pp. 2012–2014.

[133] Alexei Gruverman, Marin Alexe, and Dennis Meier. "Piezoresponse force microscopy and nanoferroic phenomena". In: *Nature Communications* 10.1 (Apr. 2019), p. 1661. ISSN: 2041-1723. DOI: 10.1038/s41467-019-09650-8. URL: https://doi.org/10.1038/s41467-019-09650-8.

[134] G. G. Guzmán-Verri, P. B. Littlewood, and C. M. Varma. "Paraelectric and ferroelectric states in a model for relaxor ferroelectrics". In: *Phys. Rev. B* 88 (13 Oct. 2013), p. 134106. DOI: 10.1103/PhysRevB.88.134106. URL: https://link.aps.org/doi/10.1103/PhysRevB.88.134106.

[135] G. G. Guzmán-Verri and C. M. Varma. "Structure factor of a relaxor ferroelectric". In: *Phys. Rev. B* 91 (14 Apr. 2015), p. 144105. DOI: 10.1103/PhysRevB.91.144105. URL: https://link.aps.org/doi/10.1103/PhysRevB.91.144105.

[136] LT Hall et al. "High spatial and temporal resolution wide-field imaging of neuron activity using quantum NV-diamond". In: *Scientific reports* 2 (2012), p. 401.

[137] B. I. Halperin and P. C. Hohenberg. "Scaling Laws for Dynamic Critical Phenomena". In: *Phys. Rev.* 177 (2 Jan. 1969), pp. 952–971. DOI: 10.1103/PhysRev.177.952. URL: https://link.aps.org/doi/10.1103/PhysRev.177.952.

[138] B. I. Halperin, P. C. Hohenberg, and Shang-keng Ma. "Renormalization-group methods for critical dynamics: I. Recursion relations and effects of energy conservation". In: *Phys. Rev. B* 10 (1 July 1974), pp. 139–153. DOI: 10.1103/PhysRevB.10.139. URL: https://link.aps.org/doi/10.1103/PhysRevB.10.139.

[139] B. I. Halperin, P. C. Hohenberg, and Shang-keng Ma. "Renormalization-group methods for critical dynamics: II. Detailed analysis of the relaxational models". In: *Phys. Rev. B* 13 (9 May 1976), pp. 4119–4131. DOI: 10.1103/PhysRevB.13.4119. URL: https://link.aps.org/doi/10.1103/PhysRevB.13.4119.

[140] M. Hanfland and K. Syassen. "A Raman study of diamond anvils under stress". In: *Journal of Applied Physics* 57.8 (1985), pp. 2752–2756. DOI: 10.1063/1.335417. eprint: https://doi.org/10.1063/1.335417. URL: https://doi.org/10.1063/1.335417.

[141] Jean-Pierre Hansen and Ian R McDonald. *Theory of simple liquids*. Elsevier, 1990.

[142] P. Hargraves et al. "Critical magnetic susceptibility of gadolinium". In: *Phys. Rev. B* 38 (4 Aug. 1988), pp. 2862–2864. DOI: 10.1103/PhysRevB.38.2862. URL: https://link.aps.org/doi/10.1103/PhysRevB.38.2862.

[143] A. J. Healey et al. "Comparison of different methods of nitrogen-vacancy layer formation in diamond for wide-field quantum microscopy". In: *Phys. Rev. Materials* 4 (10 Oct. 2020), p. 104605. DOI: 10.1103/PhysRevMaterials.4.104605. URL: https://link.aps.org/doi/10.1103/PhysRevMaterials.4.104605.

[144] B Hensen et al. "Loophole-free Bell inequality violation using electron spins separated by 1.3 kilometres". In: *Nature* 526.7575 (Oct. 2015), pp. 682–686.

[145] P. C. Hohenberg and B. I. Halperin. "Theory of dynamic critical phenomena". In: *Rev. Mod. Phys.* 49 (3 July 1977), pp. 435–479. DOI: 10.1103/RevModPhys.49.435. URL: https://link.aps.org/doi/10.1103/RevModPhys.49.435.

[146] H Horii and Siavouche Nemat-Nasser. "Brittle failure in compression: splitting faulting and brittle-ductile transition". In: *Philosophical Transactions of the Royal Society of London. Series A, Mathematical and Physical Sciences* 319.1549 (1986), pp. 337–374.

[147] Chris Hovde et al. "Measuring electric fields with nitrogen-vacancy ensembles for neutron electric dipole moment experiments". In: *Terahertz, RF, Millimeter, and Submillimeter-Wave Technology and Applications XI*. Ed. by Laurence P. Sadwick and Tianxin Yang. Vol. 10531. International Society for Optics and Photonics. SPIE, 2018, pp. 103–110. DOI: 10.1117/12.2300032. URL: https://doi.org/10.1117/12.2300032.

[148] S. Hsieh et al. "Imaging stress and magnetism at high pressures using a nanoscale quantum sensor". In: *Science* 366.6471 (Dec. 2019), pp. 1349–1354. ISSN: 10959203. DOI: 10.1126/science.aaw4352. eprint: 1812.08796.

[149] Fei Huang et al. "Imaging nanoscale electromagnetic near-field distributions using optical forces". In: *Scientific reports* 5 (2015), p. 10610.

[150] Ryuji Igarashi et al. "Real-Time Background-Free Selective Imaging of Fluorescent Nanodiamonds in Vivo". In: *Nano Letters* 12.11 (Nov. 2012), pp. 5726–5732.

[151] Yoseph Imry and Shang-keng Ma. "Random-Field Instability of the Ordered State of Continuous Symmetry". In: *Phys. Rev. Lett.* 35 (21 Nov. 1975), pp. 1399–1401. DOI: 10.1103/PhysRevLett.35.1399. URL: https://link.aps.org/doi/10.1103/PhysRevLett.35.1399.

[152] N Ishimatsu et al. "Experimental evidence of pressure-induced suppression of the cobalt magnetic moment in $ErCo_2$". In: *Phys. Rev. B* 75.18 (May 2007), p. 180402.

[153] H. Ishiwara. "Ferroelectric random access memories". In: *J Nanosci Nanotechnol* 12.10 (Oct. 2012), pp. 7619–7627.

[154] Mamoru Ishizuka, Kiichi Amaya, and Shoich Endo. "Precise magnetization measurements under high pressures in the diamond-anvil cell". In: *Review of Scientific Instruments* 66.5 (1995), pp. 3307–3310. DOI: 10.1063/1.1145499. eprint: https://doi.org/10.1063/1.1145499. URL: https://doi.org/10.1063/1.1145499.

[155] Tomoharu Iwamoto et al. "Magnetic measurement of rare earth ferromagnet gadolinium under high pressure". In: *Physica B: Condensed Matter* 329-333 (2003). Proceedings of the 23rd International Conference on Low Temperature Physics, pp. 667–668. ISSN: 0921-4526. DOI: https://doi.org/10.1016/S0921-4526(02)02516-4. URL: http://www.sciencedirect.com/science/article/pii/S0921452602025164.

[156] Takayuki Iwasaki et al. "Direct nanoscale sensing of the internal electric field in operating semiconductor devices using single electron spins". In: *ACS nano* 11.2 (2017), pp. 1238–1245.

[157] D D Jackson et al. "High-pressure magnetic susceptibility experiments on the heavy lanthanides Gd, Tb, Dy, Ho, Er, and Tm". In: *Phys. Rev. B* 71.18 (18 May 2005), p. 184416. DOI: 10.1103/PhysRevB.71.184416. URL: https://link.aps.org/doi/10.1103/PhysRevB.71.184416.

[158] D D Jackson et al. "Magnetic susceptibility measurements at high pressure using designer diamond anvils". In: *Rev. Sci. Instrum* 74.4 (Mar. 2003), pp. 2467–2471.

[159] P. Jacobsson and B. Sundqvist. "Thermal conductivity and electrical resistivity of gadolinium as functions of pressure and temperature". In: *Phys. Rev. B* 40 (14 Nov. 1989), pp. 9541–9551. DOI: 10.1103/PhysRevB.40.9541. URL: https://link.aps.org/doi/10.1103/PhysRevB.40.9541.

[160] Anubhav Jain et al. "Commentary: The Materials Project: A materials genome approach to accelerating materials innovation". In: *APL Materials* 1.1 (2013), p. 011002. ISSN: 2166532X. DOI: 10.1063/1.4812323. URL: https://doi.org/10.1063/1.4812323.

[161] P. Jamonneau et al. "Competition between electric field and magnetic field noise in the decoherence of a single spin in diamond". In: *Phys. Rev. B* 93 (2 Jan. 2016), p. 024305. DOI: 10.1103/PhysRevB.93.024305. URL: https://link.aps.org/doi/10.1103/PhysRevB.93.024305.

[162] R. Jaramillo et al. "Signatures of quantum criticality in pure Cr at high pressure". In: *Proceedings of the National Academy of Sciences* 107.31 (2010), pp. 13631–13635. DOI: 10.1073/pnas.1005036107. eprint: https://www.pnas.org/doi/pdf/10.1073/pnas.1005036107. URL: https://www.pnas.org/doi/abs/10.1073/pnas.1005036107.

[163] A Jarmola et al. "Longitudinal spin-relaxation in nitrogen-vacancy centers in electron irradiated diamond". In: *Applied Physics Letters* 107.24 (Dec. 2015), p. 242403.

[164] A Jarmola et al. "Temperature- and Magnetic-Field-Dependent Longitudinal Spin Relaxation in Nitrogen-Vacancy Ensembles in Diamond". In: *Physical Review Letters* 108.19 (May 2012), p. 197601.

[165] A. Jayaraman. "Chapter 9 High pressure studies: Metals, alloys and compounds". In: *Metals*. Vol. 1. Handbook on the Physics and Chemistry of Rare Earths. Elsevier, 1978, pp. 707–747. DOI: https://doi.org/10.1016/S0168-1273(78)01013-2. URL: http://www.sciencedirect.com/science/article/pii/S0168127378010132.

[166] F Jelezko et al. "Single spin states in a defect center resolved by optical spectroscopy". In: *Applied Physics Letters* 81.12 (Sept. 2002), pp. 2160–2162.

[167] K. Jensen et al. "Light narrowing of magnetic resonances in ensembles of nitrogen-vacancy centers in diamond". In: *Physical Review B* 87.1 (Jan. 2013), p. 014115. ISSN: 1098-0121, 1550-235X. DOI: 10.1103/PhysRevB.87.014115. URL: https://link.aps.org/doi/10.1103/PhysRevB.87.014115 (visited on 07/28/2019).

[168] I.-K. Jeong et al. "Direct Observation of the Formation of Polar Nanoregions in $Pb(Mg_{1/3}Nb_{2/3})O_3$ Using Neutron Pair Distribution Function Analysis". In: *Phys. Rev. Lett.* 94 (14 Apr. 2005), p. 147602. DOI: 10.1103/PhysRevLett.94.147602. URL: https://link.aps.org/doi/10.1103/PhysRevLett.94.147602.

[169] Lei Jin et al. "Single action potentials and subthreshold electrical events imaged in neurons with a fluorescent protein voltage probe". In: *Neuron* 75.5 (2012), pp. 779–785.

[170] A. C. Johnson et al. "Singlet-triplet spin blockade and charge sensing in a few-electron double quantum dot". In: *Physical Review B* 72.16 (Oct. 2005), p. 165308. ISSN: 1098-0121, 1550-235X. DOI: 10.1103/PhysRevB.72.165308. URL: https://link.aps.org/doi/10.1103/PhysRevB.72.165308 (visited on 03/13/2020).

[171] Jonathan A Jones et al. "Magnetic field sensing beyond the standard quantum limit using 10-spin NOON states". In: *Science* 324.5931 (2009), pp. 1166–1168.

[172] T. Kamimura et al. "Pressure-induced phase transition in Fe-Se and Fe-S systems with a NiAs-type structure". In: *Journal of Magnetism and Magnetic Materials* 104-107.PART 1 (Feb. 1992), pp. 255–256. ISSN: 03048853. DOI: 10.1016/0304-8853(92)90787-O.

[173] Anastasia P. Kantor et al. "Pressure-Induced Magnetization in FeO: Evidence from Elasticity and Mössbauer Spectroscopy". In: *Phys. Rev. Lett.* 93 (21 Nov. 2004), p. 215502. DOI: 10.1103/PhysRevLett.93.215502. URL: https://link.aps.org/doi/10.1103/PhysRevLett.93.215502.

[174] P Kehayias et al. "Solution nuclear magnetic resonance spectroscopy on a nanostructured diamond chip". In: *Nat. Commm.* 8.1 (2017), p. 188.

[175] P. Kehayias et al. "Infrared absorption band and vibronic structure of the nitrogen-vacancy center in diamond". In: *Physical Review B* 88.16 (Oct. 2013), p. 165202. ISSN: 1098-0121, 1550-235X. DOI: 10.1103/PhysRevB.88.165202. URL: https://link.aps.org/doi/10.1103/PhysRevB.88.165202 (visited on 06/07/2020).

[176] P. Kehayias et al. "Microwave saturation spectroscopy of nitrogen-vacancy ensembles in diamond". In: *Physical Review B* 89.24 (June 2014), p. 245202. DOI: 10.1103/PhysRevB.89.245202. URL: https://link.aps.org/doi/10.1103/PhysRevB.89.245202 (visited on 10/26/2020).

[177] I Khivrich and S Ilani. "Atomic-like charge qubit in a carbon nanotube enabling electric and magnetic field nano-sensing". In: *Nature Communications* 11.1 (2020), p. 2299. ISSN: 2041-1723. DOI: 10.1038/s41467-020-16001-5. URL: https://doi.org/10.1038/s41467-020-16001-5.

[178] Kathleen J Kingma et al. "High-pressure crystalline transformations and amorphization in α-quartz". In: *AIP Conference Proceedings*. Vol. 309. American Institute of Physics. 1994, pp. 39–42.

[179] Stephen H Kirby, William B Durham, and Laura A Stern. "Mantle phase changes and deep-earthquake faulting in subducting lithosphere". In: *Science* 252.5003 (1991), pp. 216–225.

[180] PV Klimov et al. "Electrically driven spin resonance in silicon carbide color centers". In: *Physical Review Letters* 112.8 (2014), p. 087601.

[181] S Klotz et al. "Hydrostatic limits of 11 pressure transmitting media". In: *J Phys D Appl Phys.* 42.7 (Apr. 2009), p. 075413.

[182] Hisao Kobayashi et al. *The effect of pressure on the electronic states of FeS and Fe 7 S 8 studied by Mössbauer spectroscopy*. Tech. rep. 1997, pp. 515–527.

[183] John B. Kogut. "An introduction to lattice gauge theory and spin systems". In: *Rev. Mod. Phys.* 51 (4 Oct. 1979), pp. 659–713.

[184] J. Kölbl et al. "Determination of intrinsic effective fields and microwave polarizations by high-resolution spectroscopy of single nitrogen-vacancy center spins". In: *New Journal of Physics* 21.11 (Nov. 2019), p. 113039. ISSN: 1367-2630. DOI: 10.1088/1367-2630/ab54a8. URL: https://doi.org/10.1088%2F1367-2630%2Fab54a8 (visited on 11/26/2019).

[185] S. Kolkowitz et al. "Probing Johnson noise and ballistic transport in normal metals with a single-spin qubit". In: *Science* 347.6226 (2015), pp. 1129–1132. ISSN: 0036-8075. DOI: 10.1126/science.aaa4298. eprint: http://science.sciencemag.org/content/347/6226/1129.full.pdf. URL: http://science.sciencemag.org/content/347/6226/1129.

[186] Vladyslav Kozii, Zhen Bi, and Jonathan Ruhman. "Superconductivity near a Ferroelectric Quantum Critical Point in Ultralow-Density Dirac Materials". In: *Phys. Rev. X* 9 (3 Sept. 2019), p. 031046. DOI: 10.1103/PhysRevX.9.031046. URL: https://link.aps.org/doi/10.1103/PhysRevX.9.031046.

[187] H. Kraus et al. "Magnetic field and temperature sensing with atomic-scale spin defects in silicon carbide". en. In: *Scientific Reports* 4.1 (July 2014), p. 5303. ISSN: 2045-2322. DOI: 10.1038/srep05303. URL: https://www.nature.com/articles/srep05303 (visited on 10/15/2020).

[188] R. Kretschmer and K. Binder. "Surface effects on phase transitions in ferroelectrics and dipolar magnets". In: *Phys. Rev. B* 20 (3 Aug. 1979), pp. 1065–1076. DOI: 10.1103/PhysRevB.20.1065. URL: https://link.aps.org/doi/10.1103/PhysRevB.20.1065.

[189] MB Kruger and Raymond Jeanloz. "Memory glass: an amorphous material formed from AlPO4". In: *Science* 249.4969 (1990), pp. 647–649.

[190] Y Kubo et al. "Strong Coupling of a Spin Ensemble to a Superconducting Resonator". In: *Physical Review Letters* 105.14 (Sept. 2010), p. 140502.

[191] G. Kucsko et al. "Nanometre-scale thermometry in a living cell". In: *Nature* 500 (July 2013), p. 54. URL: https://doi.org/10.1038/nature12373.

[192] Santosh Kumar et al. "Atom-Based Sensing of Weak Radio Frequency Electric Fields Using Homodyne Readout". In: *Scientific Reports* 7.1 (Feb. 2017), pp. 1–10. ISSN: 2045-2322. DOI: 10.1038/srep42981. URL: https://www.nature.com/articles/srep42981 (visited on 03/10/2020).

[193] Ngoc Diep Lai et al. "Influence of a static magnetic field on the photoluminescence of an ensemble of nitrogen-vacancy color centers in a diamond single-crystal". In: *Applied Physics Letters* 95.13 (2009), p. 133101. DOI: 10.1063/1.3238467. eprint: https://doi.org/10.1063/1.3238467. URL: https://doi.org/10.1063/1.3238467.

[194] Abdelghani Laraoui et al. "Imaging thermal conductivity with nanoscale resolution using a scanning spin probe". In: *Nat. Commm.* 6 (2015), p. 8954. ISSN: 2041-1723. DOI: 10.1038/ncomms9954. URL: http://europepmc.org/articles/PMC4673876.

[195] D. Le Sage et al. "Optical magnetic imaging of living cells". In: *Nature* 496 (Apr. 2013), p. 486. URL: https://doi.org/10.1038/nature12072.

[196] M P Ledbetter et al. "Gyroscopes based on nitrogen-vacancy centers in diamond". In: *Physical Review A* 86.5 (Nov. 2012), p. 052116.

[197] Margarita Lesik et al. "Magnetic measurements on micrometer-sized samples under high pressure using designed NV centers". In: *Science* 366.6471 (2019), pp. 1359–1362. DOI: 10.1126/science.aaw4329. eprint: https://www.science.org/doi/pdf/10.1126/science.aaw4329. URL: https://www.science.org/doi/abs/10.1126/science.aaw4329.

[198] A. O. Levchenko et al. "Inhomogeneous broadening of optically detected magnetic resonance of the ensembles of nitrogen-vacancy centers in diamond by interstitial carbon atoms". In: *Applied Physics Letters* 106.10 (2015), p. 102402. DOI: 10.1063/1.4913428. eprint: https://doi.org/10.1063/1.4913428. URL: https://doi.org/10.1063/1.4913428.

[199] Valery I Levitas. *High pressure phase transformations revisited*. 2018. DOI: 10.1088/1361-648X/aab4b0. URL: https://doi.org/10.1088/1361-648X/aab4b0.

[200] Valery I Levitas et al. "High-density amorphous phase of silicon carbide obtained under large plastic shear and high pressure". In: *Physical Review B* 85.5 (2012), p. 054114.

[201] Changhao Li et al. "All-Optical Quantum Sensing of Rotational Brownian Motion of Magnetic Molecules". In: *Nano Letters* 19.10 (2019). PMID: 31549847, pp. 7342–7348. DOI: 10.1021/acs.nanolett.9b02960. eprint: https://doi.org/10.1021/acs.nanolett.9b02960. URL: https://doi.org/10.1021/acs.nanolett.9b02960.

[202] Qiuzi Li, E. H. Hwang, and S. Das Sarma. "Collective modes of monolayer, bilayer, and multilayer fermionic dipolar liquid". In: *Phys. Rev. B* 82 (23 Dec. 2010), p. 235126. DOI: 10.1103/PhysRevB.82.235126. URL: https://link.aps.org/doi/10.1103/PhysRevB.82.235126.

[203] R Li et al. "Nanoscale Electrometry Based on a Magnetic-Field-Resistant Spin Sensor". In: *Physical Review Letters* 124.24 (June 2020), p. 247701. DOI: 10.1103/PhysRevLett.124.247701. (Visited on 07/06/2020).

[204] Robert J. Lillis et al. "Time history of the Martian dynamo from crater magnetic field analysis". In: *Journal of Geophysical Research E: Planets* 118.7 (2013), pp. 1488–1511. ISSN: 21699100. DOI: 10.1002/jgre.20105.

[205] Gang-Qin Liu et al. "Coherent quantum control of nitrogen-vacancy center spins near 1000 kelvin". In: *Nature communications* 10.1 (2019), pp. 1–8.

[206] Karin L. Louzada, Sarah T. Stewart, and Benjamin P. Weiss. "Effect of shock on the magnetic properties of pyrrhotite, the Martian crust, and meteorites". In: *Geophysical Research Letters* 34.5 (Mar. 2007). ISSN: 00948276. DOI: 10.1029/2006GL027685.

[207] Karin L. Louzada et al. "Impact demagnetization of the Martian crust: Current knowledge and future directions". In: *Earth and Planetary Science Letters* 305.3-4 (May 2011), pp. 257–269. ISSN: 0012821X. DOI: 10.1016/j.epsl.2011.03.013.

[208] Karin L. Louzada et al. "Shock and static pressure demagnetization of pyrrhotite and implications for the Martian crust". In: *Earth and Planetary Science Letters* 290.1-2 (Feb. 2010), pp. 90–101. DOI: 10.1016/j.epsl.2009.12.006.

[209] R. M. Macfarlane. "Analysis of the Spectrum of d3 Ions in Trigonal Crystal Fields". In: *The Journal of Chemical Physics* 39.11 (1963), pp. 3118–3126. DOI: 10.1063/1.1734152. eprint: https://doi.org/10.1063/1.1734152. URL: https://doi.org/10.1063/1.1734152.

[210] BJ Maertz et al. "Vector magnetic field microscopy using nitrogen vacancy centers in diamond". In: *Applied Physics Letters* 96.9 (2010), p. 092504.

[211] T. H. Maiman. "Optical and Microwave-Optical Experiments in Ruby". In: *Phys. Rev. Lett.* 4 (11 June 1960), pp. 564–566. DOI: 10.1103/PhysRevLett.4.564. URL: https://link.aps.org/doi/10.1103/PhysRevLett.4.564.

[212] Patrick Maletinsky et al. "A robust scanning diamond sensor for nanoscale imaging with single nitrogen-vacancy centres". In: *Nat. Nanotechnol.* 7.5 (2012), p. 320.

[213] HJ Mamin et al. "Nanoscale nuclear magnetic resonance with a nitrogen-vacancy spin sensor". In: *Science* 339.6119 (2013), pp. 557–560.

[214] Sasikanth Manipatruni et al. "Scalable energy-efficient magnetoelectric spin–orbit logic". In: *Nature* 565.7737 (Jan. 2019), pp. 35–42. ISSN: 1476-4687. DOI: 10.1038/s41586-018-0770-2. URL: https://doi.org/10.1038/s41586-018-0770-2.

[215] Neil B Manson et al. "NV-–N+ pair centre in 1b diamond". In: *New Journal of Physics* 20.11 (Nov. 2018), p. 113037. DOI: 10.1088/1367-2630/aaec58. URL: https://doi.org/10.1088/1367-2630/aaec58.

[216] Neil B. Manson et al. "NV-–N$\mathplus$ pair centre in 1b diamond". In: *New Journal of Physics* 20.11 (Nov. 2018), p. 113037. ISSN: 1367-2630. DOI: 10.1088/1367-2630/aaec58. URL: https://doi.org/10.1088%2F1367-2630%2Faaec58 (visited on 11/26/2019).

[217] Ho-Kwang Mao et al. "Solids, liquids, and gases under high pressure". In: *Rev. Mod. Phys.* 90.1 (1 Mar. 2018), p. 015007. DOI: 10.1103/RevModPhys.90.015007. URL: https://link.aps.org/doi/10.1103/RevModPhys.90.015007.

[218] Adrien Marizy et al. "A symmetric miniature diamond anvil cell for magnetic measurements on dense hydrides in a SQUID magnetometer". In: *High Press. Res.* 37.4 (2017), pp. 465–474. DOI: 10.1080/08957959.2017.1387255. URL: https://doi.org/10.1080/08957959.2017.1387255.

[219] X Markenscoff. "Cracks as limits of Eshelby inclusions". In: *Physical Mesomechanics* 22.1 (2019), pp. 42–45.

[220] Xanthippi Markenscoff. "Self-similarly expanding regions of phase change yield cavitational instabilities and model deep earthquakes". In: *Journal of the Mechanics and Physics of Solids* 127 (2019), pp. 167–181.

[221] Lane W. Martin and Andrew M. Rappe. "Thin-film ferroelectric materials and their applications". In: *Nature Reviews Materials* 2 (Nov. 2016), p. 16087. ISSN: 2058-8437.

[222] O Mathon et al. "XMCD under pressure at the Fe K edge on the energy-dispersive beamline of the ESRF. - PubMed - NCBI". In: *Journal of Synchrotron Radiation* 11.5 (Aug. 2004), pp. 423–427.

[223] Y Matsuzaki et al. "Optically detected magnetic resonance of high-density ensemble of NV^- centers in diamond". In: *Journal of Physics: Condensed Matter* 28.27 (July 2016), p. 275302.

[224] J R Maze et al. "Properties of nitrogen-vacancy centers in diamond: the group theoretic approach". In: *New Journal of Physics* 13.2 (Feb. 2011), p. 025025.

[225] J R Maze et al. "Properties of nitrogen-vacancy centers in diamond: the group theoretic approach". In: *New Journal of Physics* 13.2 (Feb. 2011), p. 025025. DOI: 10.1088/1367-2630/13/2/025025. URL: https://doi.org/10.1088/1367-2630/13/2/025025.

[226] JR Maze et al. "Nanoscale magnetic sensing with an individual electronic spin in diamond". In: *Nature* 455.7213 (2008), p. 644.

[227] Brendan A. McCullian et al. "Broadband multi-magnon relaxometry using a quantum spin sensor for high frequency ferromagnetic dynamics sensing". In: *Nature Communications* 11.1 (Dec. 2020), p. 5229. ISSN: 2041-1723. DOI: 10.1038/s41467-020-19121-0. URL: http://www.nature.com/articles/s41467-020-19121-0 (visited on 09/04/2021).

[228] L. P. McGuinness et al. "Quantum measurement and orientation tracking of fluorescent nanodiamonds inside living cells". In: *Nature Nanotechnology* 6 (May 2011), p. 358. URL: http://dx.doi.org/10.1038/nnano.2011.64.

[229] Gregory C McLaskey and Steven D Glaser. "Acoustic emission sensor calibration for absolute source measurements". In: *Journal of Nondestructive Evaluation* 31.2 (2012), pp. 157–168.

[230] Gregory C McLaskey and Steven D Glaser. "Mechanisms of sliding friction studied with an array of industrial conical piezoelectric sensors". In: *Sensors and Smart Structures Technologies for Civil, Mechanical, and Aerospace Systems 2010*. Vol. 7647. SPIE. 2010, pp. 440–448.

[231] Gregory C McLaskey et al. "Fault healing promotes high-frequency earthquakes in laboratory experiments and on natural faults". In: *Nature* 491.7422 (2012), pp. 101–104.

[232] Nathan J. McLaughlin et al. "Strong Correlation Between Superconductivity and Ferromagnetism in an Fe-Chalcogenide Superconductor". In: *Nano Letters* 21.17 (2021). PMID: 34415171, pp. 7277–7283. DOI: 10.1021/acs.nanolett.1c02424. URL: https://doi.org/10.1021/acs.nanolett.1c02424.

[233] D. B. McWhan and A. L. Stevens. "Effect of Pressure on the Magnetic Properties and Crystal Structure of Gd, Tb, Dy, and Ho". In: *Phys. Rev.* 139.3A (3A Aug. 1965), A682–A689. DOI: 10.1103/PhysRev.139.A682. URL: https://link.aps.org/doi/10.1103/PhysRev.139.A682.

[234] Charles Meade and Raymond Jeanloz. "Acoustic emissions and shear instabilities during phase transformations in Si and Ge at ultrahigh pressures". In: *Nature* 339.6226 (1989), pp. 616–618. ISSN: 1476-4687. DOI: 10.1038/339616a0. URL: https://doi.org/10.1038/339616a0.

[235] Charles Meade and Raymond Jeanloz. "Deep-focus earthquakes and recycling of water into the Earth's mantle". In: *Science* 252.5002 (1991), pp. 68–72.

[236] M. Mertens et al. "Patterned hydrophobic and hydrophilic surfaces of ultra-smooth nanocrystalline diamond layers". In: *Applied Surface Science* 390 (Dec. 2016), pp. 526–530. ISSN: 0169-4332. DOI: 10.1016/j.apsusc.2016.08.130. URL: http://www.sciencedirect.com/science/article/pii/S016943321631786X (visited on 03/16/2020).

[237] Julia Michl et al. "Robust and Accurate Electric Field Sensing with Solid State Spin Ensembles". In: *Nano Letters* 19.8 (Aug. 2019), pp. 4904–4910. ISSN: 1530-6984, 1530-6992. DOI: 10.1021/acs.nanolett.9b00900. URL: https://pubs.acs.org/doi/10.1021/acs.nanolett.9b00900 (visited on 10/18/2019).

[238] Vasily Minkov et al. "The Meissner effect in high-temperature hydrogen-rich superconductors under high pressure". In: (Sept. 2021). DOI: 10.21203/rs.3.rs-936317/v1.

[239] M. Mito et al. "Pressure effects on an organic radical ferromagnet: 2,5-difluorophenyl-α-nitronyl nitroxide". In: *Phys. Rev. B* 67 (2 Jan. 2003), p. 024427. DOI: 10.1103/PhysRevB.67.024427. URL: https://link.aps.org/doi/10.1103/PhysRevB.67.024427.

[240] Masaki Mito et al. "Development of Miniature Diamond Anvil Cell for the Superconducting Quantum Interference Device Magnetometer". In: *Japanese J. Appl. Phys* 40.11R (2001), p. 6641. URL: http://stacks.iop.org/1347-4065/40/i=11R/a=6641.

[241] Thomas Mittiga et al. "Imaging the local charge environment of nitrogen-vacancy centers in diamond". In: *Phys. Rev. Lett.* 121.24 (2018), p. 246402.

[242] M Hamed Mohammady et al. "Low-control and robust quantum refrigerator and applications with electronic spins in diamond". In: *Physical Review A* 97.4 (2018), p. 042124.

[243] T Müller et al. "Wide-range electrical tunability of single-photon emission from chromium-based colour centres in diamond". In: *New Journal of Physics* 13.7 (July 2011), p. 075001. ISSN: 1367-2630. DOI: 10.1088/1367-2630/13/7/075001. URL: https://iopscience.iop.org/article/10.1088/1367-2630/13/7/075001 (visited on 10/05/2020).

[244] B. A. Myers, A. Ariyaratne, and A. C. Bleszynski Jayich. "Double-Quantum Spin-Relaxation Limits to Coherence of Near-Surface Nitrogen-Vacancy Centers". In: *Phys. Rev. Lett.* 118 (19 May 2017), p. 197201. DOI: 10.1103/PhysRevLett.118.197201. URL: https://link.aps.org/doi/10.1103/PhysRevLett.118.197201.

[245] Robert M Nadeau and Lane R Johnson. "Seismological studies at Parkfield VI: Moment release rates and estimates of source parameters for small repeating earthquakes". In: *Bulletin of the Seismological Society of America* 88.3 (1998), pp. 790–814.

[246] Bartholomew Nagy and George T Faust. "Serpentines: natural mixtures of chrysotile and antigorite". In: *American Mineralogist: Journal of Earth and Planetary Materials* 41.11-12 (1956), pp. 817–838.

[247] Roland Nagy et al. "High-fidelity spin and optical control of single silicon-vacancy centres in silicon carbide". In: *Nature communications* 10.1 (2019), pp. 1–8.

[248] Jeffrey H Nguyen, Michael B Kruger, and Raymond Jeanloz. "Evidence for "partial"(sublattice) amorphization in Co (OH) 2". In: *Physical Review Letters* 78.10 (1997), p. 1936.

[249] H. E. Nigh, S. Legvold, and F. H. Spedding. "Magnetization and Electrical Resistivity of Gadolinium Single Crystals". In: *Phys. Rev.* 132 (3 Nov. 1963), pp. 1092–1097.

[250] Gichang Noh et al. "Stark Tuning of Single-Photon Emitters in Hexagonal Boron Nitride". In: *Nano Letters* 18.8 (Aug. 2018), pp. 4710–4715. ISSN: 1530-6984. DOI: 10.1021/acs.nanolett.8b01030. URL: https://doi.org/10.1021/acs.nanolett.8b01030 (visited on 10/05/2020).

[251] T. F. Nova et al. "Metastable ferroelectricity in optically strained SrTiO¡sub¿3¡/sub¿". In: *Science* 364.6445 (2019), pp. 1075–1079. DOI: 10.1126/science.aaw4911.

[252] L.M. Oberg et al. "Solution to Electric Field Screening in Diamond Quantum Electrometers". In: *Phys. Rev. Applied* 14 (1 July 2020), p. 014085. DOI: 10.1103/PhysRevApplied.14.014085. URL: https://link.aps.org/doi/10.1103/PhysRevApplied.14.014085.

[253] Lachlan M Oberg et al. "Spin coherent quantum transport of electrons between defects in diamond". In: *Nanophotonics* 8.11 (2019), pp. 1975–1984.

[254] Eric Van Oort and Max Glasbeek. "Electric-field-induced modulation of spin echoes of N-V centers in diamond". In: *Chemical Physics Letters* 168.6 (1990), pp. 529–532. ISSN: 0009-2614. DOI: https://doi.org/10.1016/0009-2614(90)85665-Y. URL: http://www.sciencedirect.com/science/article/pii/000926149085665Y.

[255] László Oroszlány et al. "Magnetism of gadolinium: a first-principles perspective". In: *Phys. Rev. Lett.* 115.9 (2015), p. 096402.

[256] Preeti Ovartchaiyapong et al. "Dynamic strain-mediated coupling of a single diamond spin to a mechanical resonator". In: *Nat. Commm.* 5 (2014), p. 4429.

[257] L. Pálová, P. Chandra, and P. Coleman. "Quantum critical paraelectrics and the Casimir effect in time". In: *Phys. Rev. B* 79 (7 Feb. 2009), p. 075101. DOI: 10.1103/PhysRevB.79.075101. URL: https://link.aps.org/doi/10.1103/PhysRevB.79.075101.

[258] Eric Parsonnet et al. "Toward Intrinsic Ferroelectric Switching in Multiferroic $BiFeO_3$". In: *Phys. Rev. Lett.* 125 (6 Aug. 2020), p. 067601. DOI: 10.1103/PhysRevLett.125.067601. URL: https://link.aps.org/doi/10.1103/PhysRevLett.125.067601.

[259] M Paściak et al. "Polar nanoregions and diffuse scattering in the relaxor ferroelectric PbMg 1/3 Nb 2/3 O 3". In: *Physical Review B* 85.22 (2012), p. 224109.

[260] M. P. Pasternak, R. D. Taylor, and Raymond Jeanloz. "Pressure-induced Mott transition in transition-metal iodides (invited)". In: *J. Appl. Phys* 70.10 (1991), pp. 5956–5960. DOI: 10.1063/1.350089. eprint: https://doi.org/10.1063/1.350089. URL: https://doi.org/10.1063/1.350089.

[261] M. P. Pasternak et al. "Pressure-induced magnetic and electronic transitions in the layered Mott insulator FeI_2". In: *Phys. Rev. B* 65 (3 Dec. 2001), p. 035106. DOI: 10.1103/PhysRevB.65.035106. URL: https://link.aps.org/doi/10.1103/PhysRevB.65.035106.

[262] Mervyn S Paterson and Teng-fong Wong. *Experimental rock deformation-the brittle field*. Springer Science & Business Media, 2005, pp. 211–237.

[263] Matthew Pelliccione et al. "Scanned probe imaging of nanoscale magnetism at cryogenic temperatures with a single-spin quantum sensor". In: *Nature nanotechnology* 11.8 (2016), p. 700.

[264] Matthias Pfender et al. "Protecting a Diamond Quantum Memory by Charge State Control". In: *Nano Letters* 17.10 (2017). PMID: 28872881, pp. 5931–5937. DOI: 10.1021/acs.nanolett.7b01796. eprint: https://doi.org/10.1021/acs.nanolett.7b01796. URL: https://doi.org/10.1021/acs.nanolett.7b01796.

[265] L M Pham et al. "Magnetic field imaging with nitrogen-vacancy ensembles". In: *New Journal of Physics* 13.4 (Apr. 2011), p. 045021.

[266] Linh Pham. "Magnetic Field Sensing with Nitrogen-Vacancy Color Centers in Diamond". PhD thesis. Harvard University, 2013.

[267] Linh My Pham. "Magnetic Field Sensing with Nitrogen-Vacancy Color Centers in Diamond". PhD thesis. Harvard University, Massachusetts, 2013.

[268] Taras Plakhotnik et al. "All-Optical Thermometry and Thermal Properties of the Optically Detected Spin Resonances of the NV– Center in Nanodiamond". In: *Nano Letters* 14.9 (2014). PMID: 25102035, pp. 4989–4996. DOI: 10.1021/nl501841d. eprint: https://doi.org/10.1021/nl501841d. URL: https://doi.org/10.1021/nl501841d.

[269] S Polisetty et al. "X-ray linear dichroism dependence on ferroelectric polarization". In: *Journal of Physics: Condensed Matter* 24.24 (May 2012), p. 245902. DOI: 10.1088/0953-8984/24/24/245902. URL: https://doi.org/10.1088/0953-8984/24/24/245902.

[270] E. L. Pollock and B. J. Alder. "Frequency-Dependent Dielectric Response in Polar Liquids". In: *Phys. Rev. Lett.* 46 (14 Apr. 1981), pp. 950–953. DOI: 10.1103/PhysRevLett.46.950. URL: https://link.aps.org/doi/10.1103/PhysRevLett.46.950.

[271] D Prananto et al. "Probing Thermal Magnon Current Mediated by Coherent Magnon via Nitrogen-Vacancy Centers in Diamond". In: *Phys. Rev. Applied* 16 (6 Dec. 2021), p. 064058. DOI: 10.1103/PhysRevApplied.16.064058.

[272] Klaus Regenauer-Lieb and DA Yuen. "Modeling shear zones in geological and planetary sciences: solid-and fluid-thermal–mechanical approaches". In: *Earth-Science Reviews* 63.3-4 (2003), pp. 295–349.

[273] Bruno Reynard et al. "Elasticity of serpentines and extensive serpentinization in subduction zones". In: *Geophysical Research Letters* 34.13 (2007).

[274] Eva Rittweger et al. "STED microscopy reveals crystal colour centres with nanometric resolution". In: *Nature Photonics* 3.3 (2009), p. 144.

[275] L Robledo et al. "Spin dynamics in the optical cycle of single nitrogen-vacancy centres in diamond". In: *New Journal of Physics* 13.2 (Feb. 2011), p. 025013. ISSN: 1367-2630. DOI: 10.1088/1367-2630/13/2/025013.

[276] Lucio Robledo et al. "High-fidelity projective read-out of a solid-state spin quantum register". In: *Nature* 477.7366 (Sept. 2011), pp. 574–578. ISSN: 1476-4687. DOI: 10.1038/nature10401. URL: https://www.nature.com/articles/nature10401 (visited on 04/02/2020).

[277] P. Rochette et al. "High pressure magnetic transition in pyrrhotite and impact demagnetization on Mars". In: *Geophysical Research Letters* 30.13 (July 2003). ISSN: 00948276. DOI: 10.1029/2003GL017359.

[278] Pierre Rochette et al. "Pyrrhotite and the remanent magnetization of SNC meteorites: A changing perspective on Martian magnetism". In: *Earth and Planetary Science Letters* 190.1-2 (2001), pp. 1–12. ISSN: 0012821X. DOI: 10.1016/S0012-821X(01)00373-9.

[279] Joaquin F. Rodriguez-Nieva, Daniel Podolsky, and Eugene Demler. "Hydrodynamic sound modes and Galilean symmetry breaking in a magnon fluid". In: *arXiv* (Oct. 2018), p. 1810.12333.

[280] Joaquin F. Rodriguez-Nieva et al. "Probing one-dimensional systems via noise magnetometry with single spin qubits". In: *Phys. Rev. B* 98 (19 Nov. 2018), p. 195433. DOI: 10.1103/PhysRevB.98.195433. URL: https://link.aps.org/doi/10.1103/PhysRevB.98.195433.

[281] L Rondin et al. "Magnetometry with nitrogen-vacancy defects in diamond". In: *Reports on Progress in Physics* 77.5 (May 2014), p. 056503.

[282] Maximilian Rühl et al. "Stark Tuning of the Silicon Vacancy in Silicon Carbide". In: *Nano Letters* 20.1 (Jan. 2020), pp. 658–663. ISSN: 1530-6984, 1530-6992. DOI: 10.1021/acs.nanolett.9b04419. URL: https://pubs.acs.org/doi/10.1021/acs.nanolett.9b04419 (visited on 10/05/2020).

[283] Avinash Rustagi et al. "Sensing chiral magnetic noise via quantum impurity relaxometry". In: *Phys. Rev. B* 102 (22 Dec. 2020), p. 220403. DOI: 10.1103/PhysRevB.102.220403. URL: https://link.aps.org/doi/10.1103/PhysRevB.102.220403.

[284] Subir Sachdev. "Quantum phase transitions". In: *Handbook of Magnetism and Advanced Magnetic Materials* (2007).

[285] Subir Sachdev. "Universal, finite-temperature, crossover functions of the quantum transition in the Ising chain in a transverse field". In: *Nuclear Physics B* 464.3 (Feb. 1996), pp. 576–595. DOI: 10.1016/0550-3213(95)00657-5. arXiv: cond-mat/9509147 [cond-mat].

[286] A. Sajid et al. "Edge effects on optically detected magnetic resonance of vacancy defects in hexagonal boron nitride". en. In: *Communications Physics* 3.1 (Aug. 2020), pp. 1–8. ISSN: 2399-3650. DOI: 10.1038/s42005-020-00416-z. URL: https://www.nature.com/articles/s42005-020-00416-z (visited on 10/08/2020).

[287] Gopi K. Samudrala et al. "Structural and magnetic phase transitions in gadolinium under high pressures and low temperatures". In: *High Press. Res.* 34.4 (2014), pp. 385–391. DOI: 10.1080/08957959.2014.977277. eprint: https://doi.org/10.1080/08957959.2014.977277. URL: https://doi.org/10.1080/08957959.2014.977277.

[288] Eike Schäfer-Nolte et al. "Tracking Temperature-Dependent Relaxation Times of Ferritin Nanomagnets with a Wideband Quantum Spectrometer". In: *Phys. Rev. Lett.* 113 (21 Nov. 2014), p. 217204. DOI: 10.1103/PhysRevLett.113.217204. URL: https://link.aps.org/doi/10.1103/PhysRevLett.113.217204.

[289] Arthur L. Schawlow. "Spectroscopy in a new light". en. In: *Reviews of Modern Physics* 54.3 (July 1982), pp. 697–707. ISSN: 0034-6861. DOI: 10.1103/RevModPhys.54.697. URL: https://link.aps.org/doi/10.1103/RevModPhys.54.697 (visited on 10/26/2020).

[290] Romana Schirhagl et al. "Nitrogen-Vacancy Centers in Diamond: Nanoscale Sensors for Physics and Biology". In: *Annual Review of Physical Chemistry* 65.1 (2014). PMID: 24274702, pp. 83–105. DOI: 10.1146/annurev-physchem-040513-103659. eprint: https://doi.org/10.1146/annurev-physchem-040513-103659. URL: https://doi.org/10.1146/annurev-physchem-040513-103659.

[291] Dominik Schmid-Lorch et al. "Relaxometry and Dephasing Imaging of Superparamagnetic Magnetite Nanoparticles Using a Single Qubit". In: *Nano Letters* 15.8 (2015). PMID: 26218205, pp. 4942–4947. DOI: 10.1021/acs.nanolett.5b00679. eprint: https://doi.org/10.1021/acs.nanolett.5b00679. URL: https://doi.org/10.1021/acs.nanolett.5b00679.

[292] R. J. Schoelkopf et al. "The Radio-Frequency Single-Electron Transistor (RF-SET): A Fast and Ultrasensitive Electrometer". In: *Science* 280.5367 (May 1998), pp. 1238–1242. ISSN: 0036-8075, 1095-9203. DOI: 10.1126/science.280.5367.1238. URL: https://science.sciencemag.org/content/280/5367/1238.

[293] Alexandre Schubnel et al. "Deep-focus earthquake analogs recorded at high pressure and temperature in the laboratory". In: *Science* 341.6152 (2013), pp. 1377–1380.

[294] Sarvagya Sharma et al. "Electric and magnetic sensing with NV ensembles in diamonds". In: *Quantum Sensing and Nano Electronics and Photonics XIV*. Ed. by Manijeh Razeghi. Vol. 10111. International Society for Optics and Photonics. SPIE, 2017, pp. 436–444. DOI: 10.1117/12.2252562. URL: https://doi.org/10.1117/12.2252562.

[295] Sarvagya Sharma et al. "Imaging Strain and Electric Fields in NV Ensembles using Stark Shift Measurements". In: *arXiv preprint arXiv:1802.08767v1* (Feb. 2018). URL: https://arxiv.org/abs/1802.08767v1 (visited on 03/28/2020).

[296] Guoyin Shen et al. "Toward an international practical pressure scale: A proposal for an IPPS ruby gauge (IPPS-Ruby2020)". In: *High Pressure Research* 40.3 (2020), pp. 299–314. DOI: 10.1080/08957959.2020.1791107. eprint: https://doi.org/10.1080/08957959.2020.1791107. URL: https://doi.org/10.1080/08957959.2020.1791107.

[297] Chang S. Shin et al. "Room-temperature operation of a radiofrequency diamond magnetometer near the shot-noise limit". In: *Journal of Applied Physics* 112.12 (Dec. 2012), p. 124519. ISSN: 0021-8979. DOI: 10.1063/1.4771924. URL: https://aip.scitation.org/doi/full/10.1063/1.4771924 (visited on 03/14/2020).

[298] Maria Simanovskaia et al. "Sidebands in optically detected magnetic resonance signals of nitrogen vacancy centers in diamond". In: *Phys. Rev. B* 87 (22 June 2013), p. 224106. DOI: 10.1103/PhysRevB.87.224106. URL: https://link.aps.org/doi/10.1103/PhysRevB.87.224106.

[299] Stephanie Simmons et al. "Magnetic field sensors using 13-spin cat states". In: *Physical Review A* 82.2 (2010), p. 022330.

[300] T Smart et al. "High-pressure nano-seismology: Use of micro-ring resonators for characterizing acoustic emissions". In: *Applied Physics Letters* 115.8 (2019), p. 081904.

[301] Benjamin Smeltzer, Lilian Childress, and Adam Gali. "13C hyperfine interactions in the nitrogen-vacancy centre in diamond". In: *New Journal of Physics* 13.2 (Feb. 2011), p. 025021.

[302] G Smolensky. "Ferroelectrics with diffuse phase transition". In: *Ferroelectrics* 53.1 (1984), pp. 129–135.

[303] Elliot Snider et al. "Room-temperature superconductivity in a carbonaceous sulfur hydride". In: *Nature* 586.7829 (2020), pp. 373–377. ISSN: 1476-4687. DOI: 10.1038/s41586-020-2801-z. URL: https://doi.org/10.1038/s41586-020-2801-z.

[304] Maddury Somayazulu et al. "Evidence for Superconductivity above 260 K in Lanthanum Superhydride at Megabar Pressures". In: *Phys. Rev. Lett.* 122 (2 Jan. 2019), p. 027001. DOI: 10.1103/PhysRevLett.122.027001. URL: https://link.aps.org/doi/10.1103/PhysRevLett.122.027001.

[305] S. L. Sondhi et al. "Continuous quantum phase transitions". In: *Rev. Mod. Phys.* 69 (1 Jan. 1997), pp. 315–333. DOI: 10.1103/RevModPhys.69.315. URL: https://link.aps.org/doi/10.1103/RevModPhys.69.315.

[306] Alastair Stacey et al. "Evidence for Primal sp2 Defects at the Diamond Surface: Candidates for Electron Trapping and Noise Sources". In: *Advanced Materials Interfaces* 6.3 (2019), p. 1801449. ISSN: 2196-7350. DOI: 10.1002/admi.201801449. URL: https://onlinelibrary.wiley.com/doi/abs/10.1002/admi.201801449 (visited on 03/16/2020).

[307] P L Stanwix et al. "Coherence of nitrogen-vacancy electronic spin ensembles in diamond". In: *Physical Review B* 82.20 (Nov. 2010), p. 201201.

[308] L. G. Steele et al. "Optically detected magnetic resonance of nitrogen vacancies in a diamond anvil cell using designer diamond anvils". In: *Appl. Phys. Lett.* 111.22 (Nov. 2017), p. 221903. DOI: 10.1063/1.5004153. eprint: https://doi.org/10.1063/1.5004153. URL: https://doi.org/10.1063/1.5004153.

[309] S Steinert et al. "High sensitivity magnetic imaging using an array of spins in diamond". In: *Review of Scientific Instruments* 81.4 (Apr. 2010), p. 043705.

[310] S Steinert et al. "Magnetic spin imaging under ambient conditions with sub-cellular resolution". In: *Nature Communications* 4.1 (2013), p. 1607. ISSN: 2041-1723. DOI: 10.1038/ncomms2588. URL: https://doi.org/10.1038/ncomms2588.

[311] E Sterer, M P Pasternak, and R D Taylor. "A multipurpose miniature diamond anvil cell". In: *Rev. Sci. Instrum* 61.3 (Sept. 1998), pp. 1117–1119.

[312] K. Syassen. "Ruby under pressure". In: *High Pressure Research* 28.2 (2008), pp. 75–126. DOI: 10.1080/08957950802235640. eprint: https://doi.org/10.1080/08957950802235640. URL: https://doi.org/10.1080/08957950802235640.

[313] Kazuyoshi Takeda and Masaki Mito. "Disappearance of Bulk Ferromagnetism of Iron at High Pressures above 9 GPa". In: *Journal of the Physical Society of Japan* 71.3 (2002), pp. 729–731. DOI: 10.1143/JPSJ.71.729. URL: https://doi.org/10.1143/JPSJ.71.729.

[314] Hiroyuki Takenaka et al. "Slush-like polar structures in single-crystal relaxors". In: *Nature* 546.7658 (2017), pp. 391–395.

[315] Ph. Tamarat et al. "Stark Shift Control of Single Optical Centers in Diamond". In: *Physical Review Letters* 97.8 (Aug. 2006), p. 083002. DOI: 10.1103/PhysRevLett.97.083002. URL: https://link.aps.org/doi/10.1103/PhysRevLett.97.083002 (visited on 08/01/2019).

[316] H. Tang et al. "Magnetic reconstruction of the Gd(0001) surface". In: *Phys. Rev. Lett.* 71 (3 July 1993), pp. 444–447. DOI: 10.1103/PhysRevLett.71.444. URL: https://link.aps.org/doi/10.1103/PhysRevLett.71.444.

[317] J. M. Taylor et al. "High-sensitivity diamond magnetometer with nanoscale resolution". In: *Nature Physics* 4.10 (Oct. 2008), pp. 810–816. ISSN: 1745-2481. DOI: 10.1038/nphys1075. URL: https://www.nature.com/articles/nphys1075 (visited on 09/04/2019).

[318] R D Taylor, M P Pasternak, and R Jeanloz. "Hysteresis in the high pressure transformation of bcc- to hcp-iron". In: *J. Appl. Phys* 69.8 (Aug. 1998), pp. 6126–6128.

[319] Ann M Thayer and Alexander Pines. "Zero-field NMR". In: *Accounts of Chemical Research* 20.2 (May 2002), pp. 47–53.

[320] Lucas Thiel et al. "Quantitative nanoscale vortex imaging using a cryogenic quantum magnetometer". In: *Nat. Nanotechnol.* 11.8 (2016), p. 677.

[321] Yuri A. Timofeev et al. "Improved techniques for measurement of superconductivity in diamond anvil cells by magnetic susceptibility". In: *Review of Scientific Instruments* 73.2 (Feb. 2002), pp. 371–377. DOI: 10.1063/1.1431257. eprint: https://doi.org/10.1063/1.1431257. URL: https://doi.org/10.1063/1.1431257.

[322] Loïc Toraille et al. "Combined synchrotron x-ray diffraction and NV diamond magnetic microscopy measurements at high pressure". In: *New Journal of Physics* 22.10 (Oct. 2020), p. 103063. DOI: 10.1088/1367-2630/abc28f. URL: https://doi.org/10.1088/1367-2630/abc28f.

[323] L. Tosi, D. Vion, and H. le Sueur. "Design of a Cooper-Pair Box Electrometer for Application to Solid-State and Astroparticle Physics". In: *Physical Review Applied* 11.5 (May 2019), p. 054072. ISSN: 2331-7019. DOI: 10.1103/PhysRevApplied.11.054072. URL: https://link.aps.org/doi/10.1103/PhysRevApplied.11.054072 (visited on 06/16/2020).

[324] D M Toyli et al. "Measurement and Control of Single Nitrogen-Vacancy Center Spins above 600 K". In: *Phys. Rev. X* 2.3 (July 2012), p. 031001.

[325] Luqi Tu et al. "Ferroelectric Negative Capacitance Field Effect Transistor". In: *Advanced Electronic Materials* 4.11 (), p. 1800231. DOI: https://doi.org/10.1002/aelm.201800231.

[326] Péter Udvarhelyi et al. "Spin-strain interaction in nitrogen-vacancy centers in diamond". In: *Phys. Rev. B* 98 (7 Aug. 2018), p. 075201. DOI: 10.1103/PhysRevB.98.075201. URL: https://link.aps.org/doi/10.1103/PhysRevB.98.075201.

[327] A. N. Vamivakas et al. "Nanoscale Optical Electrometer". In: *Physical Review Letters* 107.16 (Oct. 2011), p. 166802. DOI: 10.1103/PhysRevLett.107.166802. URL: https://link.aps.org/doi/10.1103/PhysRevLett.107.166802 (visited on 11/18/2019).

[328] Eric Van Oort and Max Glasbeek. "Electric-field-induced modulation of spin echoes of NV centers in diamond". In: *Chemical Physics Letters* 168.6 (1990), pp. 529–532.

[329] David J. Vaughan and John A. Tossell. "Magnetic transitions observed in sulfide minerals at elevated pressures and their geophysical significance". In: *Science* 179.4071 (Jan. 1973), pp. 375–377. ISSN: 00368075. DOI: 10.1126/science.179.4071.375.

[330] Gian Giacomo Guzmán Verri. *Theory of Relaxor Ferroelectrics*. University of California, Riverside, 2012.

[331] Foteini Vervelidou et al. "Constraining the Date of the Martian Dynamo Shutdown by Means of Crater Magnetization Signatures". In: *Journal of Geophysical Research: Planets* 122.11 (2017), pp. 2294–2311. ISSN: 21699100. DOI: 10.1002/2017JE005410.

[332] Viktoria Yurgens et al. "Laser-written coherent nitrogen-vacancy centers as building block for efficient quantum photonic devices". In: vol. 11295. Mar. 2020. URL: https://doi.org/10.1117/12.2559472.

[333] Michael W.R. Volk, Stuart A Gilder, and Joshua M Feinberg. "Low-temperature magnetic properties of monoclinic pyrrhotite with particular relevance to the Besnus transition". In: *Geophysical Journal International Geophys. J. Int* 207 (2016), pp. 1783–1795. DOI: 10.1093/gji/ggw376.

[334] Michael W.R. Volk et al. "Changes in physical properties of 4C pyrrhotite (Fe7S8) across the 32 K Besnus transition". In: *American Mineralogist* 103.10 (Oct. 2018), pp. 1674–1689. ISSN: 19453027. DOI: 10.2138/am-2018-6514.

[335] Pavel A. Volkov, Premala Chandra, and Piers Coleman. *Superconductivity from energy fluctuations in dilute quantum critical polar metals*. 2021. arXiv: 2106.11295 [cond-mat.supr-con].

[336] G Waldherr et al. "Violation of a temporal Bell inequality for single spins in a diamond defect center". In: *Physical Review Letters* 107.9 (2011), p. 090401.

[337] Hailong Wang et al. "Noninvasive measurements of spin transport properties of an antiferromagnetic insulator". In: *Science Advances* 8.1 (2022), eabg8562. DOI: 10.1126/sciadv.abg8562. eprint: https://www.science.org/doi/pdf/10.1126/sciadv.abg8562. URL: https://www.science.org/doi/abs/10.1126/sciadv.abg8562.

[338] Wojciech Wasilewski et al. "Quantum noise limited and entanglement-assisted magnetometry". In: *Physical Review Letters* 104.13 (2010), p. 133601.

[339] Shinji Watanabe et al. "Instability of Co Spin Moment in ErCo 2Probed by Magnetic Compton Scattering under High Pressure". In: *Journal of the Physical Society of Japan* 80.9 (Sept. 2011), p. 093705.

[340] DP Weitekamp et al. "Zero-field nuclear magnetic resonance". In: *Physical review letters* 50.22 (1983), p. 1807.

[341] HR Wenk. "Are pseudotachylites products of fracture or fusion?" In: *Geology* 6.8 (1978), pp. 507–511.

[342] Alexander D. White et al. "Static and Dynamic Stark Tuning of the Silicon Vacancy in Silicon Carbide". In: *Conference on Lasers and Electro-Optics*. Washington, DC: OSA, 2020, FTu3D.1. ISBN: 978-1-943580-76-7. DOI: 10.1364/CLEO_QELS.2020.FTu3D.1. URL: https://www.osapublishing.org/abstract.cfm?URI=CLEO_QELS-2020-FTu3D.1 (visited on 10/05/2020).

[343] S Whitehead and W Hackett. "Measurement of the specific inductive capacity of diamonds by the method of mixtures". In: *Proceedings of the Physical Society* 51.1 (Jan. 1939), pp. 173–190.

[344] E Wigner and HB Huntington. "On the possibility of a metallic modification of hydrogen". In: *The Journal of Chemical Physics* 3.12 (1935), pp. 764–770.

[345] Christopher R. Winkler et al. "Accessing intermediate ferroelectric switching regimes with time-resolved transmission electron microscopy". In: *Journal of Applied Physics* 112.5 (Sept. 2012), p. 052013. DOI: 10.1063/1.4746082. URL: https://doi.org/10.1063/1.4746082.

[346] Thomas Wolf et al. "Subpicotesla Diamond Magnetometry". In: *Physical Review X* 5.4 (Oct. 2015), p. 041001.

[347] Amy L Wolfe et al. "A method for generating uniform size-segregated pyrite particle fractions". In: *Geochemical Transactions* 8.1 (2007), p. 9. ISSN: 1467-4866. DOI: 10.1186/1467-4866-8-9. URL: https://doi.org/10.1186/1467-4866-8-9.

[348] Gary Wolfowicz et al. "Heterodyne detection of radio-frequency electric fields using point defects in silicon carbide". In: *Applied Physics Letters* 115.4 (2019), p. 043105.

[349] Y. Yafet, J. Kwo, and E. M. Gyorgy. "Dipole-dipole interactions and two-dimensional magnetism". In: *Phys. Rev. B* 33 (9 May 1986), pp. 6519–6522. DOI: 10.1103/PhysRevB.33.6519. URL: https://link.aps.org/doi/10.1103/PhysRevB.33.6519.

[350] Yasusada Yamada and Gen Shirane. "Neutron Scattering and Nature of the Soft Optical Phonon in SrTiO3". In: *Journal of the Physical Society of Japan* 26.2 (1969), pp. 396–403. DOI: 10.1143/JPSJ.26.396. eprint: https://doi.org/10.1143/JPSJ.26.396. URL: https://doi.org/10.1143/JPSJ.26.396.

[351] Kenji Yasuda et al. "Stacking-engineered ferroelectricity in bilayer boron nitride". In: *Science* 372.6549 (2021), pp. 1458–1462. DOI: 10.1126/science.abd3230. eprint: https://www.science.org/doi/pdf/10.1126/science.abd3230. URL: https://www.science.org/doi/abs/10.1126/science.abd3230.

[352] King Yau Yip et al. "Measuring magnetic field texture in correlated electron systems under extreme conditions". In: *Science* 366.6471 (2019), pp. 1355–1359. DOI: 10.1126/science.aaw4278. eprint: https://www.science.org/doi/pdf/10.1126/science.aaw4278. URL: https://www.science.org/doi/abs/10.1126/science.aaw4278.

[353] P. Yudin et al. "Ferroelectric phase transitions induced by a strain gradient". In: *Phys. Rev. Research* 3 (3 Sept. 2021), p. 033213. DOI: 10.1103/PhysRevResearch.3.033213. URL: https://link.aps.org/doi/10.1103/PhysRevResearch.3.033213.

[354] H. Zhang et al. "Spin-torque oscillation in a magnetic insulator probed by a single-spin sensor". In: *Phys. Rev. B* 102 (2 July 2020), p. 024404. DOI: 10.1103/PhysRevB.102.024404. URL: https://link.aps.org/doi/10.1103/PhysRevB.102.024404.

[355] Ke Zhang et al. "Transmission electron microscopy on iron monosulfide varieties from the Suizhou meteorite". In: *Physics and Chemistry of Minerals* 35.8 (2008), pp. 425–432. ISSN: 1432-2021. DOI: 10.1007/s00269-008-0237-3. URL: https://doi.org/10.1007/s00269-008-0237-3.

[356] Qi Zhang et al. "Single Rare-Earth Ions as Atomic-Scale Probes in Ultrascaled Transistors". In: *Nano Letters* 19.8 (Aug. 2019), pp. 5025–5030. ISSN: 1530-6984, 1530-6992. DOI: 10.1021/acs.nanolett.9b01281. URL: https://pubs.acs.org/doi/10.1021/acs.nanolett.9b01281 (visited on 10/05/2020).

[357] J. Z. Zhao et al. "Strain-tunable out-of-plane polarization in two-dimensional materials". In: *Phys. Rev. B* 101 (12 Mar. 2020), p. 121407. DOI: 10.1103/PhysRevB.101.121407. URL: https://link.aps.org/doi/10.1103/PhysRevB.101.121407.

[358] Zhiren Zheng et al. "Unconventional ferroelectricity in moiré heterostructures". In: *Nature* (2020), pp. 1–6.

[359] W Zhong, RD King-Smith, and David Vanderbilt. "Giant LO-TO splittings in perovskite ferroelectrics". In: *Physical review letters* 72.22 (1994), p. 3618.

[360] Hengyun Zhou et al. "Quantum Metrology with Strongly Interacting Spin Systems". In: *Phys. Rev. X* 10 (3 July 2020), p. 031003. DOI: 10.1103/PhysRevX.10.031003. URL: https://link.aps.org/doi/10.1103/PhysRevX.10.031003.

[361] Tony X. Zhou et al. "A magnon scattering platform". In: *Proceedings of the National Academy of Sciences* 118.25 (2021). ISSN: 0027-8424. DOI: 10.1073/pnas.2019473118.

[362] Xiaobo Zhu et al. "Observation of dark states in a superconductor diamond quantum hybrid system". In: *Nature Communications* 5 (Apr. 2014), p. 3424.

[363] James F Ziegler, Matthias D Ziegler, and Jochen P Biersack. "SRIM–The stopping and range of ions in matter (2010)". In: *Nuclear Instruments and Methods in Physics Research Section B: Beam Interactions with Materials and Atoms* 268.11-12 (2010), pp. 1818–1823.

Appendix A

Derivations for Chapter 6

A.1 Derivation of Qubit Relaxation Rate

In this section, we systematically derive the relaxation rate of an impurity qubit sensor proximate to a polar or dielectric material in both a general setting and specific settings of interest. We start by deriving a relationship between the relaxation rate of the qubit and electrical noise at its location. Subsequently, we utilize Maxwell's equations to connect this electrical noise to polarization correlations in the nearby material. After this, we express the form of $1/T_1$ in a number of settings of interest. Finally, we investigate the influence of magnetic noise for the specific case of the NV qubit.

A.1.1 Impurity Qubit Response to Electrical Noise

Recall that in the main text, we defined the impurity qubit's coupling to electric and magnetic fields as (setting $\hbar = 1$ henceforth):

$$H = H_0 + H_{q-EM} = \frac{\omega_q}{2}\sigma^z + \hat{\mathbf{d}} \cdot \mathbf{E} + \hat{\boldsymbol{\mu}} \cdot \mathbf{B}, \qquad \hat{\mathbf{d}} = d_\perp(\sigma^x, \sigma^y, 0) \text{ and } \hat{\boldsymbol{\mu}} = \mu_z(0, 0, \sigma^z) \tag{A.1}$$

where $d_\perp$ was the electrical dipole moment, μ_z is the magnetic moment, and we assume that the quantization axis of the qubit is aligned with the physical z-axis of the system, defined as the axis normal to the plane of a proximate material. We assume that our sample is in thermal equilibrium at inverse temperature β with density matrix $\rho = \frac{1}{Z}\sum_n e^{-\beta\varepsilon_n} |n\rangle \langle n|$, where $|n\rangle$ is an eigenstate of the sample at energy ε_n and $Z = \sum_n e^{-\beta\varepsilon_n}$ is the partition function. Now, we use Fermi's golden rule to compute the transition rate between $|1\rangle$ to $|0\rangle$

(we set $\hbar = 1$ and $k_B = 1$ henceforth):

$$\Gamma_{em} = 2\pi d_\perp^2 \sum_{nm} \frac{e^{-\beta\varepsilon_n}}{Z} |\langle m,0| E^x\sigma^x + E^y\sigma^y |n,1\rangle|^2 \delta(\omega_q - (\varepsilon_m - \varepsilon_n)) \tag{A.2}$$

$$= 2\pi d_\perp^2 \sum_{nm} \frac{e^{-\beta\varepsilon_n}}{Z} |\langle m,0| E^x + iE^y |n,0\rangle|^2 \delta(\omega_q - (\varepsilon_m - \varepsilon_n)) \tag{A.3}$$

$$= 2\pi d_\perp^2 \sum_{nm} \frac{e^{-\beta\varepsilon_n}}{Z} E^+_{mn}E^-_{nm}\delta(\omega_q - (\varepsilon_m - \varepsilon_n)) \tag{A.4}$$

where the argument of the delta enforces energy conservation, i.e, the amount of energy lost by the qubit ($\omega_q = E_1 - E_0$) equals the amount of energy gained by the sample ($\varepsilon_m - \varepsilon_n$). Similarly, we have that:

$$\Gamma_{abs} = 2\pi d_\perp^2 \sum_{nm} \frac{e^{-\beta\varepsilon_n}}{Z} E^-_{mn}E^+_{nm}\delta(\omega_q + (\varepsilon_m - \varepsilon_n)) \tag{A.5}$$

where $E^\pm = E_x \pm iE_y$. Thus, we can write $1/T_1 = 1/2(\Gamma_{abs} + \Gamma_{em})$ [7]. Now, to relate this quantity to the electric field fluctuations, note that the noise tensor is given by:

$$\mathcal{N}_{ij}(\omega) = \frac{1}{2}\int_{-\infty}^{\infty} \mathrm{d}t \langle\{E^i(t), E^j(0)\}\rangle e^{i\omega t}$$

$$= \pi \sum_{nm} \frac{e^{-\beta\varepsilon_n}}{Z} \left[E^i_{nm}E^j_{mn}\delta(\omega - (\varepsilon_m - \varepsilon_n)) + E^j_{nm}E^i_{mn}\delta(\omega - (\varepsilon_n - \varepsilon_m))\right] \tag{A.6}$$

Thus, it follows that:

$$\frac{1}{T_1} = d_\perp^2 \mathcal{N}_{-+}(\omega_q) \tag{A.7}$$

Subsequently, by the fluctuation-dissipation theorem

$$\mathcal{N}_{ij}(\omega) = \frac{1}{2}\coth\left(\frac{\beta\omega}{2}\right)\mathcal{S}_{ij}(\omega) \text{ where } \mathcal{S}_{ij}(\omega) = \int_{-\infty}^{\infty} \mathrm{d}t \langle[E^i(t), E^j(0)]\rangle e^{i\omega t} \tag{A.8}$$

Moreover, we can relate $\mathcal{S}_{ij}(\omega)$ in terms of the retarded correlators of the electric field, which are more convenient to calculate

$$\mathcal{S}_{ij}(\omega) = 2\ \mathrm{Im}\left[C^R_{E^iE^j}(\omega)\right] \text{ where } C^R_{E^iE^j}(\omega) = i\int_{-\infty}^{\infty} \mathrm{d}t\, \Theta(t)\langle[E^i(t), E^j(0)]\rangle e^{i\omega t} \tag{A.9}$$

A.1.2 Propagation of Maxwell's Equations

To determine the electrical noise arising from dipolar fluctuations, we propagate these fluctuations using Maxwell's equations in Lorentz gauge:

$$\partial^2 A^\mu(\mathbf{r},t) = \mu_0 J^\mu(\mathbf{r},t) = \mu_0 \begin{pmatrix} -c\nabla\cdot\mathbf{P}(\mathbf{r},t) + c\sigma(\mathbf{r},t) \\ \partial_t \mathbf{P}(\mathbf{r},t) \end{pmatrix} \tag{A.10}$$

where $\partial^2 = -\partial_t^2/c^2 + \nabla^2$, $\mathbf{P}(\mathbf{r},t) = \mathbf{P}(\mathbf{r},t)1_{[-w,0]}(z)$ (where $1_{[-w,0]}$ is 1 for $z \in [-w,0]$ and 0 otherwise), $\sigma(\mathbf{r},t) = P_z(\mathbf{r},t)\delta(z) - P_z(\mathbf{r},t)\delta(z+w)$ is the surface charge density, and w is the width of the sample. We can solve these equations by introducing a kernel $G_i^\mu(\mathbf{r},\mathbf{r}',t-t')$:

$$A^\mu(\mathbf{r},t) = \mu_0 \int_{-\infty}^{\infty} dt' d^3\mathbf{r}' G_i^\mu(\mathbf{r},\mathbf{r}',t-t')P_i(\mathbf{r}',t') \tag{A.11}$$

where i labels x,y,z and we are implicitly summing over repeated indices. We define G_i^μ to satisfy the equation:

$$\begin{aligned}&\partial^2 G_i^\mu(\rho-\rho',z,z',t-t') \\ &= \begin{pmatrix} c\delta(t-t')\partial_i[\delta^{(3)}(\mathbf{r}-\mathbf{r}')] + c\delta_{i,z}\delta^{(3)}(\mathbf{r}-\mathbf{r}')[\delta(z)-\delta(z+w)] \\ -\delta^{(3)}(\mathbf{r}-\mathbf{r}')\partial_t[\delta(t-t')]\hat{e}_i \end{pmatrix}\end{aligned} \tag{A.12}$$

where $\rho = (x,y)$ is the coordinates of the material in-plane. Now, to solve for G_i^μ, we can express A^μ, G_i^μ, and our polarization P_i in terms of their in-plane Fourier modes yielding:

$$A^\mu(\mathbf{r},t) = \frac{1}{\sqrt{L^2}} \sum_{\mathbf{q}} \int \frac{d\omega}{2\pi} A^\mu(z,\mathbf{q},\omega)e^{i(\mathbf{q}\cdot\rho-\omega t)} \tag{A.13}$$

$$G_i^\mu(\rho,z,z',t) = \frac{1}{L^2} \sum_{\mathbf{q}} \int \frac{d\omega}{2\pi} G_i^\mu(z,z',\mathbf{q},\omega)e^{i(\mathbf{q}\cdot\rho-\omega t)} \tag{A.14}$$

$$P_i(\mathbf{r},t) = \frac{1}{\sqrt{L^2}} \sum_{\mathbf{q}} \int \frac{d\omega}{2\pi} P_i(z,\mathbf{q},\omega)e^{i(\mathbf{q}\cdot\rho-\omega t)} \tag{A.15}$$

where we assumed a sample with transverse dimensions $L \times L$ for simplicity. When we plug this back into the equations of motion for G_i^μ, we get:

$$\begin{aligned}&(-\lambda^2 + \partial_z^2)G_i^\mu(z,z',\mathbf{q},\omega) \\ &= \begin{pmatrix} icq_i(\delta_{i,x}+\delta_{i,y})\delta(z-z') + c\delta_{i,z}\partial_z[\delta(z-z')] + c\delta_{i,z}\delta(z-z')[\delta(z)-\delta(z+w)] \\ i\omega\delta(z-z')\hat{e}_i \end{pmatrix}\end{aligned} \tag{A.16}$$

where $\lambda^2 = (q^2 - \omega^2/c^2)$. To solve this, we Fourier transform the z coordinate as

$$G_i^\mu(\alpha,z',\mathbf{q},\omega) = \int dz\, e^{-i\alpha z} G_i^\mu(z,z',\mathbf{q},\omega) \tag{A.17}$$

and so we get the following:

$$G_i^\mu(\alpha, z', \mathbf{q}, \omega) = -\frac{1}{\lambda^2+\alpha^2} \begin{pmatrix} icq_i(\delta_{i,x}+\delta_{i,y})e^{-i\alpha z'} + ic\delta_{i,z}\alpha e^{-i\alpha z'} + c\delta_{i,z}\int dz e^{-i\alpha z}\delta(z-z')\left[\delta(z)-\delta(z+w)\right] \\ i\omega e^{-i\alpha z'}\hat{e}_i \end{pmatrix} \tag{A.18}$$

Now, we Fourier transform back to get a useable expression for G. We do this one component at a time:

$$\begin{aligned} G_i^0 &= -\frac{icq_i(\delta_{i,x}+\delta_{i,y})}{2\lambda}e^{-\lambda|z-z'|} - \frac{c\delta_{i,z}}{2}\mathrm{sgn}(z-z')e^{-\lambda|z-z'|} \\ &- c\delta_{i,z}\int \frac{d\alpha d\tilde{z}}{2\pi}\frac{e^{i\alpha(z-\tilde{z})}\delta(\tilde{z}-z')[\delta(\tilde{z})-\delta(\tilde{z}+w)]}{\lambda^2+\alpha^2} \\ &= -\frac{icq_i(\delta_{i,x}+\delta_{i,y})}{2\lambda}e^{-\lambda|z-z'|} - \frac{c\delta_{i,z}}{2}\mathrm{sgn}(z-z')e^{-\lambda|z-z'|} \\ &- c\delta_{i,z}\int d\tilde{z}\frac{e^{-\lambda|z-\tilde{z}|}}{2\lambda}\delta(\tilde{z}-z')\left[\delta(\tilde{z})-\delta(\tilde{z}+w)\right] \\ &= -\frac{icq_i(\delta_{i,x}+\delta_{i,y})}{2\lambda}e^{-\lambda|z-z'|} - \frac{c\delta_{i,z}}{2}\mathrm{sgn}(z-z')e^{-\lambda|z-z'|} \\ &- \frac{c\delta_{i,z}e^{-\lambda|z-z'|}}{2\lambda}[\delta(z')-\delta(z'+w)] \end{aligned} \tag{A.19}$$

Also, we have that:

$$G_i^j = -i\omega\frac{e^{-\lambda|z-z'|}}{2\lambda}\delta_i^j \tag{A.20}$$

where $i, j \in \{x, y, z\}$. Now, we can decompose our Green's function as:

$$G_i^\mu(z, z', \mathbf{q}, \omega) = \mathcal{G}_i^\mu(z-z', \mathbf{q}, \omega) + g_i^\mu(z, z', \mathbf{q}, \omega) \tag{A.21}$$

where

$$\mathcal{G}_i^\mu(z-z', \mathbf{q}, \omega) = \begin{pmatrix} -\frac{icq_i(\delta_{i,x}+\delta_{i,y})}{2\lambda}e^{-\lambda|z-z'|} - \frac{c\delta_{i,z}}{2}\mathrm{sgn}(z-z')e^{-\lambda|z-z'|} \\ -i\omega\frac{e^{-\lambda|z-z'|}}{2\lambda}\hat{e}_i \end{pmatrix} \tag{A.22}$$

$$g_i^\mu = \begin{pmatrix} -\frac{c\delta_{i,z}e^{-\lambda|z-z'|}}{2\lambda}[\delta(z')-\delta(z'+w)] \\ 0 \end{pmatrix} \tag{A.23}$$

indicate bulk and surface terms respectively. Green's function in hand, we can relate the polarization back to the vector potential as:

$$\begin{aligned} A^{\mu}(\mathbf{r},t) &= \frac{\mu_0}{L}\sum_{\mathbf{q}}\int\frac{dz'd\omega}{2\pi}G_i^{\mu}(z,z',\mathbf{q},\omega)P_i(z',\mathbf{q},\omega)e^{i(\mathbf{q}\cdot\rho-\omega t)} \\ &= \frac{1}{L}\sum_{\mathbf{q}}\int\frac{dz'd\omega}{2\pi}\mathcal{G}_i^{\mu}(|z-z'|,\mathbf{q},\omega)P_i(z,\mathbf{q},\omega)e^{i(\mathbf{q}\cdot\rho-\omega t)} \\ &+ \frac{1}{L}\sum_{\mathbf{q}}\int\frac{dz'd\omega}{2\pi}g_i^{\mu}(z,z',\mathbf{q},\omega)P_i(z',\mathbf{q},\omega)e^{i(\mathbf{q}\cdot\rho-\omega t)} \end{aligned} \tag{A.24}$$

Therefore, we can compute the electric field as:

$$\mathbf{E}(\mathbf{r},t) = -c\nabla A^0(\mathbf{r},t) - \partial_t\mathbf{A}(r,t) = \frac{\mu_0}{L}\sum_{q}\int\frac{d\omega dz'}{2\pi}\mathbf{H}_i(z,z',\mathbf{q},\omega)P_i(z',\mathbf{q},\omega)e^{i(\mathbf{q}\cdot\rho-\omega t)} \tag{A.25}$$

where

$$\mathbf{H}_i = \begin{pmatrix} -icq_xG_i^0 + i\omega G_i^x \\ -icq_yG_i^0 + i\omega G_i^y \\ -c\partial_zG_i^0 + i\omega G_i^z \end{pmatrix} = \boldsymbol{\mathcal{H}}_i + \mathbf{h}_i \tag{A.26}$$

For reference, the explicit form of the bulk kernels is:

$$\boldsymbol{\mathcal{H}}_x = -\frac{e^{-\lambda|z-z'|}}{2\lambda}\begin{pmatrix} c^2q_x^2+\omega^2 \\ c^2q_xq_y \\ ic^2q_x\lambda\cdot\mathrm{sign}(z-z') \end{pmatrix} \quad \boldsymbol{\mathcal{H}}_y = -\frac{e^{-\lambda|z-z'|}}{2\lambda}\begin{pmatrix} c^2q_xq_y \\ c^2q_y^2+\omega^2 \\ ic^2q_y\lambda\cdot\mathrm{sign}(z-z') \end{pmatrix} \tag{A.27}$$

$$\boldsymbol{\mathcal{H}}_z = -\frac{e^{-\lambda|z-z'|}}{2}\begin{pmatrix} -ic^2q_x\mathrm{sign}(z-z') \\ -ic^2q_y\mathrm{sign}(z-z') \\ -c^2\delta(z-z') + \frac{c^2\lambda^2\mathrm{sign}(z-z')+\omega^2}{\lambda} \end{pmatrix} \tag{A.28}$$

and the explicit form of the surface kernels are:

$$\mathbf{h}_z = \frac{c^2e^{-\lambda|z-z'|}}{2\lambda}\begin{pmatrix} iq_x \\ iq_y \\ -\partial_z \end{pmatrix}[\delta(z') - \delta(z'+w)] = \frac{c^2e^{-\lambda|z-z'|}}{2\lambda}\begin{pmatrix} iq_x \\ iq_y \\ -\partial_z \end{pmatrix}\mathcal{S}(z') \tag{A.29}$$

with $\mathbf{h}_{x,y} = 0$.

A.1.3 Qubit Relaxation from Dipolar Fluctuations (Translation Invariant)

Having propagated the in-sample polarization to the electric fields outside of the material, we now determine the relaxation rate of our probe qubit due to in-sample polarization fluctuations. To do so, we compute electrical noise at the location of the probe qubit due to these fluctuations. In particular, by Eq. A.7 and A.8, we need to compute:

$$\langle [E_-(\mathbf{r},t), E_+(\mathbf{r},0)]\rangle = \frac{\mu_0^2}{L^2}\sum_{\mathbf{q}_1,\mathbf{q}_2}\int \frac{d\omega_1 d\omega_2 dz_1' dz_2'}{(2\pi)^2} H_i^-(z_1',\mathbf{q}_1,\omega_1)H_j^+(z_2',\mathbf{q}_2,\omega_2) \tag{A.30}$$

$$\times\langle [P_i(z_1',\mathbf{q}_1,\omega_1), P_j(z',\mathbf{q}_2,\omega_2]\rangle e^{i(\mathbf{q}_1\cdot\boldsymbol{\rho}-\omega_1 t)}e^{i\mathbf{q}_2\cdot\rho} \tag{A.31}$$

where $\mathbf{r} = (\rho, d) = (0,0,d)$ is the location of the qubit. Assuming spacetime translation invariance, we have that

$$\langle [P_i(z_1',\mathbf{q}_1,\omega_1), P_j(z_2',\mathbf{q}_2,\omega_2)]\rangle = 2\pi\delta(\omega_1+\omega_2)\delta_{\mathbf{q}_1,-\mathbf{q}_2}\langle [P_i(z_1',\mathbf{q},\omega), P_j(z_2',-\mathbf{q},-\omega)]\rangle \tag{A.32}$$

Thus, the electrical noise can be expressed as:

$$\begin{aligned}&\langle [E_-(\mathbf{r},t), E_+(\mathbf{r},0)]\rangle \\ &= \frac{\mu_0^2}{L^2}\sum_{\mathbf{q}}\int \frac{d\omega dz_1' dz_2'}{2\pi} H_i^-(z_1',\mathbf{q},\omega)H_j^-(z_2',-\mathbf{q},-\omega)\langle [P_i(z_1',\mathbf{q},\omega), P_j(z_2',-\mathbf{q},-\omega)]\rangle e^{-i\omega t}\end{aligned} \tag{A.33}$$

To proceed further, we simply need to contract the product of kernels with the polarization commutator:

$$\begin{aligned}&H_i^-(1)H_j^+(2)\langle [P_i(1),P_j(1)]\rangle \\ &= \left\langle \left[\frac{1}{2}(H_+^-(1)P_-(1)+H_-^-(1)P_+(1))+H_z^-(1)P_z(1),\right.\right. \\ &\left.\left.\frac{1}{2}(H_+^+(2)P_-(2)+H_-^+(2)P_+(2))+H_z^+(2)P_z(2)\right]\right\rangle \\ &= \frac{1}{4}\left(H_+^-(1)H_-^+(2)\langle [P_-(1),P_+(2)]\rangle + H_-^-(1)H_+^+(2)\langle [P_+(1),P_-(2)]\rangle\right) \\ &+ H_z^-(1)H_z^+(2)\langle [P_z(1),P_z(2)]\rangle \\ &+ \frac{1}{4}\left(H_+^-(1)H_+^+(2)\langle [P_-(1),P_-(2)]\rangle + H_-^-(1)H_-^+(2)\langle [P_+(1),P_+(2)]\rangle\right) \\ &+ \frac{1}{2}\left(H_+^-(1)H_z^+(2)\langle [P_-(1),P_z(2)] + H_-^-(1)H_z^+(2)\langle [P_+(1),P_z(2)]\rangle\right. \\ &\left.+H_z^-(1)H_-^+(2)\langle [P_z(1),P_+(2)]\rangle + H_z^-(1)H_+^+(2)\langle [P_z(1),P_-(2)]\rangle\right)\end{aligned} \tag{A.34}$$

where $H_i^-(1) = H_i^-(d,z_1,\mathbf{q}_1,\omega_1)$, $H_j^+(2) = H_j^+(d,z_2,\mathbf{q}_2,\omega_2')$, $P_i(1) = P_i(z_1,\mathbf{q}_1,\omega_1)$, and $P_j(2) = P_j(z_2,\mathbf{q}_2,\omega_2)$ with $\mathbf{q}_1 = -\mathbf{q}_2 = \mathbf{q}$ and $\omega_1 = -\omega_2 = \omega$ and also $H_\pm^\pm = H_x^\pm \pm iH_y^\pm$ and

$P_\pm = P_x \pm iP_y$. Although the above expression looks daunting, the first line is the only line that appreciably contributes when either it is a good approximation that the polarization is conserved or when the sample is rotationally invariant. Now we compute the product of the kernels in the approximation that $\omega/c \ll q$ (i.e. the speed of light is much faster than any velocity scale in the material). We remark that:

$$H_+^+ = -\frac{e^{-\lambda|z-z'|}}{2\lambda}c^2(q_x+iq_y)^2 \quad H_-^- = -\frac{e^{-\lambda|z-z'|}}{2\lambda}(q_x-iq_y)^2$$
$$H_-^+ = H_+^- = -\frac{e^{-\lambda|z-z'|}}{2\lambda}\left(c^2q^2+2\omega^2\right) \quad H_z^\pm = \frac{e^{-\lambda|z-z'|}}{2\lambda}ic^2(q_x\pm iq_y) \quad [\lambda\cdot\mathrm{sign}(z-z')+\mathcal{S}(z')] \tag{A.35}$$

Now, we can compute the products of these kernels. First, the polarization conserving kernels:

$$H_-^-(1)H_+^+(2) \approx \frac{1}{4}e^{-q|z-z_1'|}e^{-q|z-z_2'|}c^4q^2 = F(z,q;z_1',z_2') \tag{A.36}$$
$$H_+^-(1)H_-^+(2) \approx \frac{1}{4}e^{-q|z-z_1'|}e^{-q|z-z_2'|}c^4q^2 = F(z,q;z_1',z_2') \tag{A.37}$$

and also

$$H_z^-(1)H_z^+(2) \approx \frac{1}{4}e^{-q|z-z_1'|}e^{-q|z-z_2'|}c^4(q^2+q(\mathcal{S}(z_1')+\mathcal{S}(z_2'))+\mathcal{S}(z_1')\mathcal{S}(z_2')) \tag{A.38}$$
$$= F(z,q;z_1',z_2')\left[1+\frac{1}{q}(\mathcal{S}(z_1')+\mathcal{S}(z_2'))+\frac{1}{q^2}\mathcal{S}(z_1')\mathcal{S}(z_2')\right] \tag{A.39}$$

Now, the other terms:

$$H_+^-(1)H_+^+(2) \approx \frac{1}{4}e^{-q|z-z_1'|}e^{-q|z-z_2'|}c^4q^2e^{2i\varphi} = F(z,q;z_1',z_2')e^{2i\varphi} \tag{A.40}$$
$$H_-^-(1)H_-^+(2) \approx \frac{1}{4}e^{-q|z-z_1'|}e^{-q|z-z_2'|}c^4q^2e^{-2i\varphi} = F(z,q;z_1',z_2')e^{-2i\varphi} \tag{A.41}$$
$$H_+^-(1)H_z^+(2) \approx -\frac{1}{4}e^{-q|z-z_1'|}e^{-q|z-z_2'|}(-ie^{i\varphi})c^4\left[q^2+q\mathcal{S}(z_2')\right] = ie^{i\varphi}F(z,q;z_1',z_2')\left[1+\frac{1}{q}\mathcal{S}(z_2')\right] \tag{A.42}$$
$$H_-^-(1)H_z^+(2) \approx -\frac{1}{4}e^{-q|z-z_1'|}e^{-q|z-z_2'|}(-ie^{-i\varphi})c^4\left[q^2+q\mathcal{S}(z_2')\right] = ie^{-i\varphi}F(z,q;z_1',z_2')\left[1+\frac{1}{q}\mathcal{S}(z_2')\right] \tag{A.43}$$
$$H_z^-(1)H_+^+(2) \approx -\frac{1}{4}e^{-q|z-z_1'|}e^{-q|z-z_2'|}ie^{i\varphi}c^4\left[q^2+q\mathcal{S}(z_1')\right] = -ie^{i\varphi}F(z,q;z_1',z_2')\left[1+\frac{1}{q}\mathcal{S}(z_1')\right] \tag{A.44}$$
$$H_z^-(1)H_-^+(2) \approx -\frac{1}{4}e^{-q|z-z_1'|}e^{-q|z-z_2'|}ie^{-i\varphi}c^4\left[q^2+q\mathcal{S}(z_1')\right] = -ie^{-i\varphi}F(z,q;z_1',z_2')\left[1+\frac{1}{q}\mathcal{S}(z_1')\right] \tag{A.45}$$

where φ is the angle that $\mathbf{q}$ makes in the xy plane. Now, we can write the full expression for the electrical noise:

$$\langle [E_-(\mathbf{r},t), E_+(\mathbf{r},0)]\rangle = \frac{\mu_0^2}{L^2}\sum_{\mathbf{q}}\int \frac{d\omega dz_1' dz_2'}{2\pi} F(d,q;z_1',z_2')\times(\mathcal{C}_{bb}+\mathcal{C}_{bs}+\mathcal{C}_{ss})e^{-i\omega t} \tag{A.46}$$

where $\mathcal{C}_{bb}$ are bulk-bulk correlations, $\mathcal{C}_{bs}$ are correlations between the bulk and the surface, $\mathcal{C}_{ss}$ are correlations between the two surfaces of the sample. Let us enumerate these one-by-one:

$$\begin{aligned}\mathcal{C}_{bb} &= \frac{1}{16}(\langle[P_+(1),P_-(2)]\rangle + \langle[P_-(1),P_+(2)]\rangle + 4\langle[P_z(1),P_z(2)]\rangle)\\ &+ \frac{1}{16}(\langle[P_-(1),P_-(2)]\rangle e^{2i\varphi} + \langle[P_+(1),P_+(2)]\rangle e^{-2i\varphi})\\ &+ \frac{1}{8}[\big(\langle[P_-(1),P_z(2)]\rangle ie^{i\varphi} + \langle[P_+(1),P_z(2)]\rangle ie^{-i\varphi}\big)\\ &- \big(\langle[P_z(1),P_-(1)]\rangle ie^{i\varphi} + \langle[P_z(1),P_+(2)]\rangle ie^{-i\varphi}\big)]\end{aligned} \tag{A.47}$$

where the parenthesis in the last term indicate complex conjugate pairs. Moreover, we have that:

$$\mathcal{C}_{bs} = \frac{\mathcal{S}(z_1')}{8q}\left(2\langle[P_z(1),P_z(2)]\rangle - ie^{i\varphi}\langle[P_z(1),P_-(2)]\rangle - ie^{-i\varphi}\langle[P_z(1),P_+(2)]\rangle\right) \tag{A.48}$$

$$+ \frac{\mathcal{S}(z_2')}{8q}\left(2\langle[P_z(1),P_z(2)]\rangle + ie^{i\varphi}\langle[P_-(1),P_z(2)]\rangle + ie^{-i\varphi}\langle[P_+(1),P_z(2)]\rangle\right) \tag{A.49}$$

Finally, we have the surface-surface correlations:

$$\mathcal{C}_{ss} = \frac{1}{4q^2}\mathcal{S}(z_1')\mathcal{S}(z_2')\langle[P_z(1),P_z(2)]\rangle \tag{A.50}$$

So, we can write down our relaxation rate as:

$$\frac{1}{T_1} = \frac{1}{2}d_\perp^2\coth\left(\frac{\beta\omega}{2}\right)\frac{\mu_0^2}{L^2}\sum_{\mathbf{q}}\int dz_1' dz_2' F(d,\mathbf{q};z_1',z_2')\times\{\mathcal{C}_{bb}+\mathcal{C}_{bs}+\mathcal{C}_{ss}\} \tag{A.51}$$

Note that in the special case where the material is a stack of N 2D layers each of width w, we can re-express our correlators as

$$\langle[P_\alpha(z_1',\mathbf{q},\omega),P_\beta(z_2',-\mathbf{q},-\omega)]\rangle = \sum_{j=0}^{N-1}\langle[P_\alpha(\mathbf{q},\omega),P_\beta(-\mathbf{q},-\omega)]\rangle\delta(z_1'-jw)\delta(z_2'-jw) \tag{A.52}$$

Consequently, the expression for $1/T_1$ can be re-written as:

$$\frac{1}{T_1} = \frac{1}{2}d_\perp^2\coth\left(\frac{\beta\omega_q}{2}\right)\frac{\mu_0^2}{L^2}\sum_{\mathbf{q}}F(d,\mathbf{q})\times\{\mathcal{C}_{bb}+\mathcal{C}_{bs}+\mathcal{C}_{ss}\} \tag{A.53}$$

where $F(d,\mathbf{q}) = \sum_{j=0}^{N-1} c^4q^2e^{-2q(d+jw)}$ and $\mathcal{C}_{bb},\mathcal{C}_{bs}$, and $\mathcal{C}_{ss}$ are redefined with

$$\langle[P_\alpha(\mathbf{q},\omega),P_\beta(-\mathbf{q},-\omega)]\rangle$$

instead of

$$\langle[P_\alpha(z_1',\mathbf{q},\omega),P_\beta(z_2',-\mathbf{q},-\omega)]\rangle$$

. If we neglect the surface charge contributions $\mathcal{C}_{bs},\mathcal{C}_{ss}$ and impose rotational invariance in-plane, this is precisely Eq. 6.62 of the main text.

A.1.4 Influence of Magnetic Noise

In the main text, we quoted that the relative strength of $1/T_1$ due to magnetic noise emanating from dipoles to electrical noise is controlled by $\mu_z^2 c_s^2/d_\perp^2 c^4 \sim 10^{-4} \ll 1$ for the nitrogen-vacancy center. In this section, we derive this.

Recall that the coupling of an NV center to magnetic fields is given by:

$$\begin{aligned} H_{NV-B} &= \mu_z \mathbf{B}\cdot\mathbf{S} = \mu_z B_z S_z + \mu_z \frac{B_x}{2}(S_+ + S_-) - \mu_z \frac{iB_y}{2}(S_+ - S_-) \\ &= \mu_z \left(B_z S_z + \frac{1}{2}\left(B_- S_+ + B_+ S_-\right)\right) \end{aligned} \tag{A.54}$$

where $\mu_z = 2.8$ MHz/G and $B_\pm = B_x \pm iB_y$. We note that such a Hamiltonian is incapable of driving transitions between the $|\pm 1\rangle$ states of the NV center because each term can only change the magnetic quantum number by at most one. Hence, magnetic field noise acts to enhance the decay rate between the $|0\rangle$ and $|\pm 1\rangle$ states of the NV center. To estimate this effect, we compute the decay rate from $|+\rangle$ to $|0\rangle$, split by ω:

$$\Gamma_{em} = \frac{\pi\mu_z^2}{2}\sum_{n,m}\frac{e^{-\beta\varepsilon_n}}{Z}\left|\langle m,0|\, B_- S_+ + B_+ S_- \,|n,+\rangle\right|^2 \delta(\omega - \varepsilon_m + \varepsilon_n) \tag{A.55}$$

$$= \pi\mu_z^2 \sum_{n,m}\frac{e^{-\beta\varepsilon_n}}{Z}\left|B^+_{mn}\right|^2 \delta(\omega - (\varepsilon_m - \varepsilon_n)) = \pi\mu_z^2\sum_{n,m}\frac{e^{-\beta\varepsilon_n}}{Z} B^-_{nm}B^+_{mn}\delta(\omega - (\varepsilon_m - \varepsilon_n)) \tag{A.56}$$

Similarly,

$$\Gamma_{abs} = \pi\mu_z^2\sum_{n,m}\frac{e^{-\beta\varepsilon_n}}{Z} B^+_{nm}B^-_{mn}\delta(\omega + (\varepsilon_m - \varepsilon_n)) \tag{A.57}$$

Now, the full expression for $1/T_1 = \frac{1}{2}[\Gamma_{em} + \Gamma_{abs}]$ and can be written from the noise tensor because:

$$\begin{aligned} \mathcal{N}_{ij}(\omega) &= \frac{1}{2}\int_{-\infty}^{\infty} dt \langle\{B^i(t), B^j(0)\}\rangle e^{i\omega t} \\ &= \pi\sum_{n,m}\frac{e^{-\beta\varepsilon_n}}{Z}\left[B^i_{nm}B^j_{mn}\delta(\omega - (\varepsilon_m - \varepsilon_n)) + B^j_{nm}B^i_{mn}\delta(\omega + (\varepsilon_m - \varepsilon_n))\right] \end{aligned} \tag{A.58}$$

Thus, we have in total:

$$\frac{1}{T_1} = \frac{\mu_z^2}{2}\mathcal{N}_{-+}(\omega) = \frac{\mu_z^2}{4}\coth\left(\frac{\beta\omega}{2}\right)\mathcal{S}_{-+}(\omega) = \frac{\mu_z^2}{4}\coth\left(\frac{\beta\omega}{2}\right)\int_{-\infty}^{\infty} dt\langle[B^-(t), B^+(0)]\rangle e^{i\omega t} \tag{A.59}$$

Expression in hand, we will now estimate the rough magnitude of the magnetic contribution to $1/T_1$. Note that we compute the magnetic field as:

$$\mathbf{B}(\mathbf{r},t) = \nabla\times\mathbf{A}(\mathbf{r},t) = \frac{\mu_0}{L}\sum_{\mathbf{q}}\int\frac{dz' d\omega}{2\pi}\mathbf{H}_i(z,z',\mathbf{q},\omega)P_i(z',\mathbf{q},\omega)e^{i(\mathbf{q}\cdot\rho-\omega t)} \tag{A.60}$$

where $\mathbf{H}_i = \nabla \times (\mathbf{G}_i e^{i(\mathbf{q}\cdot\rho-\omega t)})e^{-i(\mathbf{q}\cdot\rho-\omega t)} = \boldsymbol{\mathcal{H}}_i + \mathbf{h}_i$ representing bulk and surface contributions. We can use Eqs. A.22 and A.23 to get:

$$\boldsymbol{\mathcal{H}}_i = \begin{pmatrix} iq_y\mathcal{G}_i^z - \partial_z\mathcal{G}_i^y \\ \partial_z\mathcal{G}_i^x - iq_x\mathcal{G}_i^z \\ iq_x\mathcal{G}_i^y - iq_y\mathcal{G}_i^x \end{pmatrix} = \begin{pmatrix} -q_y\delta_{iz} + i\lambda\delta_{iy} \\ -i\lambda\delta_{ix} + q_x\delta_{iz} \\ -q_x\delta_{iy} + q_y\delta_{ix} \end{pmatrix} \frac{\omega}{2\lambda} e^{-\lambda|z-z'|} \tag{A.61}$$

and $\mathbf{h}_i = 0$.

Having propagated the in-sample polarization to the magnetic fields outside of the material, we now determine the relaxation rate of our probe qubit due to in-sample polarization fluctuations. To do so, we compute magnetic noise at the location of the probe qubit due to these fluctuations. In particular, by Eq. A.7 and A.8, we need to compute:

$$\langle [B_-(\mathbf{r},t), B_+(\mathbf{r},0)]\rangle = \frac{\mu_0^2}{L^2}\sum_{\mathbf{q_1},\mathbf{q_2}}\int \frac{d\omega_1 d\omega_2 dz_1' dz_2'}{(2\pi)^2} H_i^-(z_1', \mathbf{q}_1, \omega_1) H_j^+(z_2', \mathbf{q}_2, \omega_2) \tag{A.62}$$

$$\times \langle [P_i(z_1', \mathbf{q}_1, \omega_1), P_j(z', \mathbf{q}_2, \omega_2]\rangle e^{i(\mathbf{q}_1\cdot\boldsymbol{\rho}-\omega_1 t)} e^{-i\omega_2 t} \tag{A.63}$$

where $\mathbf{r} = (\rho, d) = (0, 0, d)$ is the location of the qubit. Assuming space-time translation invariance, we have that

$$\langle [P_i(z_1', \mathbf{q}_1, \omega_1), P_j(z_2', \mathbf{q}_2, \omega_2)]\rangle = 2\pi\delta(\omega_1+\omega_2)\delta_{\mathbf{q}_1,-\mathbf{q}_2}\langle [P_i(z_1', \mathbf{q}, \omega), P_j(z_2', -\mathbf{q}, -\omega)]\rangle \tag{A.64}$$

Thus, the magnetic noise can be expressed as:

$$\begin{aligned}&\langle [B_-(\mathbf{r},t), B_+(\mathbf{r},0)]\rangle \\ &= \frac{\mu_0^2}{L^2}\sum_{\mathbf{q}}\int \frac{d\omega dz_1' dz_2'}{(2\pi)^2} H_i^-(z_1', \mathbf{q}, \omega) H_j^-(z_2', -\mathbf{q}, -\omega)\langle [P_i(z_1', \mathbf{q}, \omega), P_j(z_2', -\mathbf{q}, -\omega)]\rangle e^{-i\omega t}\end{aligned} \tag{A.65}$$

To proceed further, we simply need to contract the product of kernels with the polarization commutator:

$$\begin{aligned}&H_i^-(1)H_j^+(2)\langle [P_i(1), P_j(1)]\rangle = \Big\langle \Big[\frac{1}{2}(H_+^-(1)P_-(1) + H_-^-(1)P_+(1)) + H_z^-(1)P_z(1), \\ &\frac{1}{2}(H_+^+(2)P_-(2) + H_-^+(2)P_+(2)) + H_z^+(2)P_z(2)\Big]\Big\rangle \\ &= \frac{1}{4}\left(H_+^-(1)H_-^+(2)\langle [P_-(1), P_+(2)]\rangle + H_-^-(1)H_+^+(2)\langle [P_+(1), P_-(2)]\rangle\right) \\ &+ H_z^-(1)H_z^+(2)\langle [P_z(1), P_z(2)]\rangle \\ &+ \frac{1}{4}\left(H_+^-(1)H_+^+(2)\langle [P_-(1), P_-(2)]\rangle + H_-^-(1)H_-^+(2)\langle [P_+(1), P_+(2)]\rangle\right) \\ &+ \frac{1}{2}\left(H_+^-(1)H_z^+(2)\langle [P_-(1), P_z(2)] + H_-^-(1)H_z^+(2)\langle [P_+(1), P_z(2)]\rangle\right. \\ &\left.+H_z^-(1)H_-^+(2)\langle [P_z(1), P_+(2)]\rangle + H_z^-(1)H_+^+(2)\langle [P_z(1), P_-(2)]\rangle\right)\end{aligned} \tag{A.66}$$

where $H_i^-(1) = H_i^-(d, z_1, \mathbf{q}_1, \omega)$, $H_j^+(2) = H_j^+(d, z_2, \mathbf{q}_2, \omega')$, $P_i(1) = P_i(z_1, \mathbf{q}_1, \omega)$, and $P_j(2) = P_j(z_2, \mathbf{q}_2, \omega')$. The first line is the only line that appreciably contributes if we assume that our sample is rotationally invariant or has a conserved polarization density. Now we compute the product of the kernels in the approximation that $\omega/c \ll q$. We remark that:

$$\begin{aligned} H_i^+ = H_i^x + iH_i^y &= \left[(-q_y\delta_{iz} + i\lambda\delta_{iy}) + (\lambda\delta_{ix} + iq_x\delta_{iz})\right] \frac{\omega}{2\lambda} e^{-\lambda|z-z'|} \\ &= \left[iq_+\delta_{iz} + 2\lambda\delta_{i-}\right] \frac{\omega}{2\lambda} e^{-\lambda|z-z'|} \end{aligned} \tag{A.67}$$

$$\begin{aligned} H_i^- = H_i^x - iH_i^y &= \left[(-q_y\delta_{iz} + i\lambda\delta_{iy}) + (-\lambda\delta_{ix} - iq_x\delta_{iz})\right] \frac{\omega}{2\lambda} e^{-\lambda|z-z'|} \\ &= -\left[iq_-\delta_{iz} + 2\lambda\delta_{i+}\right] \frac{\omega}{2\lambda} e^{-\lambda|z-z'|} \end{aligned} \tag{A.68}$$

Now, just to get an estimate for the magnetic field strength, we compute only two of these kernels and use Gaussian polarization correlations to get an estimate for the noise signal. In particular, we compute

$$H_+^-(1)H_-^+(2) = \frac{\omega^2}{4\lambda^2} e^{-\lambda|z-z_1'|} e^{-\lambda|z-z_2'|} 4\lambda^2 \approx \omega^2 e^{-q|z-z_1'|} e^{-q|z-z_2'|} \tag{A.69}$$

$$H_z^-(1)H_z^+(2) = \frac{\omega^2}{4\lambda^2} e^{-\lambda|z-z_1'|} e^{-\lambda|z-z_2'|} q^2 \approx \frac{\omega^2}{4} e^{-q|z-z_1'|} e^{-q|z-z_2'|} \tag{A.70}$$

which would be the only non-zero terms if the system was translation and rotationally invariant.

Thus, we have that the total noise expression looks something like:

$$\frac{1}{T_1} = \frac{\mu_z^2}{4} \coth\left(\frac{\beta\omega}{2}\right) \int_{-\infty}^{\infty} dt \langle [B^-(\mathbf{r}, t), B^+(\mathbf{r}, 0)] \rangle e^{i\omega t} \tag{A.71}$$

$$= \frac{\mu_z^2 \mu_0^2 \omega^2}{4} \coth\left(\frac{\beta\omega}{2}\right) \int \frac{d^2\mathbf{q}}{(2\pi)^2} \int dz_1' \int dz_2' \frac{e^{-q|z-z_1'|} e^{-q|z-z_2'|}}{4} [\mathcal{C}_{+-} + \mathcal{C}_{zz}] \tag{A.72}$$

where $\mathcal{C}_{+-} = \langle [P_+(1), P_-(2)] \rangle$ and $\mathcal{C}_{zz} = \langle [P_z(1), P_z(2)] \rangle$. Now, assuming that we have a 2D sample, our polarization only fluctuates in-plane (hence we can neglect $\mathcal{C}_{zz}$), and Gaussian correlations, we can compute the retarded correlations (see next section for a derivation of this):

$$\chi_{+-} = \frac{Q^2}{a^4} \frac{\hbar}{\rho} \frac{1}{\omega_d^2 - (\omega + i\eta)^2} \delta(d - z_1') \delta(d - z_2') \tag{A.73}$$

where $\omega_d = \sqrt{c_s^2 q^2 + \omega_0^2}$ and $\mathcal{C}_{+-} = \mathrm{Im}[\chi_{+-}]$. We can plug this in to get an estimate for the magnetic noise as:

$$\frac{1}{T_1} = \frac{\mu_z^2 \mu_0^2 \omega^2}{16} \coth\left(\frac{\beta\omega}{2}\right) \left(\frac{Q^2}{a^{2d}} \frac{\hbar}{\rho}\right) \times \begin{cases} \left[e^{-2q_{res} d \frac{\pi}{2c_s^2}}\right] & \omega_0 \leq \omega \\ 0 & \omega_0 > \omega \end{cases} \tag{A.74}$$

If we divide this by the estimate for the electrical noise in the main text, we find that the ratio between these two is controlled by the dimensionless ratio:

$$\frac{(1/T_1)_{\text{magnetic}}}{(1/T_1)_{\text{electric}}} \sim \frac{\mu_z^2 \omega^2}{d_\perp^2 q_{\text{res}}^2 c^4} = \frac{\mu_z^2 c_s^2}{d_\perp^2 c^4} \sim 10^{-4} \tag{A.75}$$

for the parameters shown in the main text.

A.2 Derivation of Numerical Estimate of $1/T_1$

In the main text, we made a numerical prediction for the magnitude of $1/T_1$ as a function of frequency (ω), qubit-sample distance (d), and temperature (T) for a qubit above a dielectric material with non-interacting phonon modes. For transparency, we provide the precise derivation of the dimensionful prefactor to Eq. 6.63 of the main text. Namely, consider once again the toy-model of a ionic crystal considered in the main text (see Fig 6.11(a,b) of the main text). We can associate with each sublattice a phonon displacement field ($\mathbf{u}_+$ and $\mathbf{u}_-$ for the positive and negative ions respectively). For the lattice, there will be two classes of phonon modes: gapless acoustic branches $\mathbf{u}_{ac} = (\mathbf{u}_+ + \mathbf{u}_-)/2$ and gapped optical branches $\mathbf{u} = (\mathbf{u}_+ - \mathbf{u}_-)$. Since acoustic phonons don't carry polarization, we characterize the dynamics of the optical phonons by the (Euclidean) action [186]:

$$S_u = \int_0^{\hbar\beta} d\tau \int d^d x \frac{\rho}{2} u_j(x) \left[(-\partial_0^2 + \omega_T^2)\delta_{jl} - c_T^2(\nabla^2\delta_{jl} - \partial_j\partial_l) - c_L^2\partial_j\partial_l\right] u_l(x) \tag{A.76}$$

where β is the inverse temperature, ρ is the mass density of the lattice, $c_{T,L}$ refer to the transverse and longitudinal phonon velocity, and ω_T indicates the phonon mass. For sake of analytic tractability, we have neglected interactions between phonon modes. These phonon modes are related to the polarization via:

$$\mathbf{P} = \frac{Q}{a^d}\mathbf{u} \tag{A.77}$$

where Q is the Born effective charge of the material. Since these phonon modes generate a polarization, we must also account for the coupling between the phonon modes and the electromagnetic field. Since the electromagnetic potential will only couple to the longitudinal optical phonon mode, this is characterized by the action:

$$S_\varphi = \int_0^{\hbar\beta} d\tau \int d^d r \left[\frac{\varepsilon}{8\pi}(\nabla\varphi)^2 + iQ\varphi\partial_j u_j\right] \tag{A.78}$$

where φ is the electromagnetic potential, Q is the charge of the crystal's ions, and ε is the dielectric constant of the material. Integrating out these electromagnetic field degrees of freedom generates a phonon-phonon interaction of the form:

$$S_u' = \frac{2\pi Q^2}{\varepsilon\beta}\sum_{n,\mathbf{q}} \frac{q_i^2 u_i^\dagger(\omega_n, q)u_i(\omega_n, q)}{q^2} \tag{A.79}$$

where the sum over n is a sum over Matsabura frequencies $\omega_n = \frac{2\pi n}{\beta}$ where $n \in \mathbb{Z}$ and $\mathbf{u}(\omega_n, q)$ is related $\mathbf{u}(\tau, x)$:

$$u_j(\tau, x) = \frac{1}{\sqrt{\hbar\beta}}\sum_n e^{i\omega_n\tau}\frac{1}{L^{d/2}}\sum_{\mathbf{q}} e^{i\mathbf{q}\cdot\mathbf{x}} u_j(\omega_n, \mathbf{q}). \tag{A.80}$$

Note that the action of Eq. A.79 effectively renormalizes the mass of the longitudinal optical phonon mode to $\sqrt{\left(\frac{4\pi Q^2}{\varepsilon}\right) + \omega_T^2}$ and as such this mode will have a gap even if ω_T is small (which will be

our assumption). Hence, we can integrate out these modes to capture the low-energy dynamics. As such, our effective action, written using the Matsabura modes of Eq A.80, is given by:

$$S_{\text{eff}} = \sum_{n,\mathbf{q}} \frac{\rho}{2} u_j^\dagger \left[(\omega_n^2 + \omega_T^2)\delta_{jl} + c_T^2 q^2 \right] \frac{q^2\delta_{jl} - q_j q_l}{q^2} u_l. \tag{A.81}$$

Now, if we impose $\partial_j u_j = 0$, the integrand of our effective action is invertible and one can easily extract the two-point polarization correlations $\langle P_+^\dagger(\omega_n, \mathbf{q}) P_-(\omega_m, \mathbf{q})\rangle = \frac{Q^2}{a^{2d}} \langle u_+^\dagger(\omega_n, \mathbf{q}) u_-(\omega_n, \mathbf{q})\rangle = \chi_{+-}(\omega_n, \mathbf{q})$:

$$\chi_{+-}(\omega_n, \mathbf{q}) = \frac{Q^2\hbar}{a^{2d}\rho} \frac{1}{\omega_d^2 + \omega_n^2} \tag{A.82}$$

where $\omega_d = \sqrt{c_T^2 q^2 + \omega_T^2}$. Note that this can be transformed into the retarded correlation function by rotating $i\omega_n \to \omega + i\eta$ yielding:

$$\chi_{+-}(\omega, \mathbf{q}) = \frac{Q^2\hbar}{a^{2d}\rho} \frac{1}{\omega_d^2 - (\omega + i\eta)^2} \tag{A.83}$$

Since, it is the imaginary component of χ_{+-} that enters into the expression for T_1 (Eq. A.51), we note that:

$$\text{Im}\left[\frac{1}{\omega_d^2 - (\omega + i\eta)^2} \right] = \frac{\pi}{2\omega_d} \left[\delta(\omega_d - \omega) - \delta(\omega_d + \omega) \right] \tag{A.84}$$

where we took $\eta \to 0$ in the last step. Thus, since $\delta(\omega_d - \omega) = \frac{\sqrt{c_T^2 q_{res}^2 + \omega_T^2}}{c_T^2 q_{res}} \delta(q - q_{res}) = \frac{\omega}{c_T^2 q_{res}} \delta(q - q_{res})$, where $q_{res} = \frac{\sqrt{\omega^2 - \omega_T^2}}{c_T}$, we have that

$$\frac{1}{T_1} = \frac{1}{4}\mu_0^2 d_\perp^2 \coth\left(\frac{\beta\hbar\omega}{2}\right) \left[\frac{c^4}{16\pi} \frac{Q^2\hbar}{\rho a^4} \right] \times \begin{cases} \left[e^{-2q_{res}d} \frac{\pi}{2c_T^2} q_{res}^2 \right] & \omega_T \le \omega \\ 0 & \omega_T > \omega \end{cases} \tag{A.85}$$

from which we get the numerical prediction of $1/T_1$. Note that in this section, we referred to the transverse optical phonon mode mass and velocity as ω_T and c_T respectively (to distinguish it from the longitudinal optical phonon mode). To make contact with the notation of the main text, simply relabel $\omega_T \to \omega_0$ and $c_T \to c_s$.

A.3 Derivation of $1/T_1$ Scaling across Para-to-Ferroelectric Phase Transitions

In this section, we provide additional details regarding how qubit sensors can shed light on paraelectric to ferroelectric phase transitions. We start with an intuitive real space argument for distance scaling of noise, which hints towards a possible enhancement of $1/T_1$ as we approach the critical point. We next consider a thermal (classical) phase transition where we detail the precise derivation and additional intuition of the scaling theory of the main text. We conclude by doing the same for the quantum case.

A.3.1 Intuitive Real Space Argument for Distance Scaling of $1/T_1$

In the main text, we claimed that studying the qubit-sample distance scaling of $1/T_1$ can provide a tell-tale signature of approaching the critical point. To justify this, we provide some intuition for the distance scaling of the noise away from and near the critical regime, based on a simple real-space picture. Roughly speaking, the relaxation rate of the qubit can be expressed as the frequency-filtered correlation function of electric fields generated by polarization fluctuations. Since the qubit is sensitive to polarization fluctuations on an area of size d^2 within the 2d sample (corresponding to the solid angle subtained by the qubit at the sample), the relaxation rate takes the following form:

$$\frac{1}{T_1} \sim \sum_{i,j} \langle E_i E_j \rangle_\omega \sim \sum_{i,j} \left\langle \frac{P_i}{d^3} \frac{P_j}{d^3} \right\rangle_\omega \sim \frac{1}{d^6} \times d^2 \times \sum_i \langle P_i P_0 \rangle_\omega = \frac{1}{d^4} \langle P_i P_0 \rangle_\omega \tag{A.86}$$

where we used translation invariance of the correlation function in the third step to integrate over the 'center of mass' coordinate which gives an extra factor of d^2. For low frequencies, we may expect that the polarization correlator $\langle P_i P_0 \rangle_\omega$ is not very different from the static correlator $\langle P_i P_0 \rangle_{\omega \to 0}$ (we will revise this crude approximation later within specific models). Therefore, if the sample-probe distance d is larger than the correlation length ξ, the correlator yields ξ^2. This happens when we are far enough from the critical point so that ξ is small, or when the sample is quite far so that d is large. In this regime, $1/T_1$ scales as d^{-4}. In contrast, when we are close to the sample or near the critical point so that $d \ll \xi$, then the correlator yields d^2. So, naively we expect $1/T_1$ to scale as d^{-2}, although the precise scaling will depend on the nature of the dynamics near the critical point. Therefore, a change in the scaling of $1/T_1$ as a function of distance can signal criticality, as argued in the main text.

A.3.2 Derivation of $1/T_1$ near thermal ferroelectric transition: Mean-field theory and scaling theory

As dicussed in the main text, the transition between a paraelectric and a ferroelectric occurs due to the softening of the transverse optical phonon mode. Specifically, the gap ω_0 of this mode decreases as one lowers the temperature, and $\omega_0 \xrightarrow{T \to T_c} 0$. Near the critical regime, the temperature $T \sim T_c$ is much larger than the gap and so there is always a large occupancy of this mode and accordingly the considerations of classical hydrodynamics of a critical mode will apply. The dynamics of the polarization in the critical regime (and consequently the scaling theory of dynamical correlations) are strongly constrained by conservation laws. In our case of interest, the order parameter (polarization density) is an Ising order parameter, which is not conserved by the dynamics. We further assume that we can neglect coupling of the order parameter to a diffusive mode (such as conserved energy density). Thus, following Refs. [138, 139, 145], we can write down the expression for the dynamic electrical susceptibility at a mean-field level.

$$\chi(\mathbf{q}, \omega) \propto \frac{1}{-i\omega/\Gamma + \mathbf{q}^2 + \xi^{-2}} \tag{A.87}$$

where $\xi^{-1} \propto |T - T_c|$ is the inverse correlation length, and Γ determines the rate of approach to thermal equilibrium after a perturbation. Using this expression for $\chi(\mathbf{q}, \omega)$, we evaluate the

mean-field scaling of $1/T_1$ as a function of distance. Specifically, we find that in the experimentally relevant limit of small qubit splitting ($\omega \to 0$):

$$\frac{1}{T_1} \sim \frac{2T}{\omega}\int_0^\infty dq\, q^3 e^{-2qd}\ \mathrm{Im}[\chi(q,\omega)] \xrightarrow{\omega\to 0} \begin{cases} \frac{T}{\Gamma}\ln\left(\frac{\omega d^2}{\Gamma}\right), & d \ll \xi \\ \frac{T\xi^4}{\Gamma d^4}, & d \gg \xi \end{cases} \tag{A.88}$$

As argued in the previous subsection, we recover the d^{-4} behavior of $1/T_1$ away from criticality ($d \gg \xi$), where mean-field theory is expected to be reasonably accurate. However, it may break down in 2D near criticality, and therefore we resort to a more general scaling theory for $1/T_1$. Near the critical point, the behavior is characterized by the following scaling form of the dynamic electrical susceptibility (assuming spatial isotropy for):

$$\chi(\mathbf{q},\omega) = \chi(\mathbf{q})Y(\omega q^{-z}, q\xi), \text{ where } \chi(q) \equiv \chi(q,0) \sim q^{-2+\eta} \text{ and } Y(0,q\xi) = 1\ \forall\ q \tag{A.89}$$

At the critical point, $\xi \to \infty$ and therefore, $\chi(\mathbf{q},\omega) \sim q^{-2+\eta}Z(\omega q^{-z})$, using this gives the following scaling form for $1/T_1$:

$$\frac{1}{T_1} \sim \frac{2T}{\omega}\int_0^\infty dq\, q^3 e^{-2qd} \times q^{-2+\eta}Z(\omega q^{-z}) = \frac{2T}{\omega d^{2+\eta}}\Phi(\omega d^z) \tag{A.90}$$

Note that the above form implies that there is an apparent divergence in $1/T_1$ as $\omega \to 0$. However, this is somewhat misleading, as general considerations imply that $\mathrm{Im}[\chi(\mathbf{q},\omega)]$ is necessarily odd in ω [284]. Therefore, we can recast this scaling form by defining $\Phi(\omega d^z) = \omega d^z\, \Psi(\omega d^z)$:

$$\frac{1}{T_1} \sim \frac{2T}{d^{2+\eta-z}}\Psi(\omega d^z) \tag{A.91}$$

which was the result quoted in Eq. 6.63 in the main text. The mean-field d-scaling of $1/T_1 \sim \ln(\omega d^2)$ discussed earlier may be found from the more general scaling expression in Eq. (A.91) by using mean-field critical exponents $\eta = 0$ and $z = 2$ [145], and using the scaling function $\Psi(x) = \ln(x)$.

A.3.3 Derivation of $1/T_1$ near quantum ferroelectric transition

We now turn our attention to the quantum para-to-ferroelectric phase transition, and derive the appropriate scaling relations for $1/T_1$. Unlike the classical case where one needs to supplement the free-energy by additional phenomenological equations of motion of the order parameter, the quantum dynamics of polarization is completely determined by the Hamiltonian [284]. Furthermore, energy is always conserved if the Hamiltonian is time-independent. Therefore, in principle, once we know the quantum Hamiltonian we should be able to extract all dynamical correlations. In practice this often turns out to be quite difficult, and therefore one has to resort to certain limiting cases.

We consider the experimentally relevant limit of very low frequencies ($\omega \ll T$). In this regime, the quantum dynamics is typically relaxational and its description using weakly interacting soft modes is not accurate [284]. Nevertheless, we can write down a generic scaling function analogous to the classical case, which includes an additional scaling variable ω_0/T, where ω_0 is the gap of the soft mode that closes at $T = 0$ and $\lambda = \lambda_c$, the quantum critical point.

$$\chi(\mathbf{q},\omega) = \chi(\mathbf{q})Y_q\left(\frac{\omega}{T}, \frac{\omega_0}{T}, \frac{c_s q}{T}\right), \text{ where } \chi(q) \sim q^{-2+\eta} \text{ as in the classical case} \tag{A.92}$$

where Y_q is a dimensionless quantum scaling function. Plugging this into Eq. 6.62 in the main text gives the relaxation rate as:

$$\frac{1}{T_1} \sim \frac{2T}{\omega}\int_0^\infty dq\, q^3 e^{-2qd}\ \mathrm{Im}[\chi(\mathbf{q},\omega)] = \frac{1}{d^{2+\eta}}\Psi\left(\frac{\omega}{T}, \frac{\omega_0}{T}, \frac{c_s}{Td}\right) \tag{A.93}$$

While the scaling relation in Eq. (A.93) is formally correct, it unfortunately does not give us a lot of information. Therefore, it is useful to resort to a more phenomenological form of $\chi(\mathbf{q},\omega)$ which cannot be rigorously derived analytically, but is nevertheless well-motivated and more predictive for the behavior of $1/T_1$ in the small ω/T limit (the dynamical critical exponent $z = 1$ for this transition, but we keep a general z).

$$\chi(\mathbf{q},\omega) = \frac{\chi(0,0)}{1 - i\omega/\Gamma + q^2\xi^2},\ \text{where}\ \ \Gamma \sim T,\ \ \ \xi \sim \frac{c_s}{T^{1/z}}\ \text{and}\ \chi(0,0) \sim T^{(-2+\eta)/z} \tag{A.94}$$

To motivate the form of $\chi(\mathbf{q},\omega)$ in the vicinity of the quantum critical point, we make the following observations. First, we expect a finite relaxation rate Γ towards equilibrium even at $q = 0$ (as the order parameter is not-conserved), and finite q corrections are expected to be analytic at non-zero T when $\lambda \approx \lambda_c$. Second, we note that exactly at the critical value of the tuning parameter, i.e, $\lambda = \lambda_c$, the static uniform susceptibility $\lim_{q\to 0}\chi(q,0)$ only diverges at $T = 0$, but remains finite at non-zero T with a correlation length ξ. Next, since the only energy-scale in the quantum critical regime is T, we must have $\Gamma \sim T$, and $\xi \sim c_s/T^{1/z}$ (which corresponds to a smaller correlation length at larger T due to thermal fluctuations). Finally, static scaling theory requires that $\chi(q,0) \sim q^{-2+\eta}$ at $T = 0$ and obeys a scaling relation of the form $\chi(q,0) = q^{-2+\eta}X(q\xi)$ for any T. Non-divergence of $\chi(q,0)$ at finite $T > 0$ then essentially fixes $\chi(0,0) \sim T^{(-2+\eta)/z}$. Thus, we have all the ingredients to arrive at the postulated form of $\chi(\mathbf{q},\omega)$ in Eq. (A.94). We note that a similar form is an excellent approximation to the low-frequency dynamics of the one-dimensional by comparing with the exact solution [284, 285]; our arguments show that this should be true for non-conserved dynamics in 2D as well. Using Eq. (A.94), we can derive the scaling of $1/T_1$ for small ω/T:

$$\begin{aligned}\frac{1}{T_1} \sim \frac{2T}{\omega}\int_0^\infty dq\, q^3 e^{-2qd}\ \mathrm{Im}[\chi(\mathbf{q},\omega)] &= \frac{2T\chi(0,0)}{\Gamma_T}\int dq\, \frac{q^3 e^{-2qd}}{(1+q^2\xi_T^2)^2} \\ &\propto \begin{cases} T^{(2+\eta)/z}\ln\left(\frac{c_s}{dT^{1/z}}\right),\ d \ll \xi_T \\ T^{(-2+\eta)/z}d^{-4},\ d \gg \xi_T \end{cases}\end{aligned} \tag{A.95}$$

which is Eq. 6.65 in the main text. We note that just like the classical case, the distance-scaling of $1/T_1$ is d^{-4} for d much larger than the correlation length ξ (i.e, away from criticality), but is significantly altered as we approach the critical point ($\lambda = \lambda_c$ and $T = 0$).

A.4 Derivation of Dispersion Relation for Dipolaron Mode

In this section, we derive the dipolaron dispersion for a two-dimensional fluid of electrically neutral dipolar molecules. Like plasmons in a charged Fermi liquid, dipolarons are longitudinal collective

modes that arise due to long-range electrostatic interactions in dipolar fluids. We know that nature of plasmons in a Fermi liquid differ drastically between two and three spatial dimensions — in $d = 3$, plasmons are gapped excitations at $\mathbf{q} = 0$, while in $d = 2$, they are gapless with a dispersion $\omega_p(\mathbf{q}) \propto \sqrt{q}$. The reason is the weaker electric field created by two dimensional charge imbalance results in a weaker restoring force at large distances, compared to a three dimensional charge imbalance. Such an effect is at play for dipolarons too, resulting in gapless dispersion $\omega_d^2(\mathbf{q}) \sim aq^2 + bq^3$ for dipolarons in two dimensions. In what follows, we derive this dispersion from a simple hydrodynamic treatment of dipolar density fluctuations. We note that our results are in accordance with more a microscopic treatment of collective modes in two-dimensional dipolar gases [202].

Consider a fluid of dipolar molecules at equilibrium density n_d at chemical potential μ_{eq} and equilibrium velocity $\mathbf{v}_0 = 0$. Now we consider fluctuations about the mean density so that there is local density profile $\delta n(\mathbf{r}, t) = n(\mathbf{r}, t) - n_d$, and velocity $\mathbf{v}(\mathbf{r}, t) \neq 0$. The linearized continuity equation and Euler's (force) equation read as follows respectively:

$$\partial_t \delta n(\mathbf{r}, t) + n_d \nabla \cdot \mathbf{v} = 0, \quad m n_d \partial_t \mathbf{v} = -n_d \nabla \left(\mu_{eq} + \frac{\partial \mu}{\partial n} \delta n \right) - \nabla(\boldsymbol{\mu} n_d \cdot \mathbf{E}) \tag{A.96}$$

The generated electric field can be related to the fluctuating polarization density $\boldsymbol{\mu} n(\mathbf{r})$ as discussed previously (neglecting retardation effects):

$$\begin{aligned} E_i(\mathbf{r}, t) &= \int d\mathbf{r}' T_{ij}^d(\mathbf{r}, \mathbf{r}') \mu_j n(\mathbf{r}', t), \\ T_{ij}^d(\mathbf{q}) &= \frac{1}{4\pi\epsilon_0} \int d^d r e^{i\mathbf{q}\cdot\mathbf{r}} \partial_i \partial_j \left(\frac{1}{r} \right) = \begin{cases} -\frac{q_i q_j}{\epsilon_0 q^2}, & D = 3 \\ -\frac{q_i q_j}{2\epsilon_0 q}, & D = 2 \end{cases} \end{aligned} \tag{A.97}$$

Going to momentum space and using that the isothermal compressibility is given by $\kappa = \frac{1}{n_d^2}(\frac{\partial n}{\partial \mu})$, we can combine Eqs. (A.96) to find the following equation for $\delta n(\mathbf{q}, \omega)$:

$$\omega^2 \delta n(\mathbf{q}, \omega) = \left(\frac{1}{\kappa m n_d} \mathbf{q}^2 + \frac{\mu_i \mu_j n_d}{m} q_i T_{ij}^d(\mathbf{q}) q_j \right) \delta n(\mathbf{q}, \omega) \tag{A.98}$$

Using the form of T_d from Eq. (A.97) for $D = 2$, we finally get the collective mode dispersion in $D = 2$ that was quoted in the main text:

$$\omega_d^2(\mathbf{q}) = v^2 q^2 + \frac{n_d q (\mathbf{q} \cdot \boldsymbol{\mu})^2}{2\epsilon_0 m} \tag{A.99}$$

where $v = \sqrt{1/\kappa m n_d}$ is the speed of the collective mode at small $\mathbf{q}$. This is analogous to the linearly dispersing zero sound mode in Fermi liquids, and does not require dipolar interactions. At larger momentum, anisotropy effects due to dipolar interactions come into play and we have a dominating $q^{3/2}$ term in the dispersion. In particular, if we take the angular average over all directions of $\boldsymbol{\mu}$ (which can point anywhere on the 2-sphere), then we can replace $(\mathbf{q} \cdot \boldsymbol{\mu})^2 \to q^2 \mu^2 / 3$, and we recover the dispersion in Ref. [202] (converted to SI units).

$$\omega_d^2(\mathbf{q}) = c_s^2 q^2 + \frac{\mu^2 n_d q^3}{6\epsilon_0 m} \tag{A.100}$$

A.5 Derivation of Polarization Correlations for Relaxor Ferroelectric Model

In the main text, we investigated the relaxation rate of a qubit sensor in the vicinity of a relaxor ferroelectric modeled via the Hamiltonian:

$$H = \sum_i \left[\frac{\Pi_i^2}{2M} + V(u_i) \right] - \frac{1}{2} \sum_{i,j} v_{ij} u_i u_j - \sum_i E_i^{\text{ext}} u_i - \sum_i h_i u_i \tag{A.101}$$

where $\Pi_i = M\dot{u}_i$ is the conjugate momentum of the polarization-carrying displacement u_i (chosen to be in the z-direction), M is the effective mass, E_i^{ext} is an external applied field, $h_i \sim N(0, \Delta)$ is a random field, $V(u_i) = \frac{\kappa}{2} u_i^2 + \frac{\gamma}{4} u_i^4$ ($\kappa, \gamma > 0$), and

$$v_{ij} = -\frac{1}{|\mathbf{r}_i - \mathbf{r}_j|^3} \quad \text{if } i \neq j \tag{A.102}$$

is the dipolar interaction and $\mathbf{r}_i = (x_i, y_i, 0)$ is the 2D lattice coordinate of the i^{th} dipole. In this section, we provide details for how we derived the form of the qubits relaxation rate. We do so by computing the disorder-averaged polarization fluctuations arising from the above Hamiltonian, following the derivation in Refs. [134, 135, 330]. In general, this is hard to do because of (i) the anisotropic and long-range nature of the dipolar interaction and (ii) the anharmonicity of the local potential. We treat the former by using the leading order correction to mean field (the Onsager approximation) because such fluctuations are important in the relaxor context and we treat the latter using a quasi-harmonic approximation (we linearize the equations of motion). With this in mind, we write the equations of motion under Eq. A.101 as:

$$M\ddot{u}_i = -\frac{dV(u_i)}{du_i} - h_i u_i - E_i^{\text{local}} \quad \text{where} \quad E_i^{\text{local}} = \sum_j v_{ij} u_j + E_i^{\text{ext}} \tag{A.103}$$

To simplify this Hamiltonian, we can make a mean-field approximation:

$$E_i^{\text{local}} \approx E_i^{\text{MF}} = \sum_j v_{ij} \langle u_j \rangle + E_i^{\text{ext}} - \lambda \langle u_i \rangle \tag{A.104}$$

where $\langle \cdots \rangle$ indicates thermal averaging and we introduced the Lagrange multiplier $-\lambda\langle u_i \rangle$ which is used to enforce the fluctuation-dissipation theorem for the polarization fluctuations we compute [47]. It is precisely this Lagrange multiplier that enables encorporating fluctuations, to leading order. This yields:

$$H \approx \sum_i H_i = \sum_i \left[H_i^0 - h_i u_i - E_i^{\text{MF}} u_i \right] \tag{A.105}$$

where $H_i^0 = \frac{\Pi_i^2}{2M} + V(u_i) - (\lambda/2) u_i^2$.

A.5.1 Self-Consistent Equations for Phonon Dispersion

Given the model derived above, we can compute the phonon dispersion self-consistently which will consequently determine the form of the dipolar fluctuations that enter our expression for $1/T_1$. To do so, we aim to compute the dielectric susceptibility $\chi(\omega, \mathbf{q}) = \overline{\delta\langle u(\omega, \mathbf{q})\rangle}/\delta E^{\text{ext}}(\omega, \mathbf{q})$ where $\delta\langle u(\omega, \mathbf{q})\rangle$ indicates deviation of the displacement field from its thermal expectation and $\overline{\cdots}$ indicates averaging over disorder realizations. We do this by defining an auxiliary susceptibility, $\varphi_{h_i}(\omega)$, which characterizes the system's susceptibility to the local mean field:

$$\delta\langle u_i(\omega)\rangle = \varphi_{h_i}(\omega) E_i^{\text{MF}}(\omega). \tag{A.106}$$

Now we disorder average both sides of this expression and take the 2D discrete fourier transform of both sides. In doing so, we assume that the effects of the random fields decouple in $\varphi_{h_i}(\omega)$ and $\langle u_i\rangle$ implying that $\overline{\varphi_{h_i}}(\omega) = \overline{\varphi_h}(\omega)$ which only has a $\mathbf{q} = 0$ component. This yields:

$$\overline{\delta\langle u(\omega, \mathbf{q})\rangle} = \overline{\varphi_h}(\omega)\left[v_{\mathbf{q}}\overline{\delta\langle u(\omega, \mathbf{q})\rangle} - \lambda\overline{\delta\langle u(\omega, \mathbf{q})\rangle} + \delta E^{\text{ext}}(\omega, \mathbf{q})\right]. \tag{A.107}$$

Note that, in the above expression, $v_{\mathbf{q}}$ is the 2D discrete Fourier transform of the dipolar interaction with the assumption that the dipoles are arranged in a square lattice. The precise form of this discrete Fourier transform was worked out in Refs. [349, 100] and was found to be:

$$v_{\mathbf{q}}/n = \frac{1}{n}\sum_{i,j} v_{i,j} e^{i\mathbf{q}\cdot(\mathbf{r}_i - \mathbf{r}_j)} \approx v_0\left(1 - \frac{3}{4\pi f}|\mathbf{q}|\right) \quad \text{with} \quad v_0 = \frac{8\pi}{3} f \tag{A.108}$$

where f is a lattice specific constant and is $f = 1.078$ for a simple cubic lattice. Using Eq. A.107, we see that the dielectric susceptibility can be written as:

$$\chi(\omega, \mathbf{q}) = \frac{\overline{\delta\langle u(\omega, \mathbf{q})\rangle}}{\delta E^{\text{ext}}(\omega, \mathbf{q})} = \frac{1}{\overline{\varphi_h}(\omega)^{-1} - (v_{\mathbf{q}} - \lambda)}. \tag{A.109}$$

Expression in hand, we can now use the classical equations of motion of the displacement field under the Hamiltonian of Eq. A.105 to directly compute the form of $\overline{\varphi_h}(\omega)$ from which the above susceptibility can be computed directly. The equations of motion are:

$$M\ddot{u}_i = -\frac{dV(u_i)}{du_i} + \lambda u_i + h_i + E_i^{\text{MF}} - \Gamma\dot{u}_i = -(\kappa - \lambda)u_i - \gamma u_i^3 + h_i + E_i^{\text{MF}}(t) - \Gamma\dot{u}_i \tag{A.110}$$

where we introduced a phenomenological decay Γ to regulate our response functions. At the end, we will take $\Gamma \to 0$. Now, to treat this equation analytically, we linearize it by treating deviations of the displacement from its disorder and thermal average to be small $u_i(t) = p + \delta u_i(t)$ where $p = \overline{\langle u_i(0)\rangle}$ is the static mean displacement field. Note that, here, $\delta u_i(t)$ contains all of the time dependence of $u_i(t)$ and is not in general zero after thermal and disorder averaging. This yields:

$$M\ddot{\delta u}_i(t) = -(\kappa - \lambda)(p + \delta u_i) - \gamma(p^3 + 3p^2\delta u_i + 3p\delta u_i^2 + \delta u_i^3) + h_i + E_i^{\text{MF}}(t) - \Gamma\dot{\delta u}_i \tag{A.111}$$

In accordance with standard linear response, we assume that, in the absence of the external applied field, our displacement field has no dynamics (e.g $\overline{\langle\dot{\delta u}_i\rangle} = \overline{\langle\ddot{\delta u}_i\rangle} = 0$). After thermal and disorder averaging, this yields:

$$\left[(k - \lambda) + \gamma p^2 + 3\gamma\overline{\langle\delta u_i(0)^2\rangle}\right] p = 0 \tag{A.112}$$

which places a condition on p. Note that in the above expression, we have used the fact that $\langle \dot{\delta u_i} \rangle = \langle \ddot{\delta u_i} \rangle = 0$ to replace $\overline{\langle \delta u_i(t)^2 \rangle} = \overline{\langle \delta u_i(0)^2 \rangle}$. Now, we add the above expression to our original equations of motion from which we can compute our auxiliary susceptibility:

$$\begin{aligned}
&M\ddot{\delta u_i}(t) \\
&= -(\kappa - \lambda)\delta u_i(t) - \gamma \left[3p^2 \delta u_i(t) + \delta u_i^3(t) + 3p(\delta u_i^2(t) - \overline{\langle \delta u_i(0)^2 \rangle}) \right] + h_i + E_i^{\mathrm{MF}}(t) - \Gamma \dot{\delta u_i}(t) \\
&= -\left(\kappa - \lambda + 3\gamma \left[\overline{\langle \delta u_i^2(0) \rangle} + p^2 \right] \right) \delta u_i(t) + h_i + E_i^{\mathrm{MF}}(t) - \Gamma \dot{\delta u_i}(t)
\end{aligned} \tag{A.113}$$

where in the second line, we approximated $\delta u_i^2(t) = \overline{\langle \delta u_i^2(0) \rangle}$ and $\delta u_i^3(t) = 3\overline{\langle \delta u_i^2(0) \rangle} \delta u_i(t)$. From this, we can easily compute the auxiliary susceptibility:

$$\overline{\varphi_h}(\omega) = \frac{1}{M\Omega'^2 - M\omega^2 + i\omega\Gamma} \quad \text{where} \quad M\Omega'^2 = \left(\kappa - \lambda + 3\gamma \left[\overline{\langle \delta u_i^2(0) \rangle} + p^2 \right] \right) \tag{A.114}$$

which immediately yields an expression for the retarded polarization correlation function (also called dielectric susceptibility):

$$\chi(\omega, \mathbf{q}) = \frac{1}{M\Omega_{\mathbf{q}}^2 - M\omega^2 + i\omega\Gamma} \tag{A.115}$$

with the phonon displacement mode appearing as a pole in the denominator:

$$M\Omega_{\mathbf{q}}^2 = M\Omega_0^2 + (v_0 - v_{\mathbf{q}}) = \left[M\Omega'^2 - (v_0 - \lambda) \right] + (v_0 - v_{\mathbf{q}}) \tag{A.116}$$

Now, to determine the parameter λ, we impose fluctuation-dissipation:

$$\begin{aligned}
&\overline{\langle u_i^2(0) \rangle} - \overline{\langle u_i(0) \rangle^2} \\
&= \frac{1}{N} \sum_{\mathbf{q}} \int \frac{d\omega}{2\pi} \coth\left(\frac{\beta\omega}{2} \right) \mathrm{Im}[\chi(\omega, \mathbf{q})] \\
&= \frac{1}{N} \sum_{\mathbf{q}} \frac{1}{2M\Omega_{\mathbf{q}}} \coth\left(\frac{\beta\Omega_{\mathbf{q}}}{2} \right)
\end{aligned} \tag{A.117}$$

where we used that fact that $\lim_{\Gamma \to 0} \mathrm{Im}[\chi(\omega, \mathbf{q})] = \frac{\pi}{2M\omega} \left[\delta(\omega - \Omega_{\mathbf{q}}) + \delta(\omega + \Omega_{\mathbf{q}}) \right]$. Now, to close the self-consistency equations, we need expressions for $\overline{\langle \delta u_i^2(0) \rangle}, \overline{\langle u_i^2(0) \rangle}, \overline{\langle u_i(0) \rangle^2}$. To do so, first note that $\overline{\langle \delta u_i^2(\omega) \rangle} = \overline{\langle u_i^2(\omega) \rangle} - p^2$. Next, note that:$\langle u_i(0) \rangle = p + \sum_j \chi_{ij}(0) h_j$ by definition. Therefore, this immediately yields that:

$$\overline{\langle u_i(0) \rangle^2} = p^2 + \frac{\Delta^2}{N} \sum_{\mathbf{q}} \chi(0, \mathbf{q})^2 = p^2 + \frac{\Delta^2}{N} \sum_{\mathbf{q}} \frac{1}{(M\Omega_{\mathbf{q}}^2)^2} \tag{A.118}$$

Therefore, we have closed the self-consistency equations. Eliminating λ and Ω' from Eqs. A.116 by using the definition of Ω' in Eq. A.114, we find the following self-consistency equations:

$$M\Omega_{\mathbf{q}}^2 = \left[\kappa + 3\gamma(\overline{\langle u_i^2(0) \rangle} - p^2) - v_0 \right] + (v_0 - v_{\mathbf{q}}) \tag{A.119}$$

$$\overline{\langle u_i^2(0) \rangle} = p^2 + \frac{1}{N} \sum_{\mathbf{q}} \left[\frac{1}{2M\Omega_{\mathbf{q}}} \coth\left(\frac{\beta\Omega_{\mathbf{q}}}{2} \right) + \frac{\Delta^2}{(M\Omega_{\mathbf{q}}^2)^2} \right] \tag{A.120}$$

where p can be determined from a thermodynamic analysis by finding minima of free energies. This is a very lengthy procedure (which was carried out in Ref. [134]) and so, for our purposes, we can pick $p = 0$. To compute the polarization correlations entering into the expression for $1/T_1$, we use Eq. A.115 in the limit where $\Gamma \to 0$.

A.5.2 Computation of Critical Temperature

Using the methods above, it is possible to compute a critical temperature for the para-to-ferroelectric transition that exists in the absence of disorder ($\Delta = 0$). Recall that at the critical temperature, the mass of the transverse optical phonon mode goes to zero. Using Eq. A.119, we can express the mode mass as:

$$M\Omega_0^2 = \left[\kappa + 3\gamma(\overline{\langle u_i^2(0)\rangle} - p^2) - v_0\right] \tag{A.121}$$

Moreover, in the absence of disorder and with $p = 0$, the fluctuation $\overline{\langle u_i^2(0)\rangle}$ is found by Eq. A.120 to be:

$$\overline{\langle u_i^2(0)\rangle} = \frac{1}{N}\sum_{\mathbf{q}}\left[\frac{1}{2M\Omega_{\mathbf{q}}}\coth\left(\frac{\beta\Omega_{\mathbf{q}}}{2}\right)\right] \approx \frac{1}{N}\sum_{\mathbf{q}}\frac{k_BT}{M\Omega_{\mathbf{q}}^2} = \frac{1}{N}\sum_{\mathbf{q}}\frac{k_BT}{M\Omega_0^2 + (v_0 - v_{\mathbf{q}})} \tag{A.122}$$

We can solve for T_c by setting $\Omega_0 = 0$ and plugging Eq. A.122 into Eq. A.121, yielding:

$$k_BT_c = \frac{v_0 - \kappa}{3\gamma} \times \left[\frac{1}{N}\sum_{\mathbf{q}}\frac{1}{(v_0 - v_{\mathbf{q}})}\right]^{-1} \tag{A.123}$$

Note that this T_c does not indicate a transition in the relaxor case and is simply a reference temperature.